EVOLUTION OF LATE CRETACEOUS KALLANKURICHCHI LIMESTONE FORMATION, ARIYALUR GROUP, CAUVERY BASIN, INDIA: A PHYSICO-CHEMICAL INVENTORY

Thesis submitted to Jadavpur University

for the degree of

Doctor of Philosophy (Science)

(2024)

By

SHILPA SRIMANI

DEPARTMENT OF GEOLOGICAL SCIENCES
JADAVPUR UNIVERSITY
KOLKATA-700 032

যাদবপুর বিশ্ববিদ্যালয়
কলকাতা-৭০০০৩২, ভারত

JADAVPUR UNIVERSITY
KOLKATA-700032, INDIA

FACULTY OF SCIENCE : DEPARTMENT OF GEOLOGICAL SCIENCES

CERTIFICATE FROM THE SUPERVISOR

This is to certify that the thesis entitled "**EVOLUTION OF LATE CRETACEOUS KALLANKURICHCHI LIMESTONE FORMATION, ARIYALUR GROUP, CAUVERY BASIN, INDIA: A PHYSICO-CHEMICAL INVENTORY**" submitted by **Ms. Shilpa Srimani**, who got her name registered on **29.01.2018** for the award of **Ph. D. (Science)** degree of **Jadavpur University,** is absolutely based upon her own work under the supervision of **Prof. Subir Sarkar** and that neither this thesis nor any part of it has been submitted for either any degree/diploma or any other academic award anywhere before.

Subir Sarkar
17.5.2024

(Signature of the Supervisor date with official seal)

Dr. Subir Sarkar
Professor
Department of Geological Sciences
Jadavpur University
Kolkata - 700 032

Dedicated to,

The countless individuals
who have played a major role in shaping
my academic and personal growth…

ACKNOWLEDGEMENTS

A doctoral thesis is commonly portrayed as a solitary pursuit, but the work presented in this thesis would not have been possible without the consistent supports of certain people, both in personal and professional spheres. So, I take this opportunity to acknowledge them and extend my sincere gratitude for helping me to make this thesis a reality.

At the very outset, I would like to express my heartfelt gratitude towards my supervisor, Prof. Subir Sarkar for accepting me as a Ph.D. student. He cordially welcomed me to his lab and guaranteed a nurturing work atmosphere. Without his thorough guidance, constant encouragement and most importantly, his enduring patience during the fieldwork, manuscript preparation, and scrutiny phases, this thesis would not have come to fruition. Under his guidance, I not only gained educational enrichment but also underwent personal growth. During many challenging moments, his warmth and kind cooperation served as my source of strength and courage. I am grateful to him for entrusting me with responsibilities time and again and expanding my horizons as an independent researcher.

I am also deeply indebted to Prof. Pradip K. Bose for his proactive support, valuable advice and perseverance towards me during the entire tenure. The stimulating discussions and constructive criticism have enhanced the quality of this research. His immensely valuable ideas, and suggestions from the initial to the final level enabled me to develop an understanding of the subject.

I would also like to express my deep sense of gratitude for the help and encouragement in various forms I received from Prof. Pulak Sengupta and Prof. Sanjay Sanyal. I would also like to convey my thanks and regards to (late) Prof. Subhendu Bardhan, Prof. K. Halder, Prof. Sucharita Chattopadhyay.

My Ma'am (Jayasri Sarkar) deserves a special mention for her constant motherly care towards me. I wish to express my honest and heartiest thanks to (late) Jethima, Gopa Pisimoni, Prasun Jethu and Runai Di for their encouragement and motivation.

I embrace the opportunity to give a special thanks to Nivedita Di who initially give a motion to my research work by providing me papers, giving contacts for carrying field work in Ariyalur. Special thanks to Sunipa Madam for being there with me in field. A notable thanks to Soumik Sir who always creates a cool environment for me.

I express my humble thanks for enormous support and encouragement from every member of the JUSEDILAB: Adrita Di, Anudeb Da, Amlan Da, Sabyasachi, Indrani, Arunava, Tathagata Da, Sudakshina, Avik, Souryadip, Bibek, Masum, Anirban, Shilpa. I am specially grateful to Soumyadeep for being my last minute savior during thesis editing.

I would like to thank Department of Science and Technology (DST- INSPIRE) for providing me the funding to pursue this research work and Department of Geological Sciences, Jadavpur University for the infrastructural facilities. I am also thankful to the Department of Earth Sciences, IIT Kanpur and NCESS, Kerala for instrumental facilities.

My sincere gratitude to Shastri Indo-Canadian Institute (SICI) for selecting my project and providing me Shastri Research Student Fellowship (SRSF) grants, 2019. I am grateful to Prof. Hairuo Qing, Department of Geology of University of Regina, Canada for hosting me

there in Canada and helping me in all the possible ways during my six months stay in Canada. I am also thankful to receive all sorts of infrastructural facilities there. Prof. Dr. Chris Holmden and his entire team specially, Dr. Sandra Timsic (Isotope Laboratory in-charge), provided an excellent opportunity to execute a part of my required analytical work in Saskatchewan Isotope Laboratory (SIL), University of Saskatchewan, Canada for the thesis; furthermore, elucidating my knowledge regarding the intricate details of sample preparation and analysis, thereby making my months long stay in Canada for my analytical work, fulfilling and satisfactory.

I would like to mention the cooperation provided by S. Makesh (DGM), Mr. E. Vasudevan (AGM), Hariprasad Sir and the other employees of Dalmia (Bharat) Cement Ltd., Ariyalur during my several field visits. A noteworthy and remarkable thanks for Prasad Sir (Tancem Mines Ltd.) for his kind cooperation during my entire fieldwork. I am also thankful to Muthaiya ji for his assistance and care during my fieldwork.

A special thanks to Binu Da for helping me out in varied administrative and non-academic work. I am thankful to all non–teaching staff of the Department specially Koushik Da, Sujit Da, Arin Da.

I am thankful to Mr. Rahul Kumar and his family for their support, generous care and the homely feeling in Canada and making my staycation wonderful. My friends in Canada, Siyang, Prabhleen, Yargi, Simran and Preet, their association has made my stay a pleasurable and memorable experience. My outing and exploring Canada with them will be etched permanently in my memory.

I would like to extend my personal thankfulness to my beloved school friends for tolerating my activities. They helped me to take care of my sanity subtly being there for me on a regular basis. During the moments of difficulties their cordiality and cooperation have been my strength.

Finally, I am deeply grateful for the great inspiration and unwavering support extended to me by my entire family. The belief my parents placed in me and the encouragement from my dida, mesai, masimoni, jethu (unfortunately he is no more), bomma have been the motivation for this achievement. Their love, affection, and steadfast support during every up and down gave me the strength. Without each and every one of them, I would not have made it this far.

I am also thankful to all, whom I could not mention here who helped me directly or indirectly throughout the work. I have had an astounding and thoroughly enriching experience and would like to extend my gratitude to everyone that has been a part of the same.

This work would not have been possible without the grace of the Lord Shiva.

Shilpa Srimani

SHILPA SRIMANI

ABSTRACT

The present thesis delves into sedimentological context, both physical and chemical characteristics of Kallankurichchi Limestone Formation, Ariyalur Group, built up within the Pondicherry sub-basin of the Cauvery Basin, South India. The motivation of the study was lack of sedimentological insight of the Kallankurichchi Formation of the Ariyalur Group which has so far yielded huge number of publications on its paleontological aspects. Its objective is to enhance the sedimentological and stratigraphic comprehension, addressing issues of both local and global significance. A high-resolution state-of-art facies analysis, integrated with petrographic and geochemical investigation for the ~60 m thick Kallankurichchi Formation has been the mainstay of this research work. It is sandwiched between two siliciclastic formations namely Sillakuddi and Kallamedu Sandstone Formation respectively.

This limestone formation was initiated with the repetitive influx of the coarse clastic of mixed siliciclastic and carbonate composition, which is unique and rarely documented, specifies a resurgence of tectonic unrest in the Cauvery rift basin. The study meticulously delineates the depositional history of these basin-margin coarse clastics, characterized by clast-supported, angular, extremely poorly sorted conglomerate horizons deposited under the sea, accompanied by sporadic marine fossil occurrences. These conglomerates grades into mass flow conglomerates and eventually massive calc-arenite, collectively forming wedge-shaped basin-margin scree fans. It can be presumed that these flows were triggered by subsidence, which resulted from renewed gaps in the formation and led to the collapse of scree cones. Contemporaneous tectonic events, marked by abundant slide planes, suggested continuous sagging of the basin, causing oxygen-depleted bottom water conditions favored a rare green marine clay formation, namely berthierine (identified by the strong ~7 Å basal spacing), hosted in ~3.5 m thick dark grey limestone, associated with scree conglomerates. It is formed by the alteration of metastable framework grains e.g., palagonitized sideromelane glass, along grain boundary of quartz and feldspar cleavages, suggesting its authigenic origin. Eventually, this scree derivatives and its associated facies passes laterally into the carbonate formation basinwards.

The state-of-art facies analysis and sequence building pattern for the rest of the formation broadly divides it into two facies associations, viz., (1) Wave-dominated and (2) Tide-dominated. Started with a tide dominated succession above the scree derivatives, followed by the wave dominated facies association towards the top (likely to be a transgressive system tract/ TST) and dominated again by a shallowing upward succession where tides were the prevalent process for their formation (likely to be a highstand system tract/ HST). Petrographic study shows that the lower tidal part is repleted by quartz flux, then quartz content diminishes which strongly suggests progressive shift of paleogeography from shoreward to basinward and again shallowing up indicated by high silicic input. The TST is topped by a ‘thin muddy facies’ demarcated the boundary between these two associations likely to be the maximum flooding surface (MFS). Detailed geochemical analysis

supplements paleoenvironmental reconstruction, paleo-redox and salinity conditions across different facies associations. The Kallankurichchi Formation exhibits LREE and MREE enrichments in tide-dominated and wave-dominated parts respectively. The lowest REE content in the maximum flooding surface (MFS) aligns with its most distal paleogeography of deposition. Paleoredox data suggests anoxic conditions in the lower part, while the wave-dominated middle part indicates oxic conditions, supporting the proliferation of organisms. Paleosalinity increases with the deepening of facies, with the lower salinity index of the tidal facies association reasserting its comparatively shoreward position.

Additionally, the identification of shellbank horizons and their association with storm-dominated facies provides insights into localized depositional conditions. Four shellbank horizons have been identified within this fossiliferous limestone formation, predominantly consisting of Gryphaeidae bivalves *Pycnodonte* sp. In contrast to the shellbanks, the fossils present in other parts of the formation are fragmented in nature and haphazardly oriented, particularly those closely associated with the shellbanks, identified as storm-dominated facies. The shellbanks possibly deposited in some restricted conditions developed behind the large-scale bars. Paleoproductivity values are higher in the shellbanks compared to other facies. Calculating paleo-ocean temperatures for the reconstruction of paleoclimatic conditions, oxygen isotope analysis has been conducted within the successive growth laminae of rudist bivalve *Pycnodonte* sp. (low-Mg calcitic shell) collected from the shellbanks. The average paleotemperature, calculated from the $\delta^{18}O$ values, was around 24.8°C, supporting Late Cretaceous warming conditions.

The overall deposition apparently took place in a shallow marine to shelf-lagoonal condition. The tide amplitude accentuated in comparatively constricted parts while the wave dominated facies present relatively in open shelf part. The faunal distribution varies throughout the formation incorporates varieties of foraminifera, echinoids, brachiopoda, cephalopoda and bivalves (most dominantly *Gyphea* and *Inoceramus*). All the relevant datasets cumulatively unveil the paleoenvironmental record and enrich the sequence stratigraphic framework of the Formation through space.

The multipronged study of the Kallankurichchi Limestone Formation of Ariyalur Group reveals a colourful history of the then Cauvery basin, starting from renewed rifting to the deposition of the entire limestone and their sequence building with change in hydrodynamic conditions, sediment supply in a warm and humid climate.

CONTENTS

Part-II: Aspect of Special Interests

CHAPTER-1

GENERAL INTRODUCTION

1.1 Introduction:

India is a graceful natural laboratory of Cretaceous period (145 Ma–65 Ma), the longest time period of the Phanerozoic Eon. It was a period of intense tectonics, when India drifted in the context of global paleogeography. Cretaceous time records an exceptional episode of accelerated breakup of the last supercontinent Pangaea, associated with numerous rift basins formation and volcanic episodes (Föllmi, 2012). It was the era when India departed from its conjugated association of Gondwanaland to the South Pole and travelled to the longest passage in the northern direction. It is the most impactful time when India witnessed three renowned volcanic episodes: Rajmahal in eastern part and Sylhet flood basalts in northeastern part and Deccan volcanism in the western part (Chakraborty et al., 2021). During this time there was a gradual shift in the climatic condition, which got reflected in the sedimentation pattern and fossil record. Generally, Cretaceous was unique for its warm and equable climate (Hay, 2008). Tropical sea-surface temperature was 4-7 °C higher than current days but polar regions were usually more than 20 °C warmer (Norris et al., 2002; Jenkyns et al., 2004). Continent to ocean temperature gradients were weaker. The warmer climate is an indication of higher amount of greenhouse gasses e.g., CO_2, Methane (CH_4) etc. and water vapor (Hay, 2008). The release of a substantial amount of CO_2 occurred at subduction zones due to the decomposition of Tethyan carbonates, contributing to global warming (Kent and Muttoni, 2008). The estimated atmospheric $_PCO_2$ level being approximately 2500 parts per million volume (ppmV) and 800-12,000 ppmV in the early and Late Cretaceous respectively (Cerling, 1991). In the Late Cretaceous period, the climate was notably warmer compared to contemporary atmospheric temperatures, and there were no persistent polar ice caps; the average annual temperatures at the equator reached 38°C (Chatterjee et al., 2017). Cretaceous was almost ice-free except at the poles (Scotese, 2015). It was a time of rapid sea floor spreading and creation of new epicontinental seas (<300 m deep). Late Cretaceous (94-65 Ma) observed the most extensive continental inundation since Ordovician (Hancock and Kauffman, 1979). During that time seas were calcitic in nature and had significantly shallower calcite compensation depth (CCD) compared to present day (Tucker and Wright, 1990). The Cretaceous period is known for ocean anoxic events, carbonate sedimentation, ecological and biotic evolution in the seas (Rodríguez-Tovar et al., 2009 and references therein; Chakraborty, 2016; Mandal, 2017). The era is notable for widespread development of

carbonate platforms, especially in and around the Tethyan Ocean (Schlager and Philip, 1990). The first appearance of many Cretaceous life-forms, the most significant one was the first appearance of angiosperms. Sea grasses, which play a significant role in carbonate sedimentation, are generally considered to be originated in the Tethys Ocean during the Late Cretaceous time (Perry and Beavington-Penney, 2005). These platforms were favored by the rudists for their prolific growth and diversification (Gili et al., 1995). The initial proliferation of the diatoms occurred in the Cretaceous oceans. A notable increase of bioturbation is reflected from the Cretaceous onwards.

Cauvery Basin is the largest epicontinental Mesozoic basin situated in the southernmost sedimentary basin of the east coast of India and preserved an exceptionally continuous succession of the entire Cretaceous age (syn-rift and post-rift Cretaceous sediments) from Sivaganga Formation (Barremian) to Kallamedu Formation (Maastrichtian) (Watkinson et al., 2007). The Late Cretaceous, specifically early Maastrichtian Kallankurichchi Formation of Ariyalur Group, addressed here, belongs to the Ariyalur outcrop of Ariyalur-Pondicherry sub-basin (northernmost sub-basin) of Cauvery Basin, India (Fig. 1.1a; Sastri et al., 1973, Prabhakar and Zutshi, 1993; Tewari et al., 1996a; Watkinson et al., 2007). This formation is one of the significant limestone horizons within the Cretaceous succession of the studied basin. As these Ariyalur outcrop preserves more or less a complete Albian-Maastrichtian sedimentary succession, it has been the subject of numerous paleontological, stratigraphic and geochemical studies. Blandford (1862) was the pioneer worker to initiate the paleontological work in Cauvery Basin. Stoliczka (1861-1873) carried out systematic study of the invertebrate fauna collected by Blanford and published the findings of his study in a series of volumes under the renowned 'Palaeontologia Indica', encompassing diverse groups such as echinoidea, brachiopoda, bivalvia, gastropoda, cephalopoda, and more. Stoliczka (1861-1873) and Kossmat (1897-1898) authored comprehensive monographs on macropaleontology, although their mentioned locations are difficult to find in field nowadays because of change of locality name. Stoliczka endorsed Blanford's three-fold classification through his paleontological research, and considered Uttatur, Trichinopoly and Ariyalur Group. Ayyasami (2006) documented the significance of oysters in the biostratigraphy of the Ariyalur area. He suggested that the presence of ostreids indicates the transgressive characteristics of sediment deposition. Paleoecological studies of

benthic bivalves Veneroid (Jaitley and Mishra, 2007, 2009), shell microstructure of oyster *Hyotissa semiplana* (Jaitley and Mishra, 2014), Inoceramid bivalves (? *Platyceramus*, *Cataceramus*) and the origin and environmental significance of shell concentrations of Kallankurichchi Formation (Fürsich and Pandey, 1999) from the Cauvery Basin have been documented. Foraminifera and its biostratigraphic classification were the mainstay of the study by most of the workers (Rao, 1957; Banerjee, 1968; Malarkodi et al., 2017). Besides biostratigraphy, Lydekker (1879) undertook the initial exploration of vertebrate fauna within the Ariyalur Group, documenting the existence of a dinosaur, *Megalosaurus*. Yadagiri and Ayyasami (1979) have reported *Stegosaurus* sp. from the Ariyalur Group. Further, occurrences of Serpulid with Ophiomorpha-rich sedimentary units, their ecosystem and variations in environmental parameters have also been documented (Ramkumar et al., 2021). Detailed study on brachiopod (Radulovic and Ramamoorthy, 1992), echinoid (Aziz, 1988), bivalves (Chiplonkar and Tapaswi, 1974, 1979) ammonite (Ayyasami and Jagannatharao, 1978; Ayyasami and Banerji, 1984; Ayyasami, 1990, Ayyasami, 2006) and also in geochemistry (Madhavaraju et al., 2004; Zakharov et al., 2006; Madhavaraju and Lee, 2009; Ramkumar, 2009; Ramkumar, 2010; Zakharov et al., 2011) have been done so far. The collective effort of researchers was dedicated to the undertaking of biozonation studies focused on the Ariyalur Group (Jacob and Sastry, 1950; Sastry et al., 1965; Banerji, 1968; Sastry et al., 1968; Banerji and Mohan, 1970; Sastry and Mamgain, 1971; Banerji, 1973; Narayanan and Scheibnerova, 1975; Govindan, 1977; Sastry and Misra, 1977; Govindan, 1978; Rasheed and Ravindran, 1978; Banerji and Sastri, 1979; Govindan, 1980; Ramanathan and Rao, 1984; Govindan and Ramesh, 1995; Venkatachalapathy and Ragothaman, 1995; Govindan et al., 1996; Guha and Nathan, 1996; Tewari et al., 1996a, b). In geochemical aspects, studies of REE and clay minerals in the fossiliferous limestones of Kallankurichchi Formation of Ariyalur Group have revealed its oxic nature of the depositional environments and temperate climate (Madhavaraju and Ramasamy, 1999; Madhavaraju et al., 1999, Madhavaraju et al., 2002, Madhavaraju and Lee, 2010; Nagendra et al., 2011, Madhavaraju et al., 2015). Some of the sedimentological work has been carried out by Nagendra et al. (2001), Nagendra et al. (2011), Sarkar et al. (2014); Nagendra R. (2015); Chakraborty et al. (2017); Chakraborty and Sarkar (2018), Nagendra et al. (2018); Nagendra and Nallapa Reddy, (2021) in the pre-Ariyalur Group. A general consensus is that the highly fossiliferous succession developed in a shallow marine realm. Previous workers have done the lithostratigraphic

classification and interpreted that the whole deposition took place in a distally steepened ramp condition (Ramkumar, 2000; Watkinson et al., 2007). Nagendra et al. (2011b; 2018) interpreted as shallow marine settings, more specifically as middle neritic, based on the biotas. Watkinson et al. (2007) interpreted the Kallankurichchi Formation as post-rift mega sequence from the tectonostratigraphic viewpoint. Despite significant contributions in all of these above-mentioned fields, there are lack of proper sedimentological investigations, especially a state-of-art process-related and paleogeography-related facies analysis is still lacking for the Ariyalur Group of rocks, and more specially the Kallankurichchi Limestone Formation.

The Kallankurichchi Limestone, abundantly rich in varied kinds of marine fossils, that leaves little doubt for its shelf origin (Nagendra et al., 2011a; Ramkumar, 1999; Ramkumar et al., 2004; Reddy et al., 2013). Sedimentary structures led Ramkumar (2006) to recognize a single storm event within this carbonate formation. Fürsich and Pandey (1999), while considering shell concentrations, interpreted deposition under very shallow water, but below the fair-weather wave base.

This research work primarily intends to unveil the evolution of the ~60 m thick Kallankurichchi Limestone Formation of the Ariyalur Group of the Cauvery Basin, India considering the renewed post-rift tectonic resurgence, sediment dynamics and biotic response. The depositional environment of the limestone formation and their sequence building patterns in response to sea-level fluctuations within this pericratonic rift basin have been established. One of the major focuses of this study is to investigate the distinctive sedimentation history of the Formation considering its tectonic milieu and some unique mineral assemblages which was not reported earlier.

1.2 Geological Background:

1.2.1 Geographic Distribution:

The Cauvery Basin is situated along the south-eastern edge of India, and it is the southernmost sedimentary basin along the east coast of Indian peninsula. It covers the latitudes of 8°30' N and 12°30' N and longitudes 78°30' E and 80°30' E (Fig. 1.1). It is a NE-

SW trending pericratonic rift basin, having a linear geometry with a longer length (400 km) than its breadth (170 km) (Chari et al., 1995). It started forming during the Mesozoic break-up of the eastern Gondwanaland (Powell et al., 1988; Pravakar and Zutsi, 1993; Rangaraju et al., 1993; Nagendra et al., 2011). The basin forms a high angle with the east-coast margin of India and the underlying continental crust has undergone tilting during the Indo-Antarctic fragmentation (Chari et al., 1995). It covers ~22,500 km^2 area on land and 25,000 km^2 offshore between Pondicherry in the north and Ramanathapuram in the south and extends into the Bay of Bengal and the Gulf of Mannar (Prabhakar & Zutshi, 1993; Chari et al., 1995). The extension was initiated in a NW-SE direction, resulting in rifting along a pre-existing older Precambrian lineament (Proto Boundary Fault, PBF) between India and Sri Lanka connecting three triple junction points (Burke and Dewey, 1973). A major basinal uplift during the late Turonian caused by the Marion hot mantle plume resulted in widespread volcanism in the southern part of the Cauvery Basin (Nagendra and Reddy, 2017). This uplift, caused by the detachment of Madagascar from India, is also linked to this volcanic episode (Keller et al., 2009). The basement is characterized by structural highs and lows, both the margins of the basin bounded by basin margin faults. The basement faults are generally of the listric, gravity-type fault (Chand and Subrahmanya, 2001). The horst-graben basin architecture is a result of normal faults trending parallel to the Eastern Ghat range (NNE-SSW) of Precambrian age. The WNW-ESE and WSW-ENE trending conjugate normal faults further subdivided the Cauvery Basin into multiple sub-basins/depressions including Ariyalur-Pondicherry, Thanjavur, and Ramanathapuram (Fig. 1.1a; Murthy et al., 2008; Sastri et. al., 1973, 1981). In the northern most Ariyalur-Pondicherry sub-basin, it contains three important outcrops at Ariyalur, Vridhachalam, and Pondicherry from north to south-west (Rao and Sastry, 1964; Sastri et al., 1973; Sastri et al., 1981; Watkinson et al., 2007). Amongst these, the Ariyalur outcrop provides the more or less complete succession of the Cretaceous period bordering ca. 1200 km^2 in Ariyalur and Perambalur district of Tamilnadu (Sastri and Rao, 1964). Cretaceous outcrops are mainly exposed in the limestone quarry, pits, and stream sections.

Cretaceous exposure of the Cauvery Basin comprises the Uttatur and the Ariyalur Groups of rocks (Watkinson et al., 2007; Chakraborty and Sarkar, 2018). The sedimentation of Cauvery Basin commenced with Gondwana rock deposition of early Cretaceous age and

then the deposition of the Dalmiapuram Formation, and it continues up to the Karai Shale Formation with a gradational boundary in between followed by Garudamangalam Sandstone (Chakraborty and Sarkar, 2018). The Ariyalur Group of rocks consists of three formations: The Sillakuddi Sandstone Formation at the base, followed upward by the Kallankurichchi Limestone Formation, and is topped by the Kallamedu Sandstone Formation (Srivastava and Tewari, 1967; Sundaram et al., 2001).

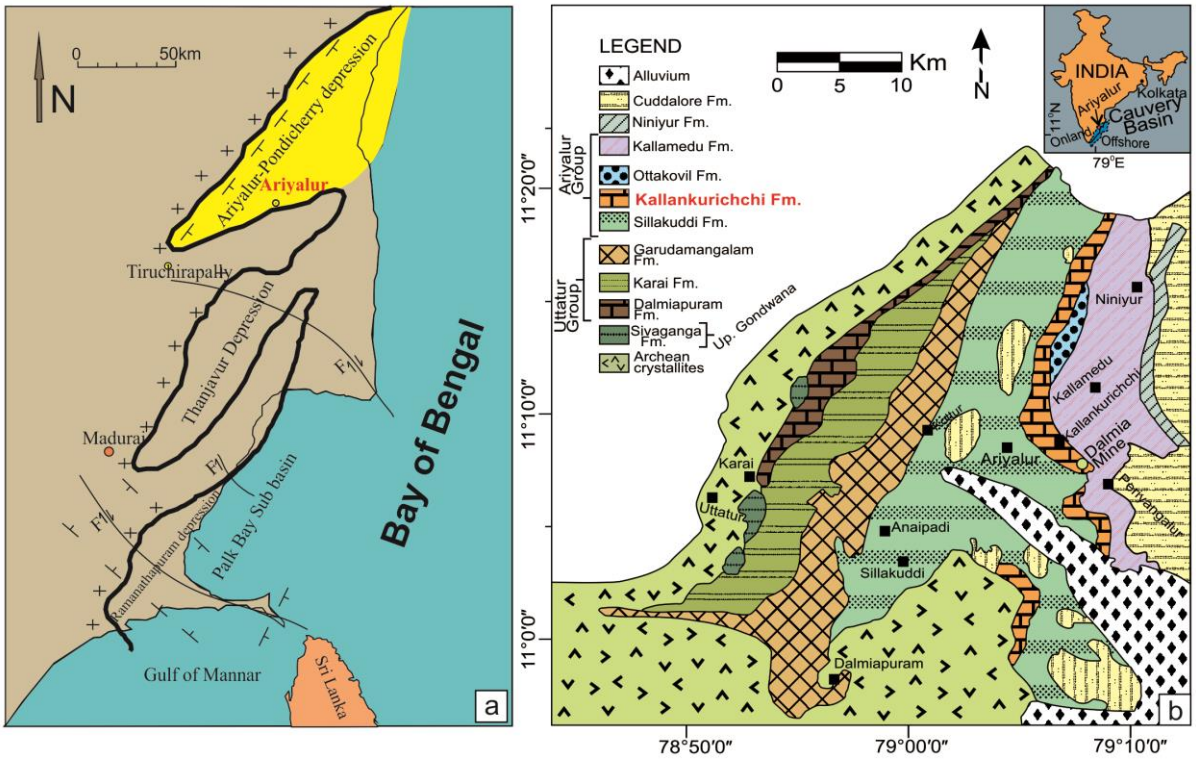

Fig. 1.1 Basement configuration map of the Cauvery Basin (after Sastri et al., 1979) (a); lithological map of the Cauvery Basin with the constituting formations and stratigraphy of the 'Ariyalur-Pondicherry' sub-basin, note the geographic extent of the Cauvery Basin shown in inset (modified after Nagendra and Reddy, 2017 and Chakraborty and Sarkar, 2018) (b).

1.2.2 Tectonic settings and sedimentation:

The tectonic evolution of the Indian plate signifies the most extensive journey among all drifting continents, covering approximately 9000 km over a span of 160 million years (Bandyopadhyay et al., 2010). There was a sudden acceleration during the Cretaceous, with

plate velocity reaching approximately 18 cm/year during the latest Cretaceous at the K-Pg boundary and marking the maximum velocity achieved during the entire journey (Chatterjee et al., 2017). During the early Cretaceous, the center of the Indian subcontinent was positioned at 40°S and underwent a 90° clockwise rotation in relation to its current orientation (Powell et al., 1988). Whereas India's north-south dimension was oriented approximately 30°-40° eastward (Markl 1974; Krishna, 1987). The significant tectonic detachment, leading to India's separation from Gondwanaland towards north as an independent entity, occurred rapidly (Fig. 1.2). The Eastern Continental Margin of India (ECMI) is a passive margin which has evolved as a consequence of the breakup of eastern India from East Antarctica (Powell et al, 1988). In this scenario, the Late Jurassic to earliest Cretaceous rifting of east Gondwanaland led to the separation of India from Australia and Antarctica, consequently opening up the Indian Ocean. The outcome of this process is the formation of numerous NE–SW trending basins, including the Cauvery Basin over the Indian Precambrian crystalline basement along the east coast of India (Banerjee, 1983; Powell et al., 1988; Chand and Subrahmanyam, 2001; Lal et al., 2009). The basin is segmented into several grabens with intervening inter-basinal horsts. The basement rock is represented by Precambrian crystallines, including granite gneiss/diorites and charnockites. The development of NE-SW trending grabens and valleys in the Cauvery Basin was linked to wrench faulting caused by the shear motion between India and East Antarctica (Chand and Subrahmanyam, 2001; Chakraborty and Sarkar, 2018). The initiation of the extension occurred in a northwest-southeast (NW-SE) direction and to some extent controlled by north-west lineaments present in the pre-existing basement of peninsular India (Powell et al., 1988). The failed third arm formed an aulacogen in the eastern passive margin of India and served as main locus of paralic-deltaic sedimentation (Chakraborty et al., 2021). The initial extensional faulting during the late Jurassic to early Cretaceous was succeeded by a gradual rifting, which appeared to have persisted until Turonian (Watkinson et al., 2007).

The paleogeography of the Indian plate, particularly in the Late Cretaceous period, provides a unique opportunity to explore its intricate tectonic evolution (Chatterjee & Bajpai, 2016). The Ariyalur Group of rock exhibits the widest distribution in the Cauvery Basin, extensively covering the older units (Acharya and Lahiri, 1991).

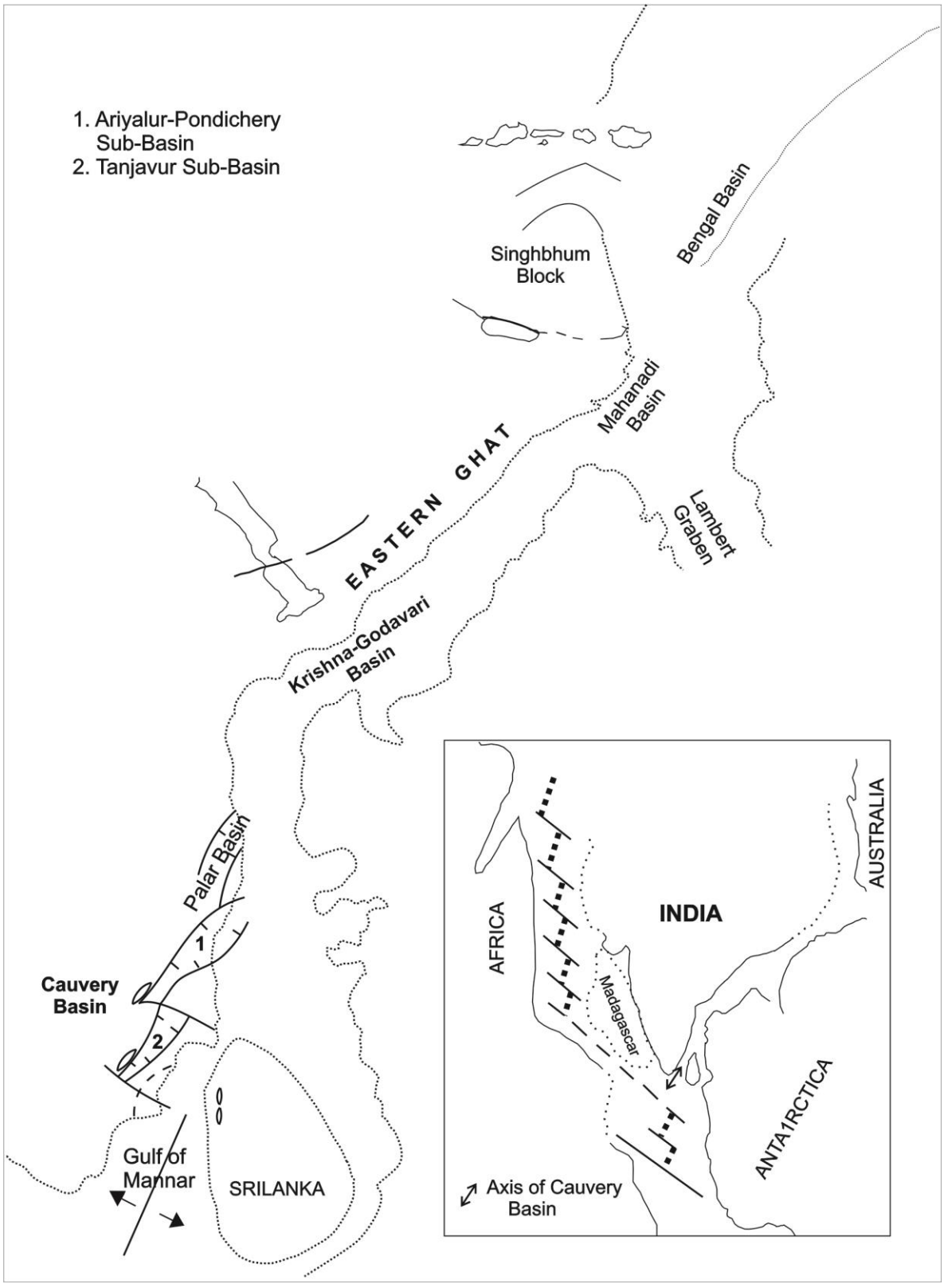

Fig. 1.2 Initiation of formation of Cauvery Basin during the early stages of Gondwana breakup (modified after Lal et al., 2009).

1.2.3 Stratigraphy:

Several researchers have proposed the stratigraphy of the Cauvery Basin. Pioneering contributions by researchers such as Blanford (1862), Stoliczka (1871), and Kossmat (1897) marked the initial endeavours, providing the first classifications of Cretaceous rocks in the Cauvery Basin. Subsequently, numerous scholars have extended this research. Various workers (Sastri and Raiverman, 1968; see Table 1.1 of Banerji, 1973; Sastri et al., 1973; Sundaram and Rao, 1979; Sastri, 1980; Sundaram and Rao, 1986) have established major lithostratigraphic units for the entire Cretaceous succession preserved in Cauvery Basin. Generally, opinions among the workers vary, with a majority proposing new terminologies without taking other perspectives into account. Due to this, an abundance of stratigraphic terms and varying ages assigned to the same deposit and along with their consistent use in literature, create unnecessary confusion and challenges in accurately correlating them. Sastri et al., (1981) had attempted a formal definition of lithological characteristics for the entire succession (Table 1.2). Sundaram and Rao in 1979 (later revised in 1986) adopted an approach to develop a more comprehensive lithostratigraphic classification for these rocks (Table 1.3). Sundaram and Rao (1986) considered the Niniyur Formation as underlying the Ariyalur Group. Ayyasami et al. (1992) recorded the stratigraphy of Cretaceous rocks near Kilapalavur, Tiruchchirappalli district of Tamil Nadu. Tewari (1996a) put forward a revised lithostratigraphy for the Cretaceous succession in the Cauvery Basin (Table 1.4) and classified them based on the name of quarry section where the rocks were exposed. The biostratigraphic zonations have been carried out based on the foraminifera (Table 1.5, Srivastava and Tewari, 1967; Sastry et al., 1968; Rasheed and Ravindran, 1978; Govindan et al., 1996), ammonites (Chiplonkar and Phansalkar, 1976; Ayyasami and Rao, 1978; Phansalkar and Kumar, 1983a; Ayyasami and Banerji, 1984; Chiplonkar, 1985; Ayyasami, 1990) and calcareous nannofossils (Rai et al., 2013). Ayyasami (2006), had proposed the biozonation based on ammonites as well as oysters (Table 1.6). Most of these research works are published in Indian journals, many of which are even inaccessible to Indian geoscientists. Nagendra et al. (2011b) classified the Kallankurichchi Formation of Ariyalur Group based on the lithology exposed at quarry sections (Fig. 1.3).

Table 1.1 Lithostratigraphic Succession of Cauvery Basin proposed by Banerji, 1973.

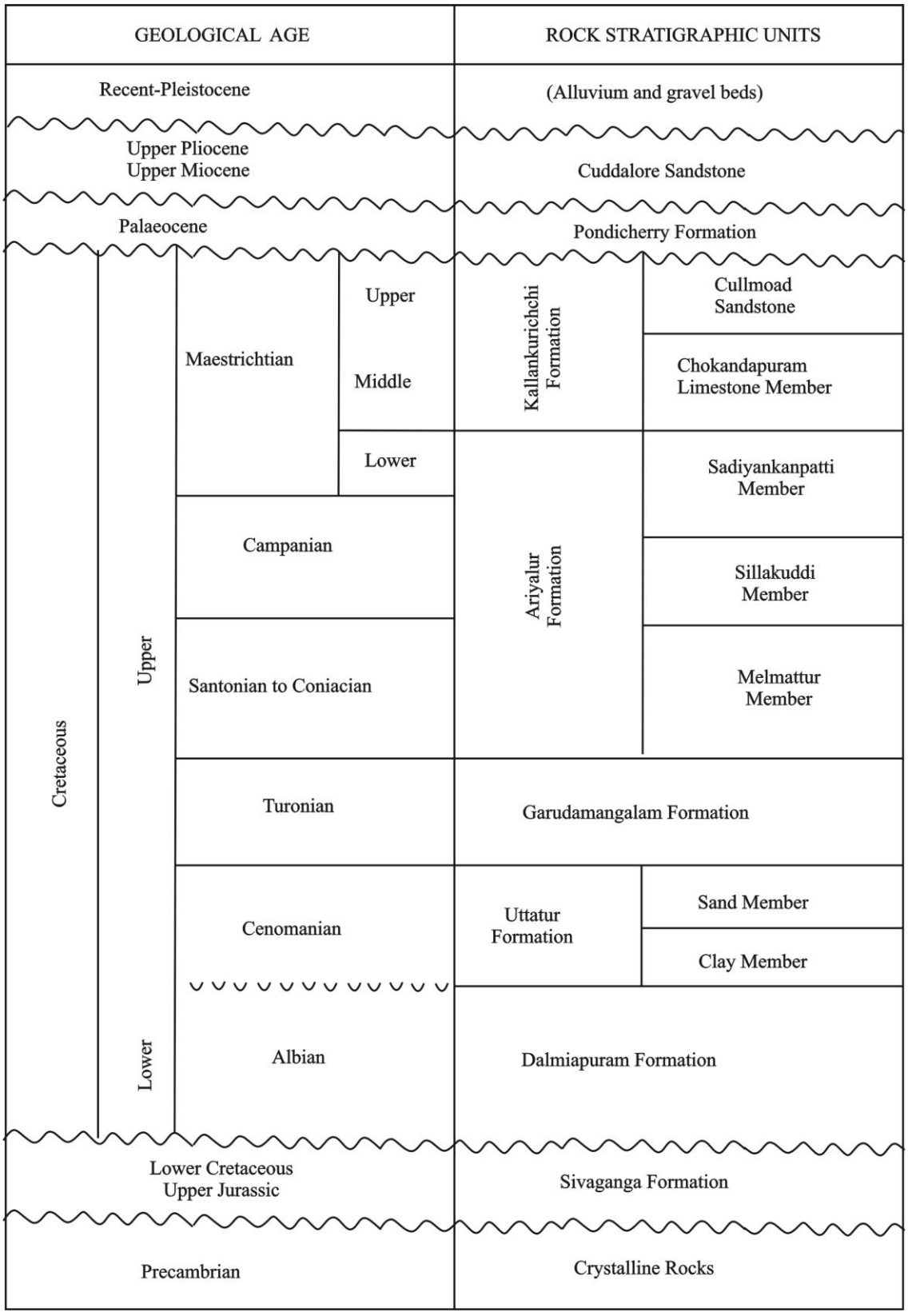

Table 1.2 Generalized Succession of Cauvery Basin proposed by Sastri et al., 1981.

Recent-Pleistocene	Alluvium (80-100 m)	alluvial sands and clays, lateritic sand, earthy limestone and ferruginous grits
unconformity		
Pliocene	Cuddalore Sst. (150-600 m)	sandstone, clay, conglomerate with thin coal beds
unconformity		
Early and Middle Miocene	(0-1190 m)	sandstone, clay, limestones, shale, siltstone with occassionally thin coal beds not present in the outcrops
unconformity		
Oligocene	(0-340 m)	sandstone, shale and limestone; not present in the outcrops
Eocene	(0-1150 m)	sandstone, shale, claystone and bioclastic limestone; not present in the outcrops
Paleocene	(70-700 m)	sandstone, clay, marl and limestone (Niniyur/Pondicherry Formation) in the outcrops; sandstone, claystone, shale, siltstone and bioclastic limestone in the subsurface
unconformity		
Late Cretaceous	(1190-2700 m)	subdivided as Uttatur, Trichinopoly and Ariyalur Formations; in the outcrops gypseous clays, fossiliferous limestone, gritty and conglomerate sandstone, argillaceous sandstone and clays; undifferentiated in subsurface; mainly sandstone and shale with thin bioclastic limestone
unconformity		
Early Cretaceous	(400 m)	reefoidal limestone and black shales (400 m) in the outcrops (Dalmiapuram Formation); not differentiated in the subsurface
unconformity		
Early Cretaceous	(Upper Gondwana) (350-1090+)	coarse gritty and pebbly sandstone in the outcrops; shale with argillaceous sandstone, at places conglomeratic in the subsurface
unconformity		
Precambrian		granites, gneisses and other metamorphic rocks

Table 1.3 Lithostratigraphic Classification of Cretaceous sediments of Ariyalur (modified after Sundaram and Rao, 1986).

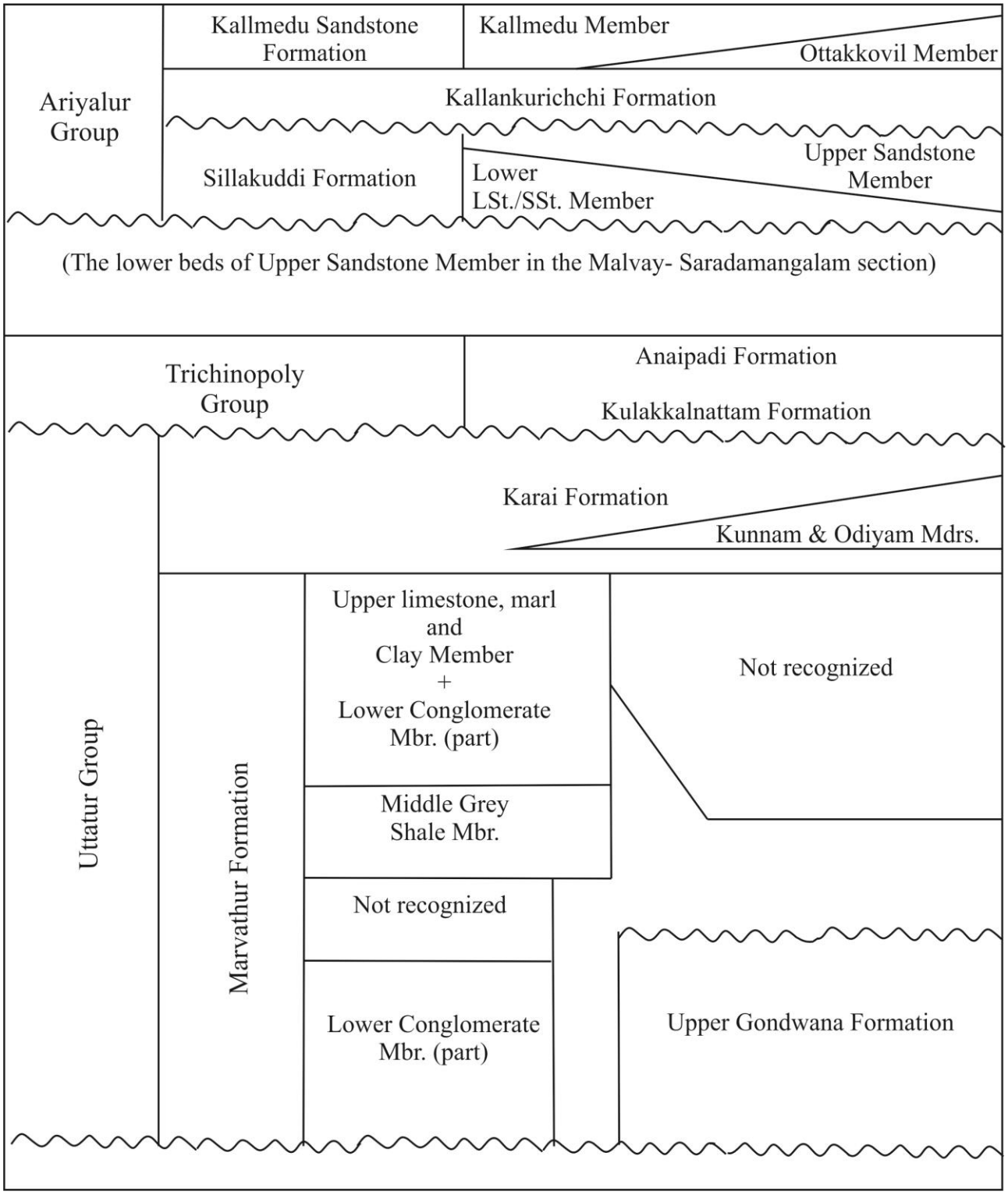

Table 1.4 Revised lithostratigraphic classification for the Cretaceous succession in the Ariyalur outcrop of Cauvery Basin (proposed by Tewari et al., 1996a) (modified after Watkinson et al., 2007).

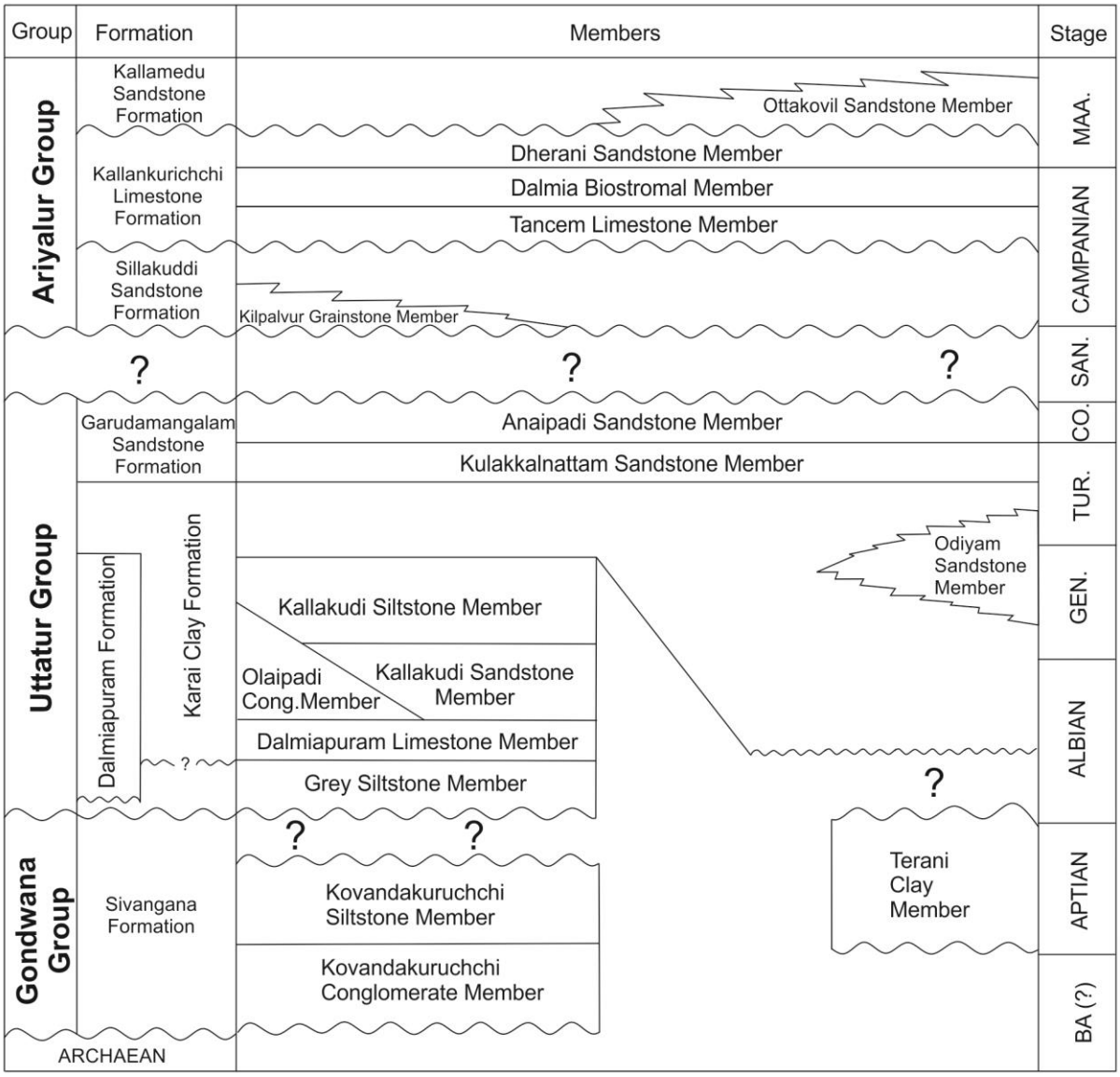

Table 1.5 Biostratigraphic zonation based on Foraminifera (modified after Srivastava and Tewari, 1967).

Formation	Biostratigraphy	Lithostratigraphy	Age
Kallamedu Fm.	.....	Sands, sandy shale and calcareous concretions	Maastrichtian
Kallankurichchi Fm.	*Globotruncana gansseri*	Yellowish-brown soft marl and hard arenaceous limestone	
Sillakuddi Fm.	*Globotruncana lapparenti tricarinata*	Argillaceous and calcareous sandstones interbedded with cream and buff coloured sandy clays	Campanian

Table 1.6 Biostratigraphic zonation based on Ammonite and Oyester (modified after Ayyasami, 2006).

Formation	Ammonite Zones	Oyster Zones	Age
Kallamedu Fm.	*Eubaculites vagina* Zone	*Agerostrea ungulata* Zone	Maastrichtian
Kallankurichchi Fm.	*Hauericeras rembda* Zone	*Pycnodonte vesicularis* Zone	
Sillakuddi Fm.	*Karapadites karapadense* Zone	*Ostrea zitteliana* Zone	Late Santonian to Campanian

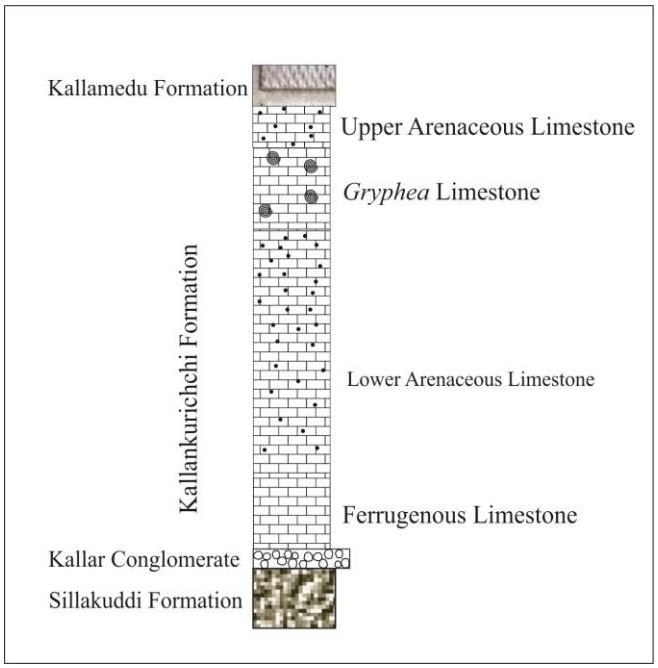

Fig. 1.3 Stratigraphic section of Kallankurichchi Formation showing the lithology exposed at quarry sections (modified after Nagendra et al., 2011b).

1.3 Cretaceous Biota:

The marine Cretaceous formations of southern India are huge repositories of fossil bivalves belonging to the order Pholadidae, Myidae, Mactridae, Tellinidea, Solenidea, veneridae etc. (Stoliczka, 1971), gastropods of four divisions including Scaphopoda, Opisthobranchia, Prosobranchia and Pulmonata Stoliczka (1867), ammonites, brachiopods, echinoids as well as micro-fossils (foraminifera, dinoflagellates, diatoms) and were mainly targeted by Paleontologists for biostratigraphic classification. These fossils also provide information on the paleoenvironment (e.g., near-shore, shelf, slope or deep water) and paleoecology (e.g., warm, cool, oxic, dysoxic, anoxic, degree of salinity etc.) (Saraswati et al., 2016).

The oldest lithostratigraphic unit of Cretaceous successions of Cauvery Basin is Basal Siliciclastic Formation (equivalent to Sivanganga Formation). Although the basal part of this unit is devoid of any kind of fauna and flora, *Ptilophyllum acutifolium*, a plant fossil, has been reported from the lower part of the floodplain sediments at Terani area (Mamgain et al. 1973; Sundaram et al. 2001; Venkatarengan et al.1993, Nagendra et al., 2018). The

Dalmiapuram Formation is rich in algae, bryozoans, rare coral fragments, foraminifera and also cephalopods. It contains *Neomeris cretaceae, Parachaetetes asvapattii, Sporolithon* sp., *Lithothamnion* sp., *Salpingoporella verticelata*, *Pseudoamphiroa propria* and *Agardioliopsis cretaceae* (Mishra et al. 2004). Marine cephalopods, such as *Acanthoceras* sp., *Mammites conciliatus, Nautilus huxleyanus* and *Turrilites costatus,* are also abundant (Kossmat 1897; Govindan et al. 1998, Namgendra et al., 2018). The index species of dinodlagellates are reported namely *Odontochitina costata, Epelidosphaeridia spinosa, Cyclonephelium* cf. *C. vannophorum, Dioxya* sp., *Kiokansium unituberculatum, Ovoidinium verrucosum* and *Batioladinium micropodium* (Nagendra et al. 2002a). Eight Rhodophycean taxa belonging to corallinaceae family, Peyssonneliaceae family, Sporolithaceae family are also present. The presence of planktic foraminiferal assemblages viz. *Planomalina buxtorfi, Rotalipora reicheli, Praeglobotruncana stephani,* and *Hedbergella portsdownensis* (Nagendra et al., 2013) and *Rotalipora, Preaglobotruncana, Whiteinella* and *Hedbergella* (Govindan et al.1996) are documented from the Karai Formation. Belemnite rostra are exceptionally well preserved within the middle part of the Karai Shale Formation (Zakharov et al., 2011); however, they are completely absent in the post-Cenomanian succession (Mondal et al., 2023). The Garudamangalam Sandstone Formation is rich in ichnofossils containing *Skolithos, Ophiomorpha* and *Thalassinoides*. Ayyasami and Rao, (1978) reported gastropod shells and ammonites (such as *Kossmaticeras theobaldianum* and *Placenticeras tamulicum*) preserved within the rocks in Anaipadi area.

The thick-shelled rudist bivalves (*Gryphea*, *Pycnodonte, Ostrea* etc.) are reported from east coast of India by Fürsich and Pandey, (1999). Ayyasami (2006) among others reported ammonites from Cauvery Basin e.g., *Australiceras jacki*, *Eubaculites vagina*, *Mortoniceras rostratum*, *Calycoceras newboldi*, *Eucalycoceras pentagonum*, *Pseudaspidoceras footeanum* etc. Stoliczka (1873) described Echinoid *Stygmatopygus elatus* from Cenomanian rocks of Ariyalur group. A new species (*Gongrochanus Kier*) of Cassiduloid echinoid had been discovered by Srivastava (2003). Jain (1976) described Dinoflagellate's assemblages e.g., Dinogymniaceae, Spiniferitaceae, Apteodiniaceae, etc from Upper Cretaceous Vridhachalam area. Govindan (1972) and many other researchers worked on foraminifera (*Globigerina hoterivica*, *Hedbergella planispira*, *Planomalina buxtorfi* etc.) in the entire Ariyalur Group. Nagendra et al., (2011) summarized the macro-

and microfossils present in the Ariyalur area, Cauvery Basin. The overlying Sillakkudi Formation, Ariyalur Group, includes I*noceramus*, lamellibranches, echinoid fragments, foraminifera, and ammonites pointing to a Campanian age. Ichnofossils, *Thalassinoides* and *Ophiomorpha*, are reported (Ramkumar et al., 2004; Nagendra et al., 2011). The assemblage of foraminifera species zone [benthonic foraminifer *Bolivinoides culverensis* and *B. decoratus*; planktonic foraminiferal *Globotruncana elevata-G. ventricosa* (Govindan et al., 2006)] further strengthens this age assignment, particularly in a deeper middle neritic environment. Rasheed and Ravindran (1978) recorded the presence of the benthic foraminifera *Bolivinoides decoratus*. Fluviatile Kallamedu Formation (Late Maastrichtian) contained profuse vertebrate fossils, e.g., ganoid fishes, amphibians, turtles, crocodiles, and dinosaurs (Prasad et al., 2013). The first attempt to identify the vertebrate fauna from this formation was made by Lydekker (1879), reported the presence of a dinosaur *Megalosauras* based on its isolated tooth.

The Maastrichtian (Late Cretaceous) units are the fossil dominant horizons in India. The Kallankurichchi Limestone is very rich in bivalve fossils. The faunal distribution covers two conspicuous groups of bivalves namely *Gryphea* and *Inoceramus*. *Inoceramus* (bivalves) serves as an excellent index fossil for the Late Cretaceous period. *Platyceramus*, a common genus of *Inoceramus* present throughout this succession. *Alectronia*, Besides, there also occur bryozoa, dominantly the encrusting variety, echinodermata, varieties of Foraminifera, Brachiopoda and Cephalopoda in this order of frequency. The formation contains smaller benthic foraminifera, including *Gavelinopsis bembix, Gyroidinoides globosa, Lingulogavelinella* and *Cibicides.* The presence of planktic foraminifera *Globotruncana linneiana, G. aegyptiaca* and *G. arca* indicate an early Maastrichtian age. Similarly, Tewari et al. (1996a, b) assigned an early Maastrichtian age based on the larger foraminifera *Siderolites* as well as abundant bryozoans.

A few nanofossils (e.g., *E. floralis, T. exiquus, A. Cambiformis, C. Crenulatus, P. angustus, Th. Operculata)* and *Globotruncana ganserii* zone of Late Cretaceous age of Pondicherry Basin have been reported (Rai et al., 2013). The tectonic evolution of the Indian plate created a “reticulate” biogeographical history (Sanmartín et al., 2011), where Indian biotic populations got fragmented and re-merged again, disappeared and reappeared through

geological time. Ariyalur exhibits a striking similarity in both faunal composition and assemblage to the Upper Cretaceous formations found in the American Gulf Coast region.

1.4 Age:

There is no such reliable geochronological data in support of the age of Cauvery Basin. On the basis of lithostratigraphy, the foraminiferal biostratigraphy, substantiated by age-diagnostic ammonite oyster zonations, a Maastrichtian age for the Kallankurichchi Formation was suggested (Ayyasami, 2006). The prevailing microfaunal composition in this member is characterized by the dominance of orbitoids and sideralolites. Major fauna within this context includes *Gryphaea* and *Alectronia*, suggests an age corresponding to the Lower Maastrichtian (Nagendra et al., 2011a). Furthermore, the identification of the *Globotruncana ganrseri* zone within the Kallankurichchi Formation is based on the extensive occurrence of *Globotruncana* species, such as *G. gansreri Bolli* and *G. arca* (Cushman) (Srivastava and Tewari, 1967). These observations unequivocally establish the age of this zone as Lower Maastrichtian. Ammonite assemblages also indicate the Maastrichtian age (Sastry et al., 1968; Ayyasami,1990). Additionally, Srivastava and Tewari (1967) have recorded age-diagnostic planktic foraminifera, confirming the formation to be of early Maastrichtian age. Ayyasami et al. (1992) postulated the lower age limit of the Ariyalur Group as Campanian based on faunal assemblages.

The lower age limit of the Ariyalur Group and the contact of the Trichinopoly and Ariyalur groups and their extension late Campanian (Nagendra et al., 2011). There was debate about the lower age limit. Banerji (1972) argued that the lower age limit of the Ariyalur Group is Santonian, based on the presence/absence of *Globotruncana fornicate*, but Plummer (1931) himself admitted in the paper that *G. fornicata* is a long ranging from (Santonian to Maastrichtian). Thus, his arguments for an age older than Campanian cannot be supported. Sastry et al. (1965) have opined that the lower beds might be assigned to Campanian as evidenced by the presence of foraminifera such as *Globotruncana lapparenti* (*lapparenti Brotzen*), *G. bulloides* (Volger), *and G. tricarinata* (Quereau) and *G. ventricosa* (White). Tewari and Srivastava (1965) recorded Campanian foraminifera from a well cutting

presumably to the east of Sillakuddi. Based on the megafossil assemblages, they assigned the lower level to the Campanian age (not Santonian).

1.5 Objectives:

Late Cretaceous time period, the most important time frame in earth history has been chosen for the present study. The thesis is aimed to study the course of evolution of the Kallankurichchi Formation of Ariyalur Group, Cauvery Basin, which is poorly studied so far from sedimentological viewpoint. The outcrop is exposed in and around Ariyalur districts of Tamil Nadu, primarily in open-cast cement mines, small quarries, nala sections, road and railway cutting sections. Since, subsurface data is inaccessible, focus is directed solely towards the outcrop study. Accordingly, the effort has been made on the basis of formerly discussed background, to achieve the goal of this thesis. A survey of previous literature indicates that many of the aspects so far studied were either largely on biostratigraphy, more precisely biozonation or it is limited to lithostratigraphy, classified mainly as members based on name of the mines. Besides monograph of bivalves and gastropods, some salient and specific occurrences of biota have also been reported. Though the bulk rock geochemistry had done, but there is lack of proper correlation with the state of art facies analysis, rather as such no attempt had been made to know the characteristics sedimentary facies, sedimentary structures of this thick limestone formation. This work has been primarily oriented on facies classification, system tracts and sequence building pattern, associated sedimentary structures and their significance in the interpretation of the paleoenvironmental conditions of deposition. The facies wise geochemical studies of limestones help to evaluate the paleoenvironment. Also, a detailed study of the diagenetic effects in the formation helps to reveal the environment of deposition as well as post-depositional textural and mineralogical modifications. Besides, the clay mineralogy of a particular layer of limestone, XRD and staining technique have also been applied in this study, which may throw a better light as to the geological setting i.e., post-rift adjustment and the nature of deposition of the sediments. Study of conglomerate is almost absent so far, that gives us idea about the role of subsidence during the sedimentation. Fossil content was also prioritized for being Cretaceous section. The presence of different fossil assemblages along with dominant rudist colony, considered

separately during the interpretation of depositional environment. The reconstruction of ancient climatic conditions analyzed using geochemical proxies from the rudist bivalve fossil *Pycnodonte* sp. The Kallankurichchi Limestone has been chosen for the present study because of the following reasons:

- No detailed sedimentological work has been done so far in this targeted formation.
- Significance of the scree conglomerates and its derivative present at the basal most horizon of the Kallankurichchi Limestone yet to be worked out.
- Reconstruction of state of art sedimentary facies analysis.
- Identification of stacking pattern of the formation considering sequence stratigraphic concept.
- Identification of the microfacies of the carbonate rocks, nonexistent so far from this formation.
- Significance of the relatively fossil-free dark grey limestone hosting rarely reported berthierine clay mineral, present at the basal part of the formation.
- Identification and characterization of shellbanks within this formation.
- Paleoenvironmental interpretation from bulk rock geochemistry.
- Record of paleotemperature calculated from isotope data of rudist fossil *Pycnodonte* sp. and a comparative study from the available data of the Late Cretaceous.

1.6 Methodology:

Field study is the mainstay for this research work. To facilitate the field study the essential equipment like hammer (30cm East Wing), chisel, trowel, measuring tape, clinometers, Abney level, digital camera, GPS (Garmin GPSMAP76CSX with PC interface cable and accessories), magnet, acid (for carbonate testing), hand lens, diagonal scale, permanent rock marker, knife, etc. were used. The toposheets 58I/16, 58J/13 and 58M/4 (Scale 1:50,000) were used during field work to collect the basic data required to know the geological history of the area published by the Geological Survey of India. Besides, maps from different published papers on Cretaceous of Cauvery Basin (Watkinson et al., 2007; Nagendra et al., 2011) were used to locate the exposure. Field data has been collected

observing the lithofacies and their physical relationship and macrofossil content from mines areas. Due to inaccessibility of sub-surface data, attention is paid to the outcrop only (Fig. 1.4). Vertical logging is limited to the mines' depth.

Fig. 1.4 Surface outcrop of Kallankurichchi Limestone Formation at Dalmia quarry section.

Numerous samples are collected systematically, vertically as well as laterally from the ~ 60m thick succession. Friable samples were handled with extra care during collection and transportation. Sampling is done to represent complete petrographic profile. Thin sections are prepared from collected rock samples and studied thoroughly under microscope to obtain microfacies data. Field studies along with microscopic observation are attempted towards understanding depositional textures. Rock samples for microscopic studies were collected in plastic satchel and fresh, unaltered and dry samples were taken separately wrapped with Aluminum foil to avoid contamination and oxidation for geochemical analysis. Thin sections, probe slides and polished sections were prepared from the rock samples. Soft and friable samples were consolidated with the help of Buehler Vacuum Impregnation Unit for preparing thin sections. Analysis of field data, petrography including were executed in the Sedimentology Laboratory, Department of Geological Sciences, Jadavpur University. Petrographic studies were carried out on thin sections using a Leica DM 2700P polarizing microscope, and photomicrographs were taken using a Leica MC 170 HD camera attached to the microscope, housed at the Sedimentology Lab of Jadavpur University, Kolkata. Computers with higher configurations with dual setup attached with HD camera facilitated the work enormously. Staining is the preliminary and most important technique to differentiate between calcite and dolomite because of their similar optical properties. Many of the samples have etched and stained by Alizarin Red S, dissolved in a mild hydrochloric acid solution (Dickson, 1965; Adams & MacKenzie, 1998). Dilute acetic acid and hydrogen peroxide have been utilized for selective chemical separations of mineralogical constituents

of limestones. The resulting fractions are then analyzed to assess the mineralogical associations of trace and major elements (Barber, 1974). Geochemical analysis e.g., XRD, EDAX and SEM were performed in the Department of Geological Sciences and of Jadavpur University, Kolkata. XRF was performed in NCESS, South India. Stable Isotope was done in University of Regina, Saskatchewan, Canada. Samples were centrifuged in the Sedimentology Lab before doing XRD to eliminate the heavy quartzo-feldspathic mass in case of sensitive detection. Vertical lithologs, maps, models, panels of multiple photographs, rose diagrams, binary and ternary diagrams, graphs, scatter diagrams, pie diagrams were prepared for reconstructions, correlation, paleocurrent data processing and geochemical data interpretation. Computer software, like CorelDraw X5, Adobe Photoshop CS3, OpenRoseV.0.01, Microsoft Office Picture Manager were used for these purposes. The major oxide weight percentages are recalculated by eliminating the LOI values from the dataset. The elemental concentration is expressed in its atomic weight percentage.

1.7 Instrumentations:

A number of instruments housed at Jadavpur University, Kolkata, India as well as University of Saskatchewan, Saskatoon, Canada was handled and utilized to fulfil the project. Petrographic and geochemical analyses were performed for betterment and precise understanding. A brief account of the instrumentation techniques followed has been described here.

1.7.1 X-Ray Diffraction (XRD):

X-Ray Diffraction (XRD) study was performed on the whole rock powder sample (<63 μm grain size) using a Malvern PANalytical X'pert Pro with Cu Kα radiation operating at 40 kV 40 mA and utilizing a flat sample stage and theta-theta goniometer setup (goniometer model PW3050/60), situated at the Jadavpur University, Kolkata. The sample was analyzed at room temperature, and the diffraction patterns were first recorded for 5–70° 2θ with a step size of 0.0150° 2θ and a scan speed of 1sec/step, and again on the same sample, for 5–28° 2θ and 55–65° 2θ ranges, respectively.

1.7.2 X-Ray Fluorescence (XRF) and μX-Ray Fluorescence (μ-XRF):

Major oxide compositions were analysed using 1 gm of powdered sample mixed with 5 grams of flux (LiT/LiM/LiBR 49.75/49.75/0.50, Pure) in a platinum crucible with the help of Katanax X-300 X-Fluxer (each flux was melted at 1050^0 C) in the sample preparation laboratory of the National Centre for Earth Science Studies (NCESS), India. The samples were analysed with a Bruker model S8 Tiger and S4 Pioneer sequential wavelength-dispersive X-ray spectrometers. The analyses were performed on the whole rock samples collected from all of the facies systematically. Standards used during the analyses are G2, GSP2, STM1, SARM1, SARM2, SY3, RGM, GA, GH, GS-N, AC-E, MDOG, ISHG, VS-N, JG-1, JG-2, JG-3, JR-3, and JSY-1. The data were recalculated with the LOI (Loss on Ignition) values.

High-resolution elemental abundance mapping of shell surfaces was conducted using a Tornado M4 micro-X-ray fluorescence (μXRF) scanner (Bruker nano GmbH, Berlin, Germany) housed at IIT Mumbai. The fossil samples are cut along their growth lines. The surface has made smooth and placed to the instrument for analysis. Mapping was performed along a 2D grid with 50 μm spacing, employing a spot size of 20 μm and an integration time of 30ms per pixel. The X-ray source operated at maximum energy settings (600 μA, 50 kV) without the application of source filters.

1.7.3 Scanning Electron Microscope (SEM) and Energy Dispersive X-Ray Spectrometer (EDS):

The micro-textural study of the limestone was performed on the carbon-coated thin section using Carl Zeiss Evo-18 Scanning Electron Microscope housed at Jadavpur University, Kolkata. The SEM has been operated within the voltage range of 0.5 to 30 kV, with 55 discrete steps, using a tungsten filament as the electron gun. The magnification range of the SEM spans from 5X to 300X, extending up to 1000X, with a resolution approaching 5 nanometres. The probe current using here 500mA to 1250mA. The instrument offers operation in two distinct image modes: Secondary Electron Image and Backscattered Electron Image. The EDS is connected with the same SEM. For Energy Dispersive X-Ray gold coated samples were also analyzed. The instrument has the capability to detect elements from Be (4) to Uranium (92), though not all instruments are equipped for 'light' elements (Z <

10). For present study a few elements e.g., Mn, Fe, Ni, Co, Pb etc. were detected. Qualitative analysis involves the identification of the lines in the spectrum and is fairly straightforward owing to the simplicity of X-ray spectra. Quantitative analysis (determination of the concentrations of the elements present) entails measuring line intensities for each element in the sample and for the same elements in calibration Standards of known composition. By scanning the beam in a television-like raster and displaying the intensity of a selected X-ray line, element distribution images or 'maps' can be produced. Also, images produced by electrons collected from the sample reveal surface topography or mean atomic number differences according to the mode selected.

1.7.4 Electron Probe Microanalyzer (EPMA):

Geochemical analysis of the green marine clay-bearing limestones was performed on selected points in the thin section using CAMECA SX5 Electron Probe Micro Analyzer (EPMA) at the Department of Earth Sciences, Indian Institute of Technology (IIT), Bombay, with an accelerating voltage of 15 kV, specimen current 40 nA, and a beam diameter 1μm (peak: 10-20s and background counting: 5-10s). Natural minerals, including albite (for Na Kα), orthoclase (for K Kα), diopside (for Ca Kα, Mg Kα), apatite (for P Kα), and rhodonite (for Mn Kα), and synthetic mineral phases including $CaSiO_3$ (for Si Kα), Fe_2O_3 (for Fe Kα) and Al_2O_3 (for Al Kα) were used as standards for the calibration of major oxide analysis. Duplicate analysis of individual points showed an analytical error of less than 1%. Wet chemical analysis (redox titration using $K_2Cr_2O_7$) was performed to determine the Fe^{2+}/Fe^{3+} ratio at the geochemical laboratory at IIT Bombay (Banerjee et al., 2016a).

1.7.5 Inductively Coupled Plasma Mass Spectrometry (ICP-MS):

Trace-element concentration analyses were performed at the Department of Earth Sciences in Indian Institute of Technology, Kanpur. Approximately 0.05 g of the sampler powder was first digested in pre-cleaned Teflon beakers (Savillex) at 130 ± 5 °C using a 4 mL mixture of concentrated HF (1 part), concentrated HCl (1 part), and concentrated HNO3 (2 parts) for 48 h. The acid was then slowly evaporated at 80 ± 5 °C, and again, the samples were redissolved in 3 mL of Aqua Regia acid (2 mL of concentrated HNO3 + 1 mL of concentrated HCl). Aqua Regia was fluxed for 24 h. After Aqua Regia digestion step, the samples were dried and re-dissolved in 2% HNO3. The acid digestion steps were only

repeated when digestion was incomplete. For all analytical work, trace-element grade pure acid and 18.2 MΩ cm water from a Millipore water purification system was used. Pure acids were produced by sub-boiling distillation in the Department of Earth Sciences using the Cupola Still system from PicoTrace. Trace-element concentrations were determined at 500 ppm total dissolved solid solutions, whereas for the REEs, it was determined at~2000 ppm total dissolved solid solutions. Three procedural blanks and reference materials SBC-1 (shale standard, USGS) and AGV-2 (Andesite, USGS) were also digested following the same procedures. The blanks were analysed to quantify the total procedural blank, whereas SBC-1 and AGV-2 were analyzed as an unknown to assess the data quality. A 10 μg/g multi-element standard solution from SigmaAldrich was diluted to 7 appropriate concentrations to construct the calibration curve (0.1 ng/g, 1 ng/g, 10 ng/g, 20 ng/g, 50 ng/g, 75 ng/g, and 100 ng/g), and trace-element concentrations were determined against the calibration curve. Since rock-matrix-matched reference materials were unavailable, all the samples and standards were spiked by~5 ppb in solution, which was used as an internal standard. The intensities were corrected for matrix effect using in as an internal standard.

1.7.6 Isotope Ratio Mass Spectrometry (IRMS):

Isotope data had been analysed in the Canadian Sophisticated laboratory of University of Saskatchewan. For chemical analysis the shells are cut along the major growth axis of the shell using a slow rotating rotary saw. A parallel slab was cut out of one-half of the shell, while the other half was preserved (archive half). cutting section is cleaned in 250 ml of distilled water and drilled with micro driller following the laminae to get fine dust. Carbonate samples are roasted in a vacuum oven at 200°C for 1 hour to remove water and volatile organic contaminants that may confound stable isotope values of carbonates. Stable isotope values are obtained using a Finnigan Kiel-IV carbonate preparation device directly coupled to the dual inlet of a Finnigan MAT 253 isotope ratio mass spectrometer. 20-50 micrograms of carbonate are reacted at 70^{o}C with 3 drops of anhydrous phosphoric acid for 420 seconds. The CO_2 evolved is then cryogenically purified before being passed to the mass spectrometer for analysis. Isotope ratios are corrected for acid fractionation and ^{17}O contribution using the Craig correction and reported in per mil notation relative to the VPDB scale. Data are directly calibrated against the international standard NBS-19 that has the following values: $\delta^{13}C$ = 1.95‰ VPDB and $\delta^{18}O$ = -2.20‰ VPDB. Precision/accuracy of data are monitored through

routine analysis of NBS-19. Precision/accuracy of $\delta^{13}C$ and $\delta^{18}O$ are 0.05‰ and 0.11‰, respectively (n = 25). Actual sample errors may be greater than these due to sample heterogeneity. (Canada IRMS) The ratios are presented in relation to the heavier isotope using the d notation and the VPDB scale. Analytical precision, based on duplicate samples, was typically 0.1 &for both oxygen and carbon isotope ratios. Consistency of results was achieved by comparison of laboratory standards against NBS-19. This is confirmed also by their chemistry with trace elements such as Sr, Fe and Mn distributed quite uniformly at near equilibrium values (Bruckschen et al., 1995).

1.8 Thesis Layout:

Organization of this thesis follows the scope of work outlined above. The thesis starts with a brief introduction addressing the Late Cretaceous Ariyalur Group of rocks exposed at and around Ariyalur, Cauvery Basin and its constituting formations. It also describes the already published literature about different aspects of the basin. The total work done during this study is discussed in several chapters organized into two parts mainly. Chapter 1 deals with the basic introduction of study area, local geology, tectonic set up, scope of work, methodology and organization. Within Part I, Chapter 2 discusses broadly on the different facies and facies association of the Kallankurichchi Limestone Formation. Chapter 3 deals with petrography/microfacies analysis. Chapter 4 contained geochemical characterization of the already delineated facies and its implications. Chapter 5 describes the sequence development pattern. In Part II, Chapter 6 to Chapter 9 deals with four special problems which have global significance. Chapter 6 deals with scree and its derivatives, flow evolution pattern. Chapter 7 deals with an authigenic green marine clay berthierine and its genesis as grain pseudomorph. Chapter 8 discusses the identification and characterization of shellbank within carbonate depositional environment. Chapter 9 deals with a proxy for paleotemperature and paleosalinity from rudist bivalve *Pycnodonte* sp. In Part III, Chapter 10 is of brief summary and conclusion about the depositional sequence and the final summarization of the thesis assignment has been carried out.

PART-I

FACIES ANALYSIS AND SEQUENCE DEVELOPMENT OF KALLANKURICHCHI FORMATION

CHAPTER-2

FACIES ANALYSIS

2.1 Introduction:

An organized classification is necessary for eliciting the depositional modes of ancient sedimentary rock sequences. Among the various methods available for classification, sedimentologists consistently select the one that provides concise insights of depositional environments. A state of art facies analysis has the potential to elucidate the genetic distinctions among sedimentary bodies that coexist (Hallam, 1981; Reading, 1996). Sedimentary facies is a body of sedimentary rock which can be characterised by its lithology, sedimentary structures, geometry, paleocurrent pattern, fossils and depositional environment and differing vertically as well as laterally from adjacent rock (Walker, 1984; Tucker, 1985; Walker and James, 1992; Reading 1996; Posamentier and Walker, 2006). For this, a detailed unified classification is required to avoid large scale repetition which is bound to occur due to significant similarity among the formation. The primary criteria utilized for facies classification such as lithologies, internal structures, and fundamental petrographic characteristics, and textural maturity have been incorporated in the current study. Mineralogical composition has also been considered at times for the sake of greater clarity of the facies identification. Besides, body geometries and lateral persistency are also considered for the detailed classifications. Together with the broad lithologic variations, vertical intra-bed variation in fossil content has considered as well for the unified facies classification of the Kallankurichchi Limestone Formation. The sediment dispersal pattern has been considered for delineating genetically distinct facies. After identifying the facies, their distribution in time and space along with the nature of contact among themselves, can enable one to reconstruct the paleogeographic model. So, the prime focus is to comprehend sedimentation dynamics, bedform evolution, paleogeographic and paleoenvironmental reconstruction and sequence building patterns (Walker, 1992; Bose and Sarkar, 2008). As the Late Cretaceous time was especially eventful because of tectonic unrest, volcanic eruption, significant changes in biotic history and mass extinction, so a proper comprehensive and integrated facies analysis is required to know the exact paleogeography of the sediment deposited during the then time. Overall shallow marine interpretation so far exists, because of the well-preserved fossil assemblages within the formation. But during the present endeavor a generalized lithostratigraphic succession of entire Ariyalur Group has been proposed (Fig. 2.1). A composite litholog has been done based on primary sedimentary structures (following

the facies classification) considering all the discrete exposures (Fig. 2.2). The work was done in different quarry sections in and around Ariyalur at open-cut quarries.

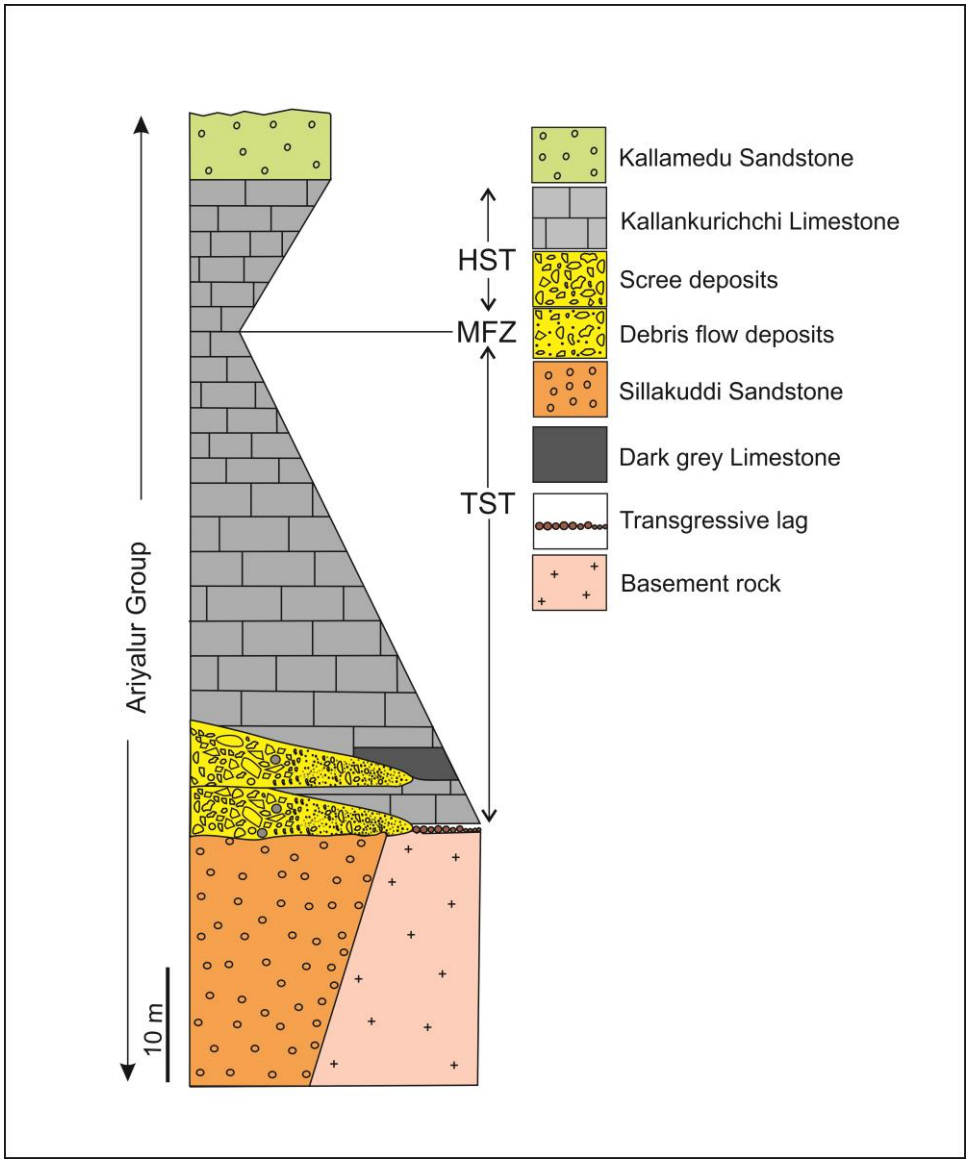

Fig. 2.1 Proposed generalized Stratigraphic Succession of Ariyalur Group (Srimani S., 2024)

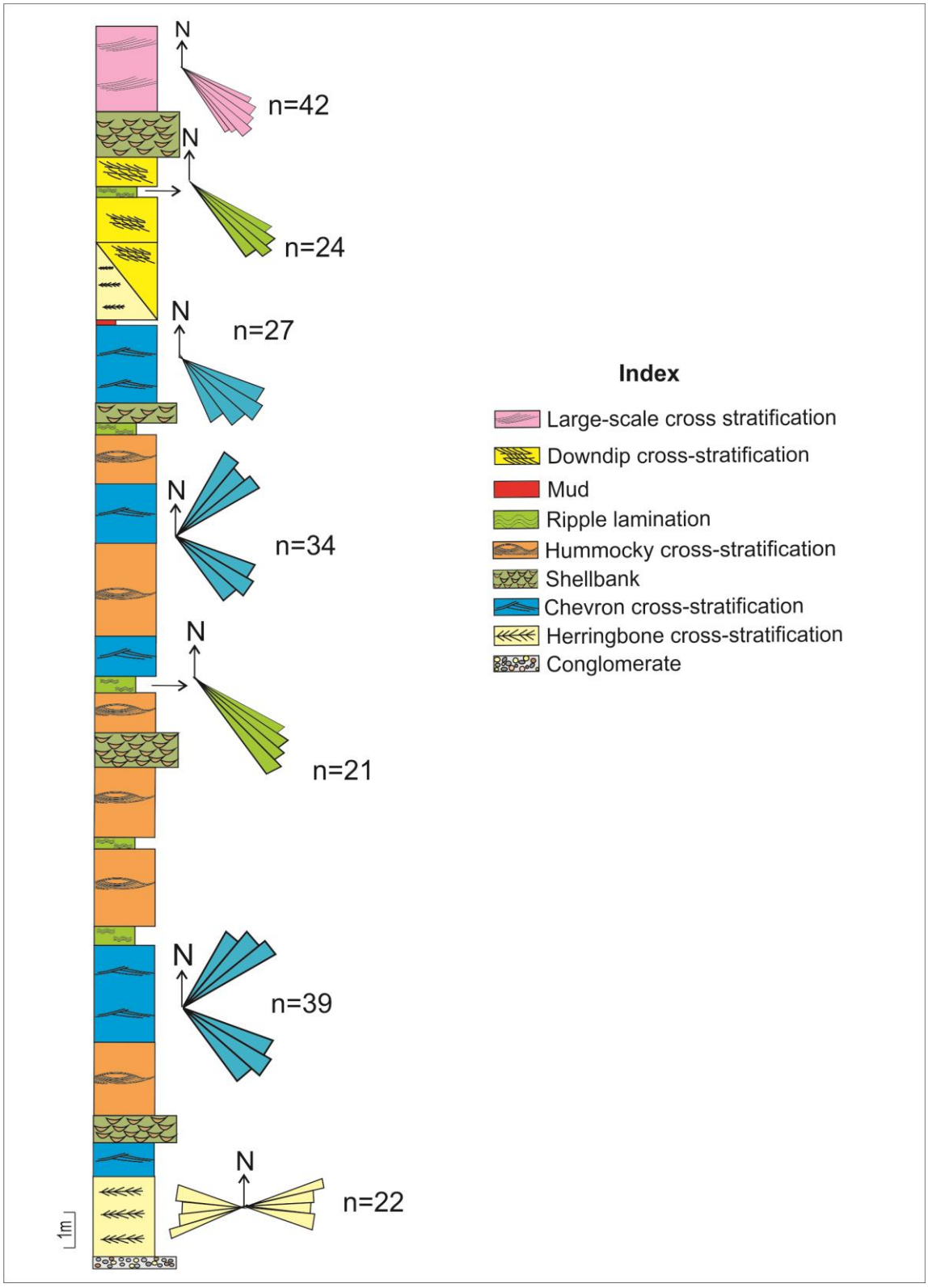

Fig. 2.2 Detail litholog of Kallankurichchi Limestone Formation with sedimentary structures. Note, the paleocurrent direction.

The Kallankurichchi Limestone Formation initiated with a clast-supported very well sorted piecemeal occurrence of a conglomerate bed. This thin conglomerate bed is made up of well-rounded clasts, though the variability in clast composition is less. The overall body geometry is sheet-like body and comparatively thinner, less than ca. 20 cm in thickness (Fig. 2.3a). The average maximum clasts size varies between 2-3 cm. The bed contains relatively few fossils. Clast compositions and concentration show dominantly quartz and basement clasts (Fig. 2.3c). The conglomerate is non-recurrent in occurrence. Though it is to some extent laterally persistent but not observed everywhere along the contact between the lower Sillakuddi Sandstone Formation and the marine Kallankurichchi Limestone Formation. The well sorted and clast-supported conglomerate (Fig. 2.3b) is likely to be a good candidate for a transgressive lag (Posamentier et al., 1988; Catuneanu, 2006; Yang, 2007; Catuneanu et al., 2011; Sarkar and Koner, 2020) which marks the initiation of a transgression. High roundness of the clasts elicits prolonged reworking. Sharpness of both the bottom and the top contacts of the conglomerate bed further corroborate the contention. The interstitial matrix at the upper part of the bed had probably infiltrated from above on relative decline in the vigour of transgression. This lag and the overlying coarse-grain debris (discussed later) previously interpreted as unconformity between the two formations (Sundaram et al., 2001; Watkinson et al., 2007; Nagendra et al., 2017, 2018) but during the present study this layer has been interpreted as transgressive lag followed by scree conglomerates and related deposits of different origin, will be discussed subsequently.

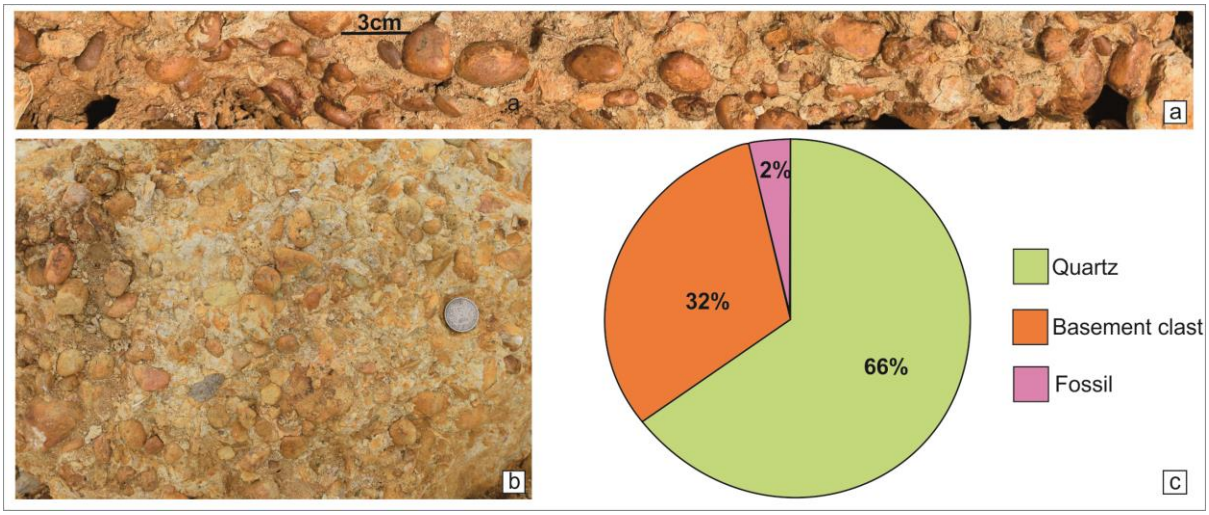

Fig. 2.3 Transgressive lag deposit (a); bedding plane view, note the roundness of clast (b); Clast compositions and concentration of transgressive lag deposits (c).

The rock assemblage representing the Kallankurichchi Limestone is broadly divisible into three (3) facies associations overlying on the transgressive lag. They are as follows: (1) Facies association I: Conglomerates and its associated facies (2) Facies association II: Wave-dominated facies association and (3) Facies association III: Tide-dominated facies association. A comprehensive description and interpretation of each facies within all facies associations is provided below.

2.2 Facies Association I:

Facies Association I is characterized by repetitive occurrence of conglomerates and a non-recurrent dark limestone facies, which is observed only at the basal part of the formation present immediate above the inferred transgressive lag deposit. At few places the limestone formation starts with a typically well-sorted and well-rounded conglomerates. Before delving into the repetitive conglomerates and pure limestone facies analysis, it is deemed necessary to have a detailed look into the conglomerate that underlies the limestone formation.

2.2.1 Facies IA, Scree conglomerates and its derivatives:

A total of 9 m thick wedge-shaped conglomerates occur at the basal part of the Kallankurichchi Limestone Formation, which is repetitive in occurrence. Although both siliciclastic and carbonate clasts are present within these facies, the basal part is dominated by siliciclastic debris (Fig. 2.4a). Conglomerate may be either clast- or matrix-supported, with mostly wedge-shaped geometry and juxtaposed successively (Fig. 2.4a).

The clast-supported conglomerate bodies are very poorly sorted along the boundary between Sillakuddi Sandstone and Kallankurichchi Limestone Formations. The clasts are chaotically arranged; some are sub-vertically oriented, reclining on other clasts. The bedding surfaces of these conglomerate beds are encrusted with fossil bivalves *Inoceramus*, though internally, they are unfossiliferous. The clasts can be traced to the underlying Sillakuddi Sandstone and the granitic basement. The clasts derived from the underlying Sillakuddi Sandstone Formation are mostly angular, measuring up to 60 cm long. The basement-derived clasts are comparatively smaller (up to 5-7 cm long) and are well-rounded. Clasts also include lime clasts, feldspar, and quartz pebbles. Some pebbles may sink into the underlying sand,

though no impact laminae are wrapping their bottom. The matrix, scarcely present between the clasts, is calc-arenite in nature. Strikingly, some clast-supported conglomerates show slide planes (NW-SE trending). Some pebbles penetrate the underlying sediments, and fractured clasts are also common. Successive occurrences of these conglomerates indicate repetitive tectonism. This massive clast-supported, ungraded conglomerate grades into a matrix-supported conglomerate in a down-wedge direction (Fig. 2.4b). The matrix-supported conglomerate shows convex-up geometry. Clasts in this conglomerate include bored limestone, fossils, and burrows. Crudely developed graded conglomerates occur locally. The conglomerates in the down-wedge direction give way to limestone deposition basinward.

Interpretation:

Clast-supported, extremely poorly sorted, and chaotically arranged, and the reclined nature of clasts indicates a scree deposit. These scree conglomerates invariably occur along the boundary between the Sillakuddi Sandstone and Kallankurichchi Limestone Formations, indicating the initiation of a new sedimentation regime. The extremely poor sorting, clast-supported framework, larger clasts from the immediate basement, and rapidly wedging bed geometry of the conglomerate facies are likely to be a scree conglomerate facies or rock fall deposit formed at a steep basin-margin slope (Bose et al., 2008; Reijmer et al., 2015; Chakraborty and Sarkar, 2018). This also suggests the continuation of the active tectonic pulses during the carbonate deposition at the lower part of the Kallankurichchi Formation. The presence of slide plane within the successive conglomerate beds also supports the contention. The successive conglomerates can be correlated with intermittent tectonic pulses, which were possibly responsible for the basin subsidence to create the accommodation space for the Kallankurichchi Limestone Formation. The growth of *Inoceramus* at places within the scree conglomerates signifies hard substrates within the scree mass. This indicates a possibility of some discrete pulses of the scree conglomerates. The time gap allowed the cementation of the upper surface. These conglomerates continually deposit even during the ongoing limestone deposition since lime-clasts are also present within the clast population. The slide planes probably facilitated the generation of these conglomerates. The preservation of feldspar clast suggests sudden and quick dumping. As no impact laminae are wrapping their bottom, it is evident that the scree fans formed under the sea permitted only slow sinking of rock fragments of large size range dropped from above. The presence of marine fossils within the scree

further corroborates this contention. The matrix-supported conglomerates, containing bored lime-clasts, delicate fossils, and haphazard orientation of clasts, indicate the presence of a highly viscous matrix, which suggests debris flow (Bose and Sarkar, 1991; Srimani et al., 2021). Chaotically embedded clast within matrix-supported conglomerates depicts a highly viscous debris flow deposit. Facies variability from clast-supported to matrix-supported conglomerates to even poorly developed normally graded conglomerates suggests the transformation of the initial flow. Along the slide plane, fluid got incorporated and diluted the flow. Scree deposits give way downslope to debris flow deposits. The flow becomes diluted, and turbulence developed downslope helps to generate normal crude grading.

2.2.2 Facies IB, Dark Grey Limestone:

This facies overlies the Sillakuddi Sandstone or conglomeratic facies but succeed to the yellowish limestone of the Kallankurichchi Formation with sharp contact (Fig. 2.4c). The non-recurring facies, with a characteristic dark hue, is laterally traceable for a maximum of 155 m within the studied section. The dark grey limestone is fine-grained, and the fossil content is relatively poor compared to the entire Kallankurichchi Formation, which is highly fossiliferous and yellowish in color. The dark grey color eventually changes to light grey at the upper part of the limestone. Fossils, if present, are mainly concentrated within this light grey zone, though a gradually increasing trend in the fossil content in the upper part is evident. The maximum thickness of this limestone is about 3.5 m (Fig. 2.4c). They are crudely cross-stratified at the upper part, while the lower part shows poorly developed planar laminae. The limestone shows a good content of siliciclastic detritus, amongst which quartz, feldspar, and sideromelane glass. The lower part of this limestone exhibits pyrite mineralization in places.

Interpretation:

The wedge-shaped, dark-colored limestone possibly formed in a relatively deeper part of the subsiding basin. It might have originated in a calm and quiet environment and its internal planar laminae also indicates slow rate of sedimentation. The depositional basin could have deepened to become more restricted. Typical dark grey color and fine-grained nature further support this view. The presence of pyrite mineral also suggests that the depositional surface must have attained significant oxygen depletion, possibly because of the repeated subsidence. Interestingly, the non-recurring nature of this dark-colored limestone indicates

that the condition of deposition required for this limestone never reappears during the deposition of the Kallankurichchi Limestone Formation. The crudely developed planar laminae suggest a low-energy environment of deposition compared to the other parts of the Kallankurichchi Limestone, which is either ripple or cross-laminated dominated by wave or tidal processes with occasional storm intervention (Fürsich et al., 2005; Srimani et al., 2021). The presence of angular and rounded sideromelane glass particles strongly suggests a volcaniclastic input during the deposition of the dark grey limestone facies (discussed in the subsequent section). The sideromelane glass particles in the dark grey limestone possibly originated from continuous rifting/post-rifting events. The scree conglomerates and slide planes within them indicate tectonic disturbance and basin subsidence. The repetitive siliciclastic influx at the lower part reflects the tectonic unrest of this rift basin. The prolonged subsidence leads to the development of relatively deeper paleogeography. The presence of numerous slide planes associated with the earlier facies described above also supports the idea that the subsidence along those planes was not the same everywhere across the basin. The discontinuous nature of dark grey limestone facies also signifies a sudden deepening of the basin because of the subsidence, which favors the formation of anoxic conditions and authigenic green clay minerals.

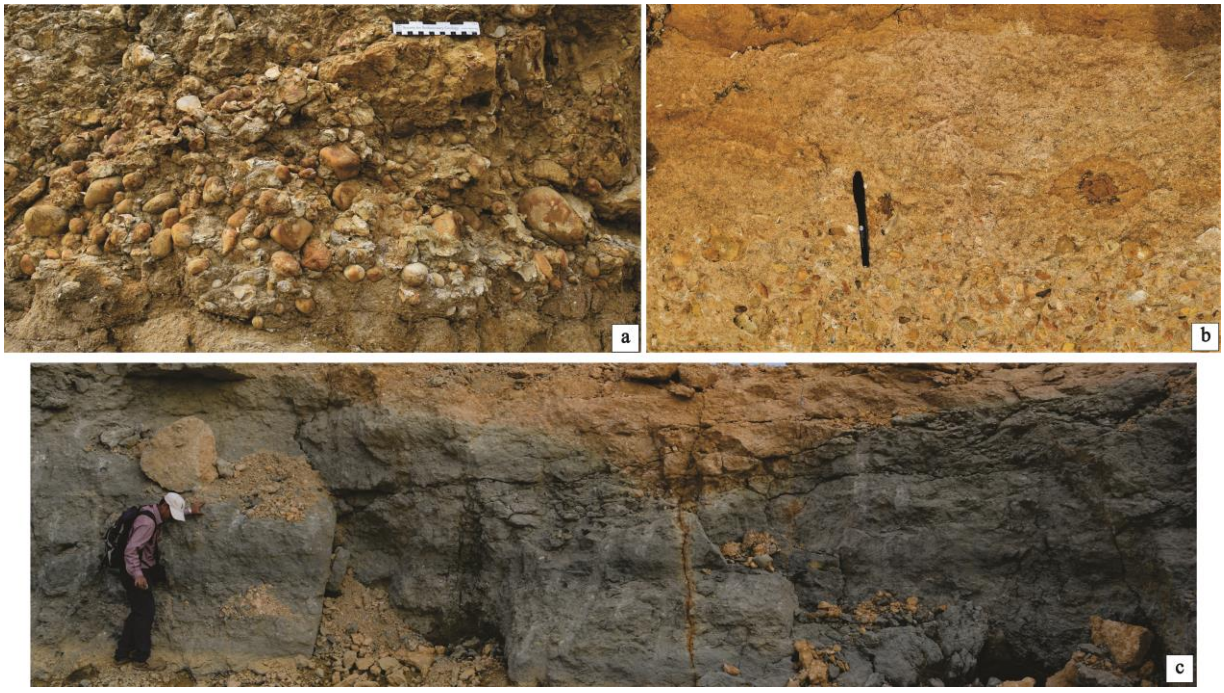

Fig. 2.4 Facies Association I: Clast-supported very poorly sorted conglomerates (a); Matrix-supported conglomerates and massive calc-arenite (b); Dark grey limestone (c).

2.3 Facies Association II:

2.3.1 Facies IIA, Herringbone cross-stratified Facies:

This calcarenite facies remains confined to the base of the measured succession and has broad lenticular geometry (Fig. 2.5a). The lenses measured ca. 2.5 m in outcrop width and maximum individual bed thickness 65 cm. The facies is characterized by oppositely oriented cross-strata in vertically adjacent beds (Fig. 2.5a) i.e., bipolar in nature showing paleocurrent direction towards NW-SE (Fig. 2.2). The cross-sets vary in thickness between 40 and 32 cm.

Interpretation:

Apparent paleocurrent reversal in successive beds tell-tales flood-ebb tide alternations. Within the wave-dominated association this facies appears a bit out-of-place. However, this facies occurs only at the base of the measured succession and its lenticular in geometry, suggests deposition took place within channels (Sarkar et al., 1991). It seems that when the transgression began, in the shallowest part of the basin, tide got accentuated within channel restrictions, while waves tended to dissipate. With progression of transgression, as the water depth increased, waves probably gained over tide and had cast greater influence on sedimentation. The herringbone cross-stratification arising from the paleocurrent reversibility implies that the tidal regime had been, more or less, symmetrical (Collinson et al., 1982).

2.3.2 Facies IIB, Graded storm facies:

These facies units are thick, measuring from 3 to 5 m. The beds are tabular in geometry. The beds have sharp bases, while their tops are comparatively less sharp. Internally the beds are graded, and this grading is manifested in vertical distribution of fossils. In some beds the dominant fossils are of *Gryphea* (Fig. 2.5b) and in others they are of *Platyceramus* (Fig. 2.5b). In the latter case the elongated bioclasts are distinctly haphazard in orientation. The majority of *Gryphea* shells in these beds are also haphazard in orientation (Fig. 2.5b).

Interpretation:

The grading indicates deposition from suspension and hence transportation of sedimentary load in a density current (Sarkar et al., 2004; 2011). Despite that, the grading

itself suggests that the sediment driving flow had been light enough in density to allow larger clasts to settle first. Chaotic orientation of the elongated *Platyceramus* fragments suggests turbulence in the flow immediately prior to deposition. The formidable thickness of the beds indicates enhanced rate of deposition from individual flows, hardly ever achievable in fair-weather processes. Probably, these beds were laid by down welling induced by storms (Harms et al., 1975; Bose et al., 1988; Walker and Plint, 1992; Sarkar and Koner, 2020). It is reasonable to assume that storms significantly enhanced the rate of delivery of organic particles (Kumar and Sanders, 1976; Wilson 2012).

2.3.3 Facies IIC, Rippled facies:

This facies is distinctly fine-grained with respect to the immediately preceding facies of inferred storm origin with which it alternates. It generally overlies either the graded storm facies or chevron and hummocky cross-stratified facies. It appears typically as sheet-like geometry (Fig. 2.5c). In some places it shows nodular nature. Close inspection reveals cross-laminae within the nodules. These cross laminae show consistent 175º direction (Fig. 2.2). Small-scale cross-laminae preserved even within the conspicuous fossiliferous succession. The average thickness of the facies units is around 40cm. The cross-lamina sets within them are around 3-6 cm thick. The cross-lamina set boundaries appear erosional and concave-up in orthogonal sections.

Interpretation:

Comparatively finer grain-size and smaller structural elements with respect to those of adjacent storm beds help to identify this facies as a fair-weather product. The facies presumably depict ripple migration. A steep depositional energy gradient seems to be implied by vertical transitions from this facies to the adjacent facies of inferred storm origin and vice versa. However, the cross-laminae indicate that the facies was deposited in an agitated condition, may not be as much agitated as during storm. Geometry of the cross-set boundaries in orthogonal sections suggest that the ripples are created by wave agitation (DeRaaf et al.,1977). In temporal alternations with storm beds, this facies is inferred to be fair-weather origin. A vertical depositional energy transition has been observed from storm facies to this facies and followed by shellbank facies.

2.3.4 Facies IID, Shellbank facies:

This carbonate facies with conspicuous enrichment in well preserved *Gryphea* shells of average diameter 14 cm is a rudstone in Dunhum's (1962) terminology. It overlies the storm beds, either graded or cross-stratified. Shell concentration varies laterally; in fact, it alternately decreases and increases. Grey colored lime-mud admixed with shell hash fill the space between the shells and within the shell cavities (Fig. 2.5f). The bed geometry is highly irregular. The beds have sharp top where shell concentration is high, but gradational at bottom everywhere. All the shells are generally concave-up in attitude, but little exceptions are also there.

Interpretation:

Frequent good preservation of a large number of thick and relatively heavy shells of *Gryphea*, and that too in living concave-up condition suggests the shell concentration is a result of in-situ growth, in other words, colonization. Random orientation of some shells is always explicable with bioturbation. Distinct lateral variation in shell density without any apparent taphonomic control probably reflects deliberate choice of living organisms about spots to flourish. Indistinct lower surfaces of the beds in contrast to their upper surfaces agree with this contention of in-situ growth. Exclusive occurrence of this *Gryphea* colonization on top of storm beds is possibly because of enhanced production rate of these sedentary organisms at the aftermath of storms.

2.3.5 Facies IIE, Chevron and Hummocky Cross-stratified facies:

These two facies include all cross-stratified rocks except those bearing herringbone cross-strata. They are entirely composed of calc-arenite with chevron and hummocky cross-stratifications. In both the cases the bases of the calc-arenites are invariably sharp while their tops are less sharp or even gradational. The chevron cross-stratified beds are, in general, tabular in geometry and their bed thickness is nowhere less than 50 cm (Fig. 2.5e). Cross-strata show dipping both the direction towards 110º and 50°. The hummocky cross-stratified beds are, on the other hand, characterized internally by hummocky cross-strata and externally by broadly lenticular to sheet like body geometry with broadly convex-up tops. The maximum height of hummocks measuring ca. 95 cm and wavelength ca. 1.5 m (Fig. 2.5d).

The bases of these beds typically mimic the surface of the bed underneath. So, although the bases are sharp, they are non-erosional in nature. The top surfaces of the beds are less sharp. Here, shells are broken, and large shells are showing haphazard biofabric. Some shells are in convex-up i.e., their current-stable position. These two facies are most dominant to the middle part of succession, and they are repetitive in occurrence. The frequency of occurrence diminishes progressively in the upward direction.

Interpretation:

These two facies, of chevron cross-strata or with HCS, appear to be dominantly wave affected. The thick chevron cross-stratified beds appear to record vertical up building of bedforms over duration relatively much longer. The HCS implies wave-current combined flow (Greenwood and Sherman, 1986; Nøttvedt and Kreisa, 1987; Tinterri, 2011; Mandal et al., 2016). Hummocky cross-strata with wavelengths exceeding 1 m suggest intense wave activity, potentially indicating a bedform induced by storm (Harms et al., 1975; Bose and Chanda, 1986; Bose et al., 1988). The large spacing of HCS also points to waves larger than usual short period fair-weather waves (Swift et al., 1983). Stacked shells are indicative of high energy processes. As some shells are in a current-stable convex-up position, indicates rapid transportation and dumping by storm flows. Hence storm down-welling as the sediment-driving mechanism is implied (McCrory and Walker, 1986; Bose et al., 1988).

2.3.6 Facies IIF, Muddy Facies:

This facies is conspicuous for its deep grey color and muddy nature and laterally persistent (Fig. 2.5f), despite its thinness (15 cm). Its base is slightly and broadly undulated, while its top is flat. This facies occurs at the top of the wave-dominated facies association and is non-recurrent.

Interpretation:

The fine-grained nature suggests deposition in a quieter area. Deposition in a deeper shelf is interpreted. The body geometry of the facies suggests limited erosion at its base. This facies occurring at the contact between the two facies associations and does not have any hall mark for either wave or tide.

In this fully fossiliferous limestone, another facies classification has been proposed combining the sedimentary structures as well as fossils present within the entire succession (Fig. 2.6).

2.4 Facies Association III:

2.4.1 Facies IIIA, Small scale herringbone cross-stratified facies:

This facies characterized by herringbone cross-strata overlies the muddy facies 1F. The cross-strata appear in reverse orientation across bed surfaces (Fig. 2.7a). The cross-sets are about 14-16 cm in thickness. The foresets bear distinctive mud drapes (Fig. 2.7a). Shell fragments remain scattered within the cross-sets. The broadly undulated set boundaries are, at places, well demarcated by shell concentrations (Fig. 2.7c). The entire facies body comprised of multiple such cross-sets is about 3.5 m in thickness. This is non-recurrent in the Kallankurichchi Limestone stratigraphy.

Interpretation:

The paleogeography appears to be tide-dominated, although shell concentrations along some cross-set boundaries are inferred as wave winnowed lag deposits (Fig. 2.7c). The bipolar paleocurrent pattern, though weakly so, corroborates reversal of current. The mud drapes on foresets and are bimodal, if not bipolar, cross-strata orientations are distinctive fingerprints of tide (Bose et al., 1997; Eriksson and Simpson, 2000; Eriksson et al., 2006; Mandal et al., 2019). The fossil content, as mentioned before, identifies this tidal facies as of a shelf. The small scale of cross-strata speaks of relatively weakly agitated environment. The depositional site thus seems to be away from the shoreline, at a distal position.

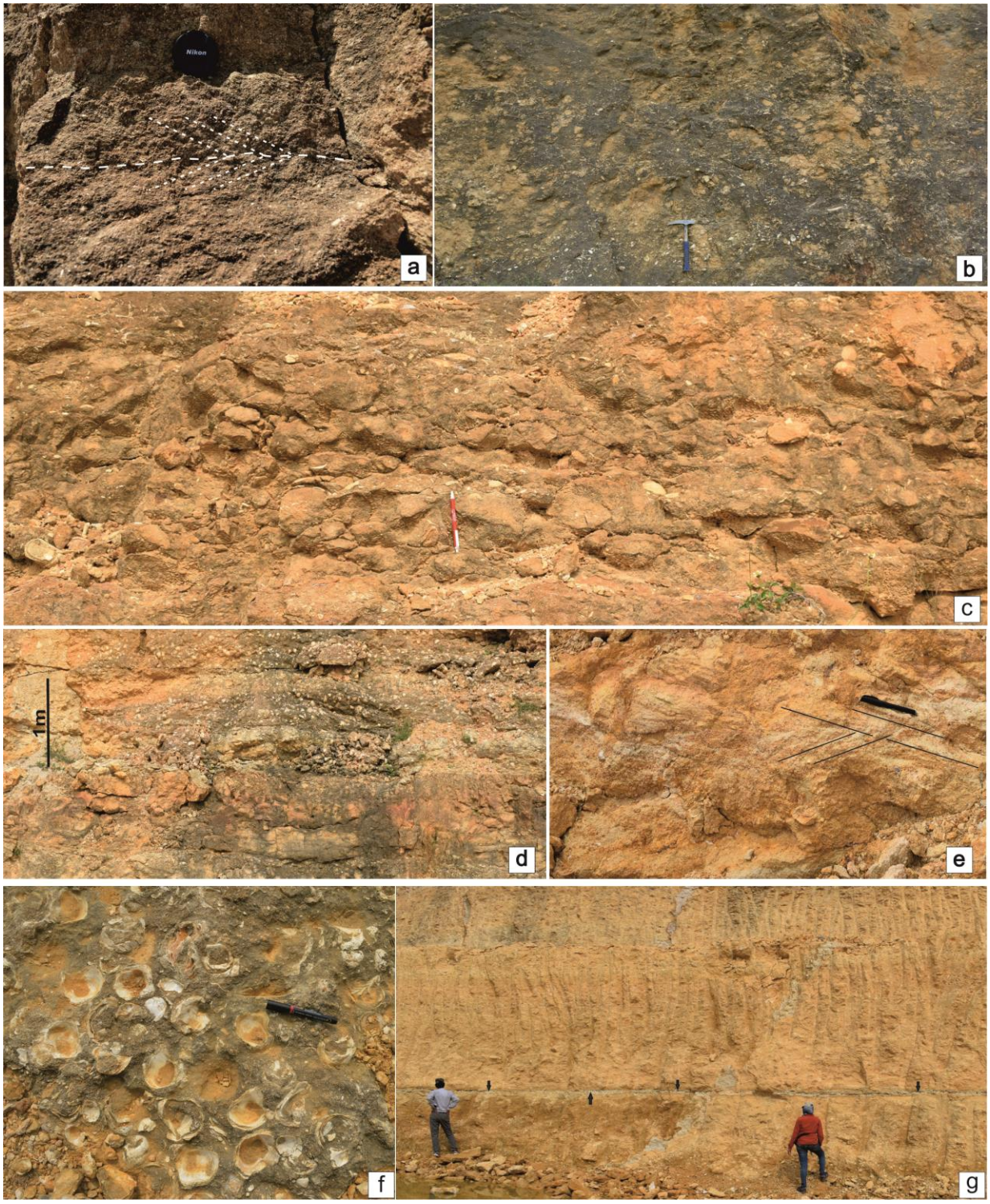

Fig. 2.5 Facies Association-II: Herringbone cross-stratified facies (a); Graded storm facies (b); Rippled facies. Note, Sheet-like body geometry (c); Hummocky cross-stratified facies (d); Chevron cross-stratified facies (e); Shellbank facies. Note, the concave-up nature of most of the shells and interstitial spaces are filled with grey colored lime-mud (f); Muddy facies (black marking) (g).

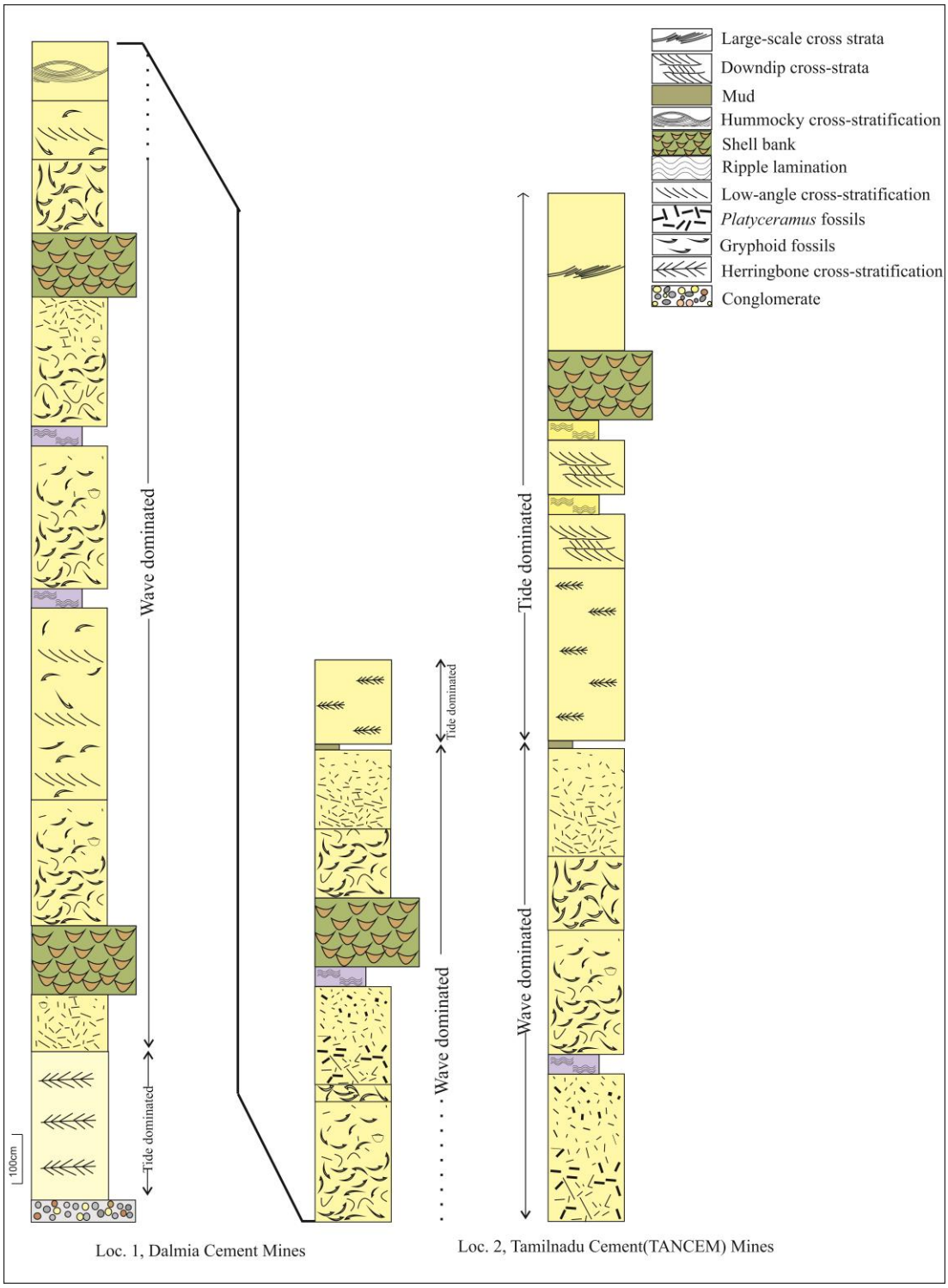

Fig. 2.6 Distribution of different facies considering the fossils at two best exposed localities (Srimani et al., 2021).

2.4.2 Facies IIIB, Down-dip cross-stratified facies:

This facies rests on the preceding facies unit and recurs further upward. Large-scale low angle cross-strata confine small-scale steeper cross-strata between every pair of them. Both the sets dip in the same direction (Fig. 2.7d). Set thickness of the small-scale cross-strata is, on average, 8-9 cm and that of the larger-scale cross-strata averages 21 cm. The smaller-scale cross-strata bear mud drapes. Cross-strata geometry also changes laterally, cyclically from steep to gentle and to steep again (Fig. 2.7d).

Interpretation:

The mud drapes suggest that the carbonate particles were transported under influence of tide. The down-dip cross-strata suggest flow-parallel elongation of bedforms that resulted. These bedforms identified as longitudinal tidal bars are inferred to have originated on a shelf (Prothero and Schwab, 1996; Reading, 1996), presumably at relatively shallower part of the shelf with respect to the preceding facies.

2.4.3 Facies IIIC, Rippled facies:

This facies is distinctly finer grained than the immediately preceding facies with which it alternates (Fig. 2.7b). It is sheet-like in geometry. The ripple forms are preserved being wrapped around by thin mud drapes.

Interpretation:

The mud drapes were possibly formed during tidal slackening phases and ripples migrated during periods intervening them. Alternating with the immediately preceding facies, this facies seems to have deposited in the same paleogeography as the former. Most probably, this facies formed in the interbar region.

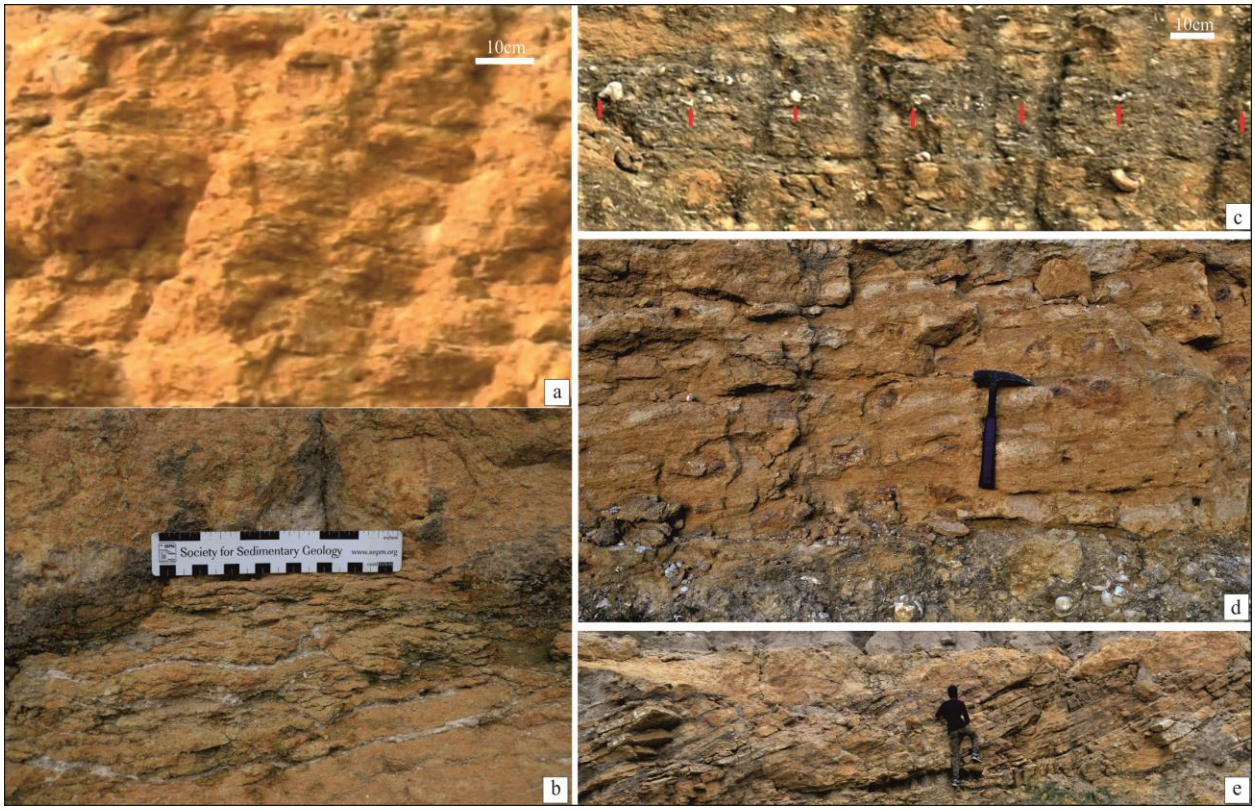

Fig. 2.7 Facies Association-III: Small scale herringbone cross-stratified facies with mud drapes (a); Rippled facies (b); Broadly undulated set boundaries are, at places, demarcated by shell concentrations (arrowed red) (c); Down-dip Cross-stratified facies (d); Large-scale cross-stratified facies (e).

2.4.4 Facies IIID, Large-scale cross-stratified facies:

This facies is at the top of the measured carbonate succession. It is non-recurrent and represented by a single large cross-set (Fig. 2.7e) of preserved thickness ranging up to 2.3 m. Cross-strata dipping towards 150º to 165º (Fig. 2.8). The forests change geometry laterally from steep to gentle and to steep again (Fig. 2.7e). While the foreset is steepest, the toeset is shortest and the gentlest foresets are accompanied by longest toesets. The forests are draped by mud.

Interpretation:

This facies is interpreted as proximal to the shore. It seems to have deposited in a tide-agitated environment. The mud drapes on top of the forests and cyclical change in the cross-stratification geometry are distinctive signatures of tide. The depositional energy level

locally and temporally allowed mud deposition, on top of the forsets and bottomsets of cross-strata. Slackening of flow between flood and ebb, especially close to the neap tide, favoured mud settling. The cross-strata geometry changes presumably record cyclical transitions between spring and neap tide (Reading, 1996; Collinson et al., 2006). Their foreset steepness and toeset lengths varied presumably with cyclically changing velocity of the parent flow (Bose et al., 1997; Sarkar et al., 1999).

Fig. 2.8 Large scale cross-strata. Note, the concentration of shell (arrowed, red) just below the cross-strata.

CHAPTER-3

MICROFACIES ANALYSIS

3.1 Introduction:

'Microfacies' coined by Brown (1943), refers to the characteristics observed in thin sections, examined under a microscope. Cuvillier (1952) reintroduced the term 'microfacies' to appertain petrographic as well as paleontological criteria studied in thin sections. According to Flügel (1982) 'microfacies' encompasses all the sedimentological and paleontological features, both qualitative and quantitative, that can be identified in thin sections and polished samples at magnifications of approximately up to 200x. Microfacies analysis of carbonates also requires a knowledge of understanding of biological and geological changes during earth history. A petrographic examination is needed to validate the field data, which are employed to reinforce the theoretical framework. The combined facies and microfacies study of carbonate rocks are always emphasized for genetic interpretations of limestones (Sorby, 1879). Accurate documentation of geological and paleontological data as well as sampling methods that account for both the vertical and lateral variations are vital for microfacies investigations (Adams & MacKenzie, 1998). However, microfacies analysis is always important for carbonate rocks. Exposure of carbonate rocks are mostly very monotonous and lack sedimentary structures, sometimes primary bedding identification is difficult (Wright, 1990, Bose et al, 2012) as they are destroyed by diagenesis and/or due to churning activities of organisms. Sometimes it is absent because of its in-situ nature of deposition. Thus, during the present study besides process-related sedimentary facies analysis microfacies analysis has also been considered.

As discussed earlier, the Kallankurichchi Limestone deposition initiated with a transgressive lag. The petrography of this facies reveals that the limestone includes both packstones and grainstones (Fig. 3.1a). The grainstones commonly bear isopachous carbonate cement (Fig. 3.1b) and locally, shelter pores are filled by similar cement. The high degree of roundness of the pebbles, irrespective of compositional variation, the fossils and the isopachous cement clearly favour deposition in marine shallow phreatic zone. It incorporates a wide variety of marine fossils, such as nummulites, echinoids, pelecypods including *Gryphea* and many kinds of foraminifera. Siliciclastic grains are present in both, but mostly in silt grade within the packstone and in sand grade within the grainstone (Fig. 3.1c). The fossils present within them are variably oxidized. Some shell borings are even rebored (Fig.

3.1d). In support of the transgression, the limestones intervening the conglomerates bear clear evidence of very slow rate of deposition in form of reworked clasts and repeated borings on the shells.

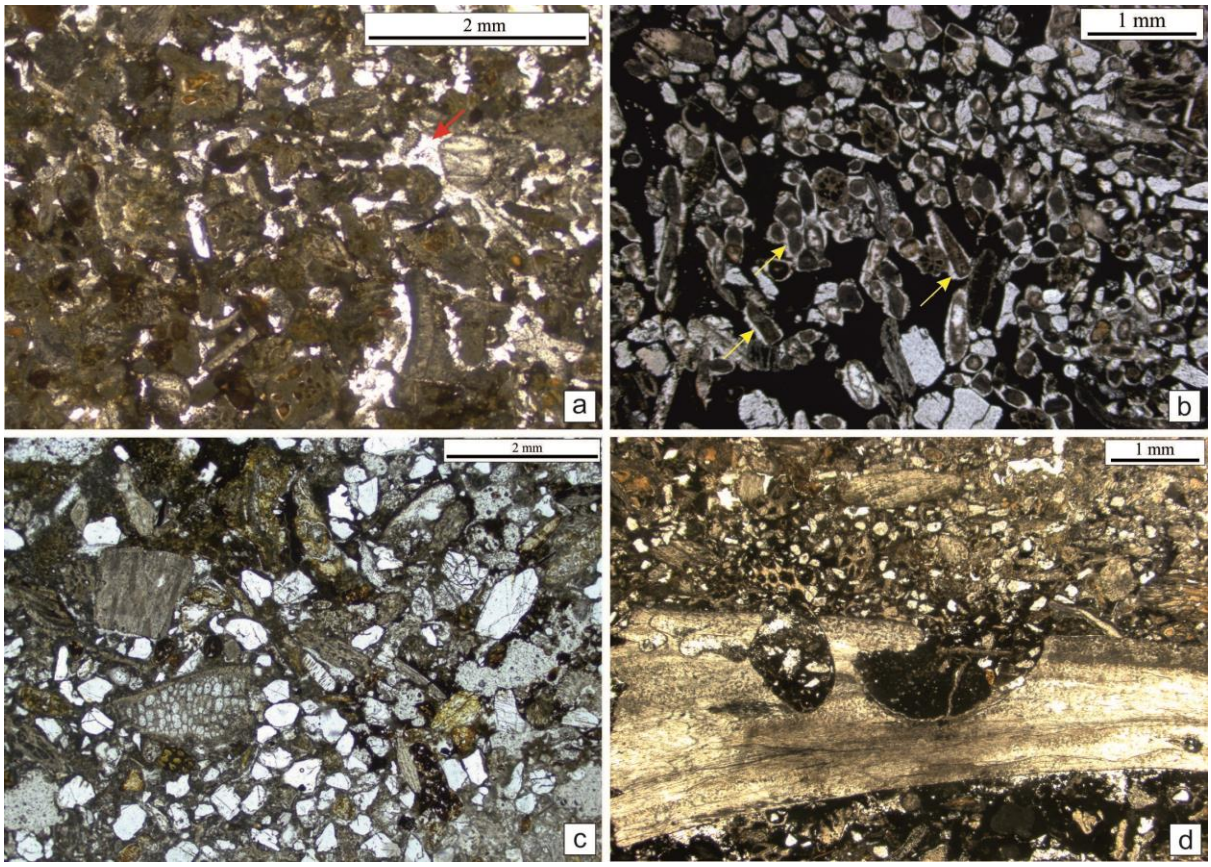

Fig. 3.1 Transgressive lag includes both packstone and grainstone (red arrowed) (a); isopachous carbonate cement (b); Siliciclastic grains within the packstone and grainstone (c); multiple boring within fossil shell (d).

Microscopic study is conducted following the field facies classification discussed earlier.

3.2 Facies Association I:

3.2.1 Facies IA, Scree conglomerates and its derivatives:

Conglomerates clasts are angular to sub-angular and very poorly sorted. There is wide compositional variability within the clasts. There is quartz, feldspar, different types of fossils

(Fig. 3.2.1a), basement clasts (Fig. 3.2.1b). Among them quartz grains are the most abundant clast type. The quartz clasts are mostly angular, though some of them have broken and have highly corroded grain boundaries (Fig. 3.2.1c). Somewhat rounded and anhedral quartz clasts are also present. Maximum of them bear micritic rims around themselves (Fig. 3.2.1d). Some quartz clasts have isopachous cement rim of aragonite identified by its cigar shape (Fig. 3.2.1e). Double rims of cements are also seen around the quartz clast (Fig. 3.2.1f). Boundary parallel cracks are observed in quartz clast. Desiccation crack has been generated around the grains as well as muddy matrix. The matrix consists of greenish to greyish micrite and sharp-edged silica fragments are embedded within muddy matrix.

Lime mud clasts are also found. Highly oxidised intraclasts with corroded boundaries are also present (Fig. 3.2.1g). Pore spaces are partially filled with matrix and subsequently cemented with sparry calcite. They are rich in organic remains, such as bryozoans and shell fragments of echinoids, foraminifera, bivalves and gastropod shells. Bryozoan zooecia are filled with lime mud. Encrusting Bryozoa wrapped the intraclast (Fig. 3.2.1h). Clustered lime-mud clast again got clustered (Fig. 3.2.1i). Some clustered echinoids are found in the lime mud. Boring is also found within the fossils and bored material is filled with the same outside matrix (Fig. 3.2.1j). Muddy matrix has been replaced by calcitic rhomb contact between them remaining sharp (Fig. 3.2.1k). In-situ desiccation cracks within mud clast (Fig. 3.2.1l). The mud tears apart due to contraction of the clast after deposition. This mud lining defines the original boundary. Shelter pore is created underneath the large fossil clast especially under convex-up pelecypod valves and filled with blocky calcite cement.

This facies is exceptionally characterized by calcite rhombs with dirty core, although some members in this facies are devoid of them (Fig. 3.2.1m). This occurs on distal front of the siliciclastic scree deposits and is often in lateral contact with the massive calc-arenite facies (detail discussion in Chapter- 6) of the purported scree-fan.

It is of a grey-coloured micritic limestone with peloidal clotted texture. The peloidal masses are surrounded studded with numerous calcite spars, giving rise to a fabric-selective texture (Fig. 3.2.1n). The calcite crystals are clear. The calcispars have long diagonals in the range of 3µm and are markedly zoned. The spary crystals are typically dirty in their cores but become clearer away from the cores.

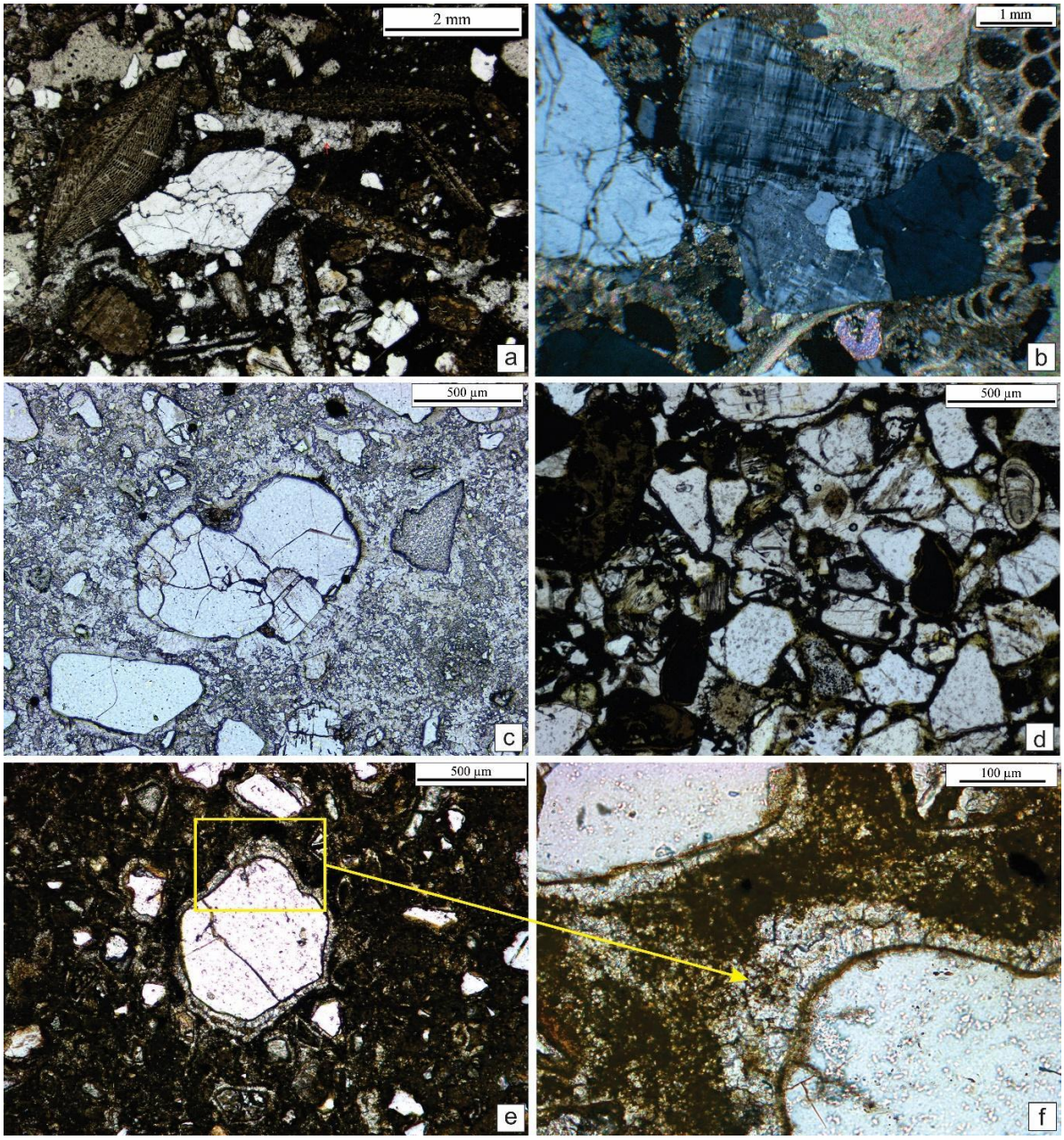

Fig. 3.2.1 Facies IA: quartz, and different types of fossils present in this facies (a); presence of basement clasts (b); broken quartz clast with corroded grain boundary (c); angular quartz bear micritic rims (d); cigar shape isopachous cement rim of aragonite (e); Double rims of cements around the quartz clast (f).

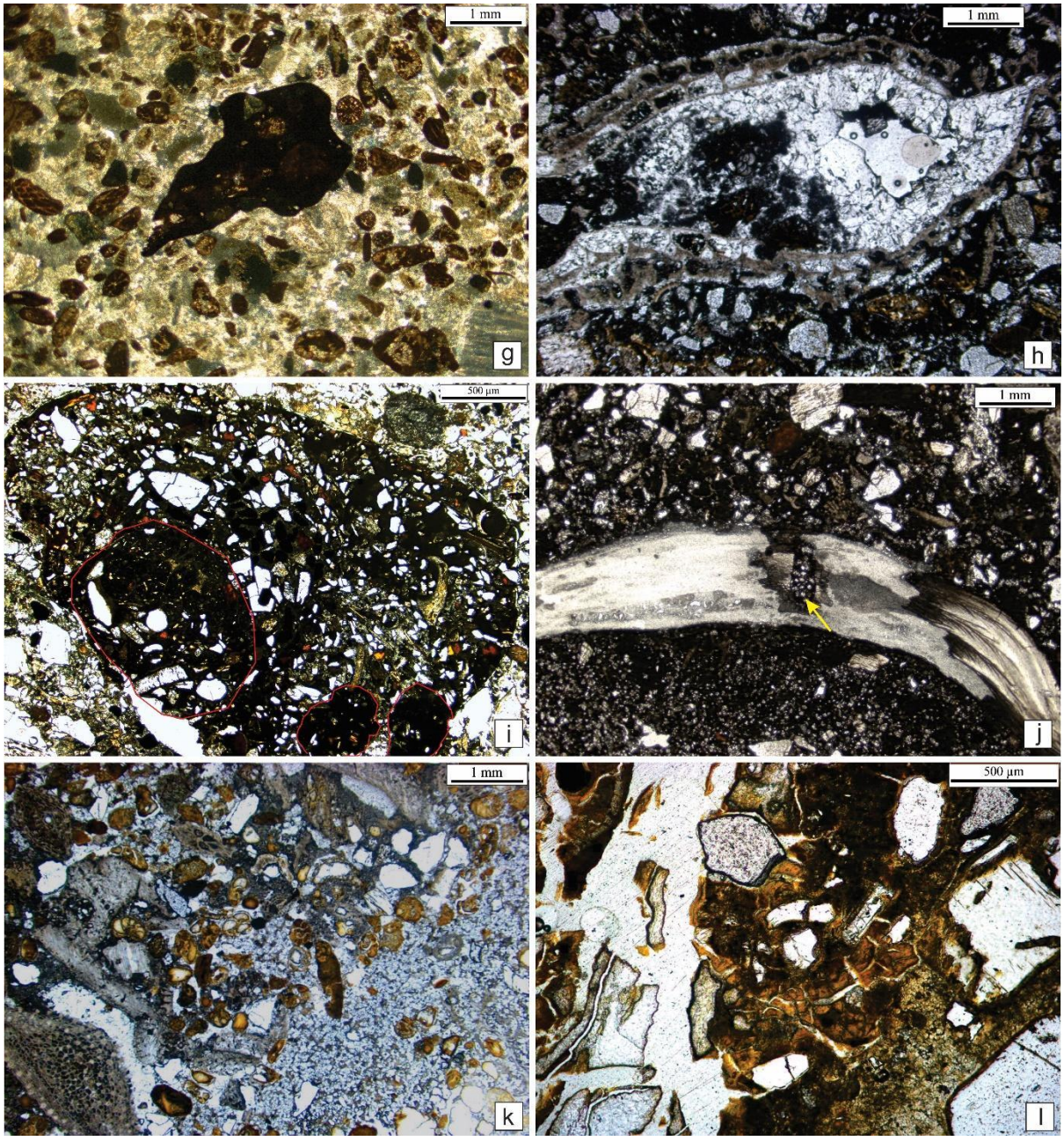

Fig. 3.2.1 Facies IA: highly oxidised intraclasts with corroded boundary (g); Encrusting Bryozoa wrapped the intraclast (h); Clustered lime-mud clast again got clustered (marked with red border) (i); Bored fossil clast and boring is filled with the same outside matrix (yellow arrowed) (j); Muddy matrix has been replaced by calcitic rhomb (k); desiccation cracks within mud clast (l).

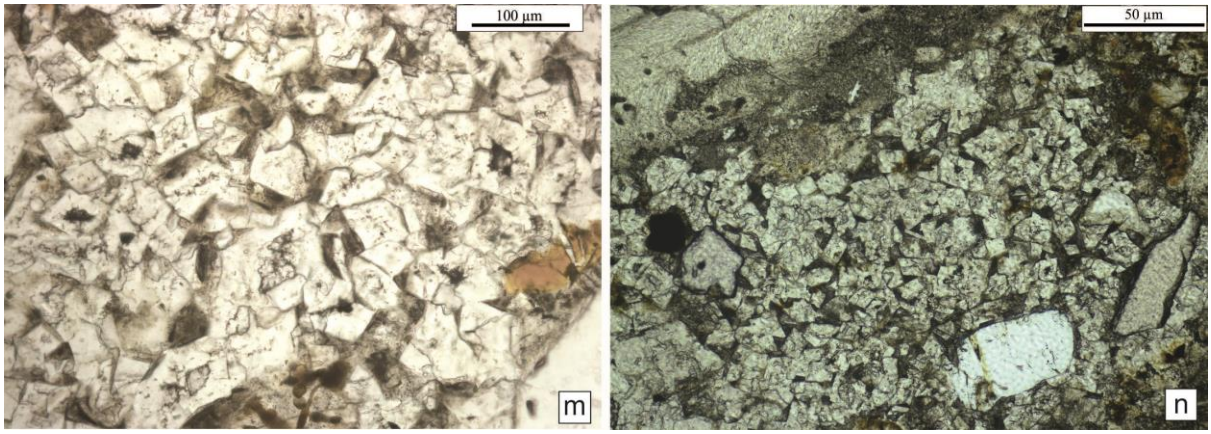

Fig. 3.2.1 Facies IA: calcite rhombs with dirty core (m); fabric-selective texture note, peloidal masses are surrounded studded with numerous calcite spars (n).

Interpretation:

Angular to sub-angular and very poorly sorted clasts interpret that there is no transportation of clasts. Double rim in some of them suggests two generations of cement. The abundance of different kind of fossils (dominantly echinoid, bryozoa and *Inoceramus*) in the matrix indicates a submarine origin for the conglomerates. Boundary parallel cracks in quartz clast suggest free fall of clasts that's why it got fractured. The wide compositional variability of the pebbles suggests their derivation from the graben walls, yielding both fragments of the Sillakuddi Sandstone as well as of the Precambrian basement. In-situ desiccation cracks within mud clast suggests some pause. Rapid precipitation favoured aragonite over calcite as the cement within the interstices. The clotted texture had apparently been deposited under water and hence, comparatively slow precipitation favoured calcite to precipitate in between the pelloidal lumps. Consequently, a fabric-selective texture has arisen. The depositional environment of this facies had likely been under water and the comparatively slow rate of precipitation favoured calcite precipitation.

3.2.2 Facies IB, Dark Grey Limestone:

The carbonate mud matrix is relatively dusty in appearance. The limestone shows a good content of siliciclastic detritus, amongst which quartz, feldspar, and fresh to partially palagonitized sideromelane glass (ranging in diameter from ~100 to ~350 µm) are common

(Fig. 3.2.2a). Corroded grains are also present. A green clay pseudomorph, called berthierine, is present throughout this limestone altering the glass (80–90%) (Fig. 3.2.2b). The typical yellow coloured devitrified glass and the quenching texture of glass has been found (Fig. 3.2.2c). Even the core and rim boundary are clearly visible in glass (Fig. 3.2.2d). The remaining green clay minerals form along the cleavages of feldspar grains, along the rims of the quartz grains (Fig. 3.2.2e), and, in rare instances, as pore-filling material within broken bioclast fragments. The lower part of this limestone exhibits pyrite mineralization, which is authigenic pyrite, present in fair abundance (Fig. 3.2.2f).

Interpretation:

The presence of angular and rounded sideromelane glass particles strongly suggests a volcaniclastic input during the deposition of the dark grey limestone facies. The sideromelane glass particles in the dark grey limestone possibly originated from continuous rifting/post-rifting events. Creation of the numerous dissolution vugs while considered together with corroded grain-margins suggests considerable presence of dissolved carbon dioxide in the porewater. Authigenic pyrites indicates development of anoxic condition in the depositional basin. Cumulatively this grain corrosion and sulfidization of the sediment suggest enrichment of basinal water in CO_2 and sulfur as commonly found in case of hydrothermal input (Large et al., 2017).

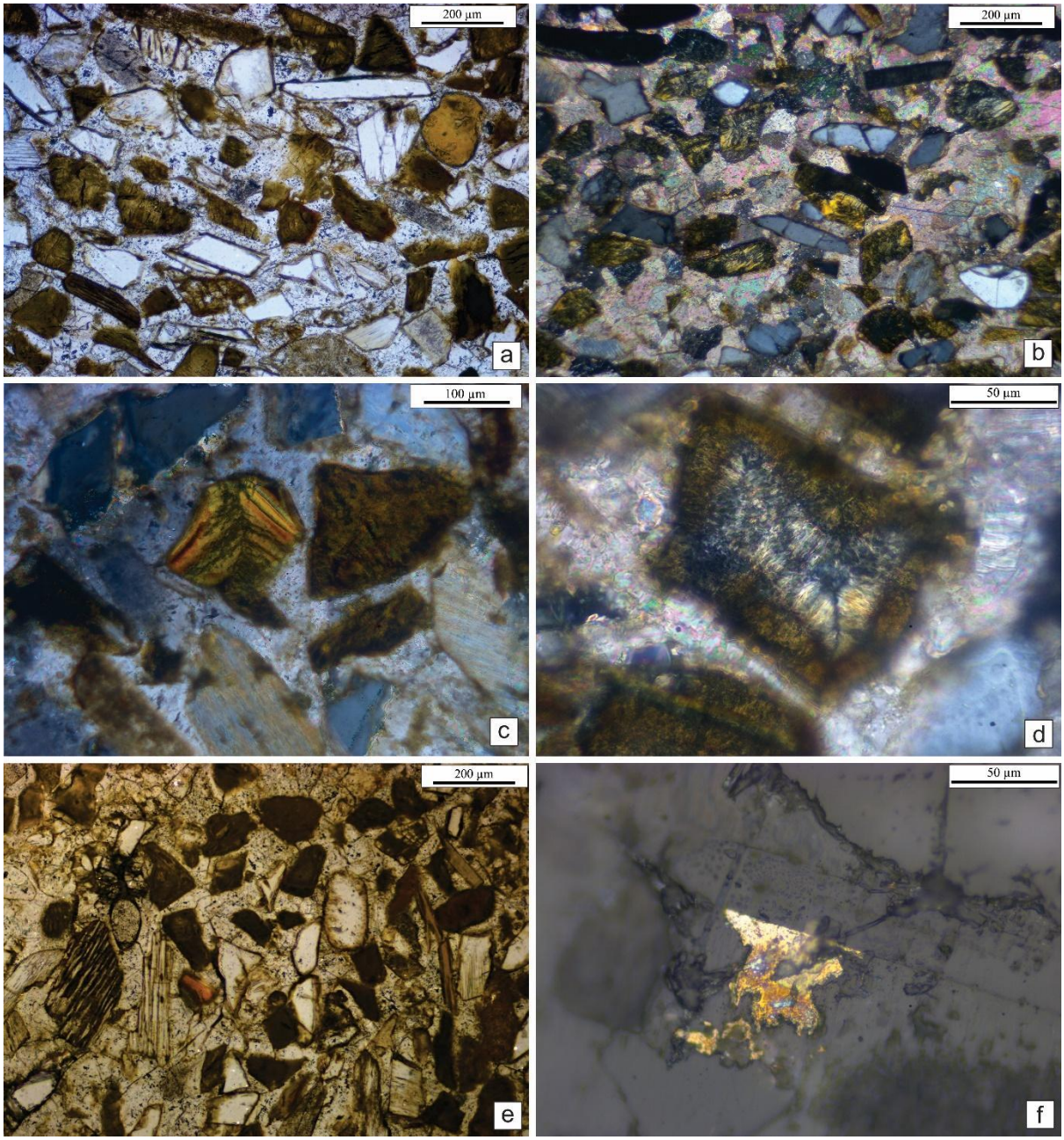

Fig. 3.2.2 Facies IB: siliciclastic detritus and fresh to partially palagonitized sideromelane glass (a); green clay pseudomorph (berthierine) altering the glass, under CPL (b); typical yellow coloured devitrified glass and the quenching texture of glass (c); core and rim boundary in glass (d); berthierine form along cleavages of feldspar grains and along the rims of the quartz grains(e); authigenic pyrite (f).

3.3 Facies Association II:

3.3.1 Facies IIA, Herringbone cross-stratified Facies:

Facies IIA is carbonate sandstone with a subordinate, but locally substantial, admixture of detrital population, mainly quartz, some feldspar and very few biotite grains (Fig. 3.3.1a). The most remarkable aspect is the division of the coarse clastic component between extrabasinal terrigenous and intrabasinal carbonate in comparable proportion. Coarse terrigenous particles include quartz, feldspar, and granite fragments. They are generally unabraded in nature and absence of overgrowth. Many of them have highly irregular corroded boundaries (Fig. 3.3.1b). However, in this facies, confined to the basal few metres of the measured succession, the siliciclastic population dwindles away rapidly upward (Fig. 3.3.1a). The coarse carbonate clastic fraction is principally made up of intraclasts (Fig. 3.3.1c) with or without bioclasts embedded within them and a few isolated bioclasts, amongst which inarticulated echinoid plates are mentionable. Significant presence of intraclasts warrants the name intramicrite for the rock in the bottom level but gradually changes into intrasparite at the topmost level of the tidal section (Folk, 1959, 1962). The intraclasts are brown in colour (Fig. 3.3.1d). Almost all the carbonate clastic grains bear micritic rims around themselves, only at the uppermost level of this tide-imprinted section, isopachous needle-shaped carbonate cement crystals take their place (Fig. 3.3.1e). In the lower part of the same section blocky cement occurs preferably at the underside of clastic grains. No such preference for blocky cement occurrence is observed in the upper level. In the latter case there is always a conspicuous ferruginous coat between the first-generation isopachous cement and the second-generation blocky cement (Fig. 3.3.1f). The isolated bioclasts have a wide range in length, while the intraclasts occupy the lower segment of this range.

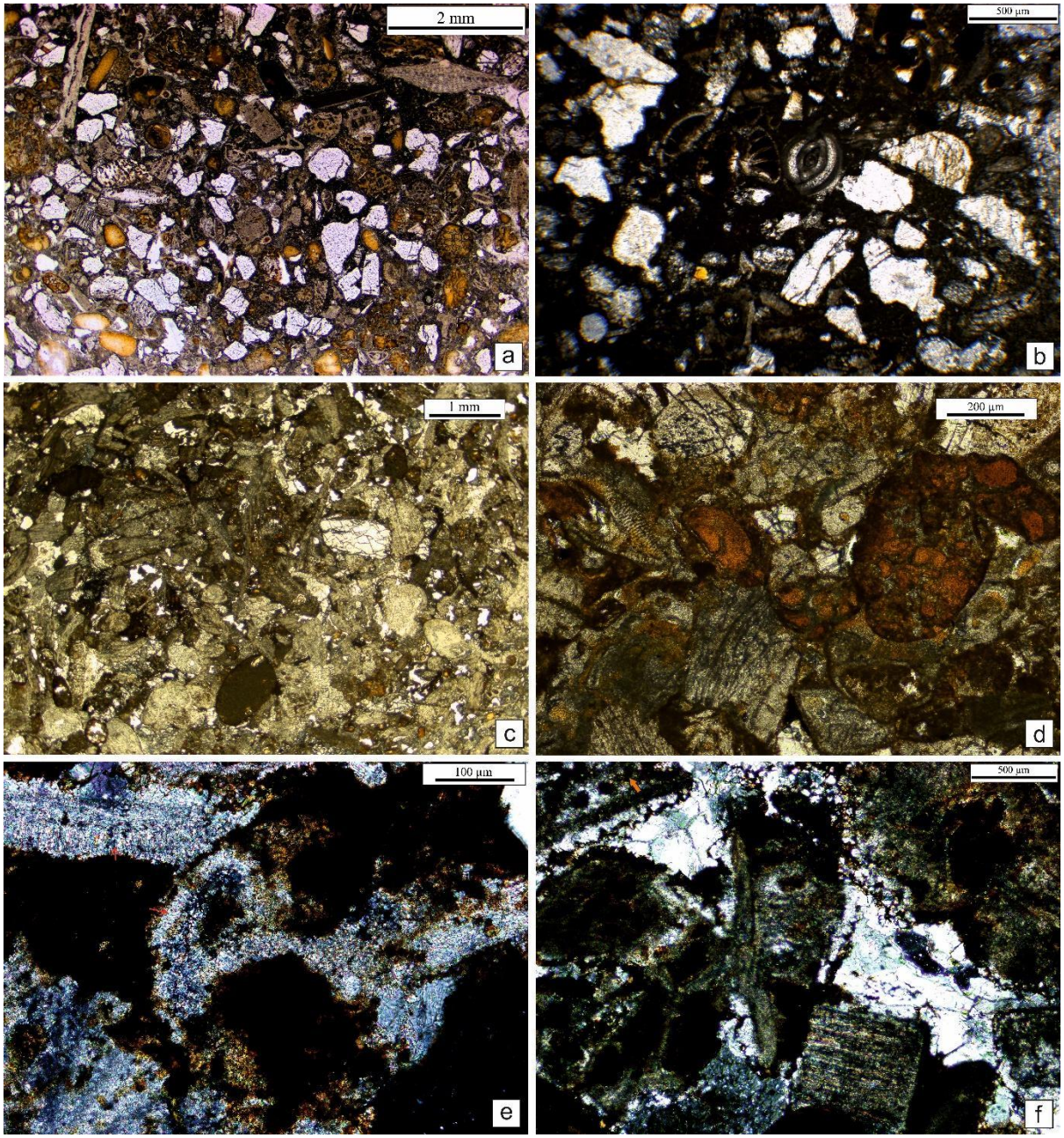

Fig. 3.3.1 Facies IIA: carbonate sandstone with subordinate admixture of detrital population (a); highly irregular corroded boundaries of quartz, note, the unabraded nature and absence of overgrowth (b); intraclasts along with quartz and bioclast (c); brown coloured intraclasts (d); isopachous needle-shaped carbonate cement (e); conspicuous ferruginous coat between first-generation isopachous cement and second-generation blocky cement (f).

Interpretation:

At the onset of carbonate deposition, at the shallowest part of the sea tide amplitude probably increased within constriction of channels while wave dissipated rapidly and that may be the reason for the presence of tide signatures at the bottom section of the wave-dominated association. Herringbone cross -strata imply that the tide had been symmetric. The transition from matrix-supported to clast-supported fabric within single facies, even within a single thin section, is though intriguing, should not be uncommon in tide-constructed cross-strata that often turn muddy within the toeset as well as at top of the normally graded foresets. Intramicritic composition at the lower level and intrasparitic composition (Fig. 3.3.1g) in the upper part of facies IIA imply progressive increase in the tidal flow intensity with the shift of paleogeography seaward. This seaward paleogeographic shift through time is strongly corroborated by upward decrease in size and frequency of occurrence of siliciclastic grains. Coarse terrigenous grains floating within mud bear clear attestation to simultaneous operation of two completely different modes of deposition. The mud must have settled from suspension, while terrigenous coarse fraction dislodged from their original sites of deposition and rolled or slide downslope to settle within the mud. At the shallowest part of the paleogeography the intraclasts were derived presumably from the banks of the migratory tidal channels, although intramicritic composition of the rock indicates low energy of tide (Fig. 3.3.1h). Preferred cement accumulation at the underside of the grains suggests vadose origin of the cement at the bottom part (Adams and Mackenzie, 1998; Scholle, 1973; Scholle and Ulmer-Scholle, 2003). This fact is compatible with the shallowness of this bottom part; probably emergence took place as the channels shifted away. With seaward paleogeographic shift tide might have been accentuated to winnow out lime mud and eliminated the possibility of emergence of the depositional surface and marine phreatic first-generation isopachous cement rimmed the clasts (Adams and Mackenzie, 1998; Scholle, 1973); intermicritic thus changes upward to intrasparite composition of the rock. Empty pore spaces were later filled by second generation blocky cement. The background sediment of dark coloured mud presumably settled during slackening tide within narrow tidal channels having restricted circulation. Isolated patches of blocky sparite within muddy matrix are interpreted as dissolution cavity-fills because of their sharp boundaries and internal drusy pattern. Dominant

occurrence of these cement patches at the junctions between clastic grains, biotic or non-biotic, suggests porewater permeation preferred sites of strong textural contrast (Fig. 3.3.1i).

Cumulatively, deposition of this facies took place in tidal inlets subjected to high degree of water depth variation. Bedload migration both downslope and upslope was accompanied by time-to-time collapse of mudbanks bordering the inlets during tidal drawdown. Mud settled on the bedload regularly during periods of tide slackening during both flood to ebb and ebb to flood transitions. That would mean deposition of this facies took place in shallow subtidal condition. In the intracontinental rift setting the inlets likely occupied narrow grabens often fringed by scree materials derived from the basement granite.

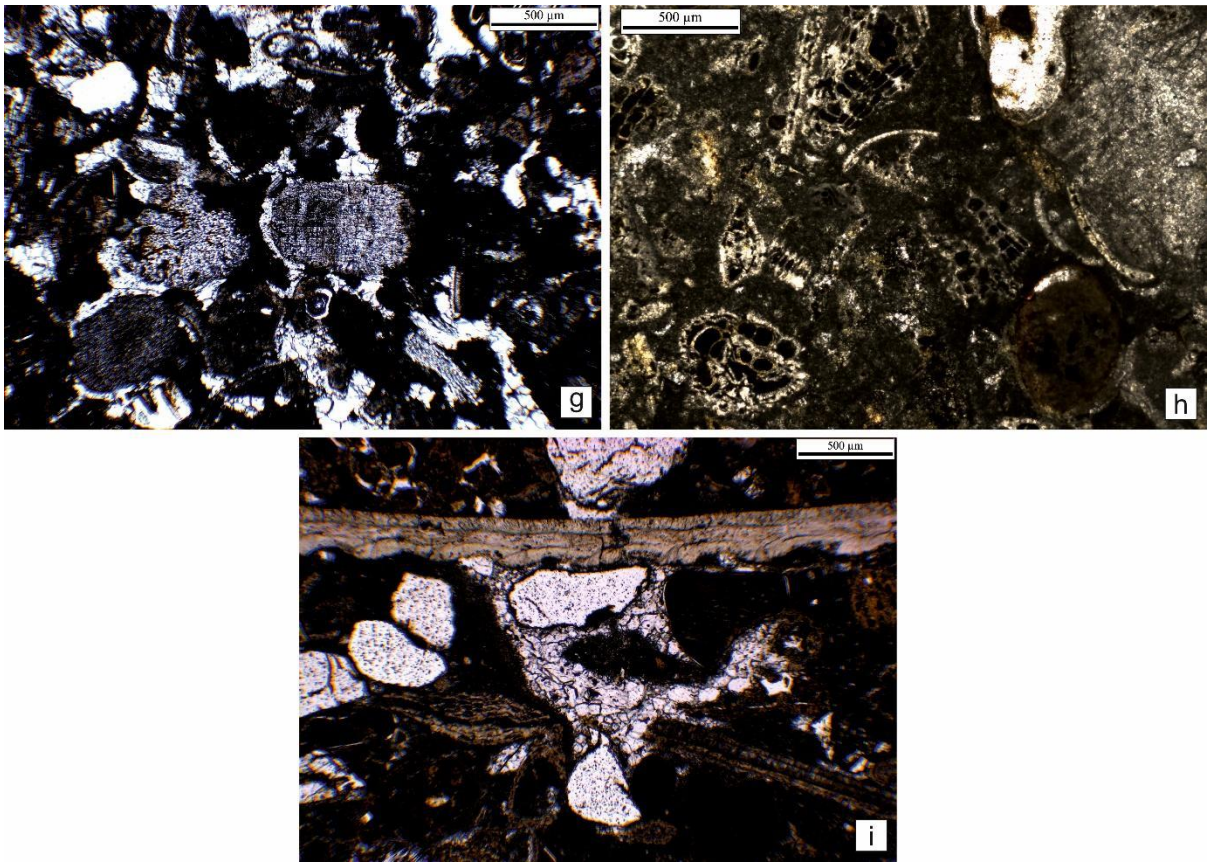

Fig. 3.3.1 Facies IIA: intrasparite (g); intramicrite indicates low energy of tide (h); cement patches under preferred site of biotic and non-biotic grains (i).

3.3.2 Facies IIB, Graded storm facies:

Facies IIB is intrasparite; drusy growth in cement is commonplace (Fig. 3.3.2a). The framework gains are haphazardly oriented (Fig. 3.3.2b). Within shelter pores, under shells, especially under convex-up pelecypod valves, the cement patches are larger (Fig. 3.3.2c). Syntaxial cement selectively grown around echinoid plates or spines is also common in occurrence (Fig. 3.3.2d). Intraparticle pores within the shells are, however, generally biomicrite. The basal part of this bed fits the term rudstone in Dunhum's nomenclature (1962). Bryozoan zooecia are often partially filled by heavily iron-stained biomicrite, while the rest of the pores are filled by blocky calcispars (Fig. 3.3.2e). The fresh-looking, apparently indigenous, bioclasts are generally admixed with almost equal number of intraclasts with or without bioclasts embedded within them. Large shells generally retain their delicate primary texture, but smaller shells embedded within intraclasts often have their shell walls replaced by calcite cement. The intraclasts are brown coloured. A micritic rims are formed around almost all the clasts (Fig. 3.3.2f).

Most of them have rounded edges, but some exhibit delicate protrusions. Steinkerns are locally found (Fig. 3.3.2g). Within some intraclasts long shell fragments have lime mud attached delicately on one side. In some such intraclasts borings pass through both the shells and the mud attached to them (Fig. 3.3.2h). In some borings the infilling matches exactly with the sediment hosting them. In some others, they are different from host. In rest of them, the infilling is partly or fully calcite spar cement (Fig. 3.3.2i). Some shells are broken, and the same blocky calcite cement fills the fractures as well as the intraparticle pores outside. Limeclasts with negligible content of bioclasts are rounded and almost always have distinct reddish colour. Some very large chunk of lime mud is encrusted by bryozoa almost all around (Fig. 3.3.2j).

Interpretation:

Intrasparite fabric points to winnowing out of fines in agitated environment, even during fair-weather condition. The fines were, however, retained in protected microenvironments of intraparticle pores. Some imported clasts might have their intraparticle pores filled at their original sites of deposition.

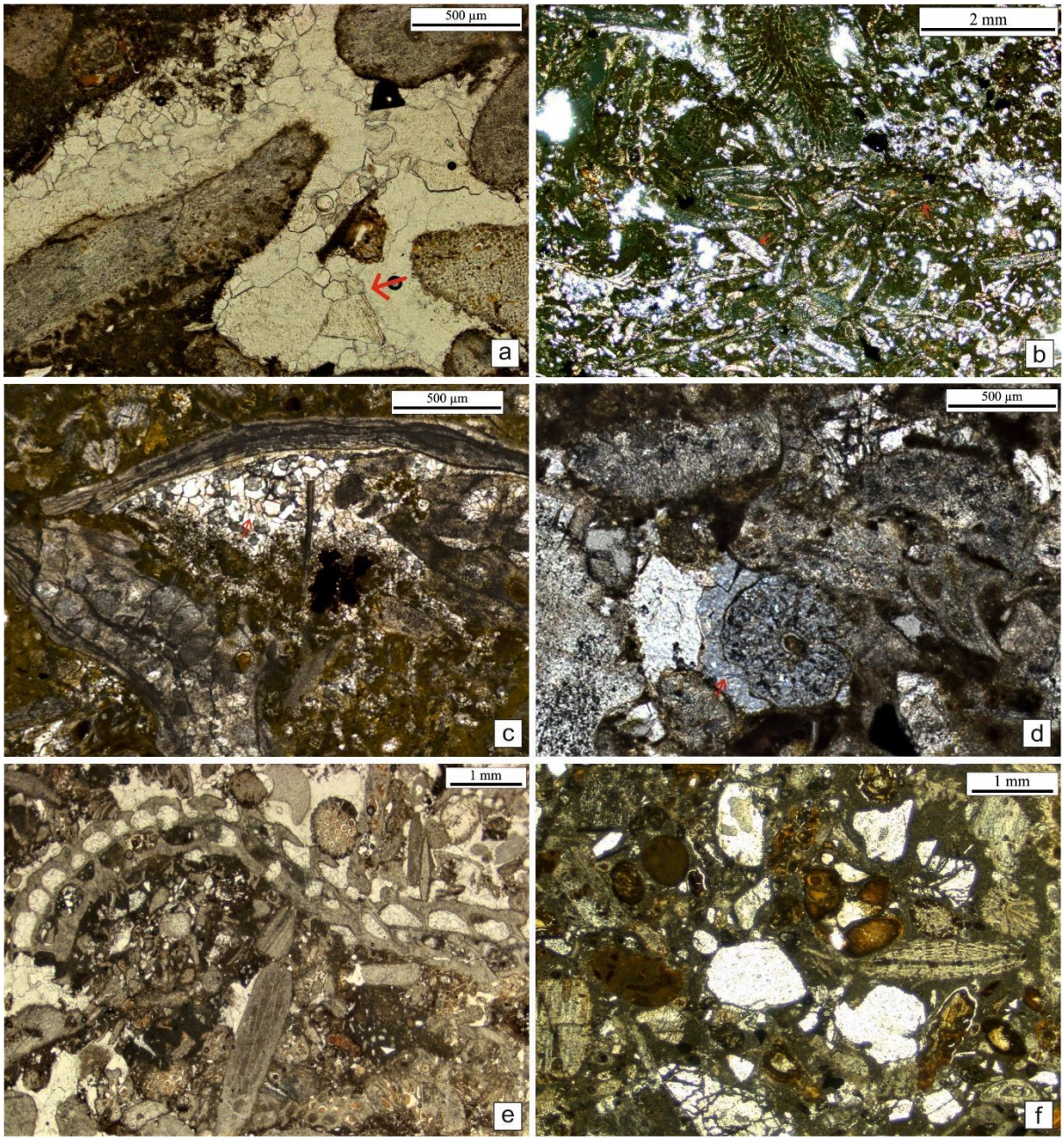

Fig. 3.3.2 Facies IIB: drusy growth in cement (a); very haphazardly oriented framework grains (b); shelter pores, under shells, especially under convex-up pelecypod valves (c); syntaxial cement around echinoid plates (d); Bryozoan zooecia are partially filled by micrite as well as cement (e); presence of intraclasts, note the micritic rims (f).

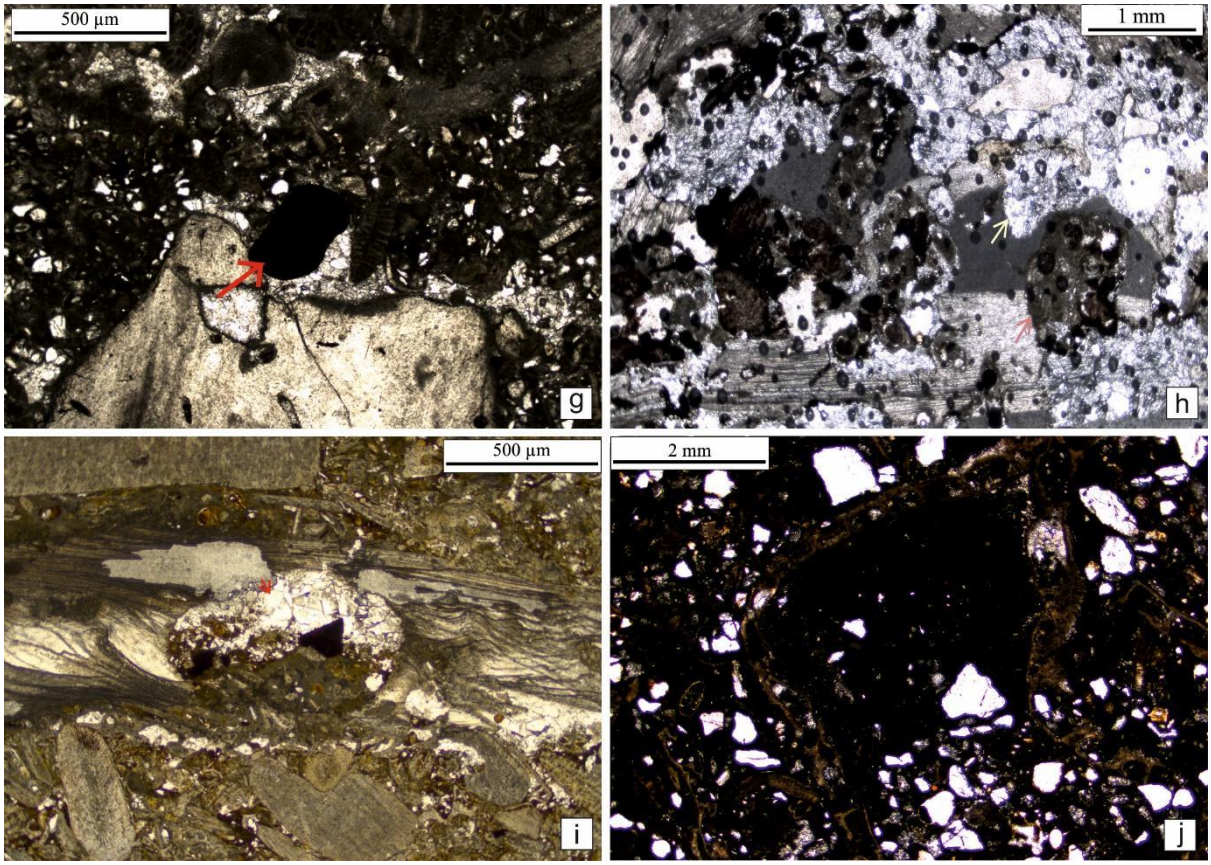

Fig. 3.3.2 Facies IIB: steinkerns (red arrow) (g); boring in mudclasts (red arrow) (h); borings are filled with micrite initially, then rest part is fully spary calcite (i); lime mud is encrusted by Bryozoa (j).

Since millions of crystals constituting the echinoid grains together behaved as single grains, syntaxial cement grew around them on the consideration of lower energy consumption (Adams and Mackenzie, 1998). The shellbank rudstones on top of storm beds do not reflect high energy sediment transport as they are products of colonization by *Gryphea* during virtual sedimentation hiatuses. In contrast, rudstone at the base of graded storm beds reflects high energy influx. Micritic rims around all the clasts strongly suggest final deposition within the photic zone (Adams and Mackenzie, 1998). The micritic rims helped to retain characteristic shapes of bioclasts even after their shell dissolution. Some shells are well retained, while others got dissolved – this fact points to differences in primary shell mineralogy (Adams and Mackenzie, 1998). Presumably shells of metastable mineralogy dissolved, but the low Mg-calcite shells escaped dissolution (Bathurst, 1972; James and Choquette, 1983). Abundance of intraclasts bears evidence of strong erosional nature of the

sediment-driving flows. Furthermore, the presence of intraclasts with delicate projections suggests that the flows eroded firm or even hardgrounds (Ramkumar, 1996). Presence of boring cutting through both sediment and bioclast without any deflection corroborates this contention (Fig. 3.3.2h). Borings filled by sediment suggests a shorter time gap between boring and its infilling compared to that when the borings are filled by cement; one can establish a biostratinomic sequence, where the infill progresses from host sediment to younger sediment, then partially by younger sediment, and finally by cement alone. The steinkerns indicate that the mud that infilling shell cavity was already cemented prior to transporting ion to the present depositional site. Hardground formation is evident and that reflects overall low sedimentation rate and sporadic (Bromley, 1968; Molenaar and Zijlstra, 1997). The varying degree of shell preservation suggest differences in shell mineralogy. The micritic cement and the isopachous needle-shaped cement around grains are probably marine, but the blocky cement is inferred to be burial in origin. Continuation of the same cement within fractures on shells corroborates this contention. The large chunk of mud draped by bryozoan chain strongly suggests sudden uprooting of sediments by storm and got deposited there.

3.3.3 Facies IIC, Rippled facies:

The facies is of calcarenite, mainly packstone, though in upper part it exhibits grainstone. The framework elements in this facies are intraclasts and bioclasts (Fig. 3.3.3a). Intraclasts are rounded at edges; in case of bioclasts evidence of abrasion is not always detectable. Grain-size distribution broadly appears to be bimodal. The smaller fraction is better rounded, includes both intraclasts as well as bioclasts and all of them are iron-stained, often strongly. The largest grain in this population ranges up to 8 mm. The larger fraction is dominantly of bioclasts, distinctly fresher in look and although all the grains bear micritic rims (Fig. 3.3.3b). Most of the bioclasts in the smaller fraction have their primary texture blurred. The mud clasts often have cracks parallel to their margins (Fig. 3.3.3c). Many of the mudclasts bear concentric bands alternately dark and light coloured (Fig. 3.3.3d). Disruption of their primary texture has, in certain instances, been created by borings, generally filled by sediment (Fig. 3.3.3e). So do the echinoid plates and the branching bryozoans. Some curved

shells, possibly of pelecypods, have dissolved their shell walls and the cavity, so generated, has been filled by sparry calcite. Benthic foraminifers, like *Miliolina* are well preserved (Fig. 3.3.3f).

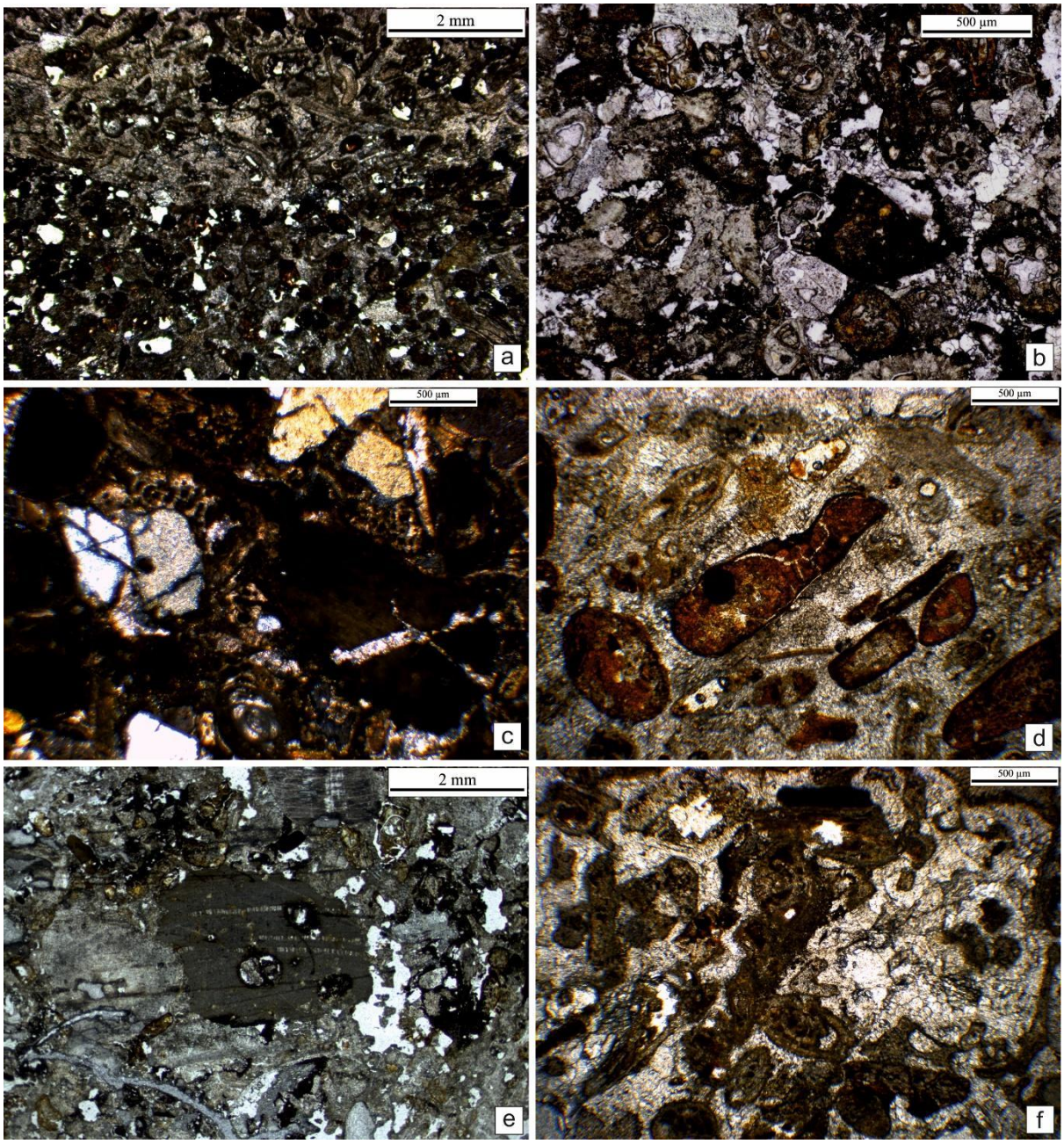

Fig. 3.3.3 Facies IIC: rich in intraclasts and bioclasts (a); fresh bioclast grains bear micritic rims, blurred primary texture (b); mud clasts have cracks parallel to their margins (c); mudclasts bear bands of alternately dark and light colour (d); disruption of their primary shell texture by boring (e); benthic foraminifers, *Miliolina* (f).

Contacts between the vertically segregated packstones and grainstones are, at places, sharp and curved, probably erosional (Fig. 3.3.3g). The clasts have isopachous needle-like cement rims around them (Fig. 3.3.3h). In the grainstones, beyond these rims, there are blocky calcite cement filling the intergranular spaces. Around the echinoid plates the cement is synchronous, extinguishing simultaneously with the uniformly oriented millions of crystals constituting the plates (Fig. 3.3.3i). In the packstones, pendant-like or stalactitic cements are abundantly present with clear preference for the underside of the grains (Fig. 3.3.3j). These cement crystals are also blocky in nature. The outer boundary of these cement patches is depositional highly irregular against the micritic matrix. Some large bioclasts are broken and the fractures, thus generated, are filled by sparry calcite cement. Besides, there is abundant presence of veins filled by sparry calcite veins. These veins are preferably localized along ferruginous clay pipes extending vertically (Fig. 3.3.3k).

Interpretation:

The ripples in this facies bear evidence of agitation, albeit limited, in the depositional environment. Slight variation in the depositional energy budget produced grainstone in one place or at a time and packstone in another place or at a different time. Bimodality in clast-size distribution and difference in nature of clasts suggests derivation of the clasts from multiple sources. The smaller clast population likely to have been derived from higher reaches where it lay bare for a considerable period and was oxidized. The alternate dark and light concentric bands and border-parallel cracks within them suggest alternate drying and wetting (Tucker and Wright, 1990). The large bioclasts without the iron-stain are possibly native in origin. The fossil composition leaves no doubt about deposition in marine environment. The benthic forams like *Textularia* and *Milioline* suggest that the depositional setting of this facies had been hypersaline (Parker et al., 2011; Chukwu et al., 2012; Chan et al., 2017). Overlapping borings on the shells point to low rate of net sedimentation. Variable degree of preservation of shells is mostly related to their variable mineralogy. Some dissolved shells still retain their characteristic shapes because of prior growth of micritic rims around them. The isopachous needle-form cement around grains likely to have formed in marine phreatic environment.

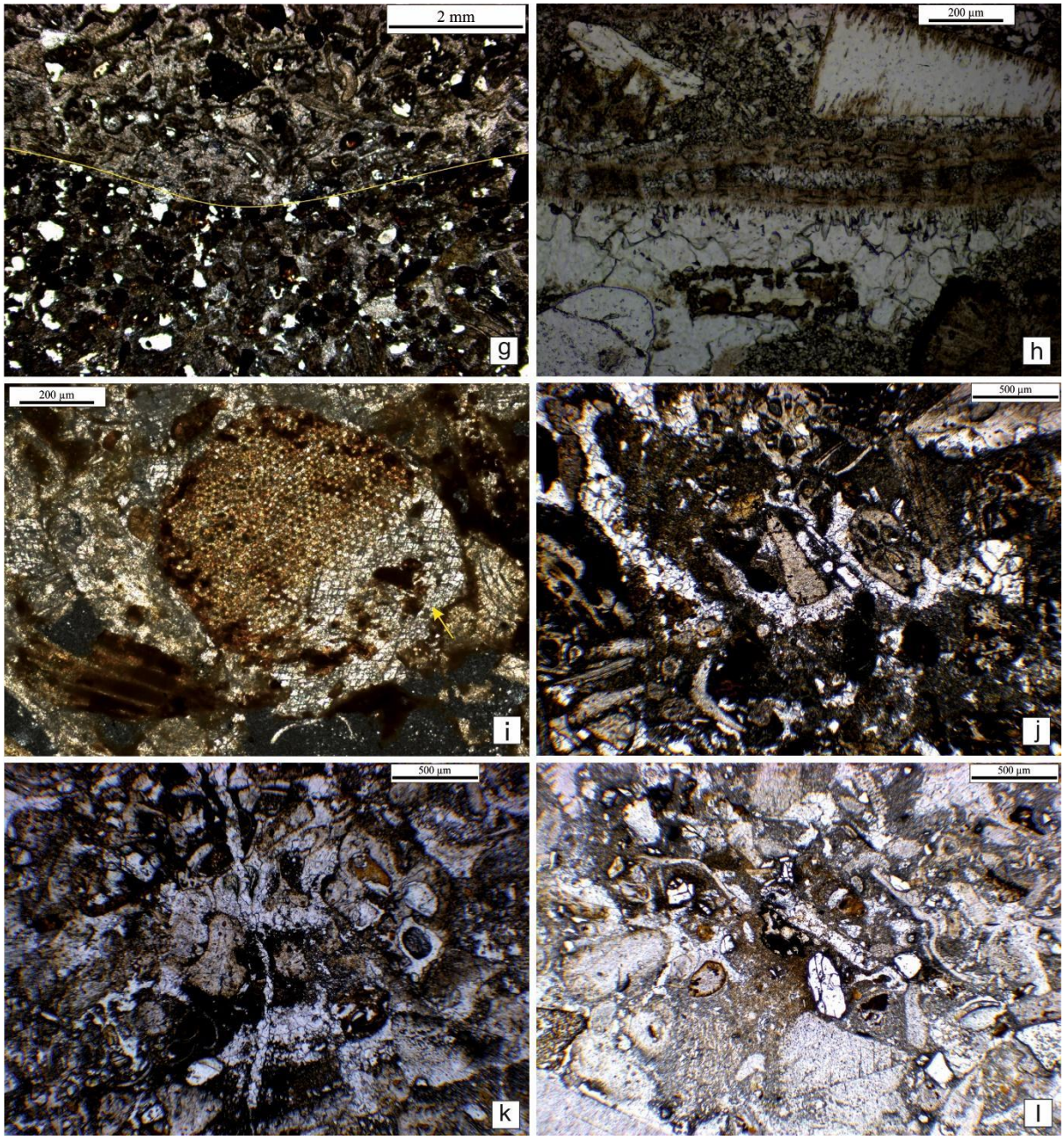

Fig. 3.3.3 Facies IIC: sharp and curved erosional boundary between packstone and grainstone (g); isopachous needle-like cement, also note the blocky cement (h); syntaxial cement around echinoid plates (i); stalactitic cements are present preferentially underside of the grains (j); vertical ferruginous clay pipes (k); drusy growth (l).

The blocky cement occurred preferentially at the underside of the grains is, in contrast, of vadose diagenetic environment. Vertical clay pipes further support the contention that the sediment was subjected to vadose diagenesis. In packstones these cement patches

have sharp, but irregular contacts with the micritic matrix and crystal size is small along the fringes, while increasing inward depicting drusy growth (Fig. 3.3.3l). Cumulatively, these observations indicate that the spaces for cement precipitation were created by prior dissolution. Solution undersaturated with Ca^{+2} and HCO_3^{-2} accumulated at the underside of the grains and preferably dissolved the micritic matrix for its finer grain size. As ionic concentration of the porewater gradually increased thereby, precipitation took place beyond a threshold filling the cavity generated beforehand. The clay pipes made the sedimentary body weak at places and the crack-filling veins formed preferably along those weak planes. These clay pipes and the accompanying veins depict incipient soil formation. Rapid variation in thickness of these veins depicts weakness of the material they cut through. In accordance the veins abut against or circumvent the calcitic shells (Fig .3.3.3k). The vein-filling cement is also thus seeming to be of vadose origin. The only cement of burial origin could be that filling the minor breakage planes on the large bioclasts. The facies was apparently deposited in coastal area of the sea or island margins where slight readjustment of relative sea level led to exposure of the depositional surface.

3.3.4 Facies IID, Shellbank facies:

The shellbank facies is primarily a biomicrite. Large fossil clasts are often in contact with each other. Most of the shells are unbroken. Many shells, especially the larger ones, mostly belonging to *Gryphea* or *Inoceramus*, preserve their spectacular primary fibrous or honeycomb texture (Fig. 3.3.4a) and Palisade texture (Fig. 3.3.4b) respectively. Some smaller shells have, however, been subjected to dissolution (Fig. 3.3.4c). Bevelled or broken edges of shells are very rare, although a few of the larger shells have suffered in-situ breakage (Fig. 3.3.4d). Besides, there are numerous intraclasts with or without bioclasts. Majority of them are strongly iron-stained and some of them bear septarian cracks (Fig. 3.3.4e). They also bear cracks parallel to their margins (Fig. 3.3.4f). Some intraclasts display concentric rims alternately dark and light (Fig. 3.3.4g). All the shells bear dark reddish micritic rims. Some convex-up curved shells encase shelter-pore cement of minute blocky cement displaying drusy growth pattern (Fig. 3.3.4h). Large shells bear sponge borings filled by blocky cement, also displaying drusy growth. In many cases the borings are floored by grey-coloured

sediment (Fig. 3.3.4i). A single shell may bear multiple borings (Fig. 3.3.4j), often partially overlapping. Cements fill them together implying their arrival later in the post depositional phase (Fig. 3.3.4j). The cement is of blocky nature depicting drusy growth. The sediment-cement successions in multiple borings maintain the same direction implying stable orientation of the shells through the multiple phases of boring. There are a few irregular patches of drusy blocky cement within the matrix in between the shells. Apparently, the deposit was subjected to localized dissolution in the post depositional phase. The space between the sturdy shells making a stable framework in the field of gravity is filled by a drab and dark coloured matrix made of very fine sub millimetre-sized carbonate crystals. At high magnification, however, it reveals a clotted texture made up of a compact mass of peloids of size varying within a limit (Fig. 3.3.4k). The largest peloid measures up to 10μm in length. Besides them, there are numerous minutes, thin and angular flakes of microbial mat, still darker in colour (Fig. 3.3.4l).

The largest flake observed is 4μm in length. The matrix has undergone recrystallization in patches whose boundaries are irregular and gradational because of outward diminishing crystal-size. Notably, the recrystallization has never been initiated at the shell-margins. The particle surfaces that induced the recrystallization possibly belonged to the minutest specks of microbial mat or the peloids; their identity remains masked under light microscope.

Interpretation:

An overall micritic nature of the shellbank sediments suggests its low energy condition. Retention of the texture of *Gryphea* and *Inoceramus* indicate that the shells are pristine. Boring filled by blocky cements is of post depositional signature. The shell dissolution and cement precipitation took place after cementation of the deposit. Multiple boring in the bivalve shell suggests the predator tried to attack them multiple time. It was the record of their failed attempt. The shells were in very shallow marine condition. The blocky cement indicates that there may be little influx of meteoric water. Degrading neomorphism in form of micritic rims, of supposed microbial origin, around all the clasts strongly suggests deposition within the photic zone; presumably on the shelf as suggested by the fossil population.

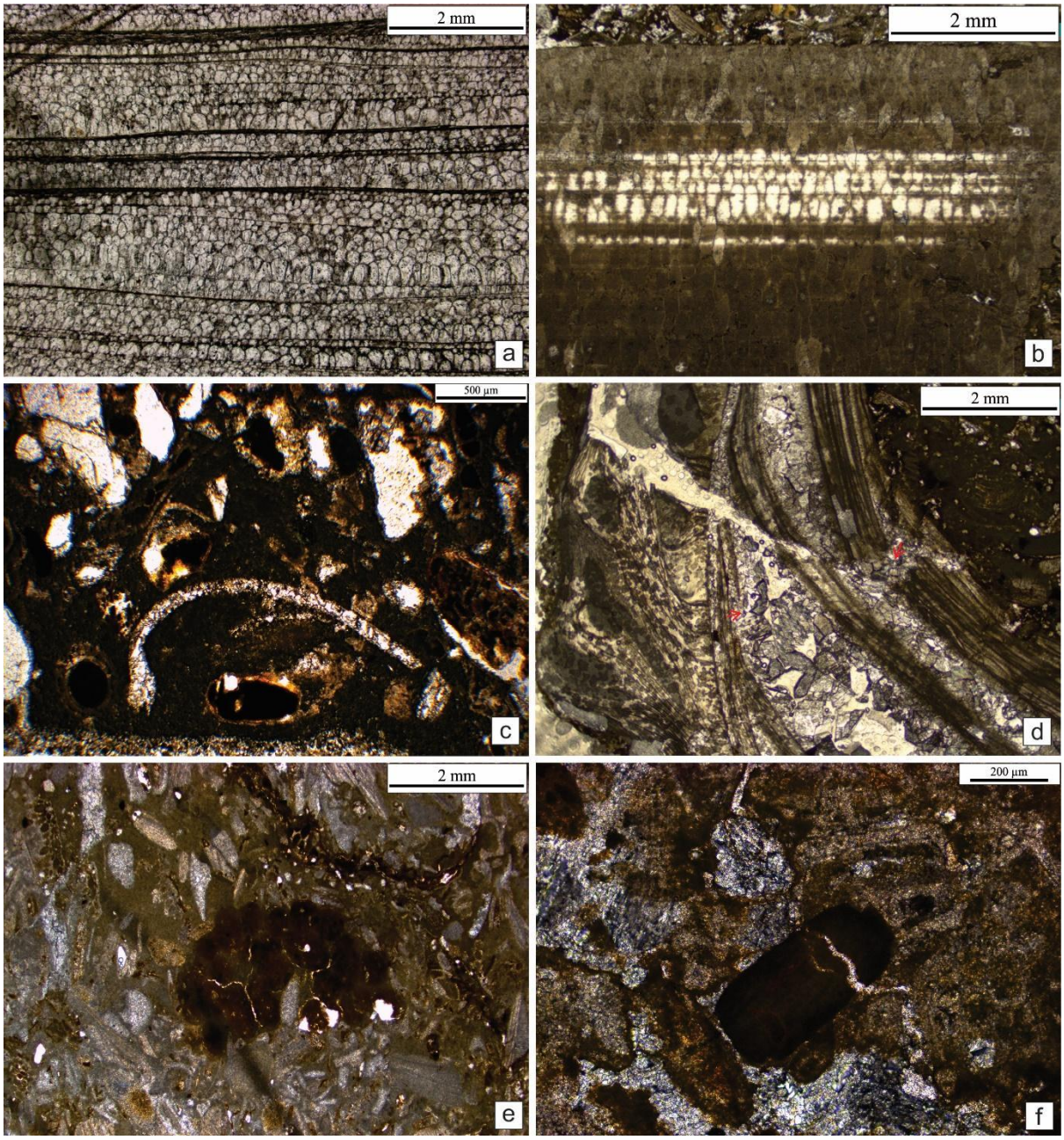

Fig. 3.3.4 Facies IID: primary fibrous or honeycomb texture of *Gryphea* (a); palisade texture of *Inoceramus* (b); dissolution of smaller shell (c); larger shells suffered in-situ breakage (d); septarian cracks in mudclasts (e); margin parallel cracks (f).

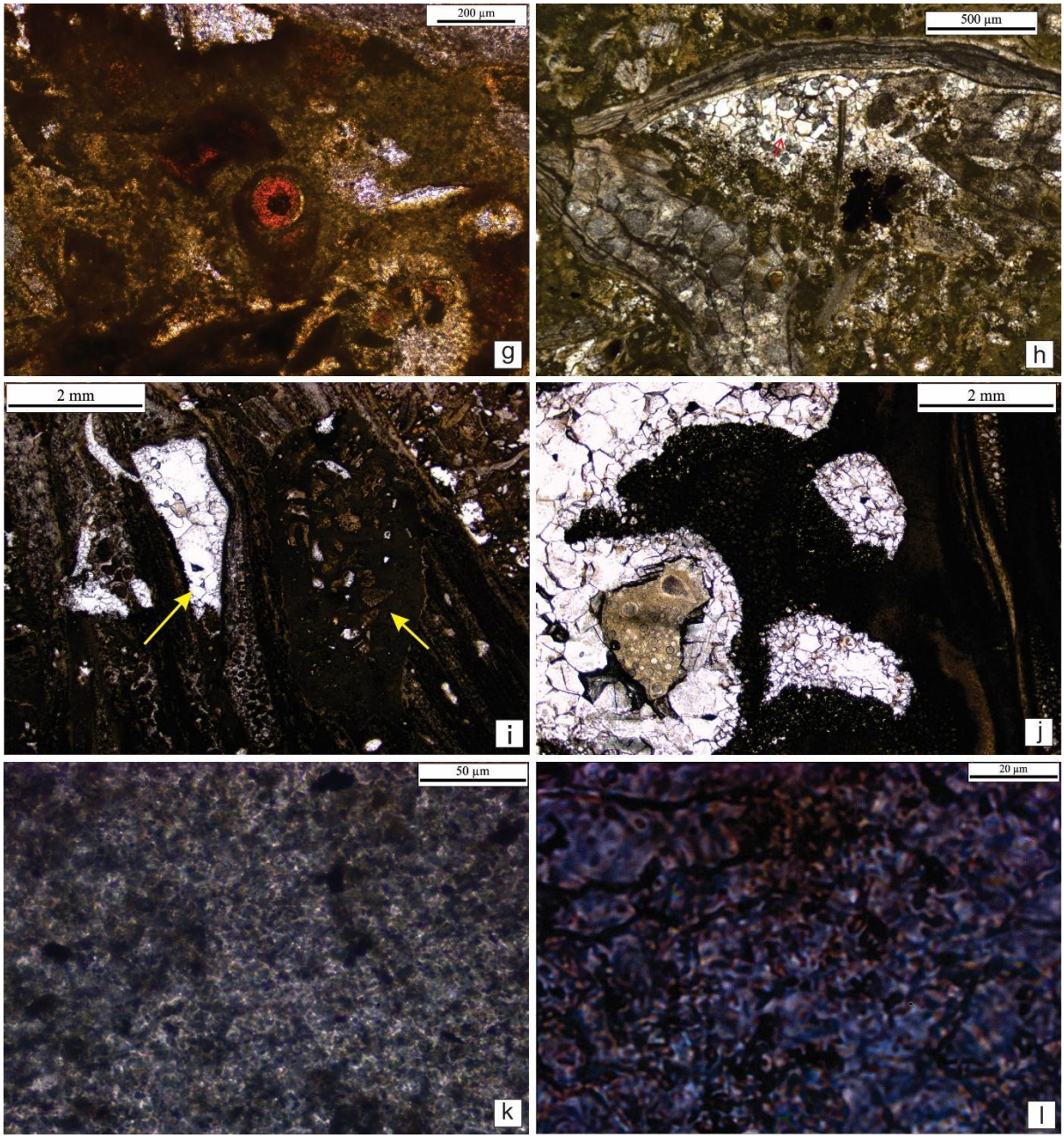

Fig. 3.3.4 Facies IID: concentric rim in intraclast (g); shelter pore displaying drusy growth (h); larger shells bear sponge borings filled by blocky cement (i); multiple borings (j); clotted texture made up of a compact mass of peloids (k); thin and angular flakes of microbal mat (l).

3.3.5 Facies IIE, Chevron and Hummocky Cross-stratified facies:

The facies is of calcarenite, mainly grainstone containing carbonate cement (Fig. 3.3.5a). The framework elements in this facies are mainly bioclasts and well-rounded intraclast. Intraclasts are rounded at edges; have corroded boundaries (Fig. 3.3.5b). Grain-size distribution broadly appears to be bimodal (Fig. 3.3.5c). Fossils are dominated by Foraminifera *Textularia* and echinoid. The bioclast especially benthic Foraminifera *Textularia* filled with strongly oxidized mud (Fig. 3.3.5d). The largest foraminifera grain present in this population ranges up to 12 mm. All the bioclastic grains bear prominent micritic rims (Fig. 3.3.5d).

The bioclasts have isopachous needle-like cement rims around them (Fig. 3.3.5e). There is blocky calcite cement, beyond these rims, filling the intergranular spaces. Isopachous needle shaped crystals are incorporated into the larger blocky crystal. Isopachous marine cement & burial cement all exhibit the same orientation. Around the echinoid plates the cement is synchronous, extinguishing simultaneously with the millions of uniformly oriented crystals which constitute the plates (Fig. 3.3.5f). Turreted gastropods and foraminifera *Elphidium* are also found in this facies (Fig. 3.3.5g). Pressure welding between framework grains is very common (Fig. 3.3.5h). Similar crystals, though smaller in size, also fill voids left by dissolution of shells. Within bryozoan fragments similar sparry calcite fills the bryozoan zooecia, often partially, while rest of the zooecia is filled by reddish mud similar to the matrix outside. Some shells have undergone in-situ breakage. The fractures, created in consequence, are filled by carbonate crystals of the same blocky nature.

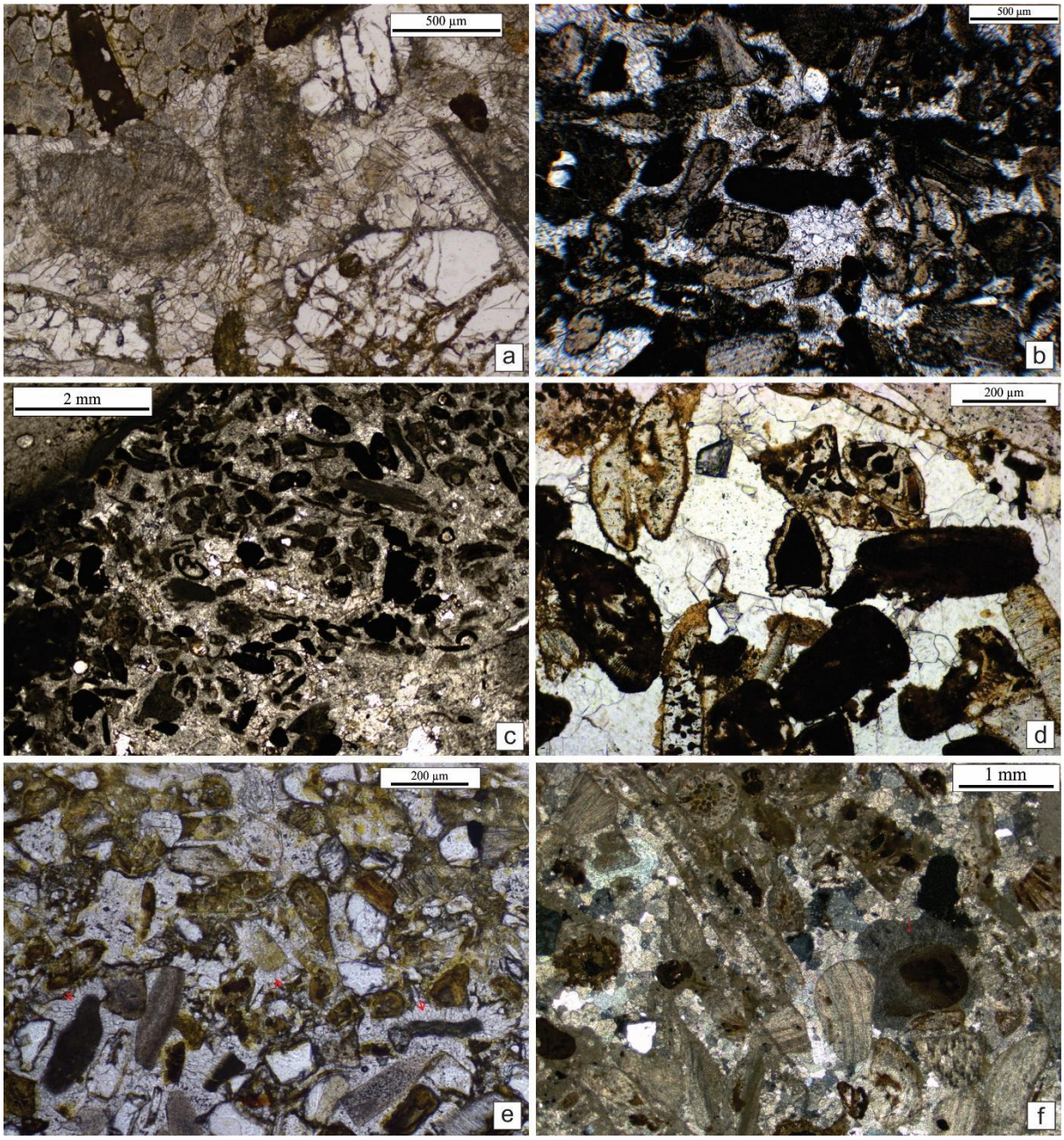

Fig. 3.3.5 Facies IIE: grainstone contain carbonate cement (a); intraclasts are rounded at edges, note, corroded boundary (b); bimodal grain-size distribution (c); bioclastic grains bear prominent micritic rims, note foram *Textularia* (d); isopachous needle-like cement rims (e); syntaxial cementation (f).

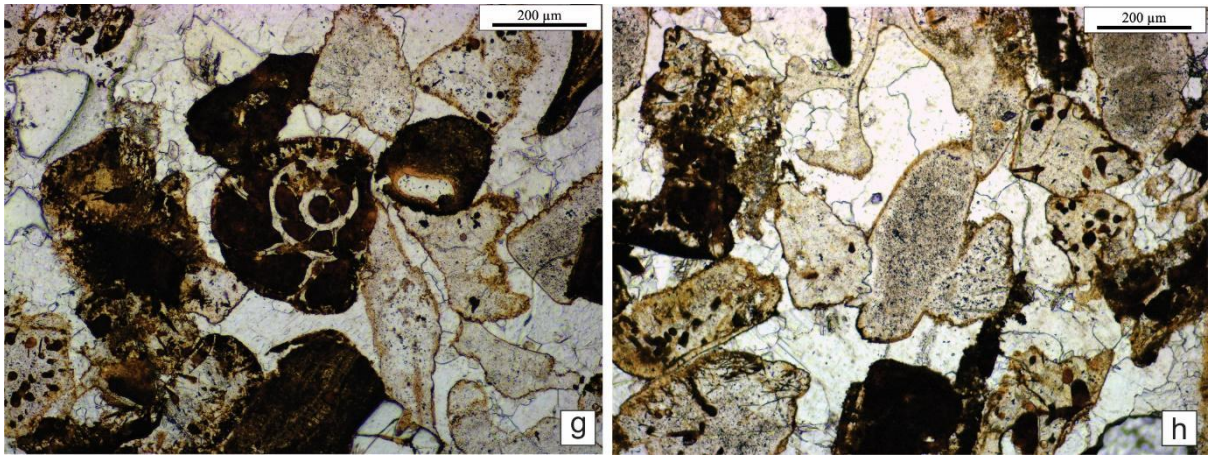

Fig. 3.3.5 Facies IIE: foraminifera *Elphidium* (g); pressure welding between framework grains (h).

Interpretation:

Grainstone suggests it is of high energy environments. Isopachous needle shaped crystals marine environments. Presence of *Textularia* and *Elphidium* are indicative of low salinity and marine shallow water environments (Kaminski et al., 2002). Pressure welding caused by overburden pressure. The fractures also support this contention.

3.3.6 Facies IIF, Muddy Facies:

It is intramicritic or biomicritic limestone depending upon the volume percentage of intraclasts (Folk, 1959, 1962). Cement is confined to intraparticle and shelter pores (Fig. 3.3.6a). Remarkable is the absence of micritic rims around clasts (Fig. 3.3.6b). Another remarkable feature of this facies is almost intact preservation of very long isolated and delicate strips of encrusting Bryozoa, twisted and folded with little breakage (Fig. 3.3.6c). With respect to other facies in the wave-dominated association, this facies exhibits another exceptional feature: silicification of bioclasts, especially of echinoids (Fig. 3.3.6d).

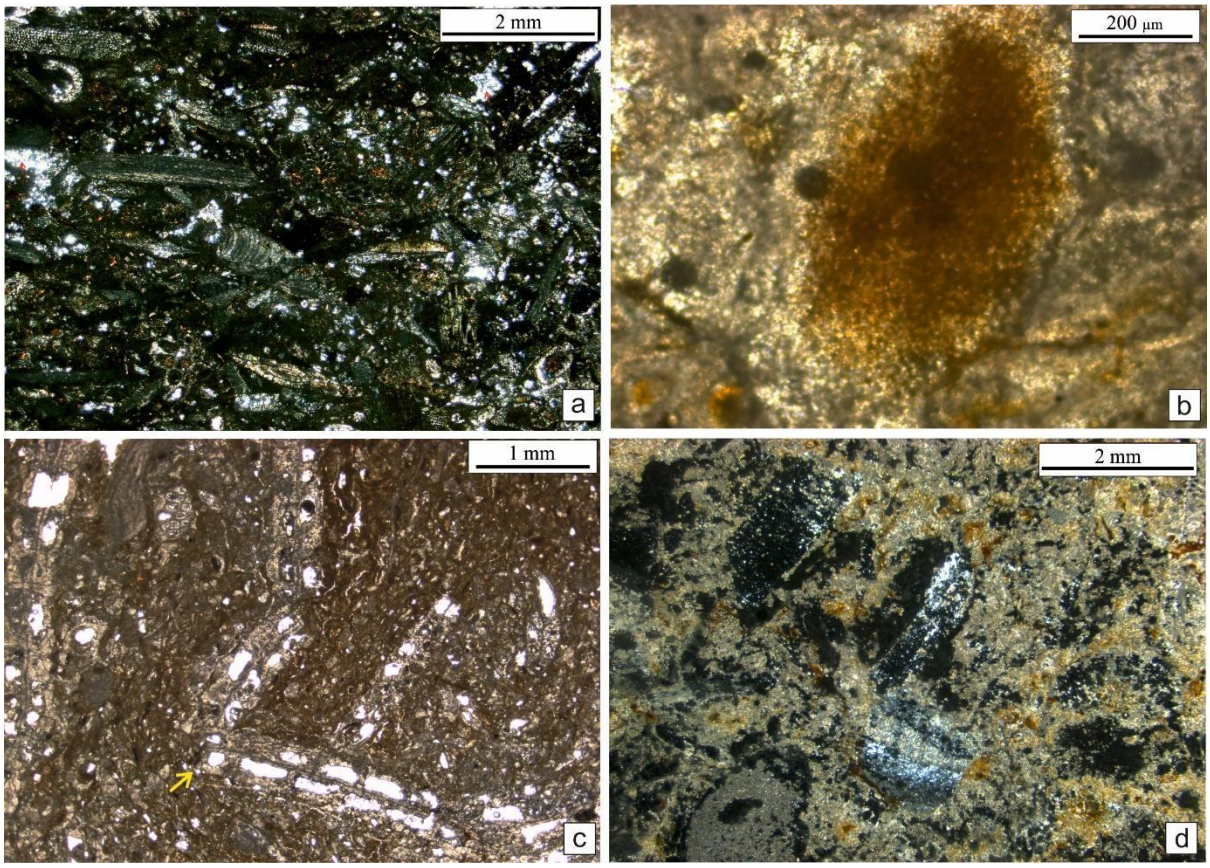

Fig. 3.3.6 Facies IIF: intraparticle cement (a); absence of micritic rims around clasts (b); delicate strips of encrusting Bryozoa, twisted with little breakage (c); silicification of bioclasts (d).

Interpretation:

In this muddy facies, clasts are virtually floating within mud matrix. Some shelter pores and intraparticle pores remained empty till they were filled by late diagenetic cement, seemingly of burial origin as in other members of the Association II. Shells of primary aragonitic mineralogy were preferably selected for diagenetic silicification presumably because their constituent crystals were not enlarged through dissolution and re-precipitation to gain stability. The sediment thus appears to be a mudflow product. Viscosity of the flow, however, allowed long strips of Bryozoa to sustain despite frequent twists and folding. The matrix probably frozen rapidly and caused rapid cessation of the flow. Rapid burial presumably ruled out as microbial boring present around the intraclasts or bioclasts. Because

of finer grain-size this facies, compared to all other facies in facies association II, seems to have deposited at relatively deeper shelf.

3.4 Facies Association III:

3.4.1 Facies IIIA, Small scale herringbone cross-stratified facies:

Petrography of this facies has remarkable spectral variability between intraclastic packstone and intraclastic grainstone, even within the short span of a single thin section (Fig. 3.4.1a). It is very rich in bioclasts, although there is also a subordinate population of intraclasts with or without bioclasts. Packing is usually very tight. The rock is biomicritic at places, biosparite elsewhere; the lateral transition appears a bit irregular in thin section. Micritic cement around clasts is a common feature. Spaces left by dissolution of shells are filled with small sparry calcite cement. Drusy cement in biomicritic rock fills shelter and intraparticle pores (Fig. 3.4.1b). Drusy cement is commonplace in interparticle pores in biosparitic rocks. These cements are all blocky in nature. Intraclasts are all brown in colour, darker than the micritic groundmass. Within one such intraclast, a steinkern is even deeper brown in colour (Fig. 3.4.1c). Many of the shells are bored repeatedly (Fig. 3.4.1d). Some brown oxidized mudclasts bear multiple cracks (Fig. 3.4.1e). The crack-filling cement is different from the blocky cement within interparticle pores outside. Mud infilling within intraparticle pores, nonetheless, has contrasting deep reddish colour (Fig. 3.4.1f). Bryozoan zooecia are often partially filled by such red mud, while rest of the pores are filled by blocky sparry calcite cement displaying drusy growth (Fig. 3.4.1g).

Interpretation:

The herringbone cross-strata, the mud drapes on cross-strata, lateral change in the geometry of the cross-strata- all tell-tale tidal action. The lateral transitions between biosparite and biomicrite are indicative of temporal variation in flow intensity, with biomicrite deposited during the slackening phase of tide. *Gryphea* shells are bored often repeatedly, and the mutually connected borings are filled by the same dark coloured mud with or without minute shell fragments. Repeated borings on bioclasts and transportation of the shells with empty boring suggests that the shells remained exposed for a considerable

period at source (Fig. 3.4.1d). Low rate of net sedimentation is made apparent by them too. In contrast, some shells arrived at the final depositional site with their borings filled (Fig. 3.4.1f). Frequent reworking of sediment is recorded in compositional variation between intraparticle mud and the mud outside. Reddish colour of the intraparticle mud depicts oxidation during prolonged exposure to air or seawater. Dehydration cracks on mudclasts (Fig. 3.4.1e), rare though, further corroborate this contention of low rate of sedimentation in a very shallow depositional setting.

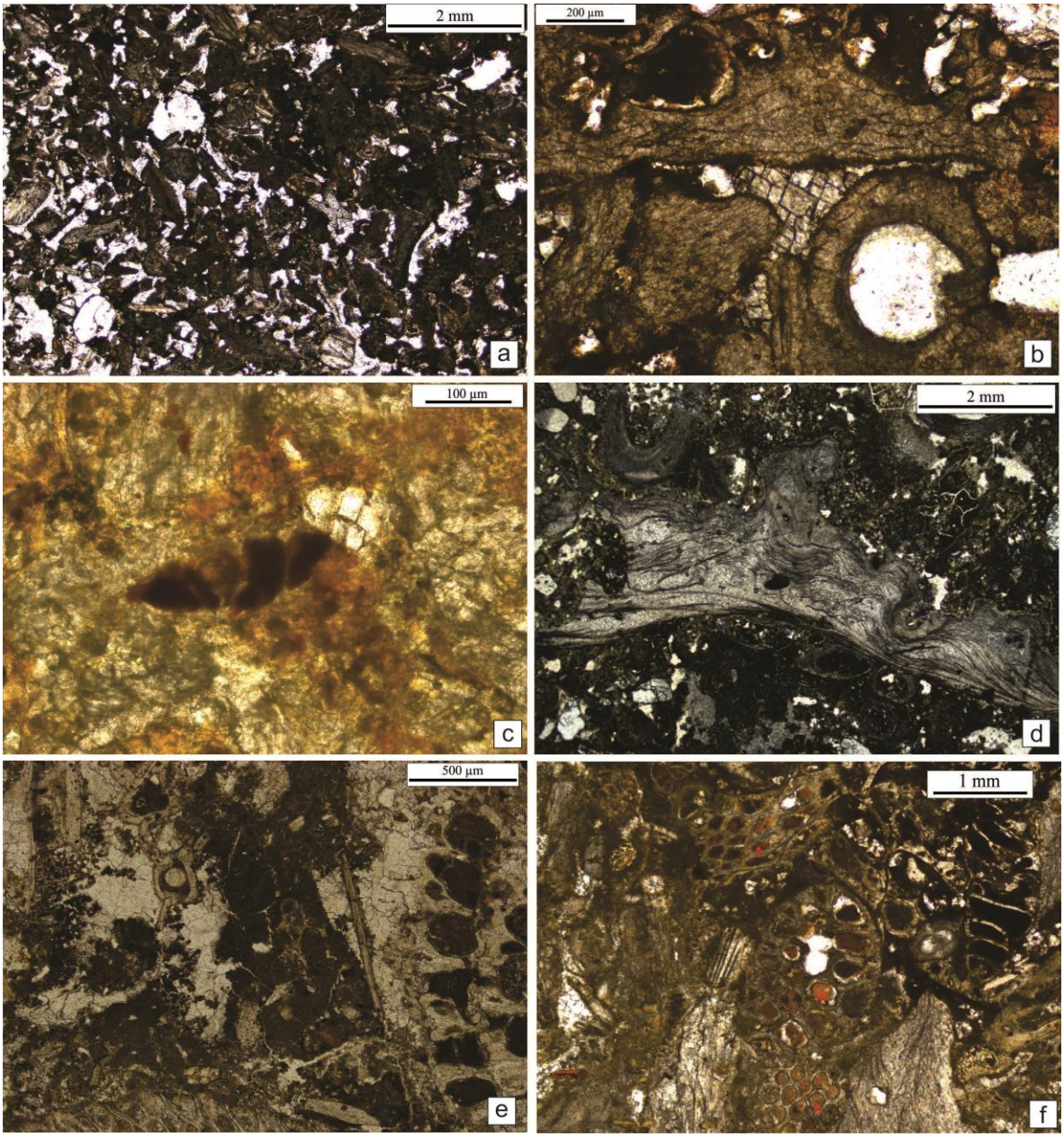

Fig. 3.4.1 Facies IIIA: packstone and intraclastic grainstone, within this short span of a single thin section (a); drusy cement in shelter pore (b); steinkern (c); repeated borings on bioclasts (d); mudclasts bear multiple cracks (e); oxidized reddish mud filled the bioclast (f).

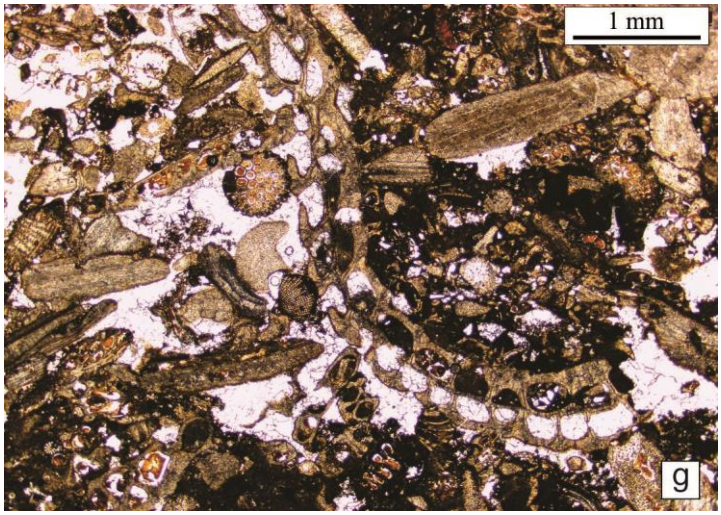

Fig. 3.4.1 Facies IIIA: Bryozoan zooecia are partially filled with dark mud, rest of the zooecia filled by blocky cement (g).

3.4.2 Facies IIIB, Down-dip cross-stratified facies:

This facies classified as grainstone. Besides bioclasts, the coarse terrigenous particles include quartz, feldspar. Although all the framework grains are well-packed, there is no signature of pressure welding. Inarticulated *Gryphea* shells dominate both in size and frequency of occurrence. Quite frequent in occurrence are encrusting Bryozoa, many of which are still attached to bivalve fossils (Fig. 3.4.2a). There is also presence of broken mudclast, bearing a few silt-sized and fine sand-sized siliciclastic grain scattered within it is almost completely encrusted by Bryozoa (Fig. 3.4.2b). Large elongated bioclasts, are broken and the fractures generated thereby are also filled by the same clear blocky crystal cement that fill the adjacent intergranular space too (Fig. 3.4.2c).

Interpretation:

The matrix-depleted grainstone, likely to have deposited as bedload under considerably high energy condition, so that mud has been winnowed out. The presumed early cementation explains lack of evidence for pressure welding between adjacent grains. The blocky calcite cement within the interparticle pore spaces, on the other hand, apparently underwent slow precipitation in non-marine condition. Again, appearance of siliciclastic

fractions indicates shallowing up succession. As the same cement fills in the fractures created by in-situ breakage of shells, it seems to be product of burial diagenesis.

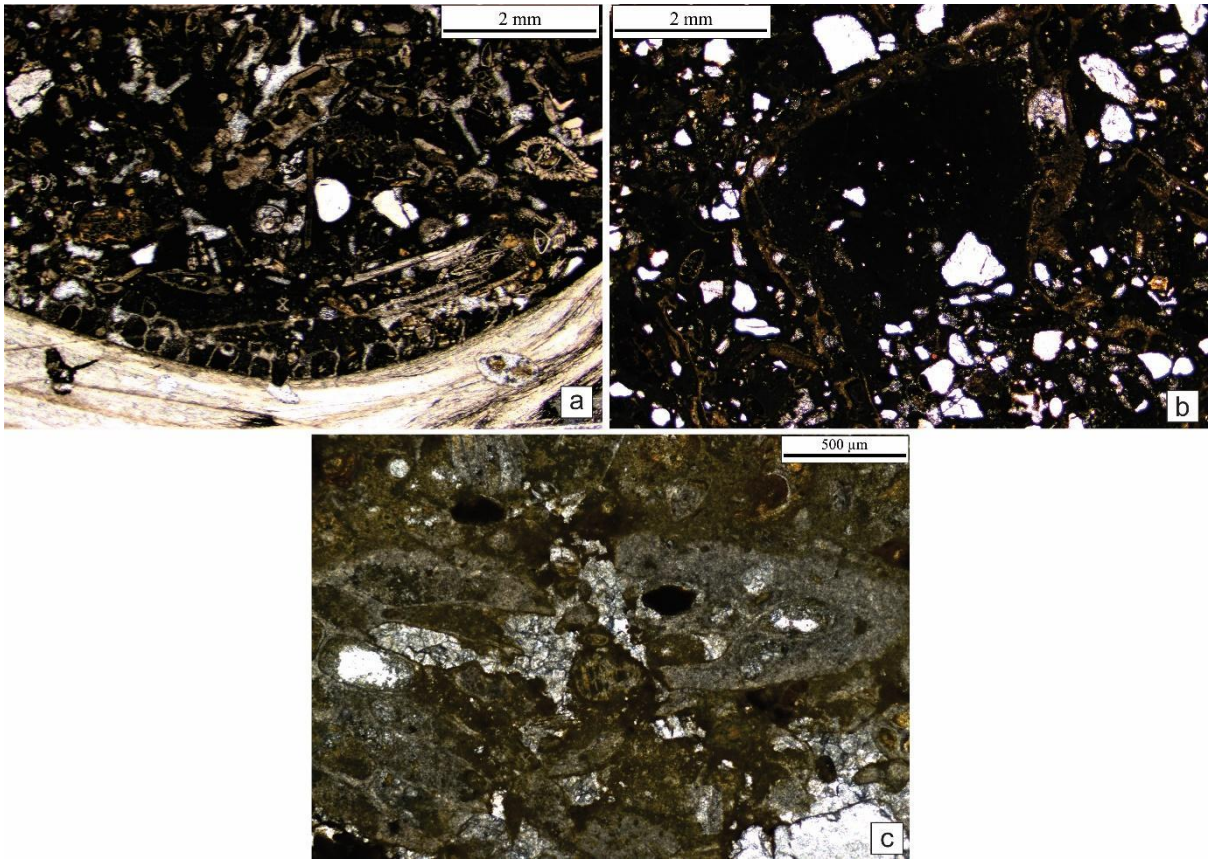

Fig. 3.4.2 Facies IIIB: encrusting Bryozoa, attached to bivalve fossils (a); mudclast encrusted with Bryozoa (b); broken elongated bioclasts and the fractures are filled by blocky crystal cement (c).

3.4.3 Facies IIIC, Rippled facies:

In this matrix-enriched carbonate rocks, cement does occur occasionally under convex-upward shells. Relatively more commonly, carbonate cement occurs at junctions between coarse clastic grains. They are often stalactitic in form (Fig. 3.4.3a). Irregular patches of similar clear blocky calcite crystals exist locally within muddy matrix. All these cements are blocky in nature and display drusy growth. Brachiopod shells preserve their

primary texture, while bryozoan zooecia and forams have their shells dissolved, but still remain recognizable as their moldic pores are filled by sparry calcite cement (Fig. 3.4.3b). Every shell and their mouldic pores have cement rims, usually well pronounced (Fig. 3.4.3c). Besides thin brown coloured micritic rims, isopachous microcrystalline calcite cement surround each of them. Intraparticle pores are filled by clear blocky calcite crystals (Fig. 3.4.3d). Echinoid grains are often surrounded by syntaxial cement, extinguishing together with the entire echinoid grains (Fig. 3.4.3e). Detached echinoid plates have rims of epitaxial recrystallization or syntaxial cement around them (Fig. 3.4.3f). The zooecia of encrusting Bryozoa are flattened on the surface of attachment but rounded on other side.

Interpretation:

The bioclasts might be grown in-situ, but those embedded within intraclasts are certainly reworked. The isopachous microcrystalline calcite rims around the clastic grains suggest cementation in marine phreatic zone. Syntaxial cement growth around echinoid plates suggest that thin coating of marine cement did not prevent the later originated burial cement to pick up the orientation of the uniform orientation of the crystals constituting the echinoid plates.

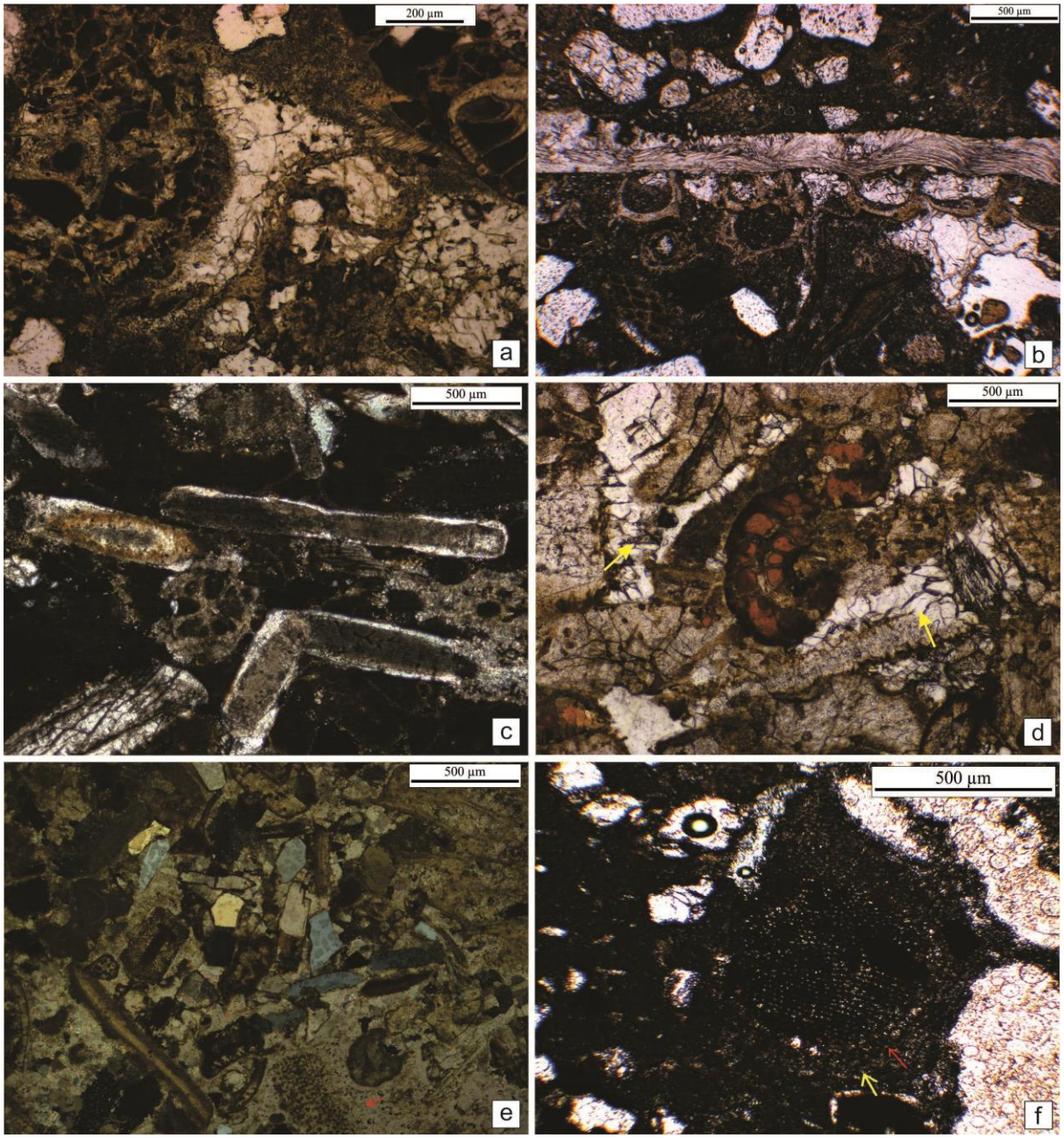

Fig. 3.4.3 Facies IIIC: stalactitic cement (a); moldic pores are filled by sparry calcite (b); mouldic pores have cement rims (c); intraparticle pores are filled with clear blocky calcite crystals (yellow arrowed) (d); Echinoid grains are surrounded by syntaxial cement (e); detached echinoid plates have rims of epitaxial recrystallization (f).

3.4.4 Facies IIID, Large-scale cross-stratified facies:

This is a highly fossiliferous mixed siliciclastic-carbonate rock; the sand grade population is divided between the two components, only mud matrix tilts the balance in favour of the carbonates. The siliciclastic sand fraction consists of quartz, feldspar, and rock fragments. Granite fragments are common among the latter (Fig. 3.4.4a). The siliciclastic grains are sharply angular, have irregular boundaries and completely devoid of any overgrowth (Fig. 3.4.4b). Some feldspar grains are glauconitized along the cleavage planes (Fig. 3.4.4c). Fossils are dominated by bryozoans and echinoids. Dark coloured intraclasts often bearing fossils are common and there are also mudclats. All the framework grains, including quartz and feldspar grains are surrounded by well pronounced isopachous micritic matrix of rapidly varying width (Fig. 3.4.4d). Similarly, there are dark coloured and well-rounded mudclasts. They may contain fractures filled by minute carbonate cement crystals (Fig. 3.4.4e). In parts, especially the lower part, the framework grains are generally embedded in dark coloured ferruginous mud matrix. Despite presence of matrix, pressure welding between framework grains, though limited in extent, is not uncommon (Fig. 3.4.4f). Sparry calcite patches are also present mostly between the framework grains and further, within the mud matrix (Fig. 3.4.4g). The patches always have sharp boundaries. Their constituent crystals are blocky in nature. Similar crystals, though smaller in size, also fill voids left by dissolution of shells. Within bryozoan fragments, similar sparry calcite often partially fills the bryozoan zooecia. The rest of the zooecia are filled by reddish mud similar to the matrix outside. Some shells have undergone in-situ breakage. The resulting fractures are filled by carbonate crystals of the same blocky nature (Fig. 3.4.4h).

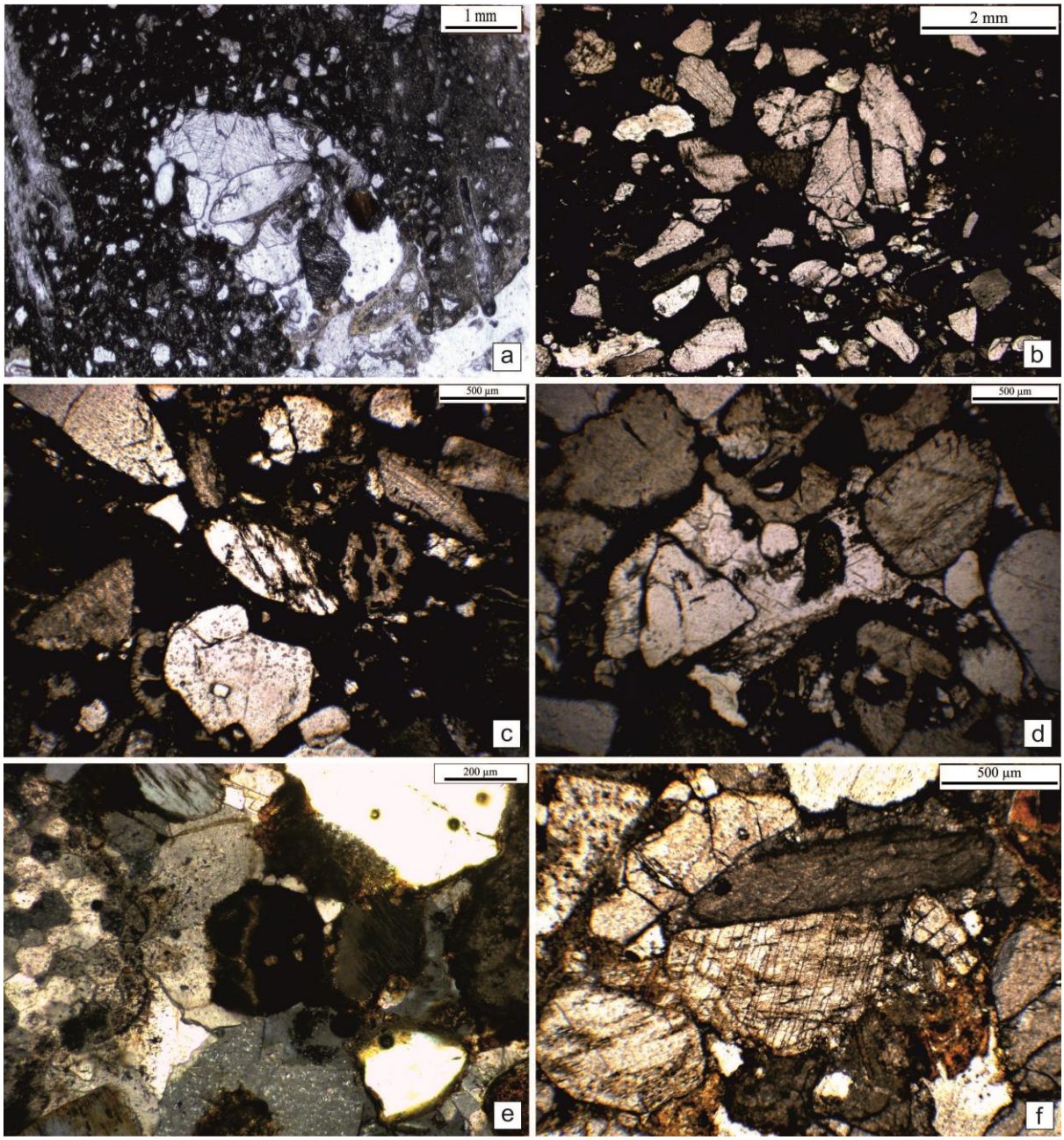

Fig. 3.4.4 Facies IIID: Granite fragments (a); sharply angular siliciclastic grains, note, irregular boundaries and completely devoid of any overgrowth (b); glauconitized feldspar grains (c); isopachous micritic matrix of rapidly varying width (d); fractured mudclast filled with minute carbonate cement crystals (e); pressure welding between framework grains (f).

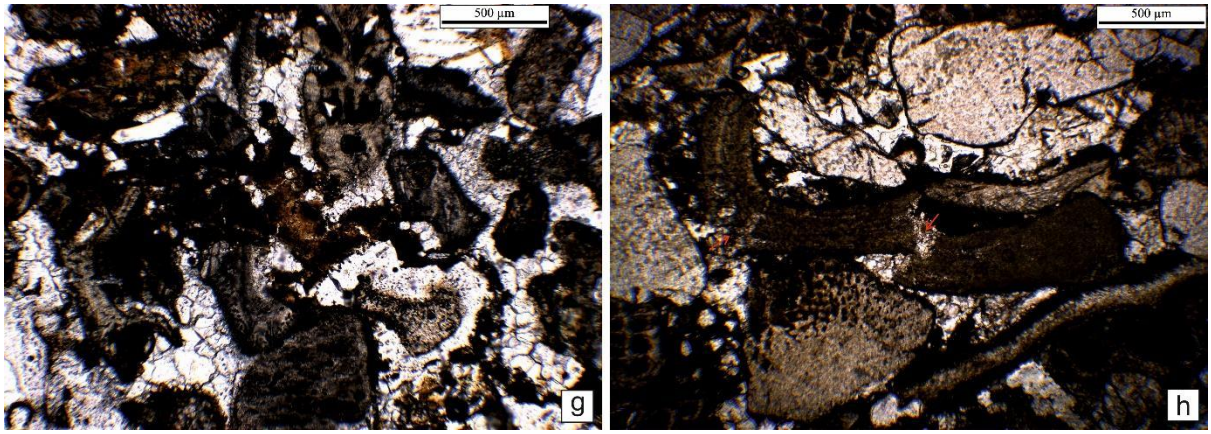

Fig. 3.4.4 Facies IIID: sparry calcite between the framework grains (g); broken shell filled with cement (h).

Interpretation:

Profuse occurrence terrestrial sand grains as well as marine fossils of carbonate composition and their thorough admixing suggests facies admixing. Among fossil clasts dissolution of some, against excellent preservation of other reflects variation in shell mineralogy. The terrestrial grains are most probably derived from the scree fans flanking the narrow fault-controlled marine tongues extended within the continent (Srimani et al., 2020; Srimani, 2024). Unabraded nature and complete lack of overgrowth of the terrigenous grains identify them as of first-generation, freshly derived from the granitic basement. The fossils bear attestation to deposition in a shallow sea and the isopachous micritic rims, presumably created by marine precipitation of calcium carbonate within microborings (James and Choquette, 1983) attest to deposition within the photic zone. The abundance of lime-mud matrix suggests deposition in a relatively calm environment which mismatches the grain-size of the terrigenous fraction. This observation again supports local derivation of the terrigenous grains. Almost similar contradiction arises with the intraclasts distinctly darker in colour than the mud matrix. Their presence clearly indicates erosion and local reworking of previously laid marine deposit too. Pressure welding between adjacent framework grains indicates that the mud matrix allowed compaction during the early stages of burial either being squeezed out from the space between harder grains or undergoing preferred dissolution. In-situ breakage of shells and intraclasts presumably took place as the overburden pressure built up

further. Fractures created thereby within the fossils and the intraclasts are filled by the same cement that formed within the intergranular spaces. Individual cement crystals occupying of both the intergranular space as well as the intragranular fracture clearly identify the cement as a burial diagenesis product. This observation leads to the conclusion that the space for intergranular cement was created by dissolution of the matrix of primary origin. Sharp nature of their boundaries rejects the idea that the sparry calcite patches could be the product of aggrading neomorphism of the mud matrix. The preferential dissolution of the matrix, while most of Low-Mg and High-Mg calcite shells retain their texture, strongly suggests that the matrix was composed of aragonite.

3.4 Conclusion:

Based on field facies analysis and petrographic examination of carbonate lithology and textures, the presence of authigenic berthierine clay mineral and different kind of fossils, it is evident that the deposition commenced with a rifting phase, leading to localized deepening of the basin. Then the sedimentary environment transitioned into an overall shallow marine shelf setting, facilitating the deposition of the fully fossiliferous Kallankurichchi Limestone Formation. Within the shallow marine shelf settings, the facies which are micritic in nature (packstone according to Dunham's carbonate rock texture classification, 1962), suggests low energy environment like rippled facies. Shellbank facies. Whereas grainstone dominated facies like storm and large-scale cross-stratified facies are of high energy facies.

CHAPTER-4

GEOCHEMICAL ATTRIBUTES AND ITS IMPLICATIONS

4.1 Introduction:

Major and trace element geochemistry of carbonates can be used as a powerful tool for paleoenvironment interpretation (Corbin et al., 2000; Adatte et al., 2005). The geochemical characteristics of carbonate serve as promising proxies to the precipitating water chemistry (redox, salinity, and alkalinity), paleoclimate and paleoproductivity (Zhao et al., 2022). The geochemistry of sediments aids in reconstructing the sedimentation history. Though, not all constitutional elements in sediments hold equal significance, yet each plays a significant role in reconstructing the sedimentation history (Chakraborty, 2016). Past earth surface conditions can be better learned from carbonates than any other group of sedimentary rocks (Scoffin, 1987).

Calcite, a carbonate rock mineral, housed a plethora of trace elements of smaller cation including, Mg, Mn, Sr, Ba, Fe, Zn. because of its small rhombohedral crystal structure. Rare earth elements (REEs) are characterized by their insoluble and immobile nature leading to a short residence time in the ocean water (Piper, 1974; Choudhuri and Cullers, 1979; Taylor & MacLennan, 1985). It offers insights about the processes of weathering, diagenesis and the provenance of sediments (Bhatia, 1985; McLennan, 1989). Seawater typically characterized by low concentration of total REE (about 1% of PASS values), positive Yttrium (Y) anomaly and Lanthanum (La) anomaly both and also negative Ce anomaly. In addition, there will be a slight enrichment of Gadolinium (Gd) (Frimmel, 2009). A geochemical inventory of redox-sensitive elements and their ratios unfurls the valuable information about the paleogeographic disposition.

This chapter represents detailed geochemical attributes of Kallankurichchi Limestone Formation of marine origin. It focuses principally on bulk chemistry and deciphers intrabasinal processes of transportation, deposition and diagenesis. Samples for the geochemical analysis were collected systematically from the facies (details already discussed in Chapter 2) except from the graded storm facies (Facies IIB) and small-scale herringbone cross-stratified facies (Facies IIIA). The geochemical analysis performed in preferred facies associations considering their field facies character as well as petrographic introspection. The geochemical investigations have been carried out to interpret the paleosalinity, paleoredox and paleoproductivity of the studied Kallankurichchi limestone.

4.1.1 Paleoredox Proxies:

The term ‘‘paleoredox” may have been first used by Clayton et al. (1966), and it has appeared in the literature with increasing frequency since the early 1970s. The trace-element abundances in sediments and sedimentary rocks allow us to reconstruct paleodepositional conditions (e.g., Rimmer, 2004; Nameroff et al., 2002; Riquier et al., 2005). Variations in the oxidation state and solubility of numerous trace elements are functions of redox condition of depositional environment. Redox-sensitive trace metals tend to be more soluble under oxidizing conditions and less soluble under reducing conditions, resulting in their authigenic enrichments in oxygen-depleted sedimentary facies. The behavior of certain trace elements, notably U, Th, V, and Mo, and to a lesser degree, metal like Cr and Co, serves as valuable indicators of paleoredox conditions (Tribovillard et al., 2006). The V/Cr, Ni/Co, and U/Th are commonly utilized as reliable proxies for discerning the redox state of seawater. This approach helps overcome the inherent limitations of using individual trace elements alone (Jones and Manning 1994; Wignall and Twitchett 1996; Rimmer 2004). There is previously published value regarding the ratio to interpret the paleoredox condition. These are as follows:

V/Cr < 2, Ni/Co < 5 and U/Th < 0.75 are indicative of oxic condition; the 2 < V/Cr < 4.25, the 5 < Ni/Co < 7 and 0.75 <U/Th < 1.25 suggestive of a dysoxic condition; and V/Cr > 4.25, Ni/Co > 7 and U/Th > 1.25 represents an anoxic environment (Jones and Manning, 1994; Rimmer 2004; Tribovillard et al., 2006).

Ce anomalies (Ce*) are excellent redox proxy in carbonate dominated marine environments. Ce anomaly <1.0 indicates oxic and >1 implies anoxic environments (Tostevin et al., 2016).

4.1.2 Paleoproductivity Proxies:

Paleoproductivity is important aspects as it provides significant insights into the ocean circulation, nutrient dispersion, and the evolution of the oceanic carbon cycle. Several studies have shown that the paleoproductivity is often estimated by the enrichment of phosphorus and barium (Tyrrell, 1999; Algeo et al., 2011; Chen et al., 2016; Li et al., 2020). As

phosphorus is the most important nutrient for plankton and is essential in many metabolic processes (Latimer and Filippelli, 2002), so that phosphorus is often used as an indicator of paleoproductivity. The productivity of organic matter relies on the dilution of terrigenous inputs. The paleoproductivity is assessed by P/Ti instead of the absolute content of phosphorus (Latimer and Filippelli, 2002; Li et al., 2017a; Lei et al., 2024) by eliminating the influence of terrigenous detrital material and autologous elements. In other words, P/Ti can be used to characterize the nutritional conditions of the ancient ocean. The assumption made are as follows:

i) The P/Ti < 0.34 indicates low productivity and

ii) The P/Ti > 0.79 indicates high productivity.

Considering that barium (Ba) accumulation is primarily attributed to the organisms in contemporary ocean, it can be extrapolated that these organisms played an even more significant role in accumulating marine Ba. Ba excess is calculated using this formula: $Ba_{excess} = Ba_{sample} - Al_{sample}*(Ba/Al)_{PAAS}$ to check the paleoproductivity.

4.1.3 Paleosalinity Proxies:

Paleosalinity played a crucial role in shaping the development of organisms and the conservation of organic material. The paleosalinity methods utilized extensively thus for, those focusing on concentrations or ratios of boron (B), gallium (Ga), strontium (Sr), barium (Ba), rubidium (Rb), and potassium (K) have garnered the most attention. Boron (B) demonstrates high water solubility, and its absorption into clay minerals correlates logarithmically with paleosalinity (Wei and Algeo, 2020). Na, K, Ba and Sr these elements are used to classify paleosalinity. Elevated paleosalinity typically corresponds to greater paleo-water depth and subdued hydrodynamic conditions, leading to oxygen-depleted environments (Li, 2020). In carbonate rocks, the Sr/Ba >1 points to a marine environment. Although, Chraiki et al. (2023) has propose a modified value of Sr/Ba > 0.5 as characteristics of marine deposits, while the Sr/Ba ratio of ~0.6-1.0 for marine-continental transition and the Sr/Ba ratio of < 0.6 to continental environment (Tribovillard et al., 2006; Wei and Algeo, 2020; Remírez et al., 2024; Liu et al., 2024).

In order to reconstruct paleoenvironmental conditions using element concentrations, it is essential to evaluate whether they are relatively enriched or depleted (Tribovillard et al., 2006; Ross and Bustin, 2009; Zhao et al., 2016). To ascertain that the element concentrations represent authigenic components, it is a common practice to normalize the element concentrations to aluminium (Taylor and McLennan, 1985; Tribovillard et al., 2006; Ross and Marc Bustin, 2009; Li et al., 2017a). The elemental concentrations are compared with respect to Post-Archean Australian Shale (PAAS) and the findings are interpreted using enrichment factors (EF). The enrichment factor of elements (EFx) is calculated with help of the formula: $EF_{element} = (element/Al)_{sample}/(element/Al)_{PAAS}$ (Calvert et al., 1993; Ross and Bustin, 2009; Ding et al., 2018). The normalizing standard used is PASS (Taylor and MacLennan, 1985). When $EF_x > 1$, the sample is relatively enriched in the element, while $EF_x < 1$ indicates depletion (Tribovillard et al., 2006). The biotic productivity rate, Ba_{bio} is calculated from the formula Ba_{bio}= Ba (Total) - (0.0075*Al) (Dymond et al., 1992). To determine Ce anomaly, the formula used is proposed by Nozaki (2008): $Ce^* = 2*Ce_N/(La_N+Pr_N)$ (N: Shale normalized value, De Baar et al., 1985; Frimmel, 2009; Zhang and Shields, 2022). The Eu anomaly is calculated from: $Eu/Eu^* = 2*Eu_N/(Sm_N+Gd_N)$ (Frimmel, 2009). The geochemical values of samples are shown in Table 4.1.

4.2 Results of bulk rock geochemistry of different facies spectrum:

Three different facies associations (FA), FA I, FA II, and FA III have been considered during geochemical analysis. This association discussed here, is exactly similar to the associations discussed earlier (Chapter 2 and 3). During the geochemical analysis the author prefers to consider the total facies association together for the sake of better understanding. Only data of graded storm facies (Facies IIB) is not considered here.

The lower part of sediments i.e., scree conglomerates facies generally silica rich than rest of the part. The upper part of the sediments is generally dominated by calcite ~75–95% along with minor quartz (0.5-3%) and phyllosilicates (5-10%) of the total composition.

Table 4.1 Facies wise elemental concentrations of Kallankurichchi Formation (all values are in ppm, BDL=Below detection level).

Sample Name	Facies	Na	Mg	Al	Si	P	K	Ca	Ti	Fe	Li	Be
TC/UL3	Largescale cross-stratified	BDL	6512.32	33.401.21	99981.79	BDL	5396.99	200549.36	1539.98	26997.52	4.20	0.74
TC/UL2		BDL	7026.93	28856.34	99591.96	BDL	5512.09	210045.84	1431.96	25899.31	4.26	0.71
TC/UL1		BDL	8080.99	35247.85	98433.00	BDL	5687.66	217470.73	1208.08	24524.20	4.36	0.72
TC/UIF		523.86	5900.79	25733.78	68373.50	BDL	5945.77	279737.71	967.63	16439.82	4.01	0.45
TC/UF2B	Downdip cross-stratified	BDL	4986.32	15841.76	59846.32	264.31	5496.32	296584.66	924.36	19785.42	2.80	0.42
TC/UF2A		BDL	5100.70	17213.58	42361.81	395.51	5182.67	308737.01	905.51	20917.49	2.69	0.39
TC/L0		BDL	5249.61	18499.31	38954.06	178.96	5087.77	359485.99	899.22	16974.21	4.25	0.35
DC/MH1	Massive Muddy Facies	BDL	2234.59	7897.69	27760.77	87.42	1330.23	382939.44	660.45	5253.63	0.94	0.09
DC/MH2		BDL	2054.43	7901.64	27072.12	BDL	1497.26	368092.50	BDL	4835.76	1.37	0.15
DC/MH3		BDL	1811.83	6254.54	19287.42	BDL	1080.81	382223.67	600.41	3502.42	1.15	0.12
TC/MH1a		BDL	4593.64	19309.15	47320.18	262.46	5907.63	321640.52	1021.51	11216.73	2.84	0.25
TC/MH1b		BDL	4970.74	21919.12	53566.59	BDL	5924.85	300306.61	1145.02	12233.75	3.64	0.28
TC/MH1		BDL	4176.40	18061.36	46682.91	BDL	5832.61	335722.24	1022.95	20990.71	2.80	0.33
TC/MHL2		BDL	4379.52	13239.28	37389.46	132.06	4605.42	348915.96	725.65	24621.96	2.10	0.36
TC/MHL3		522.01	4243.32	15854.12	40315.91	BDL	4005.53	336946.89	783.43	19264.64	2.45	0.27
UL1/WL	Rippled Facies	BDL	2304.44	5641.65	13867.11	BDL	2087.06	396736.68	BDL	4782.93	0.83	0.11
UL1/UF		BDL	3885.46	16091.19	37129.71	175.75	3008.69	329540.98	965.68	46262.71	0.50	0.55
ML2/UF2A		BDL	3090.94	6914.84	16113.73	1798.32	250.30	352681.60	361.51	43371.88	0.80	0.50
ML2/UF1		BDL	2677.46	10520.93	23489.87	264.23	335.07	303621.72	604.95	69378.67	1.12	0.83
UL/OI		BDL	3756.10	16535.77	40056.81	482.28	333.59	256327.36	662.51	69774.66	3.46	0.68
TC/PZ	Hummocky cross-stratified Facies	BDL	3090.63	7924.67	17333.43	482.43	1585.05	370601.66	BDL	11738.05	1.38	0.21
UL2/LSH		BDL	2666.42	6541.84	14514.99	BDL	1835.32	384247.85	722.95	17361.06	0.97	0.23
UL2/SH1		BDL	2852.24	7456.49	15382.16	219.59	1837.90	371123.80	422.32	18793.26	1.23	0.27
UL1/SH1		BDL	2733.89	9117.66	24676.41	175.87	2509.01	360734.64	905.97	33259.36	1.39	0.40
ML2/SH1		670.96	3454.23	10903.07	26728.25	263.14	333.69	294470.31	542.21	61361.17	1.83	0.65
ML1/SH1		BDL	2607.92	8356.87	22847.77	263.35	1836.79	353648.69	542.65	20540.52	1.27	0.21

Sample Name	Facies	Na	Mg	Al	Si	P	K	Ca	Ti	Fe	Li	Be
TC/F1	4th Bank Matrix	BDL	2156.29	542.28	1389.87	21.92	158.44	384091.35	30.11	1074.97	0.92	0.12
UL3/F2		BDL	2567.27	8525.13	22117.82	527.24	2423.66	360480.42	543.20	13097.21	1.01	0.25
UL3/F2A		BDL	2992.60	1209.63	2136.69	56.98	215.68	315987.88	85.61	6894.21	1.40	0.27
UL2/F1		BDL	2611.26	1314.18	2599.77	92.51	33.52	280624.85	72.62	8824.98	1.83	0.83
UL1/F1	3rd Bank	BDL	2667.41	1589.12	3014.00	47.26	267.87	359783.56	98.63	5963.91	1.88	0.38
UL/F1	2nd Bank	BDL	2475.05	999.85	2768.37	54.37	310.24	396676.25	89.48	6584.67	1.07	0.69
UL/SB1		BDL	2599.69	1693.49	2479.61	68.41	290.12	378994.31	75.82	5781.64	1.34	0.83
UL/SB		BDL	2568.48	1116.79	2578.62	30.70	258.59	320291.41	72.29	5868.43	1.05	0.66
ML/F	1st Bank Matrix	BDL	3068.38	1746.60	4237.47	13.17	384.21	309920.67	102.54	5524.25	1.85	0.51
LL/F1		521.49	2934.02	935.41	2210.92	74.50	175.07	355264.91	60.20	2149.29	1.35	0.30
UL1/F2	Chevron cross-stratified Facies	BDL	2856.55	8801.29	17478.32	483.84	2175.35	371684.86	543.80	26575.92	1.11	0.36
UL/UF0		BDL	3036.74	10180.98	20714.39	BDL	250.82	303760.52	BDL	97916.39	1.58	0.91
ML1/UF1		BDL	3335.04	12293.31	32337.66	263.30	3005.06	315488.93	723.39	57108.05	1.68	0.51
D/DL1	Herringbone cross-stratified Facies	BDL	7721.88	24973.73	67396.43	BDL	3599.15	216903.61	1511.16	56346.74	2.92	0.40
D/DL2		BDL	7718.76	21976.56	55591.42	967.67	2426.35	236264.79	1510.55	59919.17	5.52	0.56
D/DL3		971.70	10207.56	36261.03	109265.34	791.49	6189.51	158422.39	3261.81	34813.09	1.83	0.31
D/DL4		1047.19	9302.73	31644.07	111698.97	484.03	5022.06	144842.61	4533.48	52679.62	8.22	0.72
D/CB3		5912.98	7329.92	19668.29	54954.47	782.66	2233.13	232133.63	1314.06	49128.25	6.43	0.55
LL1/UF1		BDL	3401.49	12527.60	42515.86	659.38	668.93	295152.51	664.24	51569.80	3.08	0.60

Sample Name	Facies	B	Sc	V	Cr	Mn	Co	Ni	Cu	Zn	Ga	Se	Rb	Sr	Ba
TC/UL3	Largescale cross-stratified	90.00	4.79	119.96	56.23	497.72	13.97	16.89	1.52	18.71	5.91	1.89	29.57	207.22	506.51
TC/UL2		86.67	4.55	122.60	57.55	507.03	14.25	16.66	1.52	20.32	6.15	4.51	30.82	204.88	564.27
TC/UL1		91.84	4.94	127.87	58.21	551.94	14.56	16.81	1.60	18.35	6.17	1.57	31.03	195.47	551.58
TC/UIF		95.36	4.07	72.79	38.95	621.39	21.03	12.93	2.45	15.68	4.43	0.99	27.97	203.43	840.65
TC/UF2B	Downdip cross-stratified	94.70	3.61	85.66	37.07	192.30	8.23	19.06	2.35	19.70	3.90	1.18	27.95	200.43	151.32
TC/UF2A		85.74	3.67	80.76	35.48	191.22	7.85	18.33	2.35	19.63	3.76	1.25	27.76	207.97	144.45
TC/L0		60.81	3.33	65.59	148.54	459.06	20.81	96.75	16.14	90.40	3.97	0.72	28.79	223.30	182.90
DC/MH1	Massive Muddy Facies	60.73	0.81	15.43	8.05	220.77	1.40	3.53	0.77	1.43	0.83	1.30	4.20	43.48	42.85
DC/MH2		101.17	2.79	49.43	37.24	186.47	2.54	11.02	2.12	7.28	2.35	1.04	12.90	138.10	78.66
DC/MH3		67.42	2.32	47.41	35.31	162.39	2.43	8.69	1.87	8.11	2.15	1.15	10.97	126.60	75.45
TC/MH1a		81.30	3.80	63.85	29.48	188.68	8.41	10.64	2.33	26.93	3.82	2.09	28.62	157.76	159.01
TC/MH1b		78.51	4.03	77.00	36.66	171.21	8.95	12.98	2.83	21.13	4.23	1.72	32.55	153.09	203.11
TC/MH1		69.22	3.23	108.21	32.08	200.08	9.60	17.51	3.05	18.27	3.52	1.43	25.13	181.13	164.59
TC/MHL2		59.72	2.68	94.70	31.12	160.18	6.69	15.50	2.31	14.15	2.86	1.22	16.43	181.12	114.68
TC/MHL3		77.28	3.72	78.34	31.76	118.64	9.29	13.35	2.47	16.45	3.44	1.48	21.30	150.51	118.92
UL1/WL	Rippled Facies	93.75	1.12	14.36	16.41	322.55	5.00	7.14	1.28	6.44	1.16	0.81	7.48	244.71	50.85
UL1/UF		104.93	4.01	239.80	90.24	959.19	15.44	35.02	1.32	18.87	1.67	1.51	4.88	231.63	177.86
ML2/UF2A		78.43	4.61	172.29	70.25	747.79	11.87	23.87	3.04	16.88	1.52	3.96	2.73	236.66	21.26
ML2/UF1		124.70	6.51	346.41	156.44	812.04	26.98	48.27	1.38	37.63	2.19	1.78	2.68	197.68	46.22
UL/OI		78.16	7.00	373.24	208.37	986.58	19.47	41.19	3.05	34.85	2.84	2.13	4.30	210.52	136.34
TC/PZ	Hummocky cross-stratified Facies	95.72	2.46	55.45	23.79	375.82	21.81	11.35	1.49	11.06	1.84	1.18	9.14	388.99	60.66
UL2/LSH		96.32	2.58	87.42	36.42	357.62	8.06	14.33	2.07	11.84	1.58	1.23	8.73	193.16	82.37
UL2/SH1		82.07	2.86	112.04	44.66	314.98	7.91	18.11	2.74	12.71	1.83	1.10	8.90	211.32	52.59
UL1/SH1		109.99	3.87	193.64	79.33	425.94	15.91	24.27	1.91	19.55	2.24	1.72	11.62	283.29	102.99
ML2/SH1		87.28	5.91	332.24	154.47	725.83	20.81	40.12	2.39	35.01	2.05	1.26	2.85	314.67	104.20
ML1/SH1		104.69	3.57	118.90	87.33	630.29	8.41	15.23	1.73	12.13	1.94	1.22	9.09	246.72	60.37

Sample Name	Facies	B	Sc	V	Cr	Mn	Co	Ni	Cu	Zn	Ga	Se	Rb	Sr	Ba
TC/F1	4th Bank Matrix	65.23	1.32	37.50	72.78	469.24	6.01	47.46	7.76	41.13	1.33	0.80	6.55	249.40	54.11
UL3/F2		62.80	2.15	64.46	64.88	389.84	10.31	36.12	5.51	28.68	1.85	0.72	9.60	192.93	163.91
UL3/F2A		110.44	2.96	77.80	34.78	454.66	11.33	14.22	2.19	14.76	2.37	1.37	12.51	241.90	178.88
UL2/F1		69.84	6.72	389.06	207.53	1470.05	26.11	55.48	2.07	38.91	2.08	1.26	2.41	133.96	290.60
UL1/F1	3rd Bank	73.28	3.18	163.24	100.03	663.07	22.28	48.29	5.16	38.56	2.16	1.47	9.08	208.68	133.31
UL/F1	2nd Bank	66.06	4.13	322.08	129.74	533.00	16.90	47.58	2.24	27.93	1.79	0.97	3.03	139.09	43.49
UL/SB1		103.35	4.78	240.30	129.37	977.37	23.16	32.63	1.85	26.75	2.31	1.56	11.52	161.03	236.58
UL/SB		70.00	3.75	224.46	175.66	1058.60	22.37	73.36	8.45	59.63	2.01	0.83	9.58	138.85	238.02
ML/F	1st Bank Matrix	109.30	5.22	148.74	55.51	410.96	27.67	36.60	2.28	27.57	3.14	3.64	12.34	234.94	125.49
LL/F1		67.99	2.61	83.87	29.40	540.87	8.81	16.99	1.64	29.92	3.30	1.05	8.71	223.43	80.27
UL1/F2	Chevron cross-stratified Facies	93.54	3.08	129.87	41.81	518.27	12.81	22.41	1.68	15.88	2.02	1.22	10.07	183.57	117.86
UL/UF0		95.87	6.93	370.07	191.43	1377.55	22.26	44.80	1.18	42.47	2.04	1.94	1.74	147.84	180.04
ML1/UF1		96.00	4.78	232.02	139.52	449.54	16.47	33.08	1.55	27.37	3.14	1.39	12.50	220.02	82.51
D/DL1	Herringbone cross-stratified Facies	55.45	3.02	99.15	59.55	370.99	9.61	19.65	5.51	63.30	3.36	1.25	7.22	387.81	30.97
D/DL2		83.90	6.41	230.65	182.79	634.85	16.58	29.70	2.37	39.64	3.79	1.73	9.18	251.46	29.04
D/DL3		66.87	3.56	101.79	46.72	629.96	13.95	13.41	1.78	22.29	2.36	1.30	9.39	301.20	45.94
D/DL4		79.90	7.80	226.04	107.27	527.13	12.44	21.47	2.86	33.88	6.95	1.01	26.16	305.35	538.55
D/CB3		70.34	6.08	312.22	169.16	387.87	22.78	43.68	3.48	50.25	4.99	1.44	12.16	301.28	49.18
LL1/UF1		122.81	6.20	283.84	141.57	720.17	31.32	43.06	1.88	32.03	3.82	1.68	5.07	206.75	122.97

Sample Name	Facies	La	Ce	Pr	Nd	Sm	Eu	Gd	Tb	Dy	Y	Ho	Er	Tm
TC/UL3	Largescale cross-stratified	21.98	47.35	5.16	20.05	3.64	0.98	3.10	0.42	2.10	11.13	0.41	1.11	0.17
TC/UL2		39.13	79.85	7.87	28.81	4.85	1.01	3.76	0.47	2.18	10.79	0.40	1.09	0.16
TC/UL1		35.53	76.30	7.64	28.48	4.91	0.99	3.61	0.46	2.16	10.52	0.41	1.10	0.16
TC/UIF		18.39	37.18	3.95	15.33	2.90	0.86	2.51	0.36	1.82	9.62	0.37	0.99	0.15
TC/UF2B	Downdip cross-stratified	17.74	37.32	4.04	15.49	2.87	0.53	2.28	0.31	1.48	7.65	0.30	0.76	0.12
TC/UF2A		19.13	40.01	4.46	16.93	3.05	0.54	2.42	0.35	1.61	7.80	0.31	0.81	0.12
TC/L0		28.41	61.12	6.89	25.06	4.19	0.47	3.05	0.35	1.51	5.71	0.26	0.65	0.08
DC/MH1	Massive Muddy Facies	3.88	6.96	0.88	3.22	0.53	0.10	0.48	0.06	0.32	1.80	0.06	0.18	0.02
DC/MH2		14.96	31.18	3.56	13.74	2.61	0.48	2.19	0.30	1.31	7.06	0.27	0.67	0.13
DC/MH3		11.41	22.73	2.83	10.29	1.96	0.39	1.72	0.25	1.29	5.54	0.26	0.65	0.08
TC/MH1a		22.60	46.27	5.21	18.72	3.34	0.60	2.71	0.35	1.71	7.11	0.32	0.85	0.12
TC/MH1b		17.20	36.89	4.19	15.54	2.75	0.60	2.41	0.31	1.52	6.12	0.28	0.73	0.10
TC/MH1		19.96	38.66	4.10	14.86	2.54	0.54	2.29	0.30	1.62	6.79	0.28	0.75	0.10
TC/MHL2		15.49	33.61	3.79	13.36	2.42	0.44	2.14	0.28	1.34	5.41	0.26	0.65	0.08
TC/MHL3		19.53	40.97	4.67	17.32	2.97	0.56	2.68	0.33	1.66	7.36	0.31	0.85	0.11
UL1/WL	Rippled Facies	9.86	19.56	2.26	8.54	1.55	0.26	1.37	0.17	0.84	3.95	0.16	0.43	0.05
UL1/UF		19.10	38.94	4.65	19.11	3.99	0.82	3.84	0.56	2.89	13.75	0.55	1.44	0.21
ML2/UF2A		25.22	53.10	6.04	24.64	5.06	0.97	4.84	0.68	3.50	17.48	0.67	1.81	0.27
ML2/UF1		21.26	45.40	5.49	22.12	4.55	0.78	3.96	0.60	3.15	13.79	0.61	1.63	0.24
UL/OI		36.21	84.66	8.93	34.15	6.48	0.88	5.38	0.75	3.71	14.81	0.67	1.77	0.25
TC/PZ	Hummocky cross-stratified Facies	13.41	25.84	3.03	11.48	2.12	0.38	1.81	0.28	1.22	5.98	0.26	0.63	0.12
UL2/LSH		16.18	30.15	3.77	14.71	2.91	0.60	2.60	0.39	1.81	9.30	0.38	0.93	0.16
UL2/SH1		17.18	31.90	3.76	14.28	2.65	0.47	2.21	0.34	1.56	7.73	0.33	0.83	0.15
UL1/SH1		24.86	53.82	5.67	21.52	3.88	0.57	3.04	0.43	1.94	9.21	0.39	1.01	0.18
ML2/SH1		16.76	37.64	4.31	17.42	3.59	0.68	3.23	0.51	2.52	11.95	0.53	1.38	0.24
ML1/SH1		19.69	40.26	4.66	18.06	3.54	0.63	3.01	0.46	2.16	10.44	0.45	1.12	0.18

Sample Name	Facies	La	Ce	Pr	Nd	Sm	Eu	Gd	Tb	Dy	Y	Ho	Er	Tm
TC/F1	4th Bank Matrix	8.42	17.76	1.90	7.21	1.30	0.22	1.16	0.16	0.78	3.62	0.15	0.41	0.05
UL3/F2		15.88	31.95	3.60	13.28	2.53	0.48	2.38	0.32	1.67	7.56	0.33	0.82	0.10
UL3/F2A		18.32	37.11	4.15	16.17	3.00	0.60	2.61	0.38	1.78	9.56	0.38	0.93	0.16
UL2/F1		31.80	65.96	7.71	29.93	5.69	0.99	5.57	0.79	4.31	18.84	0.90	2.20	0.29
UL1/F1	3rd Bank	20.47	41.51	4.50	17.49	3.19	0.50	2.80	0.37	1.88	7.94	0.37	0.97	0.12
UL/F1	2nd Bank	20.72	42.03	4.52	17.50	3.65	0.72	3.73	0.53	2.91	13.32	0.64	1.51	0.20
UL/SB1		20.16	46.56	5.14	20.06	3.94	0.73	3.34	0.49	2.36	11.57	0.49	1.26	0.22
UL/SB		15.47	33.38	3.68	14.47	2.87	0.63	2.92	0.44	2.29	9.76	0.46	1.21	0.16
ML/F	1st Bank Matrix	17.02	31.65	5.03	15.86	4.09	1.89	3.62	1.65	3.03	9.30	1.69	2.24	1.48
LL/F1		13.94	29.36	3.30	12.82	2.37	0.44	2.05	0.29	1.37	5.97	0.28	0.75	0.11
UL1/F2	Chevron cross-stratified Facies	14.67	31.80	3.76	15.04	2.97	0.54	2.53	0.36	1.82	8.81	0.36	0.93	0.13
UL/UF0		25.96	54.33	6.41	25.90	5.64	1.07	5.32	0.79	4.28	19.88	0.82	2.20	0.32
ML1/UF1		20.68	44.82	5.07	19.71	4.03	0.71	3.51	0.48	2.41	11.32	0.46	1.22	0.18
D/DL1	Herringbone cross-stratified Facies	15.54	33.09	3.83	15.34	2.94	0.55	2.92	0.43	2.05	9.78	0.46	1.03	0.15
D/DL2		21.53	50.29	5.05	19.77	3.86	0.78	3.83	0.54	2.87	11.32	0.51	1.48	0.20
D/DL3		16.74	35.50	3.88	15.04	2.84	0.48	2.62	0.36	1.89	7.56	0.34	0.96	0.13
D/DL4		35.82	64.46	6.80	24.05	3.89	0.84	3.50	0.49	2.57	12.39	0.57	1.39	0.20
D/CB3		23.33	48.95	5.54	19.85	3.84	0.69	3.80	0.56	2.93	11.47	0.54	1.61	0.21
LL1/UF1		20.59	45.06	5.29	20.83	4.24	0.84	3.78	0.59	3.02	14.03	0.59	1.55	0.24

Sample Name	Facies	Yb	Lu	Pb	Th	U	Zr	Nb	Hf	Ta	Re	Ir
TC/UL3	Largescale cross-stratified	0.93	0.15	7.89	5.89	0.45	69.32	4.75	1.91	0.42	BDL	0.02
TC/UL2		0.86	0.13	8.44	10.65	0.72	62.01	5.09	1.77	0.62	0.01	0.05
TC/UL1		0.87	0.14	8.25	13.89	0.81	65.00	6.27	2.07	0.69	0.01	0.06
TC/UIF		0.84	0.14	9.10	3.61	0.50	54.11	6.87	1.75	4.81	0.02	0.12
TC/UF2B	Downdip cross-stratified	0.61	0.10	4.51	3.48	0.39	30.90	3.03	0.86	0.21	BDL	0.05
TC/UF2A		0.63	0.11	24.53	3.96	0.47	31.22	2.81	0.86	0.20	BDL	0.02
TC/L0		0.53	0.08	8.81	13.10	1.70	28.86	3.63	0.76	0.25	BDL	BDL
DC/MH1	Massive Muddy Facies	0.15	0.02	1.04	1.59	0.28	10.12	0.77	0.25	0.05	0.01	0.02
DC/MH2		0.52	0.11	2.74	3.75	0.36	30.73	2.16	0.92	0.20	0.01	0.05
DC/MH3		0.47	0.07	2.82	3.55	0.27	17.08	1.83	0.45	0.10	0.01	0.01
TC/MH1a		0.64	0.10	5.17	4.19	1.41	21.86	2.20	0.53	0.14	0.01	0.01
TC/MH1b		0.66	0.08	6.57	5.13	1.52	40.28	3.68	1.04	0.25	0.01	0.03
TC/MH1		0.64	0.10	5.67	5.33	1.01	38.14	2.77	1.08	0.26	0.01	0.06
TC/MHL2		0.53	0.07	4.05	4.37	0.45	16.73	1.99	0.42	0.14	0.01	0.01
TC/MHL3		0.65	0.09	4.30	5.61	0.50	20.09	2.22	0.51	0.21	0.01	0.04
UL1/WL	Rippled Facies	0.31	0.05	1.47	2.43	1.09	12.19	0.95	0.26	0.05	BDL	BDL
UL1/UF		1.10	0.17	2.97	3.15	0.69	13.98	2.66	0.43	0.42	0.01	0.04
ML2/UF2A		1.42	0.23	3.35	3.03	0.93	18.90	2.26	0.58	0.16	0.01	0.04
ML2/UF1		1.35	0.21	5.10	6.15	0.53	31.55	3.66	0.93	0.19	0.01	0.03
UL/OI		1.41	0.22	4.93	14.61	0.89	30.07	3.99	0.92	0.21	0.01	0.03
TC/PZ	Hummocky cross-stratified Facies	0.51	0.12	2.18	3.09	0.93	44.36	1.49	1.27	0.10	BDL	0.02
UL2/LSH		0.69	0.14	2.76	2.36	0.29	19.85	1.45	0.57	0.10	0.01	0.03
UL2/SH1		0.65	0.14	2.57	4.11	0.36	19.38	2.22	0.56	0.37	0.01	0.03
UL1/SH1		0.86	0.17	4.02	9.68	0.96	65.52	3.62	1.88	0.22	0.01	0.04
ML2/SH1		1.18	0.21	4.89	5.50	0.48	26.09	3.59	0.74	0.19	0.01	0.04
ML1/SH1		0.90	0.17	2.88	5.57	0.56	28.68	2.16	0.79	0.13	0.01	0.03

Sample Name	Facies	Yb	Lu	Pb	Th	U	Zr	Nb	Hf	Ta	Re	Ir
TC/F1	4th Bank Matrix	0.35	0.05	3.15	2.41	0.42	20.76	0.96	0.53	0.06	BDL	BDL
UL3/F2		0.62	0.09	3.65	3.91	0.65	15.79	1.55	0.40	0.42	BDL	BDL
UL3/F2A		0.70	0.14	5.14	3.83	0.48	32.26	1.67	0.86	0.17	0.01	0.04
UL2/F1		1.81	0.26	6.10	12.74	1.33	31.42	4.38	0.84	0.39	BDL	0.03
UL1/F1	3rd Bank	0.80	0.11	4.75	7.98	0.88	33.12	3.09	0.75	0.27	BDL	BDL
UL/F1	2nd Bank	1.25	0.17	4.34	5.46	0.67	20.48	2.27	0.47	0.08	BDL	BDL
UL/SB1		1.08	0.19	4.26	5.96	0.99	31.90	3.11	0.88	0.26	0.01	0.05
UL/SB		1.07	0.15	5.52	4.64	1.01	35.84	2.78	0.83	0.30	BDL	BDL
ML/F	1st Bank Matrix	2.02	1.49	3.71	4.46	0.49	29.41	2.79	0.83	0.18	0.01	0.03
LL/F1		0.60	0.10	3.68	3.20	0.52	14.13	1.64	0.36	0.18	0.01	0.03
UL1/F2	Chevron cross-stratified Facies	0.70	0.11	3.51	3.56	0.50	22.86	2.01	0.68	0.17	0.01	0.03
UL/UF0		1.80	0.27	4.73	5.05	0.59	43.32	3.48	1.30	0.17	0.01	0.03
ML1/UF1		1.00	0.15	4.16	6.49	0.77	33.52	3.55	0.94	0.23	BDL	0.01
D/DL1	Herringbone cross-stratified Facies	0.81	0.14	5.45	5.20	1.04	16.52	1.99	0.54	0.29	0.03	0.03
D/DL2		1.34	0.19	4.96	4.95	1.04	22.73	3.29	0.56	0.16	0.01	BDL
D/DL3		0.79	0.12	2.99	3.67	0.54	15.93	2.84	0.42	0.15	0.01	BDL
D/DL4		1.29	0.18	10.89	14.12	0.78	75.32	12.91	1.81	0.80	0.01	0.02
D/CB3		1.28	0.18	7.56	9.18	1.28	45.72	4.33	1.21	0.22	BDL	0.01
LL1/UF1		1.29	0.22	5.03	5.07	0.58	43.66	3.85	1.26	0.33	0.01	0.33

4.2.1 Facies Association I:

The matrix of scree conglomerates is analyzed in XRF and its bulk chemical analysis reports SiO_2 varying from 19.59–43 wt%, Al_2O_3 4.5-12.97 wt%, Fe_2O_3 1.7-2.80 wt%, CaO 2.44-31.4 wt% etc. (Table 4.2). So, silica concentration is higher.

Table 4.2 Major oxide (concentrations in Wt%) analysis of scree conglomerates and its associated matrix (Facies IA).

Sample	SiO_2	TiO_2	Al_2O_3	MnO	Fe_2O_3	CaO	MgO	Na_2O	K_2O	P_2O_5
A1	22.35	0.25	6.40	0.05	1.70	27.29	1.03	0.22	0.86	0.07
A3	31.40	0.46	9.32	0.09	2.54	30.49	0.85	0.64	1.83	0.14
A4	19.59	0.16	4.53	0.07	2.10	30.44	0.77	0.15	0.62	0.16
A-6	29.05	0.34	5.92	0.06	2.80	20.98	0.77	0.10	0.77	0.16
A7	35.11	0.24	5.36	0.04	2.07	31.49	0.61	0.43	1.04	0.06
DC16	42.94	0.32	12.97	0.04	2.74	2.44	1.88	0.23	1.23	0.10

The calcite rhombs with impure dusty core present within this association and it is the most interesting feature present in this association belongs to scree derivatives and analyzed in detail (Fig. 4.1). EPMA data indicates an overall calcitic nature of the rhomb. There is compositional variation towards their cores. EDS mapping shows significant decline in Ca^{+2} content towards core (Table 4.3). EPMA data collected from the core, rim and the outer matrix indicates growth of the calcite from and within a Fe-Mn-Mg-Al-rich clay (Table 4.4a, b). It reiterates clayey nature of the core, with a fair share of Al_2O_3 and SiO_2, and with a non-negligible share of Fe_2O_3, K_2O and MgO. Within the crystals the CaO content varies between 94-98.5%.

Table 4.3 EDS data of the calcite rhomb (core, rim and outer matrix) (Values are in wt%, BDL=Below detection level).

Spot	O K	MgK	AlK	SiK	KK	CaK	TiK	FeK	
1	53.07	2.67	10.89	21.6	1.41	6.92	0.13	3.31	**Core**
2	55.94	BDL	2.46	4.61	BDL	36.1	0.07	0.83	
3	52.02	1.59	6.5	13.47	1.41	18.63	0.14	2.91	
4	50.11	BDL	BDL	BDL	BDL	49.8	0.09	BDL	**Rim**
5	47.25	BDL	BDL	BDL	BDL	52.63	0.12	BDL	
6	48.11	BDL	BDL	BDL	BDL	51.79	0.11	BDL	
7	47.47	2.26	11.06	23.94	1.9	9.27	0.06	4.04	**Outer matrix**
8	48.98	BDL	BDL	1.09	BDL	49.8	0.13	BDL	
9	50.14	1.64	6.72	13.13	BDL	25.98	0.16	2.23	

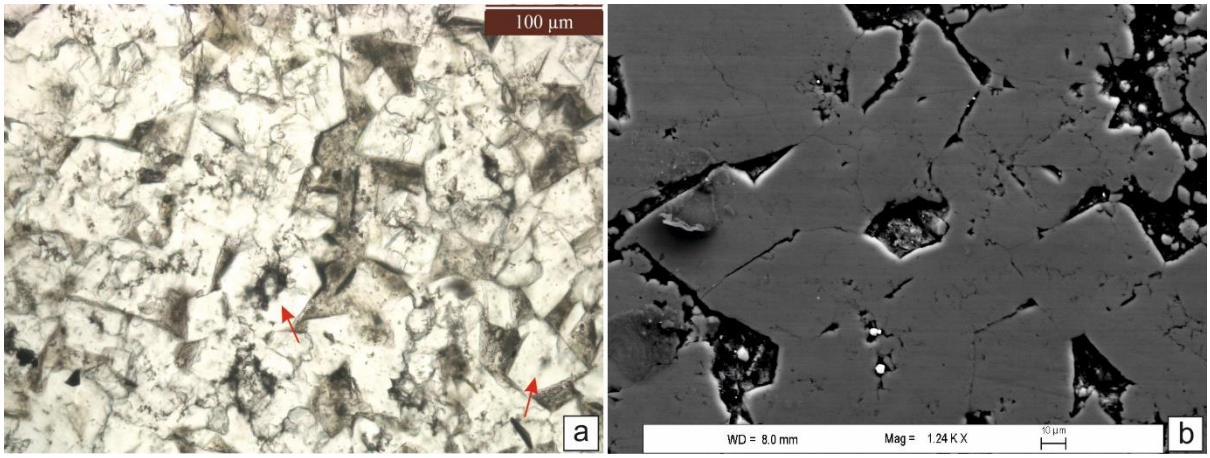

Fig. 4.1 Clayey core and outer rim of calcite rhombs: petrographic image (red arrowed) (a); SEM image (b).

Table 4.4a Major oxide analysis (EPMA) of core spot of the calcite rhombs (Values are in wt%, BDL=Below detection level).

CORE of calcite rhomb									
Na_2O	MgO	Al_2O_3	SiO_2	P_2O_5	K_2O	CaO	Cr_2O_3	MnO	Fe_2O_3
0.63	3.34	21.90	59.88	0.02	2.85	2.42	0.59	0.03	8.34
0.32	3.13	18.67	52.39	0.04	2.22	13.46	2.73	BDL	7.04
BDL	0.24	BDL	0.10	0.02	0.05	98.94	BDL	0.44	0.21
BDL	0.56	0.09	0.20	BDL	0.04	97.65	0.03	0.76	0.67
0.08	0.57	0.12	0.42	BDL	0.05	97.96	BDL	0.22	0.59
0.23	2.77	17.16	46.16	0.20	4.05	2.10	0.16	0.01	27.17
BDL	0.46	1.37	3.52	BDL	0.08	93.01	0.09	0.52	0.94
0.18	3.52	20.14	54.99	0.14	2.85	10.40	0.44	0.08	7.25
0.21	3.13	20.43	57.25	0.03	3.31	7.11	0.16	0.11	8.27
0.27	2.53	26.81	56.04	BDL	1.46	4.63	0.59	BDL	7.66
0.17	3.08	20.41	55.48	BDL	1.46	13.00	0.01	0.05	6.34
0.04	0.22	0.22	0.76	0.05	0.03	97.62	0.05	0.12	0.89
0.27	0.64	7.10	20.69	0.10	0.52	60.98	4.66	0.03	5.02
0.99	BDL	18.35	64.78	0.16	15.30	0.39	0.02	0.01	BDL
0.04	0.06	0.58	2.08	BDL	0.06	95.51	0.26	0.21	1.20
BDL	0.10	0.12	0.39	0.13	0.06	96.33	0.20	0.39	2.27
BDL	0.37	0.04	0.16	0.10	0.02	98.08	BDL	0.62	0.60
BDL	0.49	0.06	0.19	BDL	0.02	98.23	BDL	0.66	0.35
0.08	0.81	0.05	0.08	0.03	0.08	98.23	0.05	0.17	0.42

Table 4.4b Major oxide analysis (EPMA) of the rim of the calcite rhombs (Values are in wt%, BDL=Below detection level).

RIM of calcite rhomb									
Na_2O	**MgO**	**Al_2O_3**	**SiO_2**	**P_2O_5**	**K_2O**	**CaO**	**Cr_2O_3**	**MnO**	**Fe_2O_3**
0.08	0.53	0.10	0.21	0.09	0.06	97.66	BDL	0.71	0.56
0.03	0.39	0.24	1.01	0.10	0.03	96.73	0.03	0.73	0.70
0.06	0.44	0.22	0.61	BDL	0.03	97.29	BDL	0.73	0.62
0.01	0.83	0.30	0.52	0.01	0.06	97.10	BDL	0.46	0.72
BDL	0.62	0.17	0.37	BDL	0.02	97.04	BDL	0.91	0.87
0.23	1.68	0.02	0.05	0.07	0.02	97.75	BDL	0.05	0.14
0.05	0.48	0.03	0.01	0.06	0.02	98.08	BDL	0.60	0.67
0.11	0.42	0.02	0.17	0.05	0.15	97.80	0.04	0.68	0.56
0.12	0.47	0.12	0.46	0.02	0.09	97.38	BDL	0.60	0.75
0.02	0.44	BDL	BDL	BDL	0.04	98.60	BDL	0.50	0.41
BDL	0.37	0.35	1.45	BDL	BDL	96.81	0.01	0.43	0.59
BDL	0.45	0.84	2.40	BDL	0.04	94.87	0.02	0.66	0.71
0.01	0.44	0.55	1.65	BDL	0.05	95.90	BDL	0.72	0.68
0.03	0.60	0.06	0.08	0.03	0.11	97.59	BDL	0.72	0.79
BDL	0.14	0.93	2.42	0.08	0.08	94.67	0.04	0.15	1.49
0.05	0.51	0.35	1.06	BDL	0.01	96.51	0.11	0.70	0.71
0.01	0.39	0.17	0.13	0.11	0.02	97.81	BDL	0.70	0.65
BDL	0.48	0.21	0.60	0.03	0.01	97.47	BDL	0.63	0.57
0.03	0.40	0.39	1.72	0.08	0.10	95.87	BDL	0.67	0.72
0.02	0.38	0.24	0.83	0.02	0.07	97.13	0.14	0.45	0.73
BDL	0.60	BDL	BDL	0.10	0.01	97.77	0.03	0.68	0.80

The concentration of REE is very low, varying from 79.3 to 146.0 ppm (Fig. 4.2a). The Kallankurichchi Limestone is enriched with light rare earth elements (LREE) compared to heavy rare earth elements (HREE) (Fig. 4.2b), with LREE/HREE values ranging from 14.6–24.3 (Table 4.5). The PAAS-normalized spider diagram also depicts the LREE enrichment with respect to HREE with a prominent Eu-anomaly at Facies IIID (Fig. 4.2c).

Sample Name	Facies	Total REY	LREE / HREE (La/Yb)	LREE / MREE (La / Sm)	MREE / HREE (Sm / Yb)
TC/UL3	Largescale cross-stratified	118.67	23.70	6.04	3.92
TC/UL2		181.36	45.51	8.07	5.64
TC/UL1		173.28	40.85	7.23	5.65
TC/UIF		95.41	21.86	6.34	3.45
TC/UF2B	Downdip cross-stratified	91.60	29.11	6.18	4.71
TC/UF2A		98.27	30.55	6.27	4.87
TC/L0		138.36	53.71	6.78	7.92
DC/MH1	Massive Muddy Facies	18.66	25.31	7.31	3.46
DC/MH2		79.09	28.72	5.72	5.02
DC/MH3		59.93	24.54	5.82	4.21
TC/MH1a		110.64	35.53	6.78	5.24
TC/MH1b		89.37	26.19	6.26	4.18
TC/MH1		93.53	31.33	7.87	3.98
TC/MHL2		79.88	29.42	6.41	4.59
TC/MHL3		100.06	30.07	6.57	4.58
UL1/WL	Rippled Facies	49.35	31.53	6.38	4.95
UL1/UF		111.14	17.34	4.79	3.62
ML2/UF2A		145.92	17.76	4.99	3.56
ML2/UF1		125.13	15.77	4.67	3.38
UL/OI		200.26	25.65	5.59	4.59
TC/PZ	Hummocky cross-stratified Facies	67.19	26.22	6.31	4.15
UL2/LSH		84.73	23.60	5.56	4.24
UL2/SH1		84.18	26.30	6.48	4.06
UL1/SH1		127.56	29.00	6.41	4.53
ML2/SH1		102.13	14.25	4.67	3.05
ML1/SH1		105.72	21.84	5.56	3.92
TC/F1	4th Bank Matrix	43.54	24.14	6.47	3.73
UL3/F2		81.62	25.48	6.27	4.06
UL3/F2A		95.98	26.18	6.10	4.29
UL2/F1		177.04	17.59	5.59	3.15
UL1/F1	3rd Bank Matrix	103.01	25.63	6.41	4.00
UL/F1	2nd Bank Matrix	113.40	16.64	5.67	2.94
UL/SB1		117.57	18.70	5.12	3.65
UL/SB		88.95	14.49	5.39	2.69
ML/F	1st Bank Matrix	102.05	8.42	4.16	2.02
LL/F1		73.73	23.38	5.89	3.97
UL1/F2	Chevron cross-stratified Facies	84.54	20.92	4.94	4.24
UL/UF0		154.99	14.43	4.60	3.13
ML1/UF1		115.75	20.68	5.14	4.03
D/DL1	Herringbone cross-stratified Facies	89.07	19.16	5.28	3.63
D/DL2		123.57	16.13	5.58	2.89
D/DL3		89.25	21.14	5.90	3.58
D/DL4		158.44	27.76	9.20	3.02
D/CB3		124.79	18.17	6.07	2.99
LL1/UF1		122.17	15.92	4.85	3.28

Table 4.5 Facies wise REE distribution of Kallankurichchi Formation (all values are in ppm).

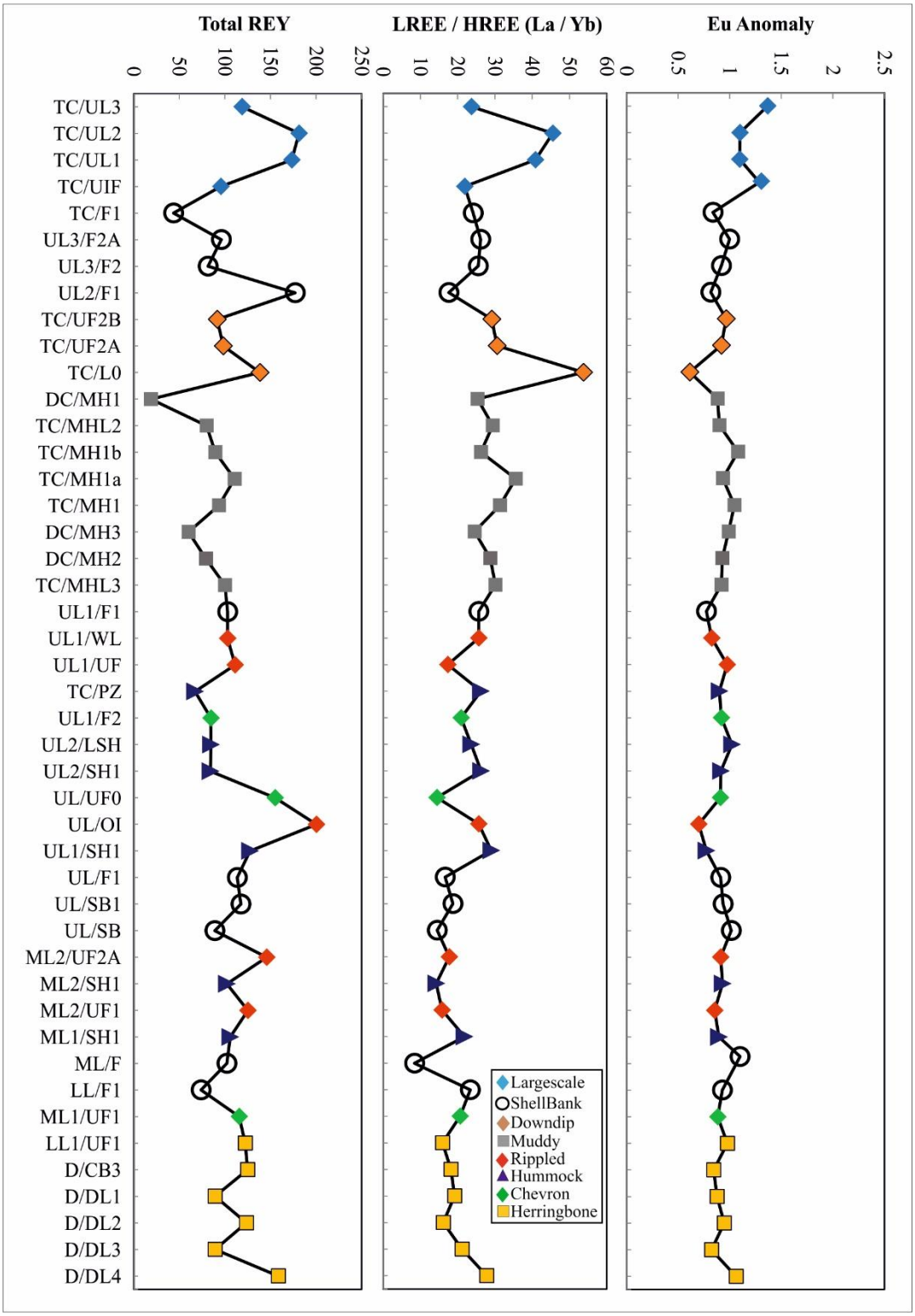

Fig. 4.2 Total REE distribution throughout the Formation; LREE/HREE values of the lower tide-dominated part (sample no- D/DL4-D/CB3) to upper large-scale cross-stratified part (TC/UIF-TC/UL3); Eu anomaly observed at the upper part of Formation.

The Th content is, however, close to that of PAAS. The Fe content is lower (~30306.19 ppm) than its preceding facies and the B/Ga value is higher compared to other facies association. The concentrations of V, Cr, Ni, Zn and U are lower with respect to those in PAAS. Trace element content in this facies is also depleted. The PAAS normalized REE spider diagram is characteristic of volcaniclastic sediment (Plank and Langmuir, 1998; Sturesson et al., 2000; Mishra and Sen, 2018). The Rb (ppm) vs. K_2O (wt%) plot also indicates a volcaniclastic source of the green-clay bearing limestone at the basal part of the Kallankurichchi Formation (Discussed detail in Chapter- 7; Fig. 7.9) (Andreozzi et al., 1997).

4.2.2 Facies Association II:

Facies association II is initiated with a herringbone cross-stratified calcarenite at the basal part, followed upward by wave dominated successions. The wave dominated association alternate between themselves vertically. Eventually this facies succession is sharply overlain by unitary facies e.g., muddy facies. Petrographic observation designates this facies as a packstone, but at places, this facies reveal a grainstone nature (Dunham, 1962). The allochems are mostly bioclasts. There is a subordinate population of siliciclastic grains, such as quartz, feldspar, mica and rock fragments, on average 22% by volume, at the basal herringbone cross-stratified facies.

The rocks are generally depleted with respect to PAAS (McLennan, 2001) in metals, like Fe, Al, Zn, Pb, U, Th and rare-earth elements while enriched in Si and Mn with respect to the standard used for normalization. The Ce anomaly (Ce*) value is negative (<1.0) consistently (Fig. 4.3a) and it does not on the wave agitated shelf, indicating terrigenous contamination did not affect the Ce/Ce* much. It implies that the overall environment was oxic and oxygen budget was sufficient enough for biotic proliferation. V/Cr and Ni/Co values also supports its oxic to dysoxic pattern (Fig. 4.3b, c; Table 4.6). The B/Ga ratio has an overall tendency to increase upward within this facies association (Fig. 4.3d).

This facies is depleted in V, Ni and Cr, while comparable in U contents with respect to the same standard. The Sr content of this facies association exhibit distinct enhancement that is measured from the high Sr_{EF} value. The Fe and Mn content is comparatively enriched

in rippled facies and even more at chevron and hummocky cross-stratified facies. The shellbank sediments exhibit relative enrichment in phosphorus (P) and sulphur (S) along with MREE and demonstrate elevated values for the P/Ti ratio with respect to all other facies (Fig. 4.4). The shellbank sediments record a consistent depletion in LREE concentration (Fig. 4.6g). The Ni/Al ratio selectively increases within the shellbanks. The dark coloured muddy matrix of this facies locally bears pseudomorphs of sulphide minerals. In the hummocky cross-stratified facies, chevron cross-stratified facies and shellbank facies, enrichment factors of paleoredox-sensitive elements, like V, Ni, Cr and U are distinctly higher than in other facies members of the entire Kallankurichchi Formation (Table 4.1). Enrichment factors of Zn, Co and Ba are also distinctly higher. Fe_{EF}, Sr_{EF} and Mg_{EF} are also greatly enhanced in facies association II, whereas enrichment factor of Zn, Cu, Co, Ni and V significantly increases within shellbank facies (Fig. 4.5).

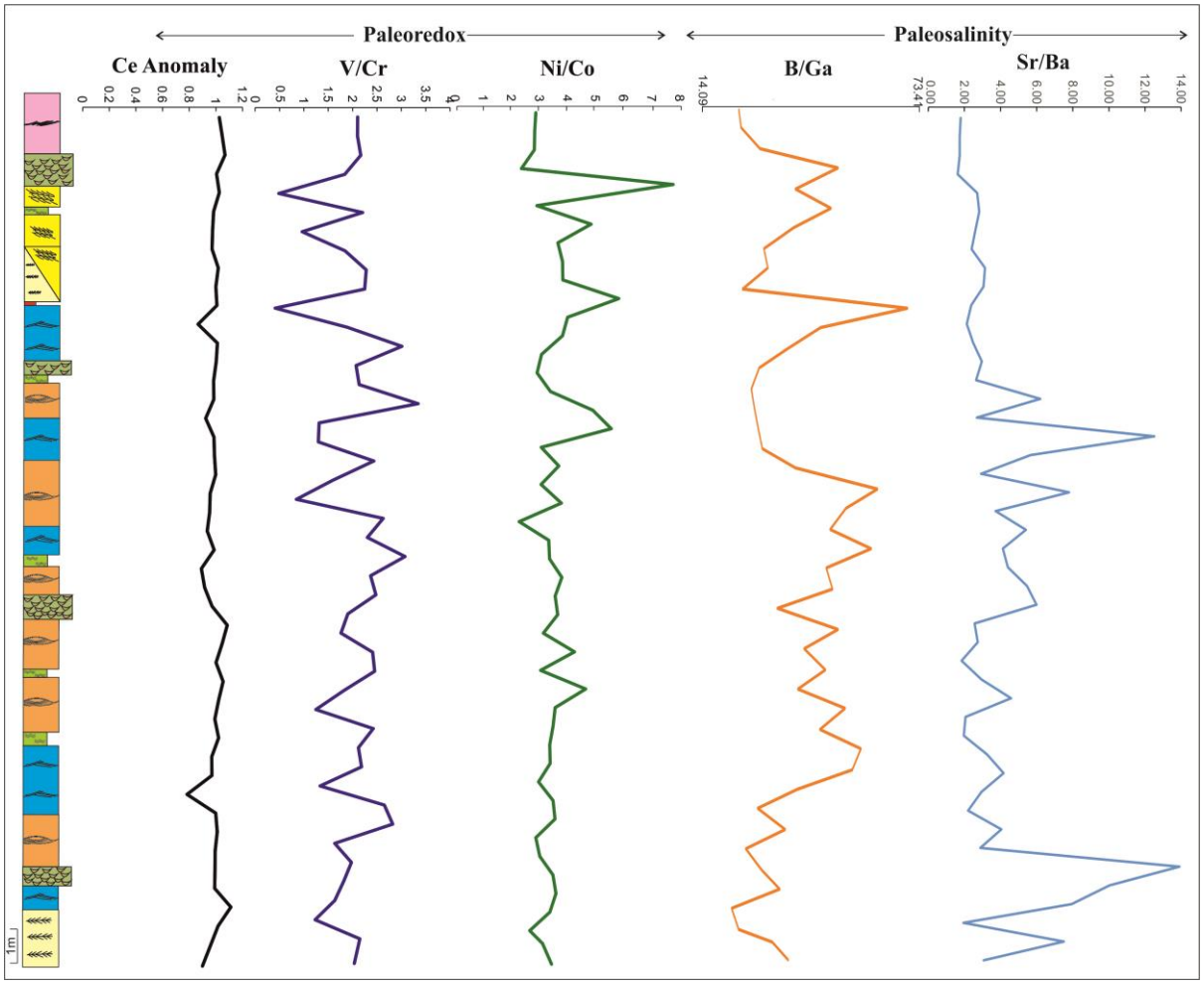

Fig. 4.3 Variation of paleoredox (Ce anomaly, V/Cr, Ni/Co) and paleosalinity (B/Ga, Sr/Ba).

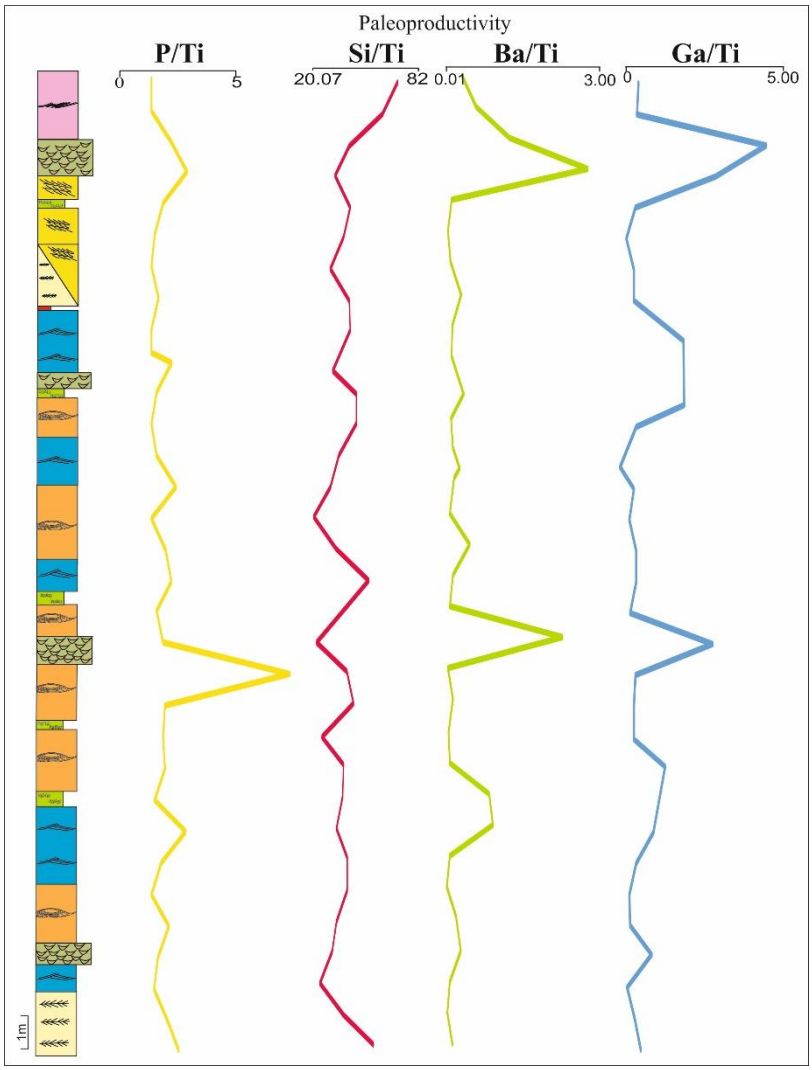

Fig. 4.4 Ratios used for Paleoproductivity proxy for this litho section.

This facies is depleted in V, Ni and Cr, while comparable in U contents with respect to the same standard. The Sr content of this facies association exhibit distinct enhancement that is measured from the high Sr_{EF} value. The Fe and Mn content is comparatively enriched in rippled facies and even more at chevron and hummocky cross-stratified facies. The shellbank sediments exhibit relative enrichment in phosphorus (P) and sulphur (S) along with MREE and demonstrate elevated values for the P/Ti ratio with respect to all other facies (Fig. 4.4). The shellbank sediments record a consistent depletion in LREE concentration (Fig. 4.6g). The Ni/Al ratio selectively increases within the shellbanks. The dark coloured muddy matrix of this facies locally bears pseudomorphs of sulphide minerals. In the hummocky cross-stratified facies, chevron cross-stratified facies and shellbank facies, enrichment factors of paleoredox-sensitive elements, like V, Ni, Cr and U are distinctly higher than in other facies members of the entire Kallankurichchi Formation (Table 4.1). Enrichment factors of Zn, Co and Ba are also distinctly higher. Fe_{EF}, Sr_{EF} and Mg_{EF} are also greatly enhanced in facies association II, whereas enrichment factor of Zn, Cu, Co, Ni and V significantly increases within shellbank facies (Fig. 4.5).

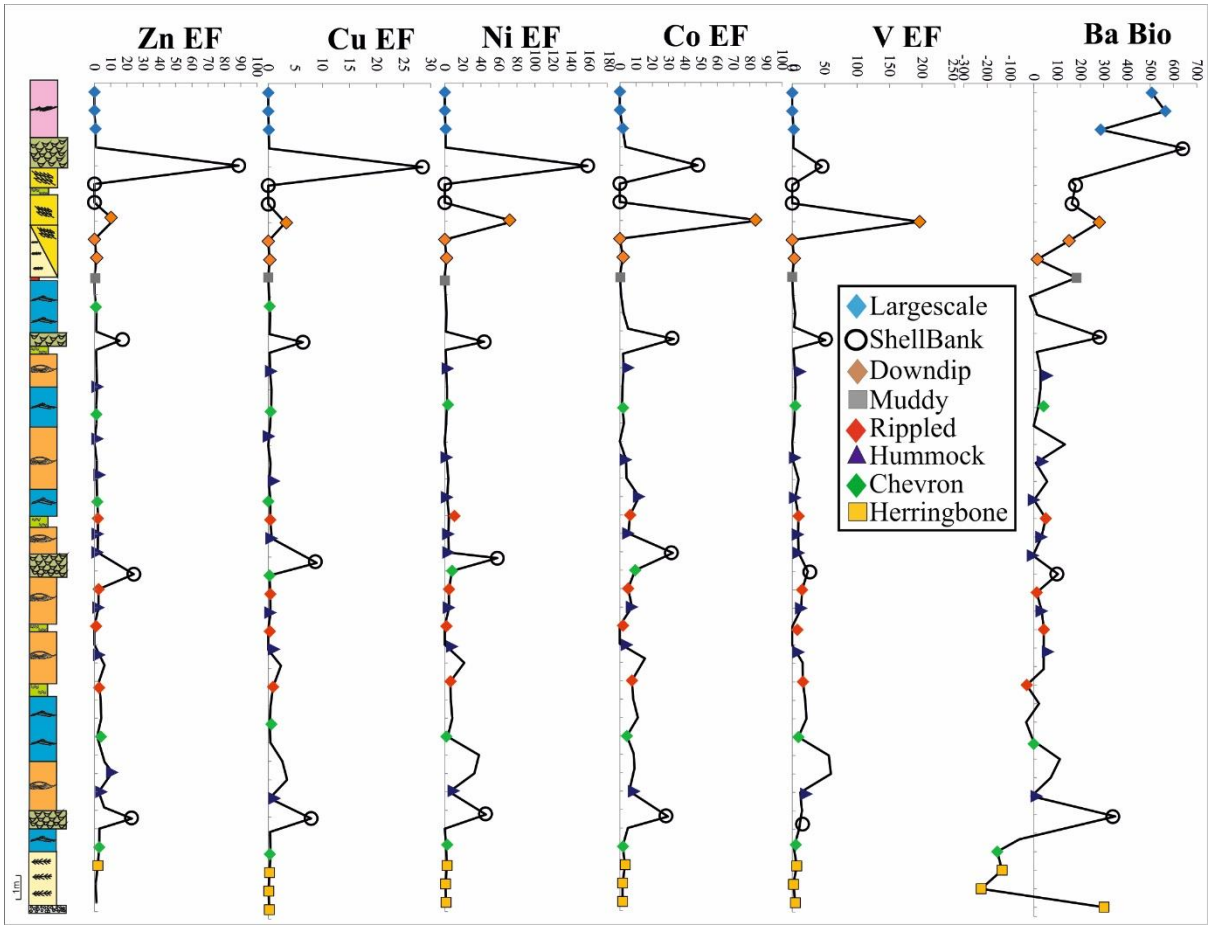

Fig. 4.5 Enrichment factors of selective elements (Zn, Cu, Ni, Co and V) and $Ba_{(Bio)}$ used as proxies to determine the paleoproductivity.

4.2.3 Facies Association III:

The facies association overlying the facies IIF is a sandy calcarenite. This facies is over largely cross-stratified. Mineralogically though it is calcarenite but facies is dominated by siliciclastic grains. The grains are haphazardly oriented, though overall there is an increment in both size and number of quartz grain. This facies contains terrigenous grains approximately 41% by volume. The concentration of terrigenous grains increases upward and reaches around 44% by volume. This facies is overlain unconformably by the Kallamedu Sandstone Formation.

Sample Name	Facies	Ni/Co	V/Cr	U/Th	Ce/Ce*
TC/UL3	Largescale cross-stratified	1.21	2.13	0.08	1.026
TC/UL2		1.17	2.13	0.07	1.047
TC/UL1		1.15	2.20	0.06	1.07
TC/UIF		0.62	1.87	0.14	1.01
TC/F1	4th Bank Matrix	7.89	0.52	0.17	1.03
UL3/F2A		1.26	2.24	0.13	0.98
UL3/F2		3.50	0.99	0.17	0.98
UL2/F1		2.12	1.87	0.10	0.97
TC/UF2B	Downdip cross-stratified	2.32	2.31	0.11	1.000
TC/UF2A		2.33	2.28	0.12	1.00
TC/L0		4.65	0.44	0.13	1.01
DC/MH1	Massive Muddy Facies	2.53	1.92	0.18	0.87
TC/MHL2		2.32	3.04	0.10	1.01
TC/MH1b		1.45	2.10	0.30	1.00
TC/MH1a		1.27	2.17	0.34	0.98
TC/MH1		1.82	3.37	0.19	0.98
DC/MH3		3.57	1.34	0.08	0.92
DC/MH2		4.34	1.33	0.10	0.99
TC/MHL3		1.44	2.47	0.09	0.99
UL1/F1	3rd Bank Matrix	2.17	1.63	0.11	1.00
UL1/WL	Rippled Facies	1.43	0.87	0.45	0.96
UL1/UF		2.27	2.66	0.22	0.95
TC/PZ	Hummocky cross-stratified Facies	0.52	2.33	0.30	0.93
UL1/F2	Chevron cross-stratified Facies	1.75	3.11	0.14	0.99
UL2/LSH	Hummocky cross-stratified Facies	1.78	2.40	0.12	0.89
UL2/SH1		2.29	2.51	0.09	0.92
UL/UF0	Chevron cross-stratified Facies	2.01	1.93	0.12	0.97
UL/OI	Rippled Facies	2.12	1.79	0.06	1.09
UL1/SH1	Hummocky cross-stratified Facies	1.53	2.44	0.10	1.05
UL/F1	2nd Bank Matrix	2.82	2.48	0.12	1.00
UL/SB1		1.41	1.86	0.17	1.05
UL/SB		3.28	1.28	0.22	1.02
ML2/UF2A	Rippled Facies	2.01	2.45	0.31	0.99
ML2/SH1	Hummocky cross-stratified Facies	1.93	2.15	0.09	1.02
ML2/UF1	Rippled Facies	1.79	2.21	0.09	0.97
ML1/SH1	Hummocky cross-stratified Facies	1.81	1.36	0.10	0.97
ML/F	1st Bank Matrix	1.32	2.68	0.11	0.78
LL/F1		1.93	2.85	0.16	1.00
ML1/UF1	Chevron cross-stratified Facies	2.01	1.66	0.12	1.01
LL1/UF1	Herringbone cross-stratified Facies	1.38	2.00	0.11	0.99
D/CB3		1.92	1.85	0.14	0.99
D/DL1		2.04	1.66	0.20	0.99
D/DL2		1.79	1.26	0.21	1.11
D/DL3		0.96	2.18	0.15	1.02
D/DL4		1.73	2.11	0.06	0.95

Table 4.6 Ratios used for Paleoredox proxies (all values are in ppm) following the stratigraphy of the studied formation starting from the lower Herringbone cross-stratified Facies to topmost Largescale cross-stratified facies.

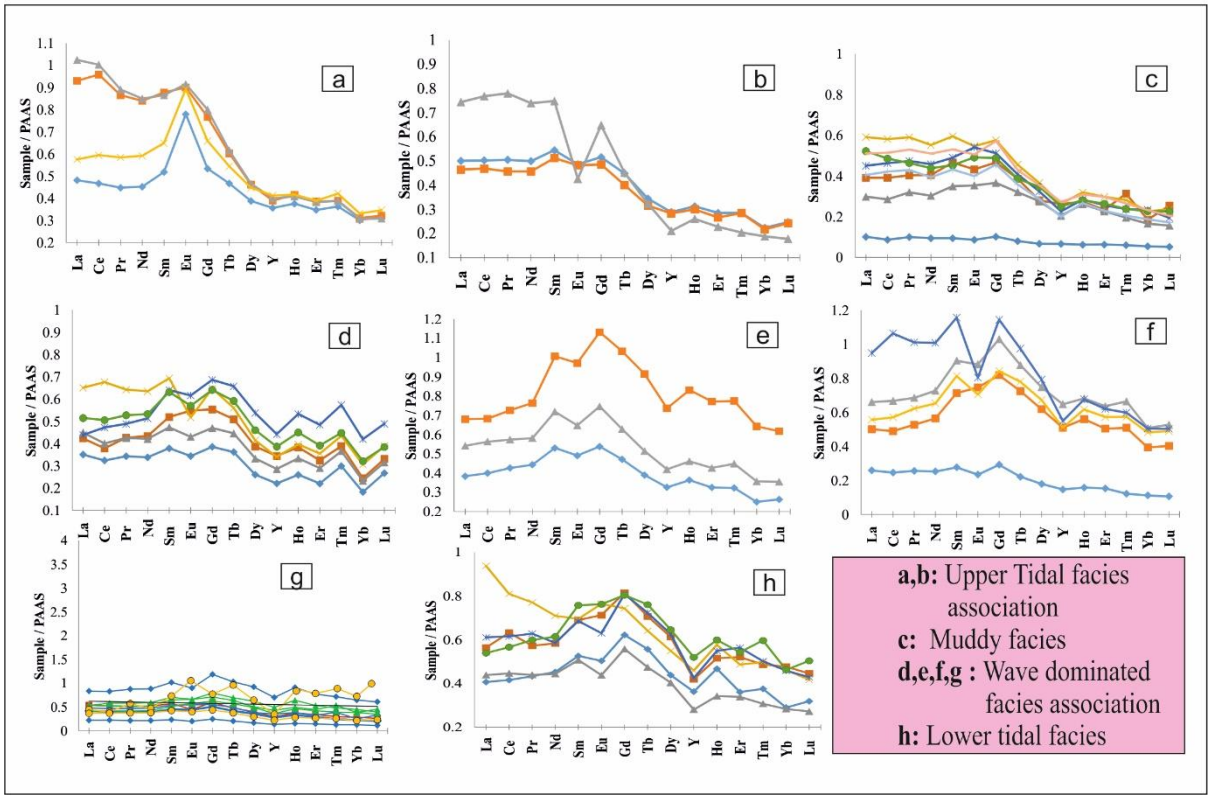

Fig. 4.6 REE distribution pattern throughout the formation (Srimani et al., 2022a).

The trace element distribution pattern in facies associations III is HREE-depleted and in some cases MREE-dominated. The calculated Ce anomaly (Ce*) values varies from 0.78-1.11. On the other hand, Eu_{EF} values vary between 0.07 to 2.2, again selectively enhancing significantly within large-scale cross-stratified facies, which is in upper stratigraphic positions (Fig. 4.2). Salinity value is lowering again (B/Ga value varies between 14.09-21.5) because of shallowing. The Ba_{bio} value is lesser compared to other facies, which indicates that the low paleoproductivity in this facies (Fig. 4.5).

4.3 Discussion:

As a whole the bulk rock geochemistry shows that, the immobile trace elements such as Y, Th, Zr, Hf, Nb, and Sc are less. These elements are considered as effective indicators for deducing the provenance of sedimentary basins (Bhatia, 1983; Bhatia and Crook, 1986) due to their limited residence time in seawater (Holland, 1978). Presence of these elements in

little amounts indicates less continental input. High Field Strength Elements (HFSEs) such as Zr, Hf, and Nb primarily originate from terrigenous sources. Additionally, the little presence low concentration of Th indicates minor influence of clastic contaminants. The ferromagnesian trace elements e.g., Pb, Zn, Cr, Cu, Ni, Co, V, Sc and Ga are good provenance indicators. The higher content of these elements indicates a mafic provenance (Madhavaraju, 1996) or there may be some mafic influences (Madhavaraju and Lee, 2010).

The compositional differences between the primary matrix and the early diagenetic fabric-selective calcite crystals indicate that the calcitization process apparently involved expulsion of Fe, Mn, Mg and commonly also Al (Fig. 4.1). The dark grey limestone (facies Ib) reveals higher salinity (B/Ga) and Y/Ho fractionation than the rest of facies suggesting greater input of water from the open sea. Comparatively lower value of Ni/Al indicating slightly higher rate of sedimentation in this part.

The initial low B/Ga values 20.8 in Facies IIA point to low paleosalinity close to the shore, apparently because of the influx of fresh water (Fig. 4.3d). This limestone facies contains significant amount of sand-sized siliciclastic grains, 22% by volume on average, indicating substantial terrestrial influence on its own accord. Quartz content gradually decreases upward. The restricted environment of deposition favoured slow rate of deposition, as indicated by presence of oxidized clasts, repeatedly bored fossils, and compositional difference between mud within and without the shell cavities. The low U/Th values 0.15 further corroborates the low rate of sedimentation. The micritized rims around the allochems restricts the depositional environment to the photic zone, although that could extend up to roughly 150 metres of water depth. The Fe content ~45000 ppm, more or less, equivalent to that of PAAS (McLennan, 2001) further suggests nearshore position of the depositional site (Vincent et al., 2006). However, high and widely fluctuating positive values of FeEF (up to 8.1) suggest local presence of substantial amount of authigenic Fe. On the contrary, the substantially high Mn content with respect to the standards used and its wide variability (9.0-30.9) suggest reductive dissolution and reprecipitation at O_2-H_2S boundary. However, generally low content of V, Ni and Cr suggests an overall oxic nature of the seafloor (Morford and Emerson, 1999). Overlapping values of U with respect to that of PAAS indicates subsurface reduction of sediments under the sea, because the element precipitates

when seawater sinks into the substratum. Lack of correlation in between Fe and Ti, suggests that the major bulk of Fe was not derived from land (Fig. 4.7).

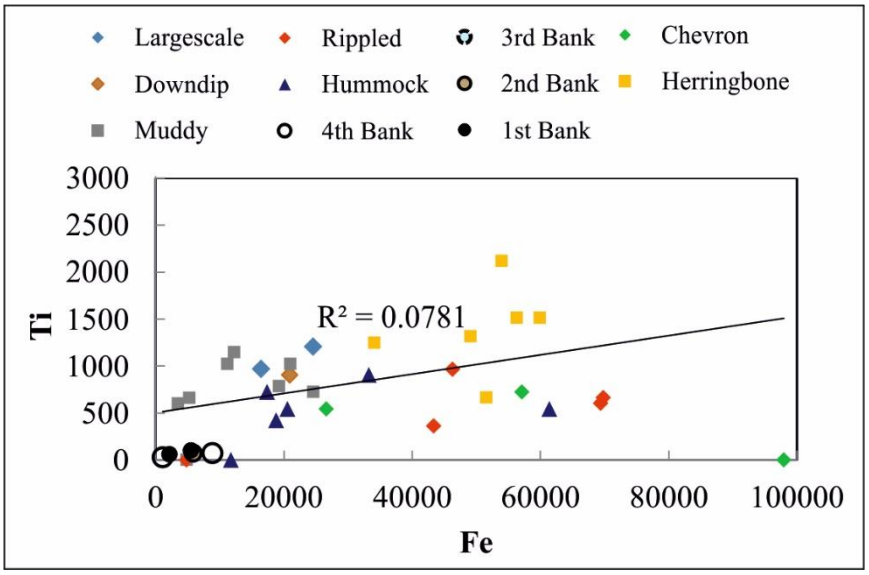

Fig. 4.7 Cross plot between Fe and Ti. Note the lack of correlation.

Very low value of U/Th, in this juncture, possibly suggests additional supply of terrestrial material than what the basinal hydrodynamics permitted. Low content of paleoredox-sensitive elements indicate that the basin-floor had, at best, been dysoxic (Tribovillard et al., 2006). In that condition Mn possibly dissolved and reprecipitated in shallow subsurface. The basin-margin likely have been flooded during the storms to pick up additional siliciclastic load. The shellbanks had apparently been enriched in phosphorus and sulfur. The dysoxic redox condition possibly resulted in organic matter enrichment in sediment and stagnation at the depositional site of the facies association II during fair-weather periods (Table 4.6). Gradual increase in B/Ga values from facies association I to II indicates gradual increase in paleosalinity (Wang et al., 2020; Wang et al., 2023b), suggesting greater supply of water from the open ocean. The facies IIf seems to be product of a mud slurry, formed presumably at the seaward margin of the shelf lagoon within which facies II, as a whole, was deposited. Omnipresent *Miliolina* and *Textularia* point to a restricted shallow marine body, like a lagoon, as the depositional environment of the facies association II (Chan et al., 2017; Hussain and Chaudhury, 2023. The mud slurry of facies IIf might have been induced by an exceptionally strong storm on a slope immediately beyond the seaward lagoon-margin. The maximum Y-Ho fractionation apparently took place at the interior of the putative

lagoon (Fig. 4.8). Similar accentuation of fractionation of, Ga and Al, another 'geochemical twin', released together during weathering, also recorded in the same facies association II. If we consider selective increase in paleosalinity in facies association II together with this observation, it appears that the restricted marine body possibly formed behind a bar. Probably increased sea-floor temperature because of restricted environment facilitated growth of the shellbanks dominated by rudist bivalve *Gryphea*. However, irrespective of their stratigraphic positions the geochemical properties of the shellbanks remain same.

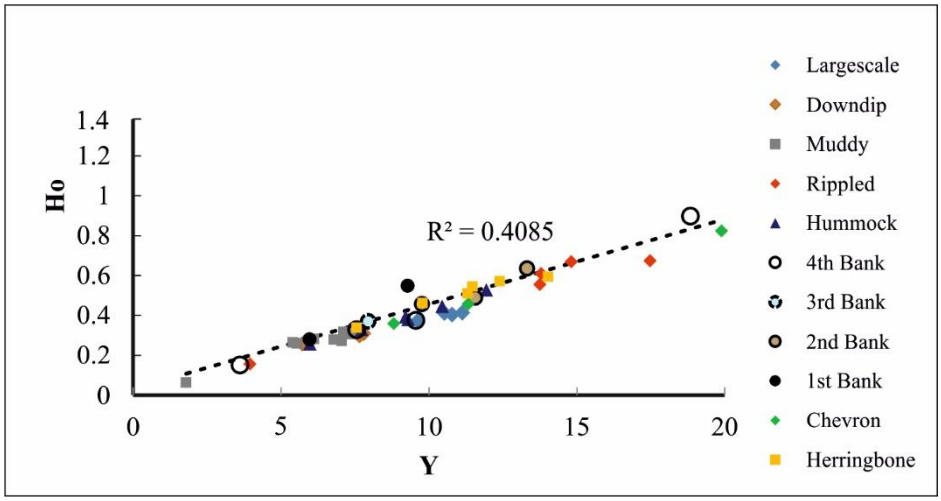

Fig. 4.8 Cross plot between Y and Ho.

Facies association III is depicted by substantial influx of terrigenous grains, 41% by volume, indicating nearshore position. The depositional environment of the fourth shellbank is presumably the same as the shellbanks in the facies association II. Facies IIID represents a barrier bar, close to the shore. Facies association II and III are generally LREE-rich. However, some of the facies, especially the shellbank facies, irrespective of association, are MREE enriched (Fig. 4.6). High P/Ti selectively within the shellbanks point to high potentiality for productivity (Debruyne et al., 2015). Ce/Ce* ratios in the facies associations II and III are invariably less than 1.0 (Fig. 4.3a), reflects depletion of Ce in seawater, as it is expected in oxic environment (Tostevin et al., 2016). The redox-sensitive elemental ratio, V/Cr suggests frequent transitions between dysoxic and oxic paleoenvironments dominantly oxic (Fig. 4.3b). Apparently, the redox front declined in the former assemblage of facies. It is relevant to mention that Sr content in seawater increased significantly during the Late Cretaceous period (Antonelli et al., 2017). Demina et al., (2009), and Gallup (1998), reported

that biomineralization preferred incorporation of Ba, Rb, Sr, Pb, Co, Cd, Zn, Cu, Cr, Mn as obtained in the facies association II sediments. In the putative reductive condition Eu^{+2} had likely been dominant with respect to Eu^{+3} in the sediment. Eu^{+2} is also favoured with respect to Eu^{+3} because of its comparatively simpler isomorphous substitution of Ca (Sverjensky, 1984). Eu^{+2} is further favoured because of weaker Eu-O bond in aqueous solution (Canaval and Rode, 2015). High EuEF values in the facies associations II and III with recognized clay imprint strongly corroborates dominance of Eu^{+2} (Tostevin et al., 2016).

4.4 Conclusion:

The exceptionally low Mg content (<0.3%) and elevated Mn concentrations (201-912 ppm) (Fig. 4.9) validate the initial precipitation of low-Mg calcite (Rao and Naqvi, 1977; Williams, 1979). The low ratios of Mn/Sr, Fe/Sr, and Ca/Sr suggest minimal post-depositional alteration. Changes in redox condition do not impact magnesium and strontium concentration (Tucker and Wright, 1990), while diagenesis have a huge impact on the concentration of Mg and Sr. The large ion lithophile elements e.g., Rb are generally in low concentration within the limestone. Strontium is considered the primary trace element in carbonates due to its efficacy as a facies indicator (Veizer and Demovic, 1974). It has been extensively utilized for interpreting depositional environments and diagenetic modifications. In carbonates, high Mg-calcite contains from 1000-4000 ppm of Sr (Kinsman, 1969) and 242-465 ppm for low Mg-calcite (Robinson, 1980). The total REE contents in pure carbonates are generally very low. If the carbonates contain significantly higher concentrations of Y, Zr, and Rb, it indicates a greater input of continental detritus from near-shore setting (Frimmel, 2009). Because elevated REE concentrations may arise from the contamination of sulphides, silicates or oxides primarily sourced from hydrothermal activity or terrestrial particulate matter, resulting in distinct REE+Y patterns (Frimmel, 2009).

In-depth geochemical analysis serves as a critical adjunct to reconstructing paleoenvironments, deciphering paleo-redox dynamics, and delineating salinity conditions across diverse facies associations. Within the Kallankurichchi Formation, distinct patterns emerging the presence of light rare earth element (LREE) and medium rare earth element (MREE) enrichments in tide-dominated and wave-dominated regions respectively. Notably,

the lowest rare earth element (REE) content coincides with the maximum flooding surface (MFS), indicating deposition in the most distal paleogeographic settings. Insights from paleoredox data reveal anoxic conditions prevailing in the lower stratigraphic levels, contrasting with the oxic conditions prevalent in the wave-dominated middle portion, which enhance the proper condition for the growth of the rudist bivalves and other organisms. B and Ga value suggests its marine environments (Fig. 4.10) (Wei and Algeo, 2020). Additionally, a progressive rise in paleosalinity is discerned with the deepening of facies, exemplified by the relatively lower salinity index within tidal facies, reaffirming their closer proximity to the shorelines.

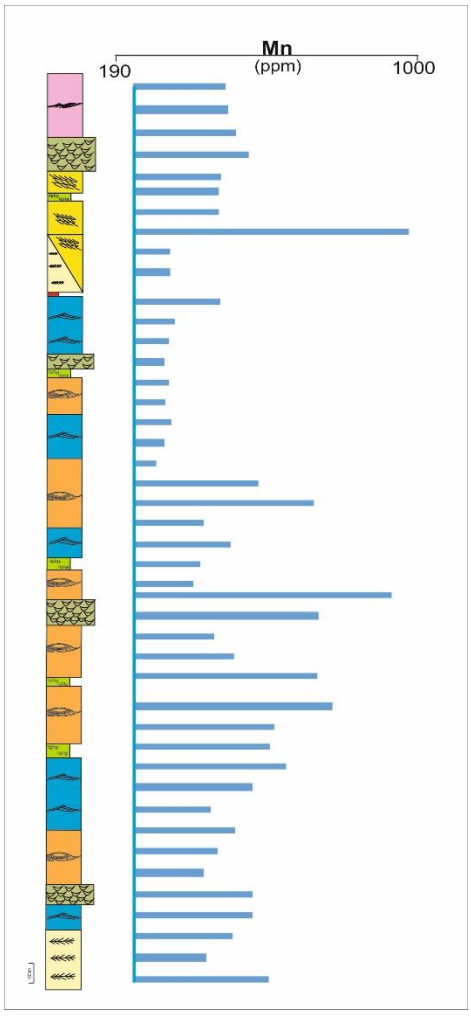

Fig. 4.9 Mn concentration throughout Kallankurichchi Limestone Formation.

Petrographic and geochemical analyses serve to reinforce the delineation of lithofacies, contributing to a more nuanced understanding of the geological processes at play.

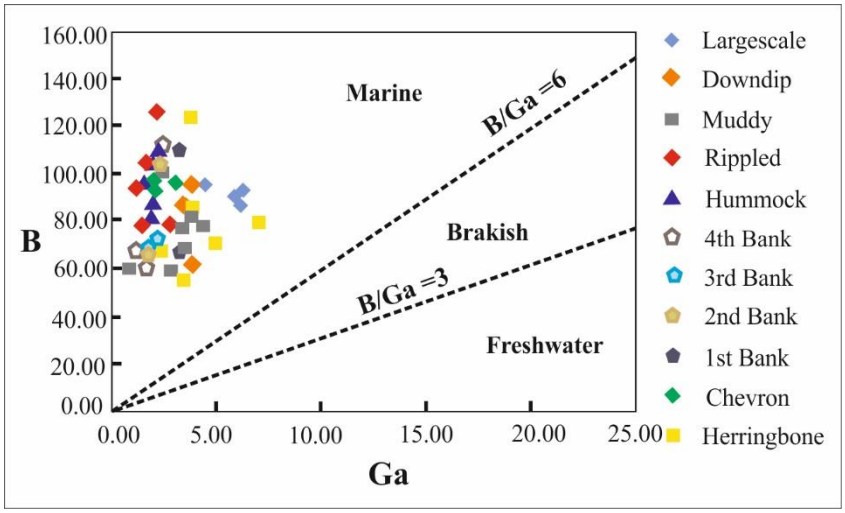

Fig. 4.10 Cross plot of B and Ga value. Note, its marine environment (after Wei and Algeo, 2020).

CHAPTER-5

SEQUENCE DEVELOPMENT

5.1 Introduction:

The sequence refers to a series of genetically related strata arranged in a relatively conformable manner, delineated by unconformities or their correlative conformities (Sarkar et al., 1998; Catuneanu, 2006; Catuneanu et al., 2011). In the geological record, a fining-upward succession is interpreted as a transgressive sequence, formed when rate of relative sea level (RSL) rise is higher than the sedimentation rate, indicating by progressive deepening and characterized by thinning and fining upward packages and termed as a transgressive systems tract (TST, retrogradational stacking pattern). Conversely, when the rate of rise in RSL decreases so much as to be superseded by the rate of sedimentation, progradation results and generally a thickening and coarsening upward trend develops (Sarkar et al., 2005). The transgression may also remain confined to a transgressive lag only, if erosion prevails during the entire phase of transgression, not allowing the TST to form. This progradational succession developed above a transgressive systems tract or a transgressive lag is designated as a highstand systems tract (HST, progradational stacking pattern). On the top of the TST, immediately under the HST, would be the Maximum Flooding Surface (Frazier, 1974; Posamentier et al., 1988; Van Wagoner et al., 1988; Galloway, 1989). It is a surface that marks a change in shoreline trajectory from transgression to highstand normal regression. Alternative terms include final transgressive surface (Nummedal et al., 1993); surface of maximum transgression (Helland-Hansen and Gjelberg, 1994); maximum transgressive surface (Helland-Hansen and Martinsen, 1996). When multiple sequences stack up basin-wide, they form a megasequence. This study aims to provide a comprehensive overview of the sequence development history of the entire Kallankurichchi Formation within the Cauvery Basin.

5.2 Sequence Stratigraphic Framework:

The Kallankurichchi Formation within the Cauvery basin is a partly developed sequence. The upperpart of the Formation is clearly demarcated by an unconformity formed in between the topmost part of the marine Kallankurichchi Formation and fluvial Kallamedu Formation (Fig. 5.1). In the lowermost part of the studied formation, facies association I is

difficult to accommodate within this partly developed sequence, but a well-developed transgressive lag deposit present at places clearly demarcated the boundary of the Kallankurichchi Formation from that of the underlying Sillakuddi Formation (Fig. 5.3a). However, earlier workers designated this scree and associated sediments (possibly they have considered the transgressive lag as well) as basal conglomerate and considered as unconformity (Ramkumar, 2009; Nagendra et al., 2011, 2018). But during the present study the author observed their occurrences in successive stratigraphic levels and presence of numerous carbonate debris, fossil clasts along with coarse siliciclastics (Fig. 5.2), disregard their status as basal conglomerate. Even the identification of maximum flooding surface likely to be the shell beds which are also occurring at different stratigraphic levels. The shellbeds identified as shellbanks (Fig. 5.3b) likely to be deposited in calm and quite conditions (possibly behind the bars) and the geochemical study also supports the idea.

A succession of facies can be traced from facies association II to III, while facies association I is a lateral input from the graben flank that takes no part in the succession dealt herewith. The facies association II is fining upward and is recognized as a transgressive systems tract (TST). The upward transition from the calcarenite to lime-mudstone within facies association II is a transgressive systems tract. The top of the TST is demarcated by a thin layer, which is characterized by a laterally persistent thin muddy surface (~15 cm) likely to be denoted as the Maximum Flooding Surface (MFS; Fig. 5.3c). Facies association II transits upward to siliciclastic-rich facies association III and thereby depicts the latter as a HST that eventually terminated by an unconformity (Srimani et al., 2021; Chakraborty et al., in press). Shallowing upward parasequences marked by chevron cross-stratification/large-scale cross stratification at the base and ripple drift cross-lamination at top have been identified during the present study. But theses cycles are often disturbed by the storm layer which is also difficult to accommodate within the parasequences.

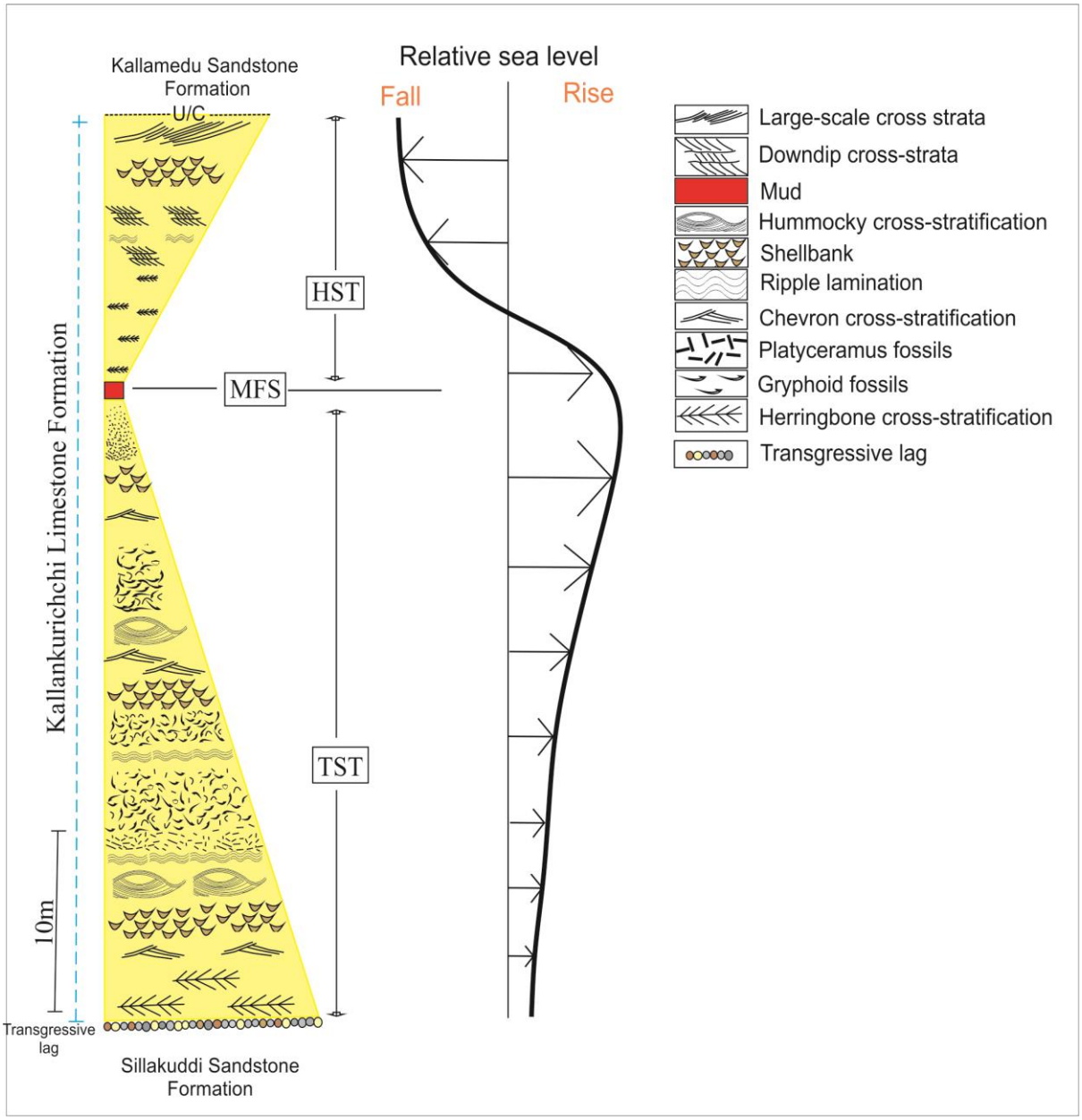

Fig. 5.1 Representative section of Kallankurichchi Formation showing systems tracts. Initiated with transgressive lag and also note the unconformity between Sillakuddi and Kallankurichci Formation. The transgressive systems tract (TST) overlain by highstand systems tract (HST) with a maximum flooding surface (MFS) in between.

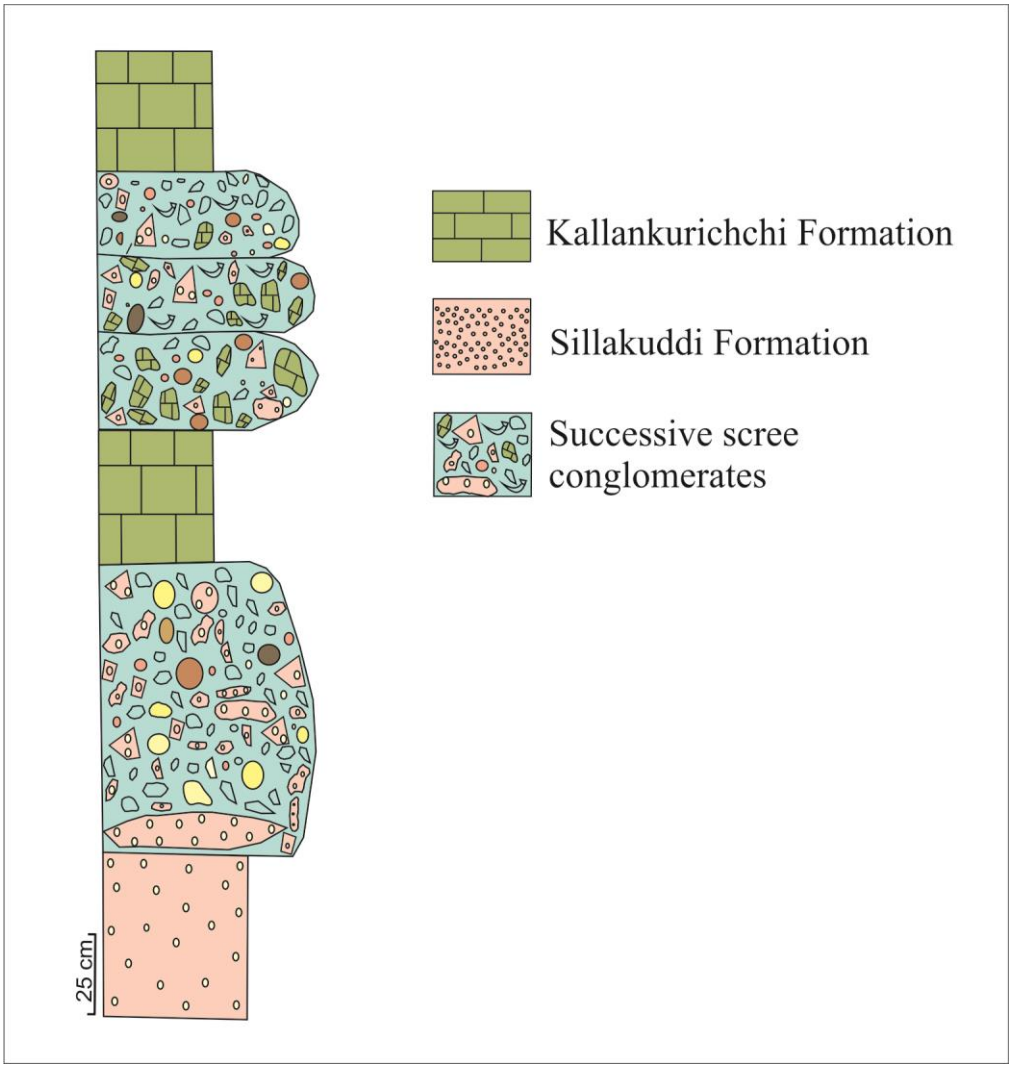

Fig. 5.2 Occurrence of conglomerates at successive stratigraphic levels and presence of numerous carbonate debris, fossil clasts along with coarse siliciclastic.

The Kallankurichchi Limestone Formation, famously rich isn marine fossils, built up on the siliciclastic Sillakuddi Formation following a major transgression of the sea. The Kallankurichchi Formation of Ariyalur Group preserves a transgressive systems tract (TST) followed by highstand systems tract (HST). The top surface, that bound this sequence is marked by a sharp basinward shifting of continental-dominated facies. The cycle is composed of transgressive–regressive sub-cycle, are readily distinguished in field. A well sorted conglomerate characterized by well-rounded pebbles of granite and sandstone, and marine fossils at its top makes strong erosion under prolonged to-and-fro wave motion evident before the onset of carbonate deposition. The primary deposition occurred during locally renewed

basin rifting (Srimani, 2024) and post-rift phase of the basin (Watkinson et al., 2007). In the constricted intracratonic basin tide had dominated initially. Ere long it gave way to wave as the relative sea level continued to rise. Terrigenous influx steadily dwindled through time. The depositional system is mainly marine-dominated, and show well-defined records of

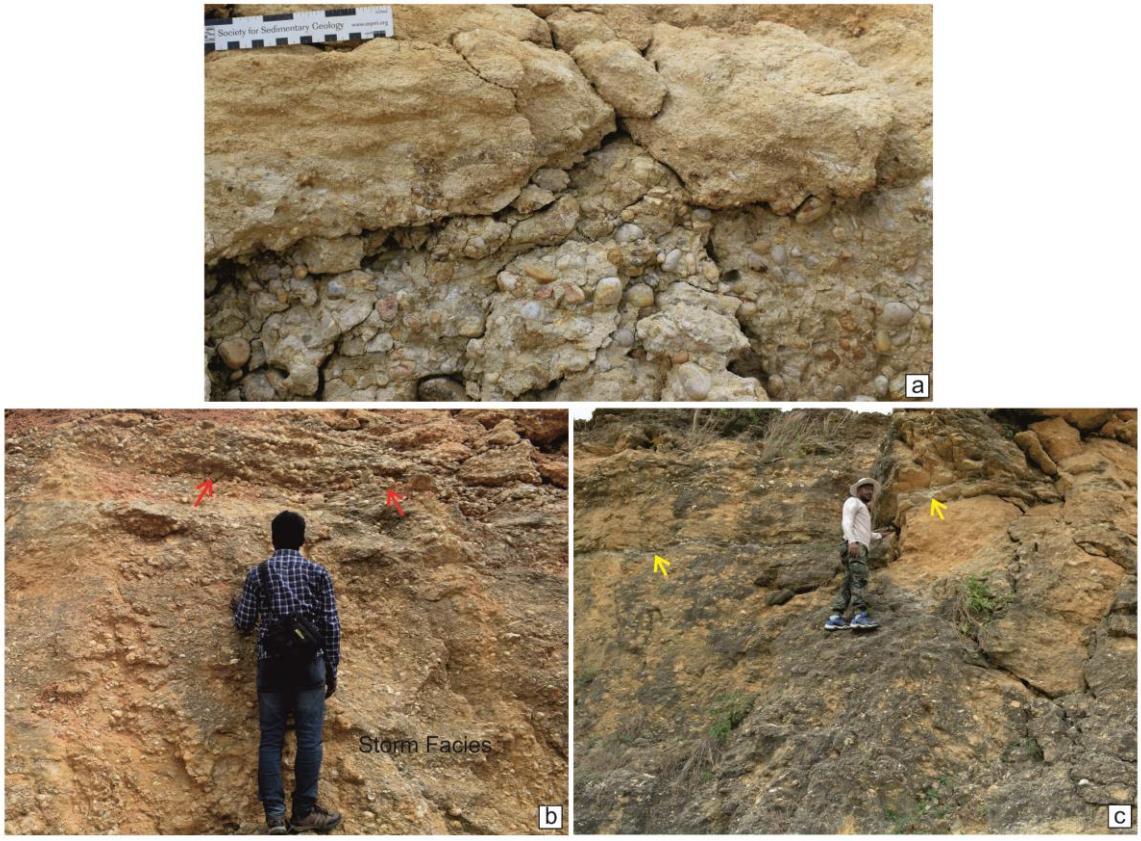

Fig. 5.3 Significant facies for sequence stratigraphic framework: Transgressive lag (a); shellbank (red arrowed) (b); muddy facies (yellow arrowed) (c).

cyclic sea-level change. This cycle was a product of the interaction of eustatic oscillations, rift related extension tectonics and thermal subsidence, and seeks attention for sequence stratigraphic studies of the sedimentary record in the basin. In consequence both the fair-weather and storm deposits alternated, although the latter largely escaped reworking by fair-weather waves because of basin constriction. The restricted basinal setting favored growth of colonies of sedentary bivalves and bryozoa in profusion with addition of other marine invertebrates, like brachiopods and ammonites. Overall, the transgressive systems tracts are mainly composed of offshore lime mud deposits incorporating maximum flooding surface (MFS), though the basal part is disturbed by intrabasinal tectonics. At the deepest part of the

depositional basin features of restricted marine circulation is evident. The transgressive systems tract culminated with a thin carbonate mudstone with well-preserved very delicate long chains of encrusting bryozoa as a dominant constituent. The highstand systems tract is mainly consists of a mixture of offshore siliciclastics and carbonates, transitioning upwards into progradational fluvial deposits of Kallamedu Sandstone Formation. The highstand systems tract on top of the maximum flooding surface is again replete with tidal features, similar biotic elements and terrigenous quartz flux.

Carbonate sedimentation initiated on shallow shelf gradually developing a widespread carbonate ramp. The platform holds the record of a rapid marine transgression and the transgression probably was induced by tectonics. Carbonate deposition initiated just above the Sillakuddi Sandstone Formation and it continued after the phase of tectonic interference i.e., even after conglomerate depositions. Further above, the ramp became tidally influenced and overtook into a marginal-marine setting depositing the overlying Kallamedu Sandstone.

5.3 Detrital quartz distribution:

Away from the basin-margin detrital quartz occurs generally sparingly. Systematic measurements of frequency of occurrence (Fig. 5.4) reveal an interesting pattern of variation in the vertical section. From the base of the measured section quartz grains have been detected upward up to about 5 m. The frequency of occurrence of quartz grains decreases upward. Quartz grains are detected again at a level around 30m from the base of the measured succession, immediately above the non-recurrent muddy facies unit. From this level upward both median size and frequency of occurrence of quartz grains increase rapidly, more rapidly than their decreasing trend at the base of the measured succession. The non-recurrent very large-scale cross-stratified facies at the very top of the studied stretch is fairly rich in quartz, though not exceeding 50%. From the top of the muddy facies the succession is preserved up to about 19 m.

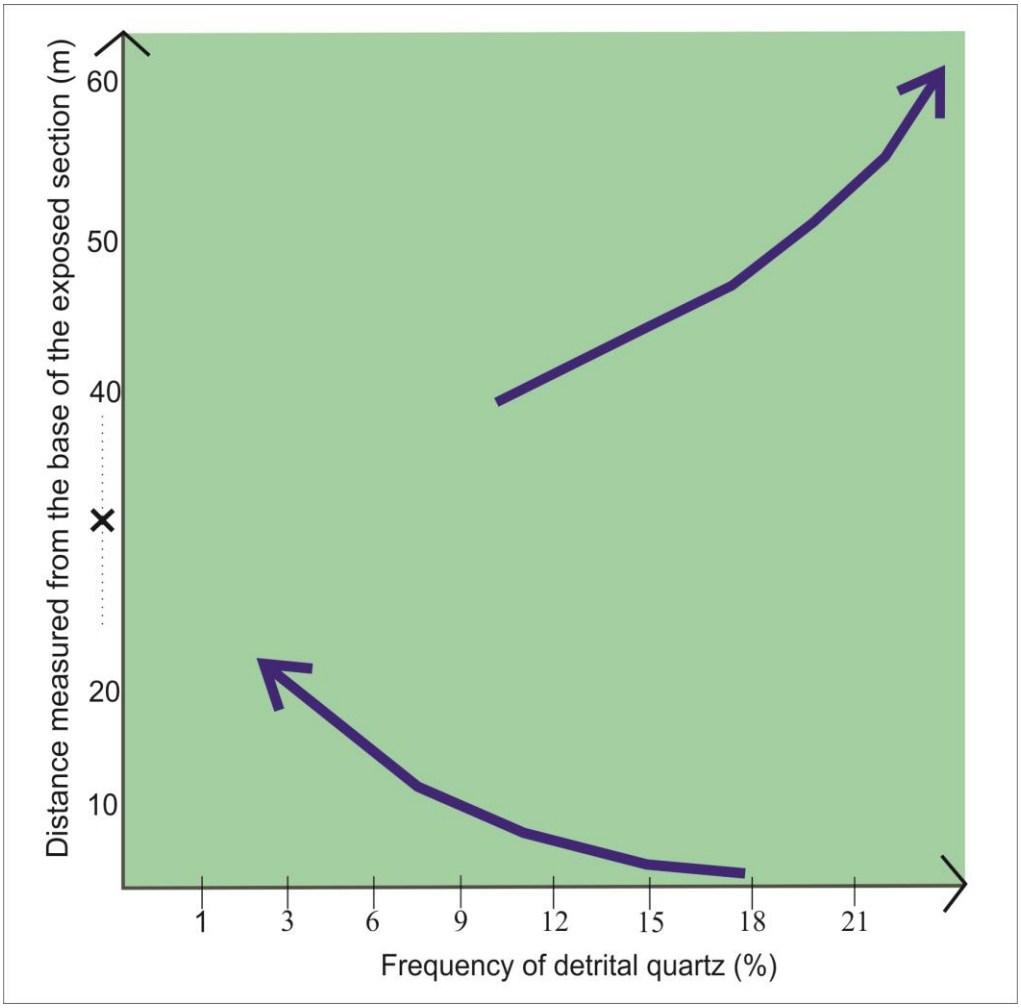

Fig. 5.4 Variation in frequency of occurrence of detrital quartz grains along the vertical stratigraphic section. Note the occurrence of quartz grains maximum in the lower and upper part of the tide dominated section.

5.4 Conclusion:

From the top of the well sorted siliciclastic conglomerate identified as transgressive lag, decrease in size and frequency of land-derived detrital grains strongly suggests progressive shift of paleogeography basinward. Further upward passage into a 25 m-thick vertical zone barren of detrital grains suggests further progressive deepening of the sea (Fig. 5.4). Paleogeographic shift further basinward is an imperative. This contention about progressive basin deepening is further corroborated by placement of the only muddy facies

on top of the quartz-barren zone likely to be the maximum flooding surface (MFS). From the putative transgressive lag to the muddy facies may, therefore, reasonably be recognized as a transgressive systems tract (TST). The sea encroached inland through narrow fault-bounded valleys. At the land-margin narrower valleys and coves between promontories tide had been accentuated at the expense of wave. With progressive deepening of the basin, wave became progressively dominant.

From top of the muddy facies quartz influx increases and detrital quartz grain-size also increases rapidly upward. The mode of sequence development resembles what is expected in highstand systems tract (HST). Tide regained its strength and outdid wave action in leaving their signature in sediments. The paleogeography and paleoenvironment of deposition of this Formation, and water depth variation through time during its sequence development. Stratigraphic cycles have been established to demonstrate fluctuations in the A/S ratio (accommodation rate/sedimentation rate) and reflecting changes in accommodation space.

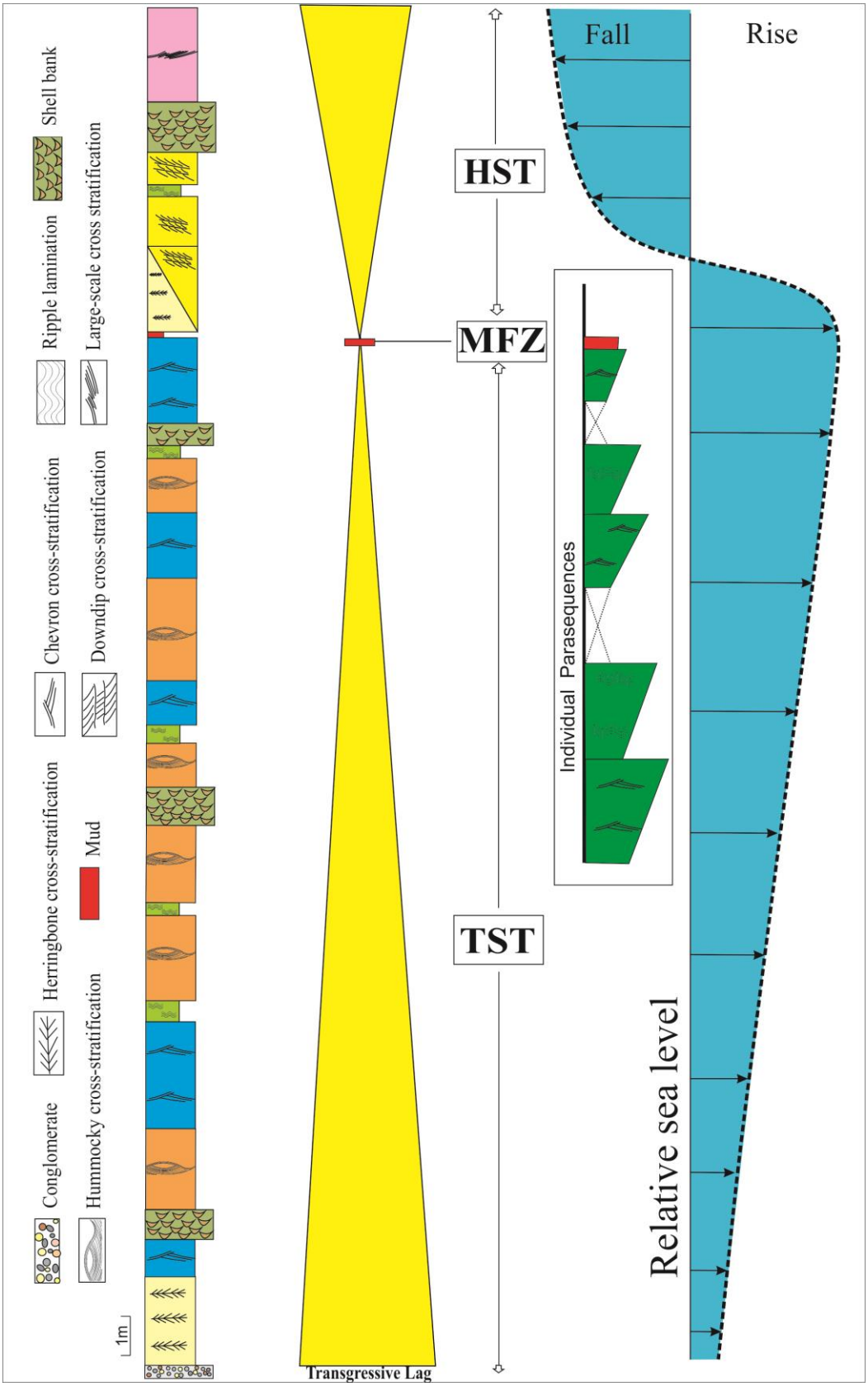

Fig. 5.5 System tracts and variation of relative sea level curve. Note, the parasequences inset.

PART- II

ASPECTS OF SPECIAL INTERESTS

CHAPTER- 6

SCREE CONGLOMERATES AND ITS DERIVATIVES

6.1 Introduction:

Conglomerates and its derivatives associated with basin margin sedimentary cones are always informative for deciphering the tectonic evolution of a sedimentary basin. Not only do these deposits record the initiation of new depositional events, but their lithology, facies, and internal organization also provide insight into basin subsidence, sea-level fluctuations, and the evolution of sedimentary sequences. Compared to siliciclastic basin margins, carbonate slope deposits are less well explored, although they have gained renewed interest for hydrocarbon exploration in recent years (Reijmer et al., 2015). Modern boulder cones are common, but their ancient counterparts in the rock record are rare (Dolnicki and Grabeic, 2022; Dong et al., 2022). In addition, the Upper Cretaceous was a particularly tectonically active period. The wedge-shaped layers of conglomerate, previously interpreted as basal conglomerates, named as Kallar conglomerate, marking the beginning of the Kallankurichchi Limestone deposit (Fig. 6.2; Nagendra et al., 2011, 2018; Nagendra and Reddy, 2017). Watkinson et al., (2007) considered the conglomerates as initiation of new sedimentation event after cessation of deposition of the underlying Sillakuddi Sandstone Formation. Ramkumar (1999) considered the conglomerates as channel deposits and coastal conglomerates considering their form, extent, geometry and petrographic characteristics. Kale (2011) pointed out this contradiction. During the present study, lenticular wedge-shaped conglomerate horizons were identified at multiple stratigraphic levels. Although conglomerates are concentrated in the basal part of the formation, they continue upwards as indicated by limestone and fossil clasts. These conglomerates are of mixed composition, containing both siliciclastic and carbonate clasts in a sandy matrix. The conglomerates are clast-supported and poorly sorted, with angular to subangular clasts, although rounded clasts are also present. They are haphazardly arranged, even sub vertical attitude with irregular lower boundary. The preferential occurrence of such cones in a passive margin setting makes them special because of their rare occurrences; nonetheless, slopes are being generated possibly because of subsidence, which may help to form sedimentary cones. These conditions readily induced slope failure and help to generate screes, debris-flows and related deposits. The occurrence of siliciclastic scree deposits in a carbonate-depositing environment is unique and rarely documented. Siliciclastic scree cones containing recycled clasts in a carbonate depositional environment requires detailed study. The present paper focuses on the

origin of these conglomerates and its derivatives based on detailed sedimentological output and correlated them with the then depositional milieu and basin tectonics. Thereby, this work will help to understand the proper cause of their generation and their role on the initiation of a carbonate platform on a siliciclastic platform. Thus, helps in assessment of the geodynamic evolution of the Cauvery Basin in the late stages of its development. There are controversial views regarding the depositional environment of this conglomerates. Several geoscientists published their understandings in different ways.

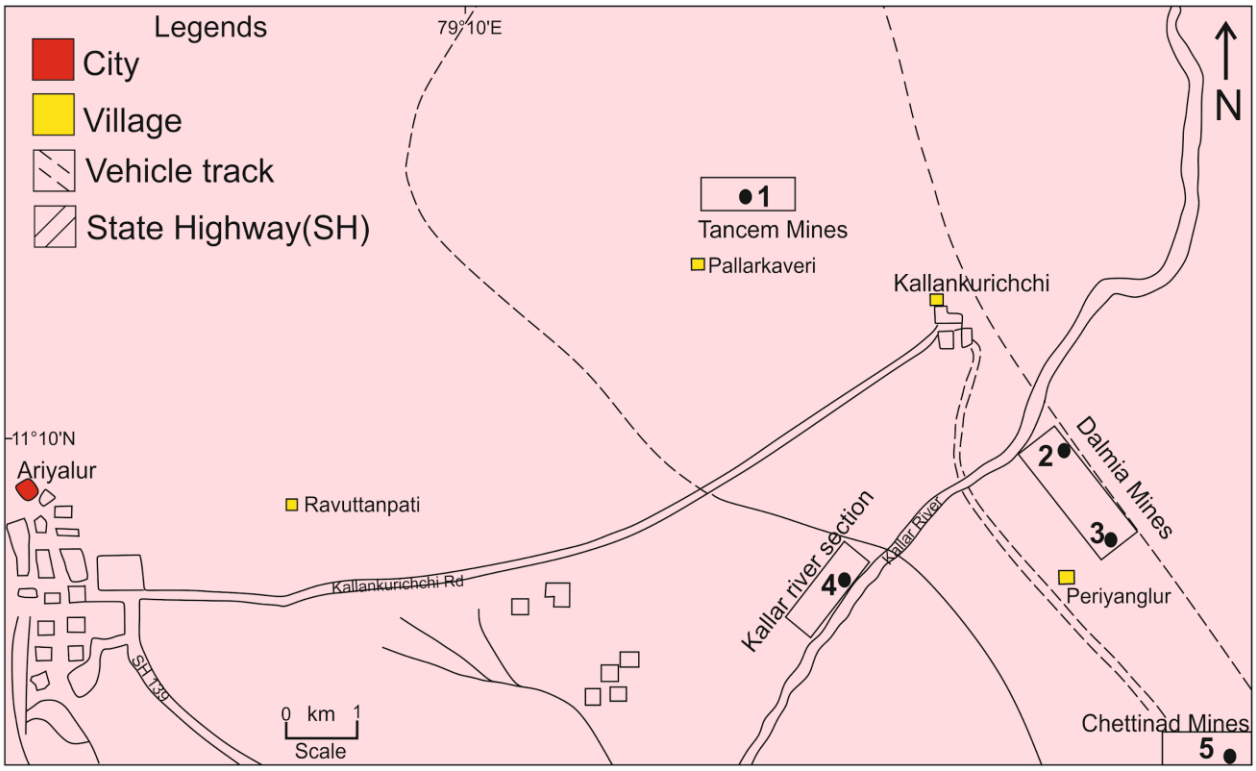

Fig. 6.1 Location map of the studied section. Note the rectangles with 1, 2, 3, 4, 5 mark the locations.

6.2 Conglomerates and their derivatives:

The conglomerate and its derivatives present at the basal 9m of the Kallankurichchi Limestone are consist of different types of clasts (Fig. 6.3a). The clast compositions of the

conglomerates and its derivatives varies from basement rock fragments, sandstone clasts, quartz pebbles to fossils and limestone clasts. The sandstone clasts present at the basal parts are mostly angular. The conglomerates and its derivatives contain sub-rounded to well-rounded clasts as well. Overall, the conglomerates are clast-supported in the basal part while they become matrix-supported towards the top part. The roundness of the grains is also accompanied by diminution in size of the clasts in successive beds (Fig. 6.3b). Interestingly, the coexistence of large angular clasts with relatively smaller rounded clasts at the basal part of the conglomerate horizon is common.

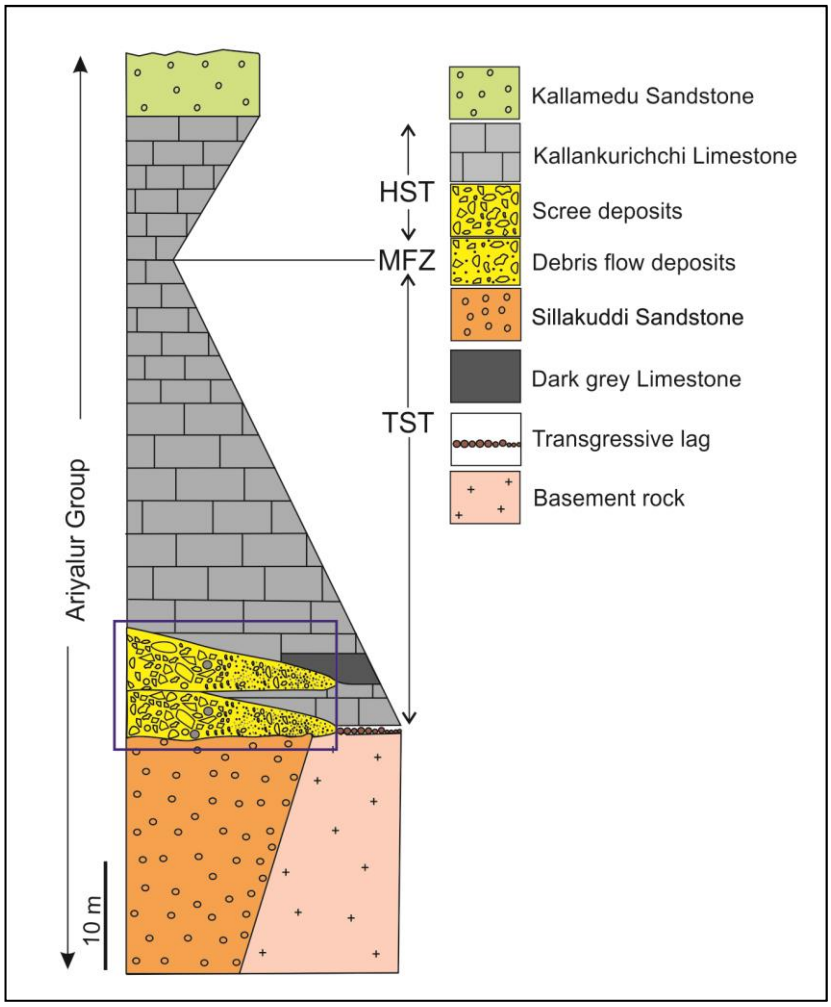

Fig. 6.2 Stratigraphic succession of the Ariyalur Group. Note the concentration of scree conglomerate and its derivatives at the basal part of the Kallankurichchi Limestone (marked area). Also note, two system tracts (TST: Transgressive systems tract; and HST: Highstand systems tract) and the MFS (Maximum flooding surface) demarcated within the Kallankurichchi Limestone.

The crudely developed normal and frequency grading along with the haphazard orientation of the clasts are common within the conglomerates. Crudely developed cross-bedding within some conglomerate beds are also present. All these features indicate that mass flow origin for the conglomerate. Two distinctive facies associations are recognized based on their geometry, nature of contacts, clasts shape, size, orientation of grains and matrix content. The term 'facies' is used here to reflect the depositional processes and proximity to the deposition with respect to the slope change during sedimentation (Bose and Sarkar, 1991). The relationships are interpreted with regard to the conglomerates and the delineated mass flow facies associations. The panel diagram shows the spatial distribution of the facies (Fig. 6.4).

6.3 Facies and Flows:

6.3.1 Facies Association A:

This facies association (Fig. 6.5) is consisting of coarser clasts than association B, concentrated at the basal part of the studied succession and composed of the following facies:

6.3.1.1 Facies A1: *massive clast-supported ungraded conglomerate facies*

The A1 conglomerate facies is best exposed in the area of the TANCEM mines (11°09.055′ and 79°05.819′). This facies is clast-supported and extremely poorly sorted, with interstices filled with sand-sized grains. The clasts are elongated, chaotically arranged, with some oriented sub-vertically, lying on top of other clasts (Fig. 6.5a). The facies are dominated by sandstone clasts. Besides, basement clasts, feldspar and some rounded quartz pebbles are also present. The larger sandstone clasts are mostly bed parallel, especially in the lowermost part. Some clasts are fractured and penetrate the substrate immediately below (Fig. 6.5b). They are rapidly wedging away from the contact and is only present at the basal part of the Formation. The clasts composition can be traced back to the underlying Sillakuddi Sandstone and the granitic basement. Most of the clasts are derived from the immediate underlying sandstone formation are angular and measure up to 60 cm in length, while the other clasts are

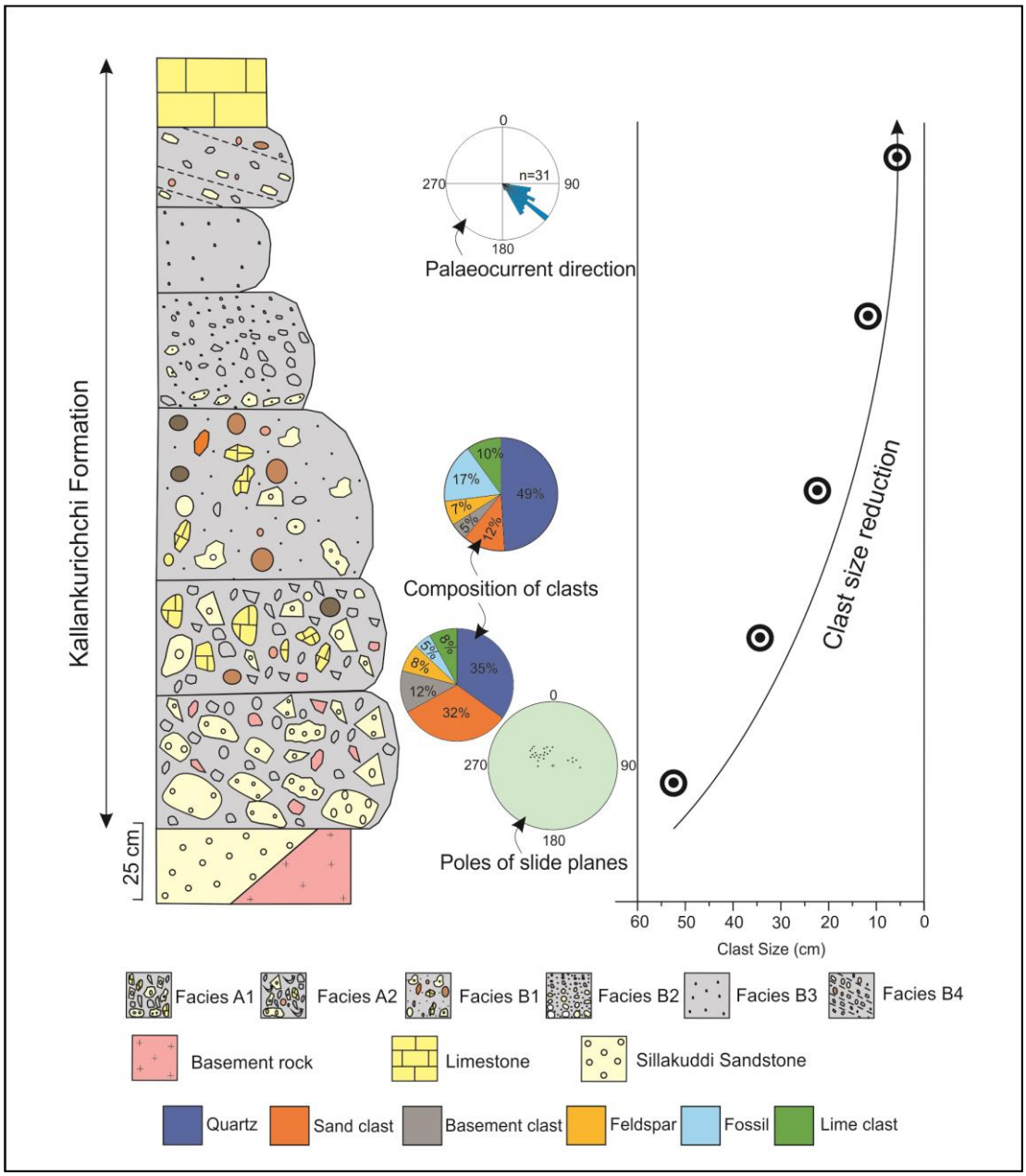

Fig. 6.3 A generalized litholog showing successive occurrences of scree conglomerates (facies A1 and A2) and its derivates (facies B1-B4) present at the basal part of the Kallankurichchi Limestone. Note the clast compositions in facies association A and B (with different colours) (a); the overall clast size reduction within conglomerate facies succession upwards (b). Also note the poles of slide plane denoting the direction of sliding; Paleocurrent directions are plotted from the crudely-developed cross-stratification at the penultimate stage of the flow transformation.

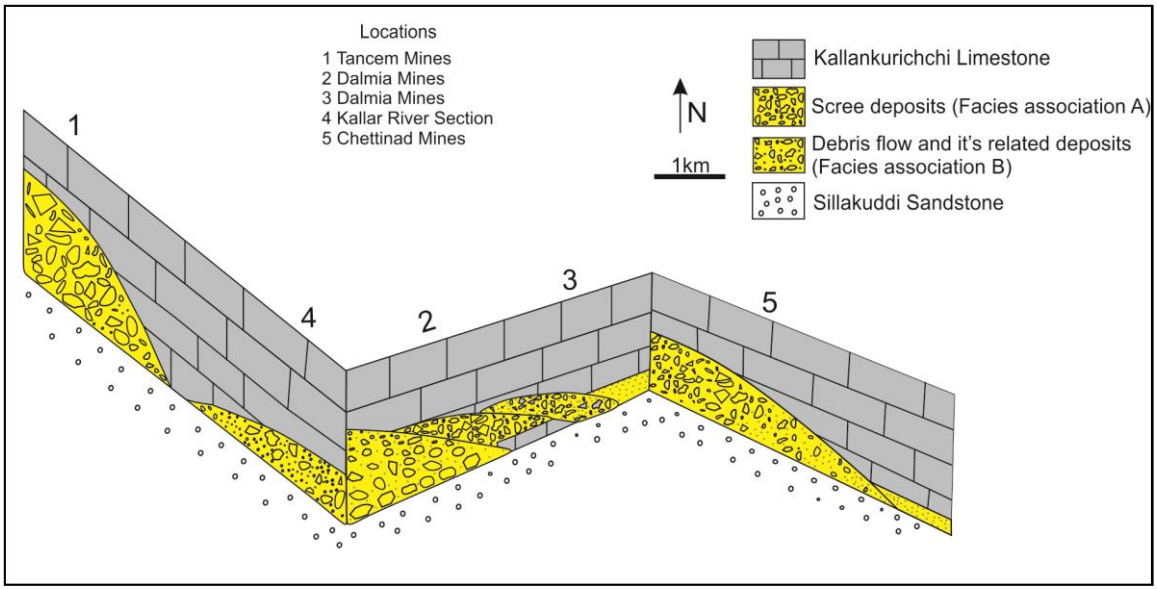

Fig. 6.4 A panel diagram showing position of scree conglomerates and their derivatives within the studied area marked in Fig. 6.1. Note, the wedge-shaped nature of the conglomerates and their successive juxtaposition.

comparatively smaller (maximum diameter measured 17 cm). The maximum bed thickness observed is 1m. Syn-sedimentary slide planes have been unequivocally identified at the base of this facies (Fig. 6.5c). Successive occurrences of facies is also observed (Fig. 6.5e).

6.3.1.2 Facies A2: *massive clast-supported conglomerates with fossil clasts*

The clast-supported conglomerate layers of facies A2 are similar to those of facies A1 except for the presence of fossils and limestone fragments. They are massive in nature. The clasts composition varies and include sandstone, limestone, quartz pebbles, basement, feldspar, fossils (Fig. 6.5h) and reworked clasts (Fig. 6.5g). The bivalve *Inoceramus* and Gryphoid dominate within the fossil clasts. Fossil bivalve ?*Platyceramus* (Ayyasami, 2006), a variety of *Inoceramus* is occurred within this facies and the fossils are preserved in bed parallel orientation (Fig. 6.5d). The largest limestone fragments are present within this facies,

measuring up to 33cm, are present in facies A2. Although most of the clasts are angular but all degrees from sub-rounded to rounded clasts are also noticed (Fig. 6.5f). The average bed thickness of Facies A2 is c.a., 62cm. The base of the facies is sharp and exhibits a wedge-shaped geometry. Pebble penetration into the matrix, vertical orientation of the clasts and fractured sandstone clasts are also common. There are no impact laminae wrapping their bottom of the clasts were ever observed.

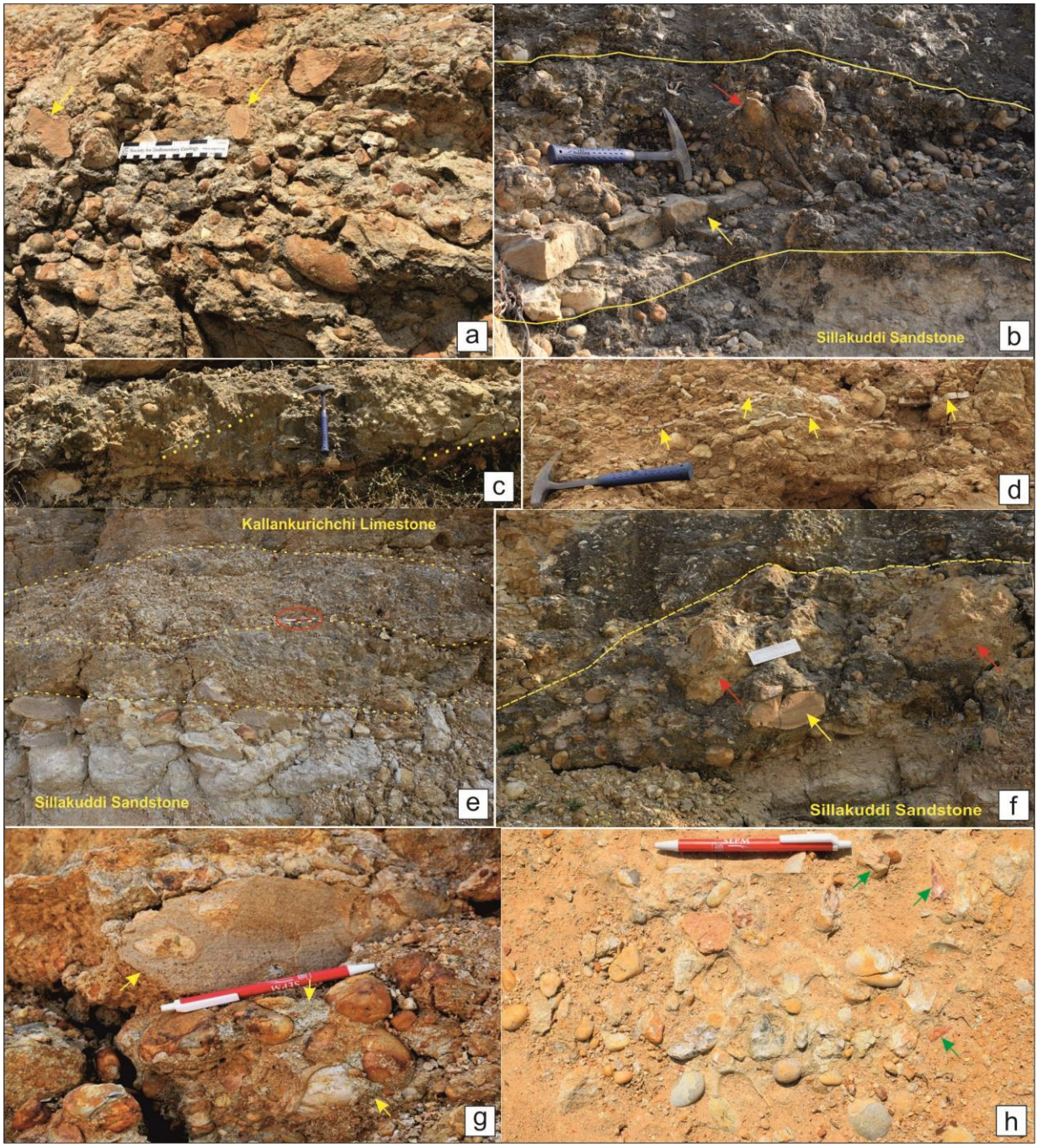

Fig. 6.5 Field photographs showing characteristic features in facies association A. Scree conglomerate present at the basal part of Kallankurichchi Limestone. Note, the reclining nature and vertical orientation of clast (arrowed), also note dominance of sandstone clast within calcarenite matrix (a); fractured intruded clast (red arrowed) and large bed-parallel sandstone clast (yellow arrowed) (b); syn-sedimentary slide planes within this scree conglomerate (dotted) (c); *Platyceramus* concentration along preferred planes, possibly the hard substrate (yellow arrowed) (d); successive occurrence of scree conglomerate and its derivatives (dotted) overlying the Sillakuddi Sandstone (e); larger blocks of limestone clasts (red arrows) tumbled down along slopes above Sillakuddi Sandstone (marked with white dashed line). Note, the fractured sandstone clast (yellow arrow). Also note the wedge-shaped nature of the conglomerate body (dashed line) (f); Recycled, resedimented clasts (yellow arrows) present within scree (g); Different types of clasts, note, the feldspar clast (green arrowed) (h). Pen length in E, G and H = 14.5 cm; Ruler length in A and F = 16 cm; Hammer length in B, C and D = 33 cm.

Interpretation:

Considering its extremely poor sorting, clast-supported framework, local origin of larger clasts from immediate basement and rapidly wedging bed geometry of facies association A is identified as a scree conglomerate facies or rock fall deposit formed at a steep basin-margin slope (Reijmer et al., 2015; Shanmugam and Wang, 2015; Chakraborty and Sarkar, 2018). The chaotically arranged clasts with sub-vertical orientation at times and reclining nature of the clasts points towards scree interpretation. Penetration of clasts into the matrix indicates a free-fall origin. The absence of impact laminae evidently suggests that these debris fans formed underwater and allowed large fragments of rock thrown from above to slowly sink. Similar accumulations of underwater debris and boulders observed in canyons and along steep reef slopes (Mullins et al., 1991). The large bed parallel slab-like sandstone blocks probably sliding down along the steep slopes. The association of slide planes and plotting of their poles supports the assertion (Fig. 6.3). Overall, the scree conglomerates likely to be deposited closest to the basin-margin. However, the formation of these scree conglomerates continued even after the deposition of Kallankurichchi Limestone as indicated

by limestone clasts in the A2 facies. Facies A1 was probably deposited at the immediate slope break, while A2 was later deposited. Presence of marine fossils within A2 facies, despite paucity, further corroborates this contention. The growth of *Platyceramus* within A2 facies requires a hard substrate indicating presence of pause planes during the deposition of these scree cones.

The wedge-shaped geometry of the facies association A with lateral and vertical juxtaposition, resulting in a facies mosaic indicate that the clasts tumbled down along steep slopes, forming scree cones. Possibly, the larger blocks may have moved along the identified slide planes. Recent scree cones are common but there are few records of scree cones from siliciclastic depositional regime (Bose et al., 2008; Alberti et al., 2017; Chakraborty and Sarkar, 2018; Samanta et al., 2022). The presence of these scree cones present at the base of Kallankurichchi Limestone Formation consists of both siliciclastic and carbonate clasts are rare in occurrence.

6.3.2 Facies Association B:

This facies association is dominated by matrix-supported conglomerates and their successive derivatives. The average clasts are smaller in size compare to the facies association A and there are more carbonate clasts compared to the previous association. The facies association B comprises four facies types (Fig. 6.6).

6.3.2.1 Facies B1: *matrix supported conglomerate facies*

The facies is matrix-supported (Fig. 6.6a), exhibits convex up body geometry with non-erosive bases. Facies B1 is dominated by quartz, limestone and fossil clasts with maximum average grain size of approximately 18cm. Besides, some sand and basement clasts are also observed within the facies. The clasts are mostly randomly oriented. The average size of the clasts is between 12 and 21 cm. It The matrix has a calc-arenitic composition. The strength of the matrix varies along the downcurrent direction. Larger sand clasts with jagged boundaries are also found in areas of relatively high matrix strength (Fig. 6.6b). Bored lime-

clast (Fig. 6.6c), delicate fossil clasts, and protruded clasts (Fig. 6.6d) are also common. Occasionally clasts show bed parallel orientation in the lowermost part of the conglomerate bed become haphazard towards top.

6.3.2.2 Facies B2: *Crudely developed Normal graded conglomerate facies*

This particular facies is characterised by crudely developed normal grading, but rarely present in the succession (Fig. 6.6e). The maximum thickness of the facies is 47 cm. The lower contact is undulatory. The clast composition ranges from dominantly quartz to rarely basement clasts, feldspar and fossil fragments. Its average size ranges from 8cm to 14cm. Occasionally this facies grades up to massive clast free facies (Fig. 6.6e).

6.3.2.3 Facies B3: *Massive sandy facies*

This facies is sandy in nature. They are internally massive and composed of coarse sand sized grains in general. Both carbonate and siliciclastic sand sized material are present. The maximum bed thickness is 42cm. The massive sand body shows lenticular body geometry, though their lateral extent is greater compare to other conglomerate bodies of the facies association B (Fig. 6.6f).

6.3.2.4 Facies B4: *Crudely developed cross-stratified conglomerates*

The crudely developed cross-stratification is occasionally encountered within this association (Fig. 6.6g). The cross stratifications are gently inclined and set thickness set thickness varies from 22cm to 32cm. Foreset dip angles vary from 10 to 12°. The maximum clast size is 7 cm, with the clasts aligned along the forests. The basal contact of the cross-stratified conglomerates is generally sharp. Paleocurrent directions derived from crude cross-stratification shows towards south-east consistently (Fig. 6.3).

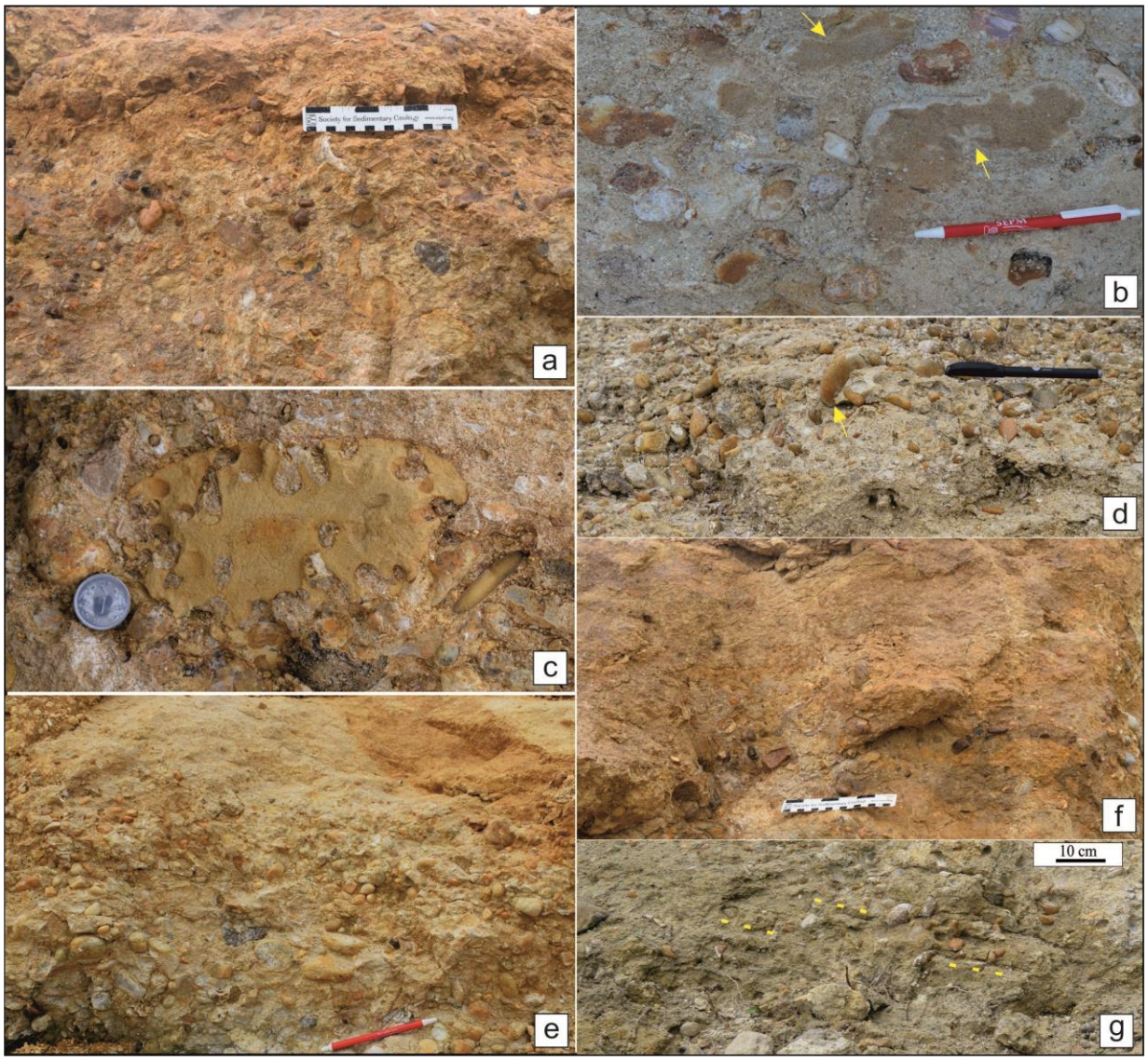

Fig. 6.6 Field photographs showing characteristic features in facies association B. Matrix-supported conglomerate (a); jagged boundaries (arrowed) of sandstone clast within the matrix-supported conglomerate (pen length 14.5 cm) (b); bored limestone clast present within sandy matrix (coin diameter 2 cm) (c); protruded clasts (arrowed) (pen length 14 cm) (d); crudely-developed normally-graded conglomerate followed by massive sandy deposits (pen length 14.5 cm) (e); massive calcarenite (f); Crudely-developed cross-stratification (marked with yellow dashed lines) within the facies B4 (g).

Interpretation:

The matrix-supported conglomerate beds with its convex-up body geometry and randomly oriented clasts are interpreted as deposits of laminar debris flow. The clasts were held in suspension by matrix; the larger clasts (>20cm) are also floating, supported by matrix that owes its mechanical strength because of high sediment-fluid ratio. This help to transform the flow into a cohesive one, supports the debris-flow origin of the beds (Rodine and Johnson, 1976; Nemec and Steel, 1984; Arguden & Rodolfo, 1986; Chakraborty, 2011; Chakraborty and Sarkar, 2018). The lack of erosional features underneath and relatively high matrix proportions suggest a highly cohesive behaviour of these facies as debris flow deposits (Mulder and Alexander, 2001). The incorporation of large jagged sand clasts and bored limeclasts within this flow also signify high matrix strength. Deposition occurred by freezing the mud matrix (Bose and Sarkar, 1991). The bases of debris flow beds are non-erosional, the preserved thicknesses of their deposits likely to be reflected their original thicknesses. The crudely developed normal grading indicate occasional development of turbulence within the flow. The undulatory nature of the bases supports the contention. Normally graded conglomerates are likely to be products of high-density cohesionless debris flows. However, considering the large size of the clasts it is difficult to propose that only turbulence was responsible to held those clasts within the flow, may be fluidization and water entrapment within the flow facilitated the lifting of the clasts in suspension. The grading indicates presence of fluidal turbulence within the flow. The transition from the chaotic arrangement of clasts in the debris flow to ordered arrangement in the crudely developed normally graded beds reflects decreasing slope gradients along the slide planes. The gradational transition from normally graded to sandy massive conglomerate implies that a rapid thinning of the flow and inability of flow to keep the larger clasts in suspension except sand size grains. Massiveness also indicates rapid settling of the grain. The fluidity of the flow even increased when crudely developed cross stratification arises within this association. Crudely developed cross-stratification indicates incipient turbulence or presence of traction current. The overall finning and thinning up trend within a short interval indicate deposition from surges and the flow overall wanes downslopes. The transition possibly took place because of settling of clasts and consequent increase in matrix content. Reduction of depositional slope must have been the root cause for the flow transformation. The transition from bed-parallel to chaotic

clast fabric and introduction of matrix depicting transformation of an internally sheared flow into a debris flow.

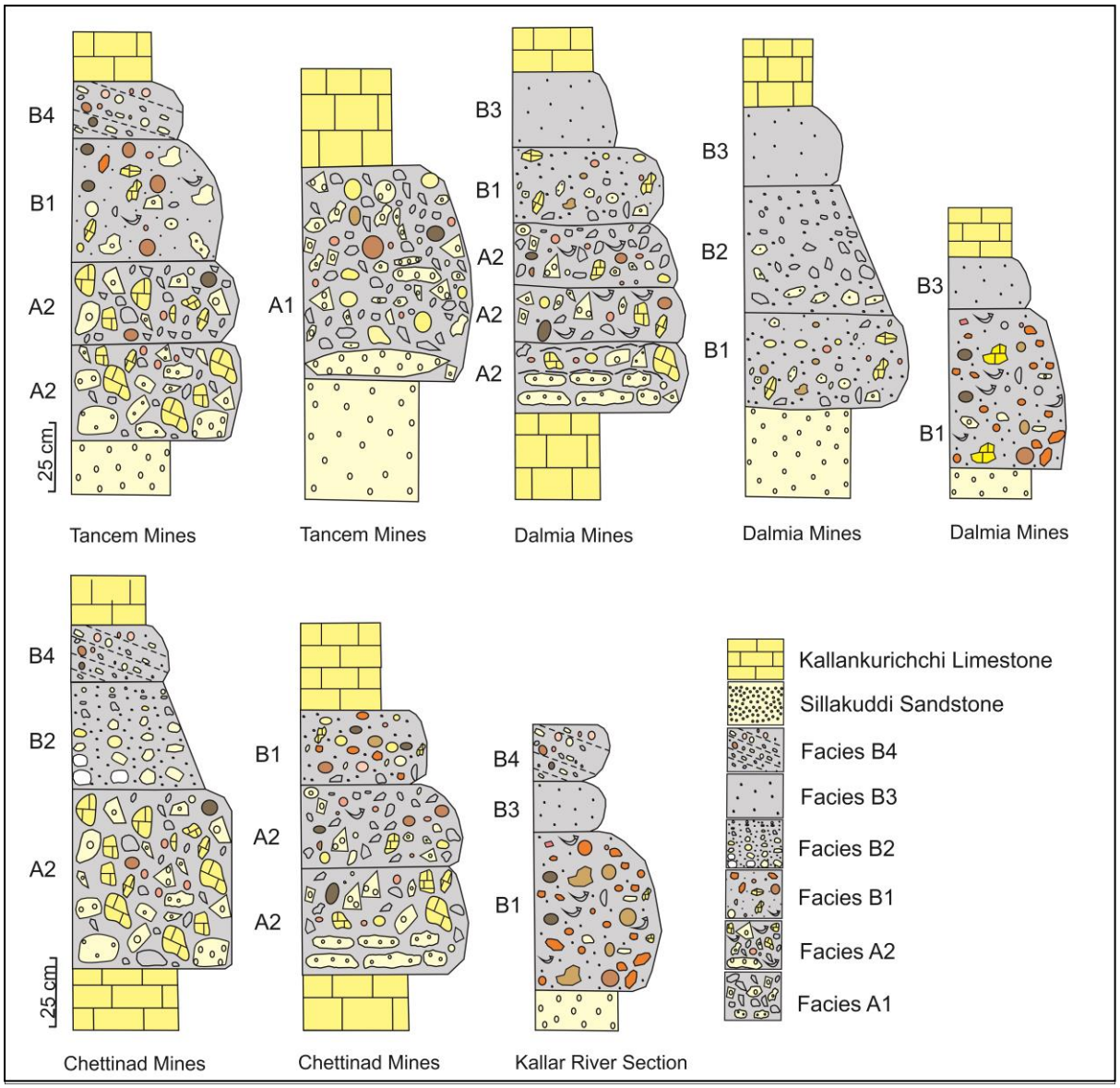

Fig. 6.7 Vertical packages of the conglomerates present at different quarry sections.

6.4 Disposition of Conglomerates and their flow evolution:

Discrete vertical packages of the conglomerate assemblages embedded within the basal part of the Kallankurichchi Formation are the conspicuous and occurred at successive interval (Fig. 6.7). The nature of disposition of the different facies in facies association A and

B indicate the transformation of the initial flow. The change of facies character from a base of slope (facies association A) to matrix supported debris flow and associated facies (facies association B) shows a gradual slope change towards down slope direction. The transition within the facies association B shows a gradual change from proximal to distal facies disposition within the basin. Downward transition from clast-supported scree deposit to matrix-supported debris flow to clast free massive to crudely developed cross stratified conglomerate indicate gradual transition. These transitions from basal scree deposits to crudely developed cross-stratified conglomerates signify progressive transformation and dilution of flow (Fig. 6.8)

These changes may take place because of incorporation of the water by mixing with the flow in sub-aqueous settings along with change of gradient. Downdip thinning and finning up of the conglomerate beds is common also suggests proximal to distal transition. The crudely developed normally graded conglomerate are present distally. The feebly developed cross stratified conglomerate might have developed during the penultimate stage denoting waning of the flows (Fig. 6.9).

Based on facies relationships, it can be inferred that the basin margin scree deposits give way to debris flow before eventually transforming into high and then low-density turbidity flows. The lack of correlation between the thickness of bed and size of the individual clasts within the debris flow, supports its cohesive nature (Fig. 6.10; Nemec and Steel, 1984).

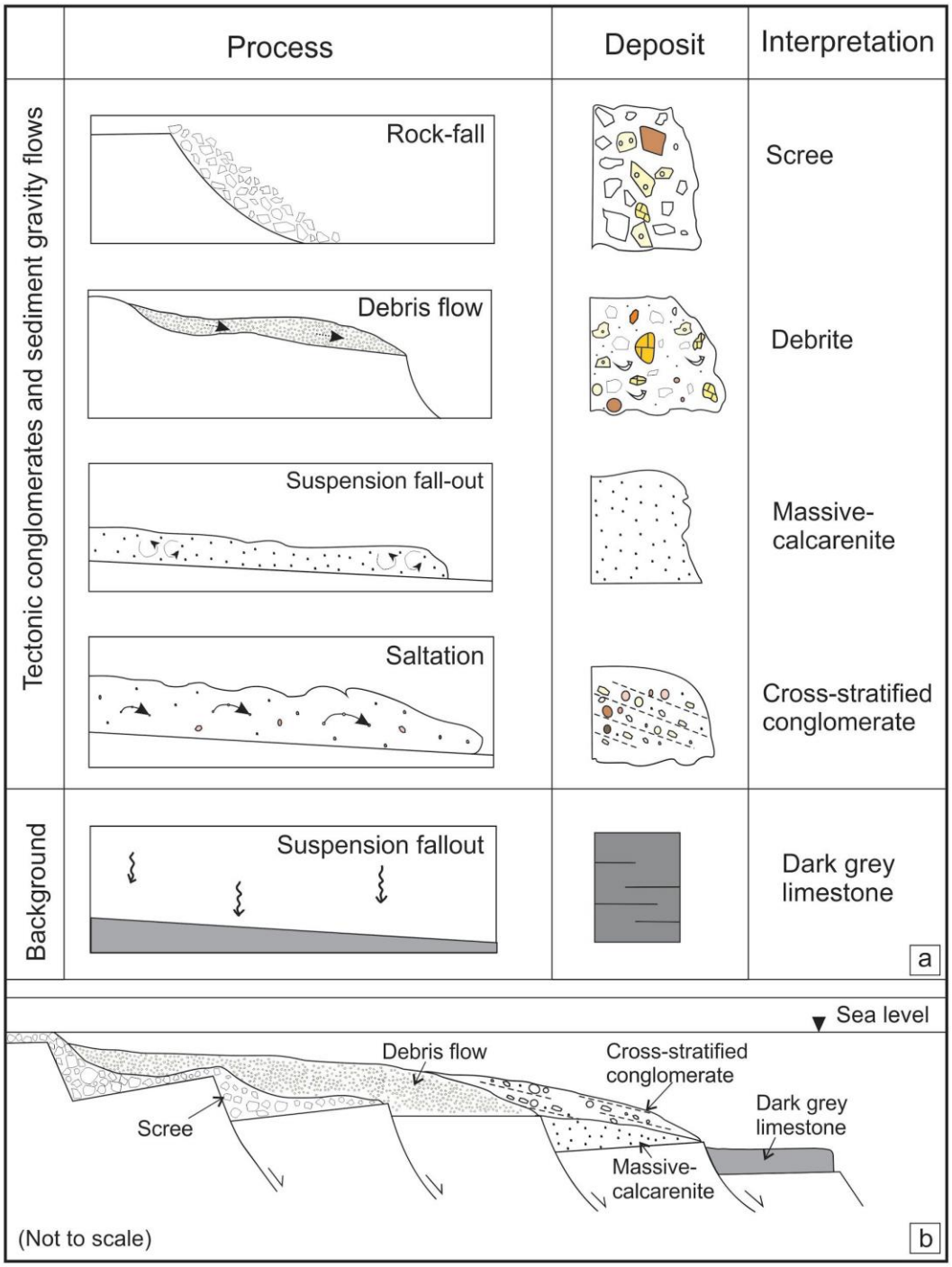

Fig. 6.8 A schematic diagram illustrating the relationship between flow mechanism, deposition and interpretation of the constituents of scree facies (modified after Porten et al., 2016) (a); diagram showing distribution of scree conglomerates and mass-flow units associated with dark grey limestone, (b; schematic, not to scale) (modified after Chakraborty and Sarkar, 2018).

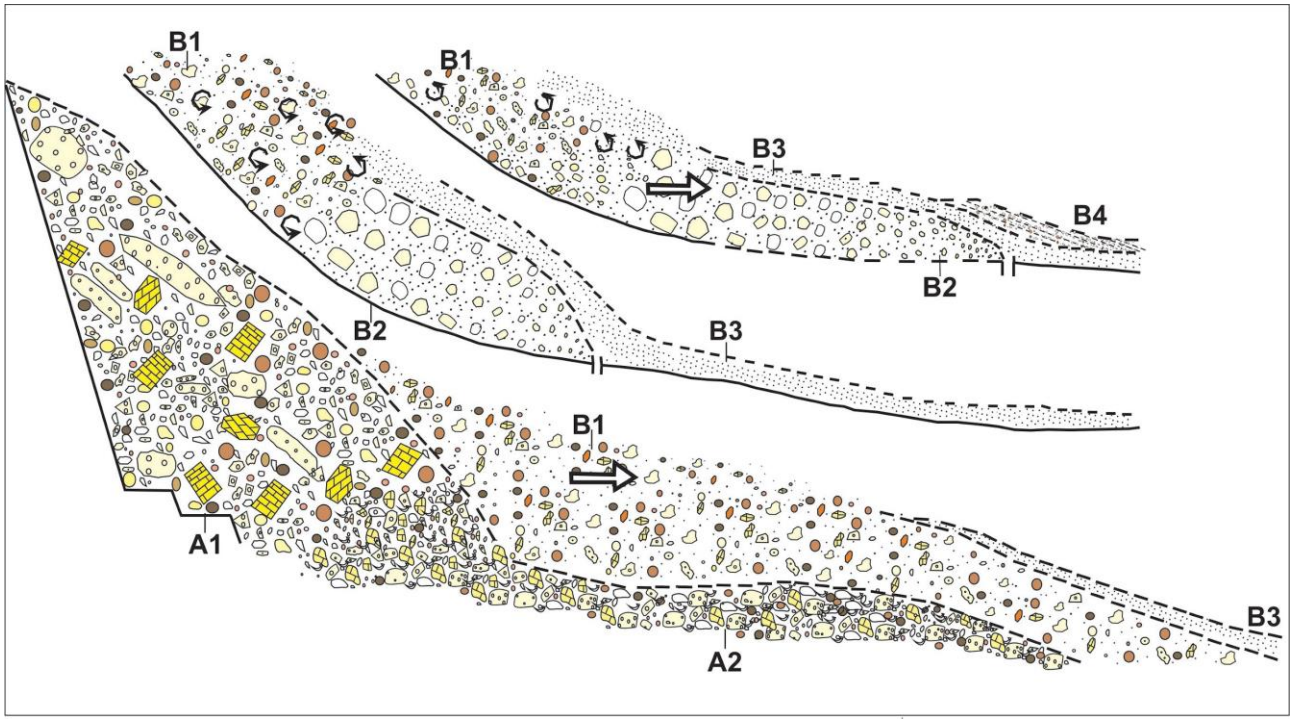

Fig. 6.9 The correlation between the gradient of the slope where mass failures occurred and the flow series, as derived from the observed transition of facies (not to scale). Note, the vertical aggradation of mass flow facies (modified after Bose and Sarkar, 1991).

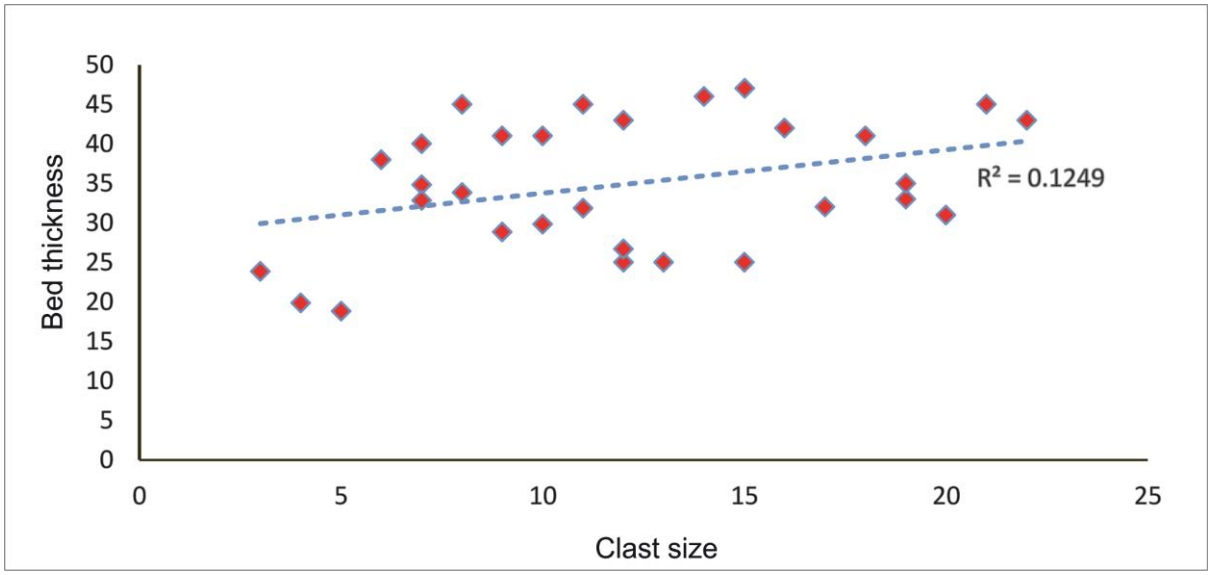

Fig. 6.10 Correlation between bed thickness vs size of the clast of Facies B1. Note the poor correlation.

This is aided by maximum clast size, conglomerate bed thickness and transitions from clast-supported conglomerate to matrix-supported conglomerate to massive sandy facies. Significantly, the lateral facies transition of the conglomerate beds is less compared to their vertical transitions. Areal lithologic variations and facies transitions documenting scree deposition and debris flow transitions down to the basin (Fig. 6.11).

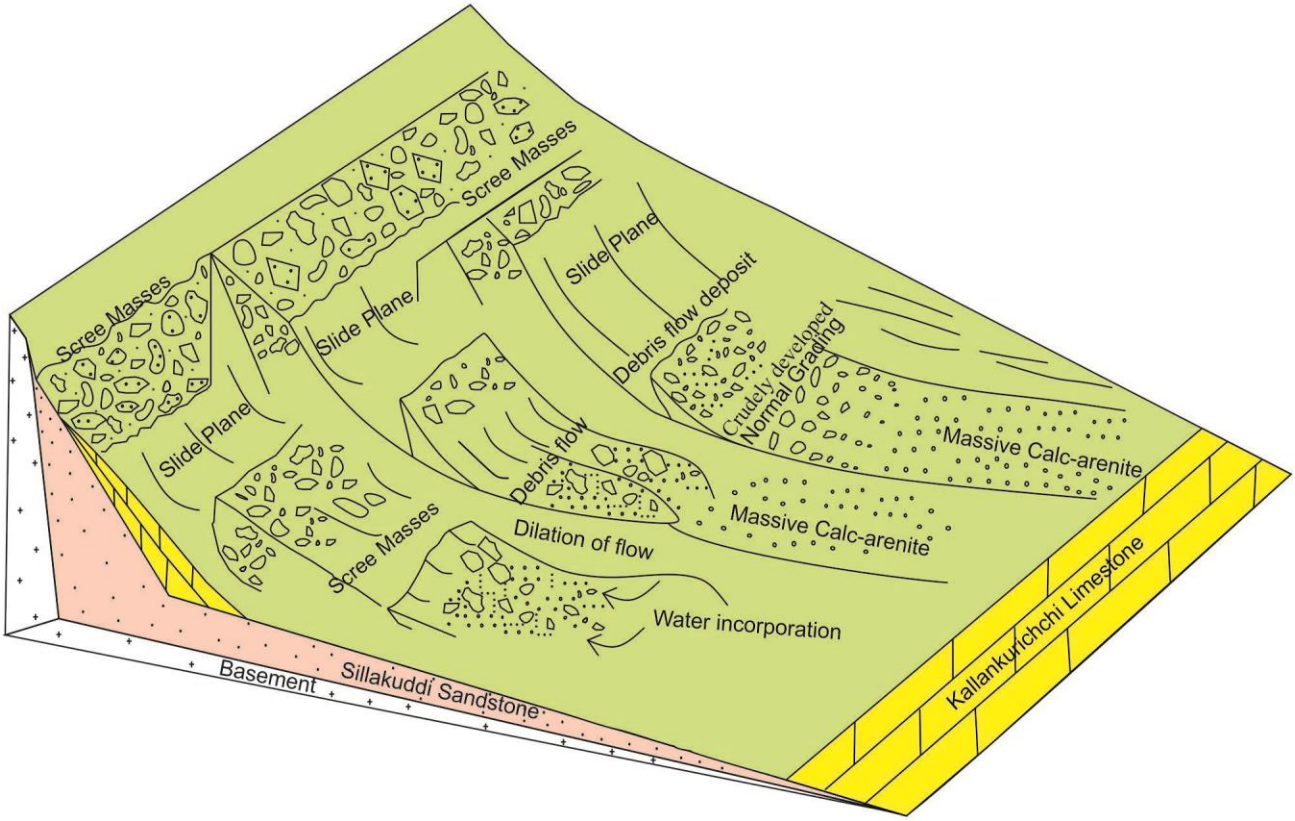

Fig. 6.11 Diagram showing formation of scree conglomerates and their derivatives. Note, the base of slide planes is dominated by scree followed by their derivatives due to water incorporation and segregation of clasts along down slopes (modified after Bose and Sarkar, 1991).

6.5 Discussion:

The deposition of Kallankurichchi Limestone started on a siliciclastic platform, viz. Sillakuddi Sandstone. The carbonate platform developed over it signify beginning of a fresh sedimentation event possibly because of renewed rifting of the then continental margin,

(Chand et al., 2001). The extensional tectonics and followed by a subsidence likely to be continued till Turonian (Watkinson et al., 2007). In this carbonate platform, the tectonism manifested as a local scale rifting and associated block movement along the steep slopes (Nagendra and Reddy, 2017). The conglomerates have so far been interpreted as basal conglomerate (named Kallar Conglomerate). However, they occur in successive horizons. A large no of rounded grains is present within these conglomerates unlike one would expect from basal conglomerate deposits. Limestone blocks of Kallankurichchi Limestone and fossil fragments present within these conglomerates also contradict its basal conglomerates origin. This also suggest that the deposition of the scree and its derivatives continued even after initiation of limestone deposition (Fig. 6.5d and f). Further, these conglomerates are likely to be deposited at the base of steep slopes as indicated by the presence of very large sandstone clasts derived from the underlying formation. The dark grey limestones (maximum 3.5 m thick) associated with one of the boulder conglomerate horizons probably reflect the development of anoxic environment because of maximum basin subsidence. Interestingly, pyrite and anoxic clay mineral e.g., berthierine (Fig. 6.12) abundantly present within this dark grey limestone also supports the present conclusion.

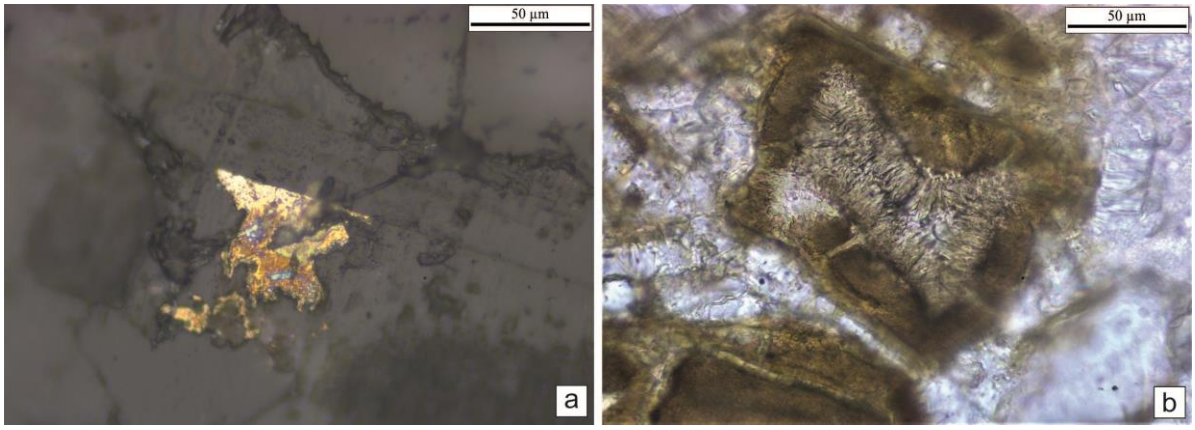

Fig. 6.12 Pyrite (a) and Clay mineral berthierine (b) present in the dark grey limestone present in association of the basal conglomerate.

The massive clast-supported ungraded conglomerate facies association with haphazardly oriented large angular clast, presumed to have been closest to the faulted basin-margin (Sarkar et al.,1995; Mandal et al., 2024). The evolution of the flow occurred along these slopes. The presence of slide plane in this association supports this view (Fig. 6.5c).

Occurrence of scree deposits suggests considerable relief difference also support tectonic uplift of the basement and progressive sagging of the basin. The poorly sorted conglomerates along with some feldspar clasts (Fig. 6.5h) supports sudden dumping, may be because of rock fall, likely to be for the inferred steep slopes. The scree conglomerate represents free fall of clasts and sudden increase in the rate of basin subsidence. The sudden free fall of clasts and increase in depth may be attributed to locally activated basin margin steep slopes. Penetration of clasts into the underlying substrata also supports free-fall of clasts. The protrusion of some of the clasts above the bed surface indicate high matrix strength of the original flow material. The renewed tectonism must have played a vital role to create the slope and in turn the slope changes also have the role to generate of different types of gravity flows. The studied sequence of the basal part of the Kallankurichchi Formation of Ariyalur Group exhibits the signatures of a scree deposits and represents the local tectonic activation/post rift adjustment during the Cretaceous time in the southern part of the Indian Craton (Fig. 6.13). The attenuation of subsidence transitioned the scree and its derivates to deposition of fossiliferous Kallankurichchi Limestone.

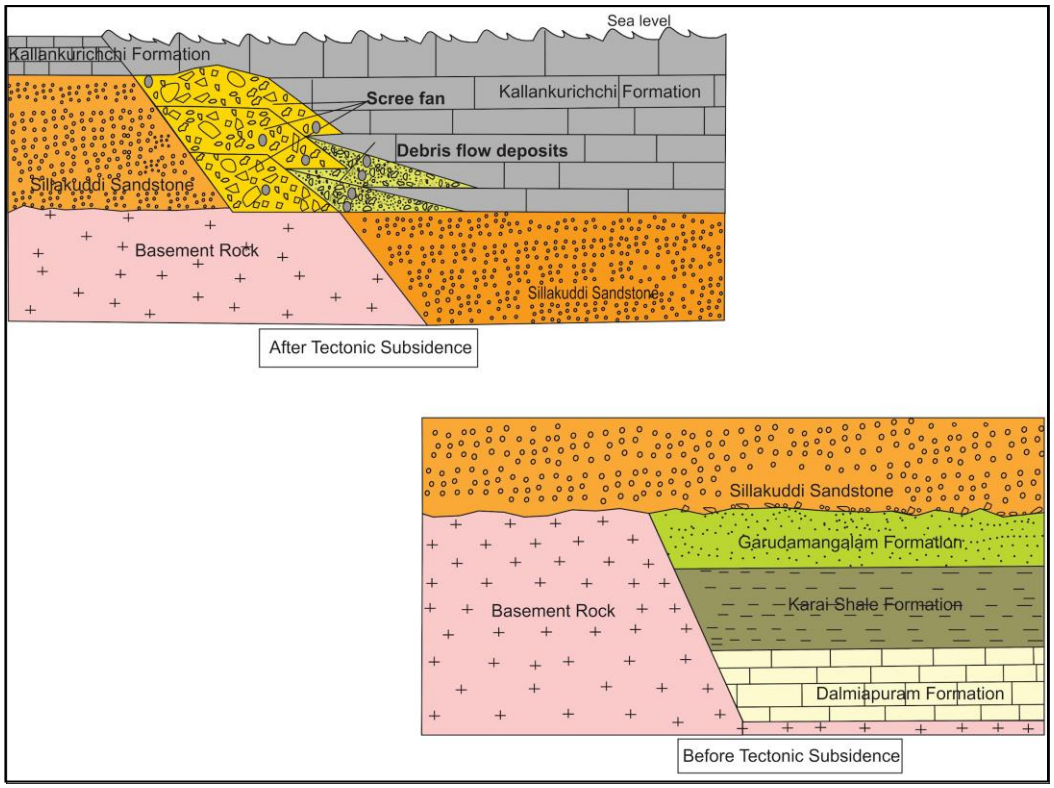

Fig. 6.13 Tectono-depositional model for the formation of scree and its derivatives.

6.6 Conclusion:

1. Lower part of Kallankurichchi Limestone is infested with scree and related mass flow deposit. Both siliciclastic and carbonate clasts are present within those conglomerates.

2. The presence of carbonate clasts and fossil fragments along with other clasts indicates that the rifting/subsidence continued, even after the carbonate deposition started, may be in local scale.

3. The scree conglomerates and its derivatives are present in successive intervals and consist of both angular and rounded/well rounded clasts, which is inconsistent with basal conglomerates interpretation.

4. Intermittent time gap is also expected between successive intervals of scree conglomerates because *Platyceramus* required hard substrate to grow.

5. The subsidence because of renewed rifting help to generate accommodation space for the Kallankurichchi Limestone. Depth variation within this Limestone can be explained by the presence dark colored limestone with anoxic minerals in contrast to the fossiliferous entire deposits.

CHAPTER- 7

AUTHIGENIC CLAY MINERAL BERTHIERINE

7.1 Introduction:

The authigenic green marine clays, represented by K-poor berthierine and chamosite to K-rich glauconite and celadonite, are present abundantly in sedimentary depositional environments ranging in age from Proterozoic to recent and have enormous geological significance (Baldermann et al., 2022; Huggett et al., 2010; Odin and Matter, 1981; Roy Choudhury et al., 2022; Velde, 2003; see Banerjee et al., 2020 for more references). These green marine clays are characteristically iron-rich and often form at the sediment-seawater interface via the active chemical exchange (Baldermann et al., 2022; Huggett et al., 2010; Odin and Matter, 1981; Roy Choudhury et al., 2022; Velde, 2003; see Banerjee et al., 2020 for more references). Although the K-rich green marine clays, more importantly, glauconite, have received significant attention because of their high abundance in the stratigraphic record as well as their applicability in radiometric dating, the K-poor green marine clays are still poorly explored (Brindley, 1982; Taylor, 1990; Toth and Fritz, 1997; Huggett et al., 2010; Banerjee et al., 2016b, 2020; Tang et al., 2017b; Bansal et al., 2019; Ma et al., 2022). The formation of these authigenic green clays is often facilitated by an oxygen-depleted depositional environment with abundant supply of iron, possibly sourced by continental weathering, volcanism, and/or hydrothermal processes (Harder, 1978; Berner, 1981; Odin and Matter, 1981; Van Houten and Purucker, 1984; Kimberley, 1994; Jeans et al., 2000; Huggett et al., 2010; Kozłowska and Maliszewska, 2015; Mu et al., 2015; Tang et al., 2017b; Ma et al., 2022; Roy Choudhury et al., 2022b). The role of ferruginous seawater condition is also proposed as a viable source of iron for the K-poor green marine clay formations in Precambrian shallow marine sediments (Tang et al., 2017a; Ma et al., 2022). The K-poor green marine clays, often associated with Phanerozoic oolitic ironstone facies, comparatively have limited occurrences, although they are important for deciphering the paleogeographic and subsidence history of the basin (Van Houten and Bhattacharyya, 1982; Van Houten and Purucker, 1984, 1985; Kimberley, 1994; García-Frank et al., 2012; Rudmin et al., 2018; Wang et al., 2023a). Berthierine, a ferrous-ferric 1:1 trioctahedral clay with a basal spacing of 7 Å, is an important K-poor authigenic green clay species (Brindley, 1982; Iijima and Matsumoto, 1982; Van Houten and Purucker, 1984; Taylor, 1990; Kimberley, 1994; Toth and

Fritz, 1997; Sheldon and Retallack, 2003; Tang et al., 2017b). Although it forms dominantly in marine environments, it is also reported from brackish water, laterite deposits, and hydrothermal sites (Iijima and Matsumoto, 1982; Taylor and Curtis, 1995; Toth and Fritz, 1997; Kozłowska and Maliszewska, 2015; Tang et al., 2017a; Wang et al., 2023a). The formation of K-poor green marine clays remains enigmatic due to their frequent transformation to chlorite or chamosite (Fe-rich chlorite) via the formation of mixed-layer berthierine-chlorite and/or odinite-chlorite during diagenesis at elevated burial temperatures (70–200° C) (Toth and Fritz, 1997; Beaufort et al., 2015; Mu et al., 2015; Tang et al., 2017a; Šegvić et al., 2020; Tounekti et al., 2021). Although berthierine formed in recent marginal marine settings as authigenically formed green granules and pellets (e.g., Loch Etive, Scotland, and Niger Delta), its counterpart is not identified in the rock record (Odin and Matter, 1981; Porrenga, 1967; Rohrlich et al., 1969; Van Houten and Purucker, 1984; see Toth and Fritz, 1997 for more references). The identification and characterization of authigenically formed berthierine grains is thus essential for a better understanding of the origin of this green marine clay. Moreover, the clay mineral assemblages often represent the combined effect of tectonic and volcanic events associated with the evolution of the sedimentary basin (see Do Campo et al., 2010 for more references). While tectonic events can significantly alter the relief and hydrological conditions of the basin, volcanic episodes (co-eval or ancient) can supply a new suite of metastable minerals such as olivine, pyroxene, amphiboles, and glass shards (both pyroclastic and/or epiclastic) into the depositional environment, signatures of which are often documented in the clay mineral assemblage. Furthermore, the formation of authigenic green marine clays on the ocean floor releases CO_2 into the atmosphere, which is currently being considered as an important paleoclimatic regulator (Isson and Planavsky, 2018; Baldermann et al., 2022; Ma et al., 2022).

The current research focuses on the conspicuous green marine clays hosted by the limestone bed within the lowermost part of the late Cretaceous Kallankurichchi Formation of the Cauvery basin (Fig. 7.1). The upper Cretaceous sedimentary deposits across the Indian sub-continent have received much attention because of their diverse biotic assemblages and the proximity to the end-Cretaceous mass extinction event (Acharyya and Lahiri, 1991; Keller et al., 2016). The green clay minerals in different parts of the Cauvery basin have

rarely received attention, barring a few (Banerjee et al., 2016a; Bansal et al., 2021), though they have significant sedimentological and sequence stratigraphic implications. The objectives of the paper are to a) understand the origin of the green marine clay and infer its depositional implications at the basal part of the Kallankurichchi Formation, b) delineate the tectonic implications of abundant authigenic green clay mineral formation, and c) to understand the source and fate of iron associated with authigenic clay mineral formation. To meet the objectives, we carried out an in-depth sedimentological investigation, combined with geochemical and mineralogical characterization of the authigenic green marine clay fraction.

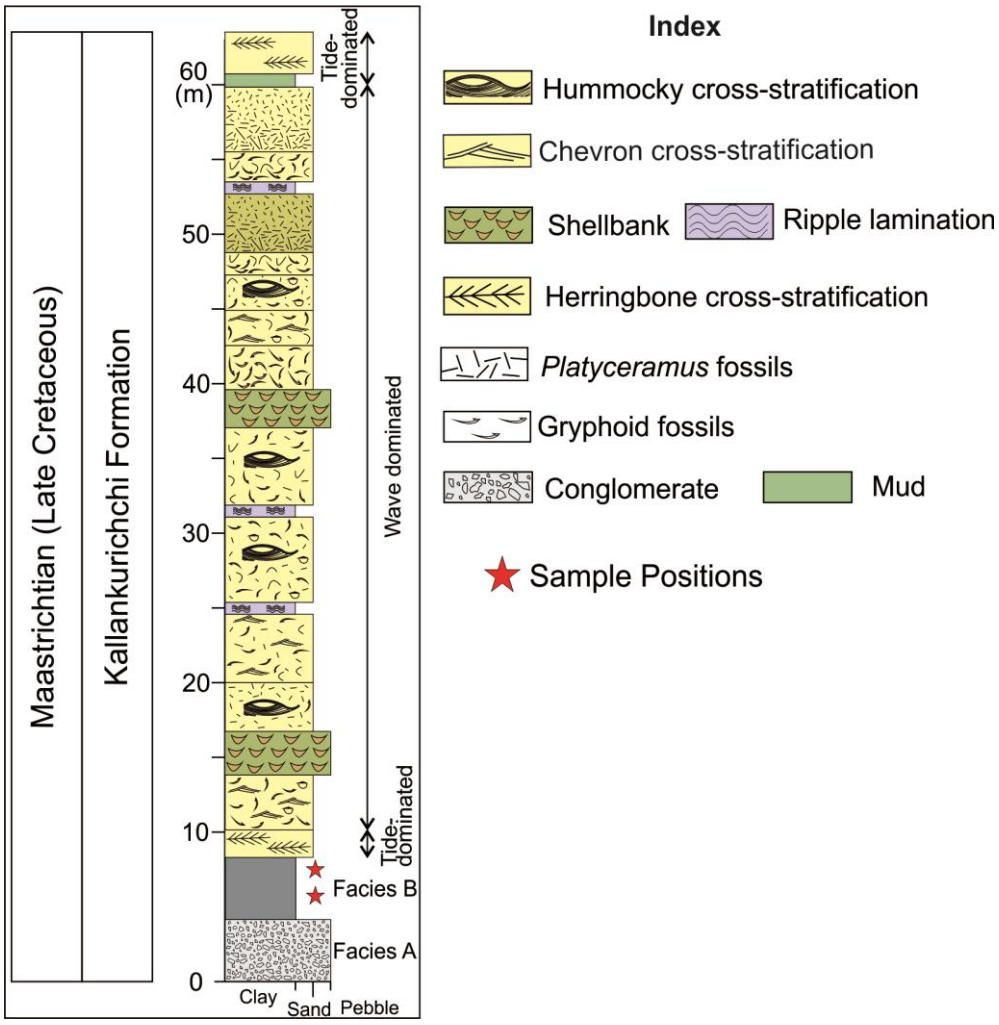

Fig. 7.1 A generalized litholog of the Kallankurichchi Formation with the sample positions.

7.2 Sedimentological background:

The shallow marine Kallankurichchi Formation is underlain and overlain by the Sillakuddi Sandstone and Kallamedu Sandstone Formations, respectively (Sundaram et al., 2001; Watkinson et al., 2007). The Kallankurichchi Formation is dominantly calcarenitic, with a high fossil content (Tewari et al., 1996; Fürsich and Pandey, 1999; Hart et al., 1999; Srimani et al., 2021). The detailed facies and micro-facies analysis of the Kallankurichchi Formation demarcated two distinct facies association characterized by tide-dominated and wave-dominated facies (Srimani et al., 2021). A distinctive lithology, marked by conglomerate and fossil-poor dark grey limestone characterizes the lowermost part of the Kallankuruchhi Formation. The rest of the succession is highly fossiliferous and bears the signatures of tide and wave regime (Fig. 7.1) (Srimani et al., 2021). Authigenic green marine clays occur exclusively at the lowermost part of the succession and thus a detailed sedimentological investigation of this part of the Kallankurichchi Formation is presented here to understand the subsidence history, depositional environment, and authigenic mineralization.

Based on the lithology, bed geometry, and internal organization, the basal part of the Kallankurichchi Formation is divided into two facies viz. Facies A: Conglomerate and Facies B: Dark Grey Limestone are described below.

7.2.1 Facies A: Conglomerate facies

A total of 9 m thick wedge-shaped conglomerates occur at the basal part of the Kallankurichchi Formation, which is repetitive in occurrence. Although both siliciclastic and carbonate clasts are present within this facies, the basal part is dominated by siliciclastic debris (Fig. 7.2a). Conglomerate may be either clast- or matrix-supported, with mostly wedge-shaped geometry and juxtaposed successively (Figs. 7.2a, b).

The clast-supported conglomerate bodies are very poorly sorted along the boundary between Sillakuddi Sandstone and Kallankurichchi Formations. The clasts are chaotically

arranged; some are sub-vertically oriented, reclining on other clasts. The bedding surfaces of these conglomerate beds are encrusted with fossil bivalves *Inoceramus*, though internally, they are unfossiliferous. The clasts can be traced to the underlying Sillakuddi Sandstone and the granitic basement. The clasts derived from the underlying Sillakuddi Sandstone Formation are mostly angular, measuring up to 60 cm long. The granitic basement-derived clasts are comparatively smaller (up to 5-7 cm long) and are well-rounded. Clasts also include limestone clasts, feldspar, and quartz pebbles, commonly showing fractures. Some pebbles may sink into the underlying sediment, though no impact laminae are wrapping their bottom. The matrix, scarcely present between the clasts, is calcarenite in nature. Strikingly in places, the clast-supported conglomerates show NW-SE trending slide planes (Fig. 7.2c). Successive occurrences of these conglomerates, bounded by slide planes, indicate repetitive tectonism. This massive clast-supported, ungraded conglomerate grades into a matrix-supported conglomerate in a down-wedge direction (Fig. 7.2b). The matrix-supported conglomerate shows convex-up geometry. Clasts in this matrix-supported conglomerate include bored limestone, fossils, and burrows. Crudely developed graded conglomerates occur locally. The conglomerates in the down-wedge direction give way to the dark grey limestone deposition basinward.

The clast-supported to matrix-supported conglomerates invariably occur along the boundary between the Sillakuddi Sandstone and Kallankurichchi Formations, indicating the initiation of a new sedimentation regime. The extremely poor sorting, clast-supported framework, larger clasts from the immediate basement, and rapidly wedging bed geometry of the conglomerate facies are likely to be scree conglomerate facies or rock fall deposits formed at a steep basin-margin slope (Bose et al., 2008; Chakraborty and Sarkar, 2018; Reijmer et al., 2015). This also suggests the continuation of the active tectonic pulses during the lower part of the Cauvery Basin. The presence of slide planes within the successive conglomerate beds also supports the contention. The successive conglomerates can be correlated with intermittent tectonic pulses, which were possibly responsible for the basin subsidence to create the accommodation space for the Kallankurichchi Formation. The growth of *Inoceramus* at places within the scree conglomerates signifies the presence of hard substrates within the scree mass. Scree conglomerate possibly formed as discrete pulses, the

time gap between successive pulses allowed the cementation of the upper surface. These conglomerates continually deposit even during the ongoing limestone deposition since limestone clasts are also present within the conglomerates. The slide planes probably facilitated the generation of these conglomerates. The preservation of feldspar clast suggests sudden and quick dumping. As no impact laminae are wrapping their bottom, it is evident that the scree fans formed under the sea permitting only slow sinking of rock fragments dropped from above. The intermittent presence of marine fossils within the scree conglomerate further corroborates this contention. The matrix-supported conglomerates, containing bored limestone clasts, delicate fossils, and haphazard orientation of clasts, indicate their formation from a high viscosity debris flow (Bose and Sarkar, 1991; Srimani et al., 2021). Facies variability from clast-supported to matrix-supported conglomerates to even poorly developed normally graded conglomerates suggests the transformation of the initial flow. Along the slide planes, fluid got incorporated and diluted the flow. Scree deposits give way downslope to debris flow deposits. The flow becomes diluted, and turbulence developed downslope helps to generate normal crude grading.

7.2.2 Facies B: Dark Grey Limestone facies

This facies overlies the Sillakuddi Sandstone or conglomeratic facies but succeed to the yellowish limestone of the Kallankurichchi Formation with sharp contact (Fig. 7.2d). The non-recurring facies, with a characteristic dark hue, is laterally traceable for a maximum of 155 meters within the studied section. The dark grey limestone is fine-grained, and the fossil content is relatively poor compared to the overlying limestones of the Kallankurichchi Formation, which is highly fossiliferous and yellowish in colour. The dark grey colour eventually changes to light grey at the upper part of the limestone. Fossils, if present, are mainly concentrated within this light grey zone, though a gradually increasing trend in the fossil content in the upper part is evident. The maximum thickness of this limestone is about 3.5 meters (Fig. 7.2d). They are crudely cross-stratified at the upper part, while the lower part shows poorly developed planar lamination. The limestone shows a good content of

siliciclastic detritus, amongst which quartz, feldspar, and fresh to partially palagonitized sideromelane glass are common (discussed later). The lower part of this limestone exhibits pyrite mineralization in places.

Fig. 7.2 Clast-supported scree conglomerate present at the basal part of the Kallankurichchi Formation. Note, the maximum length of clast (arrowed yellow) (a); matrix-supported conglomerate overlying scree conglomerate (b); syn-sedimentary slide planes present within conglomerate (dotted) (c); dark-grey limestone overlain by the yellowish fossiliferous limestone (d). Note Hammer length = 30 cm.

The wedge-shaped, dark-coloured limestone possibly formed in a relatively deeper part of the subsiding basin. The fine-grained nature, a contrasting dark grey colour, and the lack of fossils further reinstate this interpretation. The presence of pyrite mineral also suggests that the depositional surface must have attained significant oxygen depletion, possibly because of the repeated subsidence. Interestingly, the non-recurring nature of this facies indicates that the condition of deposition required for this limestone never reappears during the deposition of the Kallankurichchi Formation. The crudely developed planar laminae suggest a low-energy environment of deposition compared to the overlying ripple or cross-laminated limestones dominated by wave or tidal processes with occasional storm intervention (Fürsich et al., 2005; Srimani et al., 2021). The presence of angular and rounded sideromelane glass particles strongly suggests a volcaniclastic input during the deposition of the dark grey limestone facies (discussed in the subsequent section). The sideromelane glass particles in the dark grey limestone possibly originated from continuous rifting/post-rifting events. The scree conglomerates and slide planes within them mark episodes of tectonic disturbance and basin subsidence. The repetitive siliciclastic influx at the lower part reflects the tectonic unrest of this rift basin. The repetitive subsidence leads to the development of relatively deeper paleogeography. The presence of numerous slide planes associated with the earlier facies described above also supports the idea that the subsidence along those planes was not the same everywhere across the basin. The discontinuous nature of dark grey limestone facies also signifies a sudden deepening of the basin because of the subsidence, which facilitates anoxic bottom water conditions and favors the formation of authigenic green clay minerals.

7.3 Mode of occurrences of the green marine clay:

The dark grey limestone facies exhibit a varying degree of mineral alteration, resulting in the formation of light green to dark greenish-brown authigenic clay minerals. The primary framework grain components include randomly oriented, angular to sub-rounded, poorly sorted quartz, feldspar (predominantly K-feldspar with rare plagioclase), and mica

(mostly biotite), in addition to rounded to sub-rounded sideromelane glass particles (Fig. 7.3a). Abundant carbonate cementation results in the destruction of the primary intergranular porosity (Figs. 7.3b). The authigenic green clay, principally occurring as angular to rounded grain pseudomorphs, comprises approx. 30–40% of the total rock by volume (Figs. 7.3a, b). The green clay mineral pseudomorphs exhibit partial to complete alteration of unidentifiable framework grains without destroying the original grain shape (Figs. 7.3a–c). Most (~60% of the total green grain population) of these green clay pseudomorphs exhibit a well-developed greenish-brown rim and a light brown core under plane-polarized light (Fig. 7.3a–b). The core exhibits a variegated yellow to green interference color under crossed polars with radial extinction pattern, and the rim shows yellow to dark green interference color with mottled extinction due to the fine aggregate of the brown clay crystals (Fig. 7.3c). These grains range from fine silt (minimum grain size: ~40 µm) to medium sand size (maximum longest dimension: ~350 µm). The green clay pseudomorphs constitute ~ 80–90% of the total green grain population. The remaining green clay minerals form along the cleavages of feldspar grains (~8-10% of the total green grain population) (Fig. 7.3c), along the rim of the quartz, and, in rare instances, as pore-filling material within broken bioclast fragments (~0–2% of the total green grain population) (Fig. 7.3d). The limestone unit also hosts abundant fresh to partially altered sideromelane glass particles, ranging in diameter from ~100 to ~350 µm. These often show micro-phenocrysts and manifest partial devitrification and/or alteration to palagonite along fractures but do not exhibit any sign of alteration to the greenish-brown clay (Fig. 7.3e). The sporadic appearance of gas bubble structure with perfectly spherical vesicles is also observed (Fig. 7.3f).

7.4 Micro-texture of green grains:

The micro-textural studies of the partially altered grain pseudomorphs reveal an interconnected network of tiny and elongated flakes (Figs. 7.4a-g). Individual flakes are a few microns (1–5 µm) long and lack the rosette arrangement or curled flakes (Figs. 7.4b, d, g). The tiny, elongated flakes show a dense network at the rim, while the core remains porous

due to the interconnected nature of the large, curly flakes (Figs. 7.4b, d). A similar micro-texture of the authigenic green clay has been observed forming along the cleavages of the feldspar grains (Figs. 7.4e-g). Some sideromelane glass particles show micro-phenocrysts and a dissolution texture (Fig. 7.4h). Some of the sideromelane glass, especially those with cracks, show palagonitization along the cracks or in small circular blebs (Fig. 7.4i), which was further evident from EDS spot analysis data and EPMA data (Table 7.1 and 7.2).

Table 7.1 EDS spot analysis of the sideromelane glass and its alteration (Values are in wt%, BDL=Below detection level).

	Grain 1 (see figure 7.4h)					Grain 2 (see figure 7.4i)					
	Spot 1	Spot 2	Spot 3	Spot 4	Spot 5	Spot 1	Spot 2	Spot 3	Spot 4	Spot 5	Spot 6
MgO	BDL	7.66	5.51	8.06	4.93	5.29	4.13	4.71	4.26	4.49	4.51
Al_2O_3	14.68	16.78	21.65	16.82	15.10	20.69	19.76	21.18	24.15	20.18	19.42
SiO_2	28.99	42.64	48.75	44.01	31.51	48.90	36.99	38.96	48.97	34.46	35.49
TiO_2	1.95	BDL	BDL	BDL	1.23	BDL	0.77	BDL	BDL	BDL	0.75
K_2O	1.18	1.59	1.49	1.78	1.22	1.64	BDL	BDL	BDL	BDL	BDL
CaO	1.23	BDL	1.51	BDL	1.05	BDL	1.22	BDL	BDL	1.06	1.16
FeO	27.74	13.24	20.62	11.12	20.82	12.44	18.26	16.58	10.82	19.49	17.93
Total	75.77	81.90	99.54	81.78	75.85	88.96	81.12	81.43	88.20	79.69	79.27

7.5 Mineralogy of green grains:

The whole rock sample of the dark grey limestone facies reveals a series of broad-based and asymmetric peaks along with several sharp, symmetric peaks (Fig. 7.5). The broad-based and asymmetric peaks are located at 12.18°, 19.71°, 24.93°, 31.47°, 47.17°, 59.34° and 60.75° 2θ (Figs. 7.5a-b). Re-analyzing the sample at lower diffraction angles reveals a broad-based and asymmetric peak at 12.18° 2θ corresponding to the d-spacing of 7.26 Å, suggesting the presence of a 1:1 clay mineral structure. The 1:1 clay mineral structure, as observed from the whole rock study, shows d-spacings of (001) at 7.26 Å, (020) at 4.50 Å, (002) at 3.56 Å, (130) at 2.68 Å and (060) at 1.55 Å (Figs. 7.5a-b). These reflections are also broad-based and

have asymmetric peaks. The air-dried, oriented, and smear-mounted clay separates of the same sample, shows d-spacings of (001) at 7.20 Å, (020) at 4.48 Å, (002) at 3.55 Å, (130) at

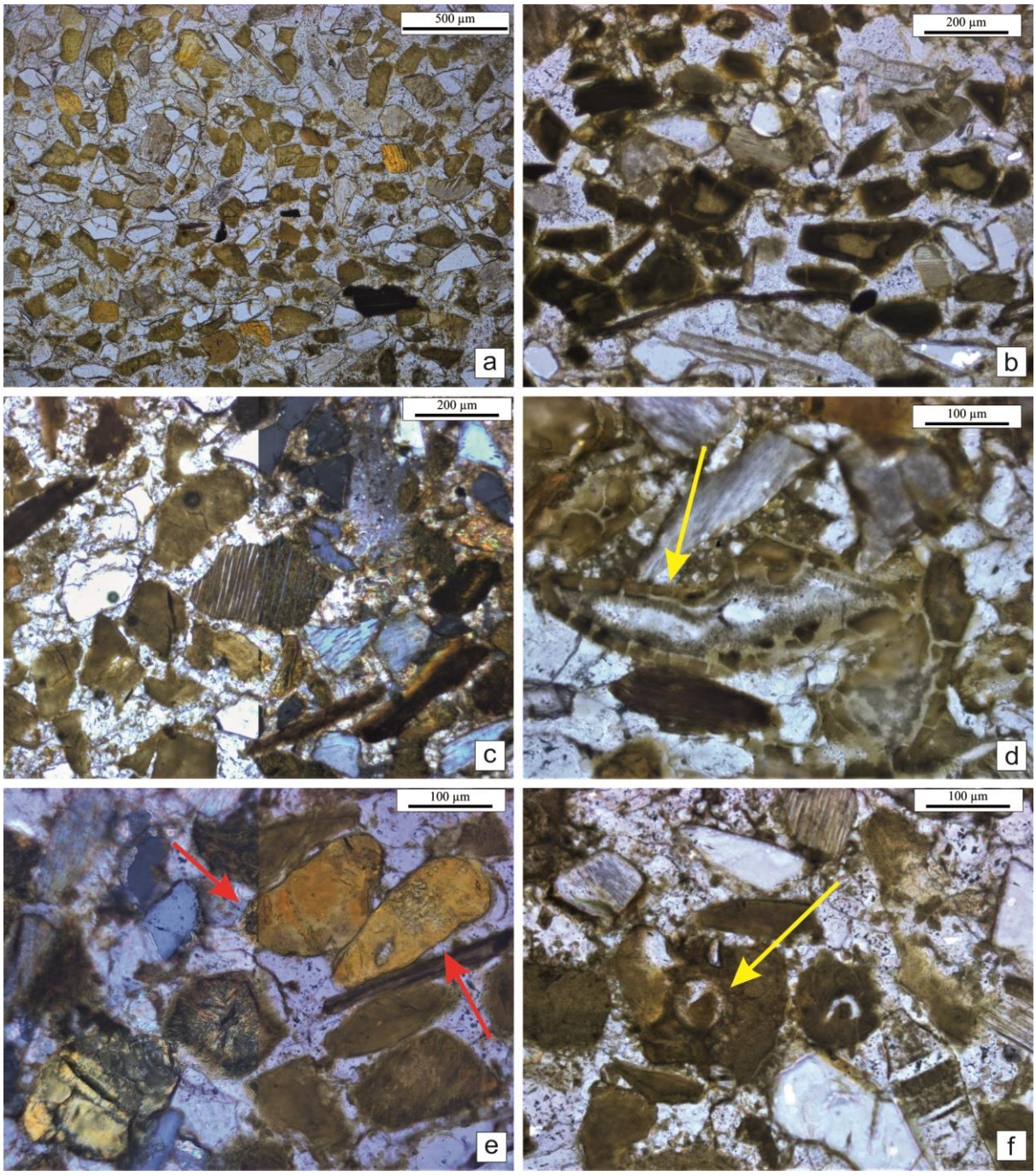

Fig. 7.3 Photomicrograph of the basal limestone of the Kallankurichchi Formation with random orientation of frameworks grains and the widespread authigenic clay formation

preserving the morphology of the precursor grain (plane polarized light) (a); strong color difference between light green core and dark green rim of the altered mineral grains (under crossed polarsized light) (b); green clay mineral formation along the feldspar cleavage along with abundant angular to sub-rounded mineral alteration and quartz grains with abundant carbonate cement (left half of the picture is in plane polarized light and the right half is in crossed polarized light) (c); authigenic green clay mineral growth vertical to the bioclast test (note the yellow arrow marks the green clay formation altering the primary test (plane polarized light) (d); authigenic green clay mineral growth vertical to the grain boundary without destroying the substrate grain shape and morphology, also note the fresh to partially devitrified (red arrow) sideromelane glass (left half of the picture is in crossed polarized light and the right half is in plane polarized light) (e); perfectly spherical gas bubble structure (yellow arrow) preserved within the berthierine grain pseudomorph (plane polarized light) (f).

2.68 Å and (060) at 1.55 Å (Fig. 7.6). The peak position does not shift after glycolation. However, the broad hump at ~14 Å disappears after glycolation. Heating the sample at 550 °C for 1 hour destroys most of the broad and asymmetric peaks of the clay separates, including the (001), (002), (130), and (060), though the (020) reflection persist (Fig. 7.6).

The presence of a ~7 Å reflection and the absence of the 14 Å reflections rule out the possibility of chlorite or smectite (Moore and Reynolds, 1997). The prominence of the (020) peak even after heating at 550 °C rules out the possibility of a kaolinite-serpentine group of clay minerals and confirms berthierine as the primary clay mineral species (Iijima and Matsumoto, 1982; Taylor, 1990; Hornibrook and Longstaffe, 1996; Tang et al., 2017a; Ma et al., 2022). The unit-cell dimensions of the berthierine are calculated to be: a = 5.01 Å, b = 9.63 Å, and c = 7 Å. The sharp and symmetric peaks, with characteristic d-spacing of 3.84 Å, 3.02 Å, 2.49 Å, 2.28 Å, and 2.08 Å, situated at 23.15°, 29.52°, 36.10°, 39.54°, and 43.30°, respectively, demarcates calcite from dolomite. The presence of quartz is marked by sharp and symmetric reflections at 4.26 Å, 3.34 Å, 1.80 Å, and 1.54 Å (Fig. 7.5).

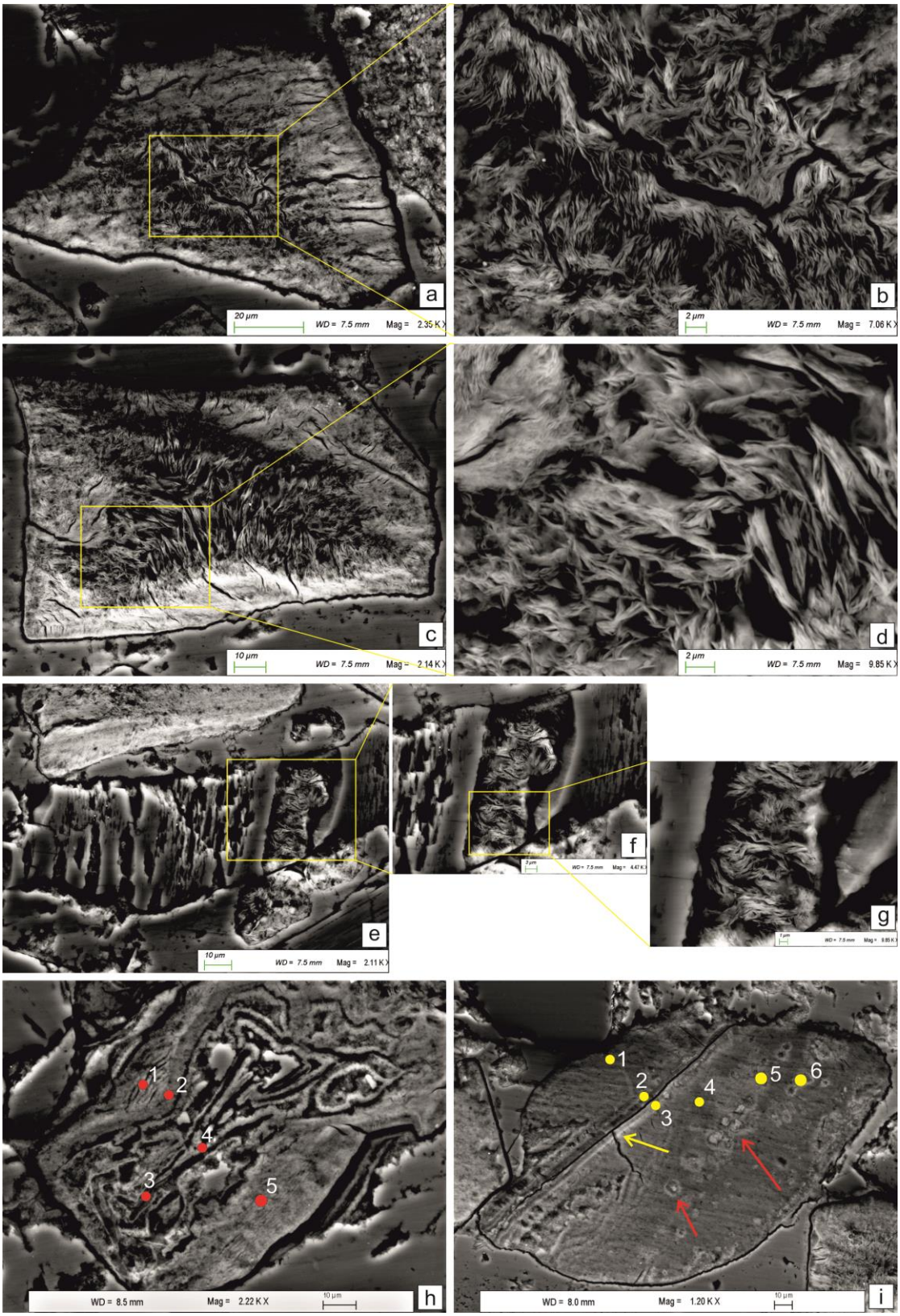
a
20 µm
WD = 7.5 mm
Mag = 2.35 K X
b
2 µm
WD = 7.5 mm
Mag = 7.06 K X
c
10 µm
WD = 7.5 mm
Mag = 2.14 K X
d
2 µm
WD = 7.5 mm
Mag = 9.85 K X
e
10 µm
WD = 7.5 mm
Mag = 2.11 K X
f
g
h
1
2
3
4
5
WD = 8.5 mm
Mag = 2.22 K X
10 µm
i
1
2
3
4
5
6
WD = 8.0 mm
Mag = 1.20 K X
10 µm

Fig. 7.4 micro-texture of the greenish-brown clay mineral formed in partially altered grains showing large, curved flakes intermixed and forming a porous texture in the core while the rims are made up of tiny flakes in dense arrangement reflecting a compact nature. Note that the tiny clay flakes grow almost perpendicular to the grain boundary (a–d); Formation of the greenish-brown clay along the feldspar cleavages (e–g); devitrified sideromelane glass exhibiting prominent dissolution texture (numbers with red dots correspond to EDS spot data provided in Table 7.1) (h); partially palagonitized sideromelane glass along a crack (yellow arrow) and in small blebs (marked with red arrow) (numbers with yellow dots correspond to EDS spot data provided in Table 7.1) (i).

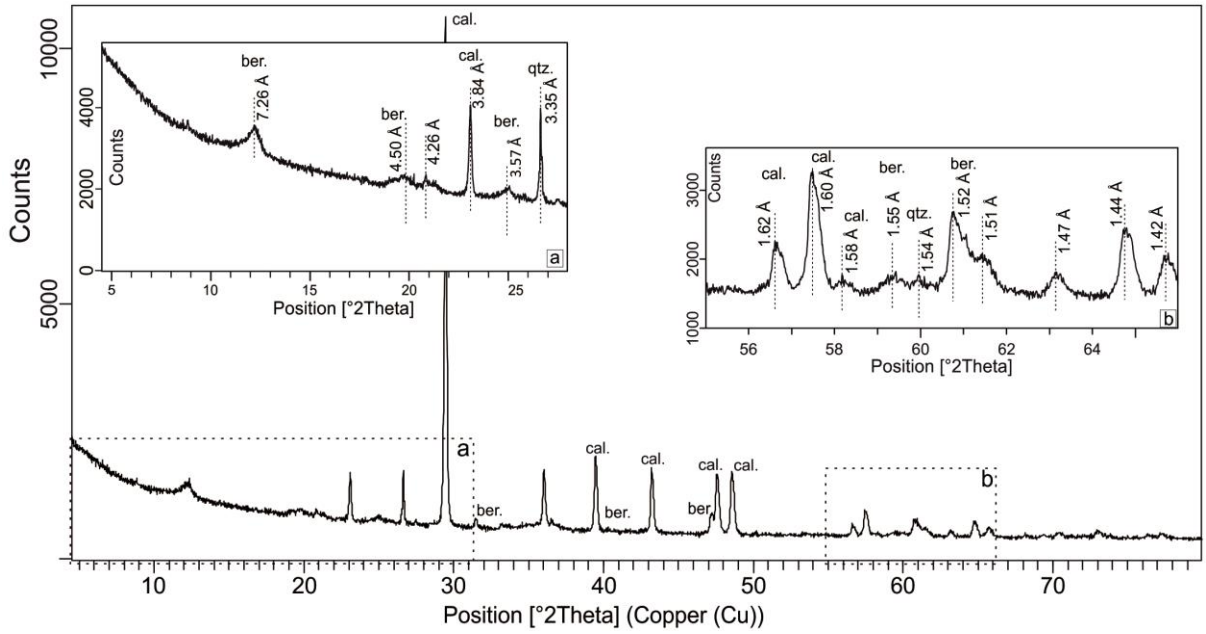

Fig. 7.5 X-Ray Diffraction of the basal limestone of the Kallankurichchi Formation. Note the high intensity of the peak at ~30° 2θ masking the lower angle reflections. Re-analysis of the same sample from 4.5–28° 2θ (see inset a) and 55–66° 2θ (see inset b) revealing characteristic peaks of berthierine (ber. = berthierine, cal. = calcite and qtz. = quartz).

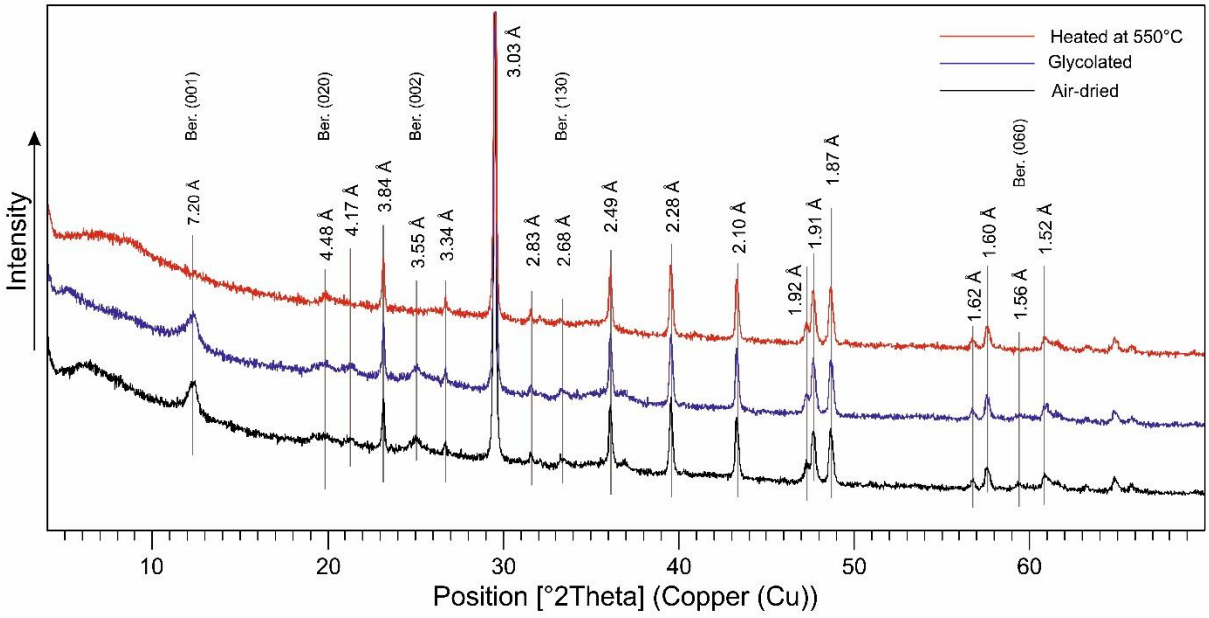

Fig. 7.6 X-Ray diffractogram of the clay separates of the dark grey limestone facies of the Kallankurichchi Formation (ber. = berthierine) (*hkl* values assigned after Taylor, 1990).

7.6 Major oxide analysis:

The major oxide analysis of individual data points from the authigenic green clay pseudomorphs demarcates a cation-poor composition with negligible Na_2O and K_2O (av. concentration ~ 0.1 wt%) (Table 7.2a, b). The EPMA backscatter images of most of the green clay pseudomorphs (observed under a petrographic microscope) exhibit a strong contrast (brightness contrast as seen in BSE images) between the core and rim (Fig. 7.7a). A few green clay pseudomorphs, however, do not show any contrast, suggesting a homogeneous composition (Figs. 7.7a-b). The cores of the green grain pseudomorphs are rich in Al_2O_3, MgO, and SiO_2 and appear dark, while the rims appear bright in the backscatter images and are rich in FeO(total). The Al_2O_3 content of the cores varies from 14.4 to 22.8 wt% (av. 18.0 wt%), while the rims contain av. 14.4 wt% of Al_2O_3 (12.5 to 16.1 wt%). The MgO content of the cores is significantly higher with av. 6.9 wt%, than that of the rims, ranging from 2.0 to 7.3 wt% (av. 3.5 wt%). The cores exhibit a wide range of FeO(total) concentration, ranging

from 15.1 to 35.5 wt% (av. 23.8 wt%). The content of FeO(total) in the rim varies from 31.9 to 42.6 wt% (av. 39.0 wt%). The SiO_2 content of the cores ranges from 31.1 to 43.3 wt% (av. 37.1 wt%), while for the rims, it ranges from 26.2 to 33.0 wt% (av. 29.6 wt%). All these analyses show consistently small amounts of CaO (av. 1.1 wt%), possibly as an impurity.

All EPMA data points were normalized to 100 wt% on an anhydrous basis for various cross-plots. The FeO(total) used in different bi-variate plots represents total iron measured using EPMA without determining the valency. All the bi-variate plots reveal two clusters of data sets reflecting the compositional difference between the core and rim of the green clay pseudomorphs. The MgO vs. FeO(total) cross-plot shows a good negative correlation (Fig. 7.8a), suggesting an increase in FeO(total) content from core to rim and a decrease in MgO. While the MgO and FeO(total) content of cores vary widely, the rims exhibit significantly narrower FeO(total) content. The Al_2O_3 vs. FeO(total) cross-plot indicates an excellent negative correlation (r^2=0.9) (Fig. 7.8b), suggesting significant Al-for-Fe substitution in the clay mineral structure. The Al_2O_3 vs. SiO_2 cross-plot shows an equally good positive correlation (r^2=0.9) (Fig. 7.8c). The Fe/(Fe/Mg) ratio is low for the core and high for the rims. Compositionally, the rims represent 'ideal' berthierine composition, while the cores are rich in Al, Si and Mg, suggesting an intermediate chemical composition between odinite and berthierine (Brindley, 1982; Bailey, 1988; Hornibrook and Longstaffe, 1996; Toth and Fritz, 1997; Ku and Walter, 2003; Huggett et al., 2010, 2017; Mu et al., 2015). However, the compositional similarity between 'odinite' can be discarded from the low molar Mg/Al and Si/Al ratio of the core and rim of the studied green grains and the fact that iron in the clay is dominantly Fe^{2+} (~82% of the total iron is calculated to be Fe^{2+}) (Table 7.2a,b) (Brindley, 1982; Bailey, 1988; Toth and Fritz, 1997; Sheldon and Retallack, 2003). Therefore, the core composition possibly represents the 'proto-berthierine' composition, i.e., the incipient phase of the berthierine clay mineral (Brindley, 1982; Iijima and Matsumoto, 1982; Bailey, 1988; Odin, 1988; Taylor, 1990; Hornibrook and Longstaffe, 1996; Toth and Fritz, 1997; Huggett et al., 2010; Tang et al., 2017b).

The average Fe^{2+}/Fe^{3+} ratio of the green clay pseudomorph is calculated to be 4.5, which is used to calculate the structural formula of the green clay pseudomorph (Table 7.3a,

b). The average structural formula (calculated based on seven (7) oxygen) of the berthierine rim is $(K_{0.01}, Na_{0.02}, Ca_{0.01})$ $(Al_{0.51}, Fe^{3+}_{0.32}, Fe^{2+}_{1.60}, Mg_{0.29})_{2.71}$ $(Si_{1.59}, Al_{0.41})$ $O_5(OH)_4$. On the other hand, the core with 'proto'-berthierine composition has an average structural formula of $(K_{0.01}, Na_{0.03}, Ca_{0.01})$ $(Al_{0.88}, Fe^{3+}_{0.18}, Fe^{2+}_{0.91}, Mg_{0.52})_{2.49}$ $(Si_{1.84}, Al_{0.16})$ $O_5(OH)_4$.

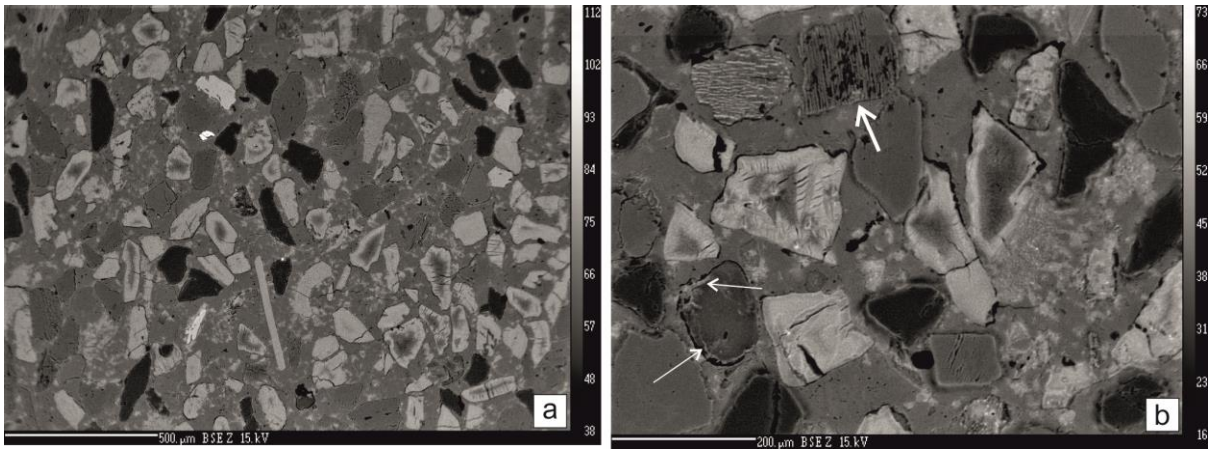

Fig. 7.7 Back-scattered Electron (BSE) images of the dark grey limestone unit showing angular to sub-angular grain pseudomorph with a strong contrast between the bright rim and dark core; note the abundance of the grain pseudomorph in the sample (a); partially palagonitized sideromelane glass (thin arrow) along with grain pseudomorph and feldspar alteration thick arrow) (b).

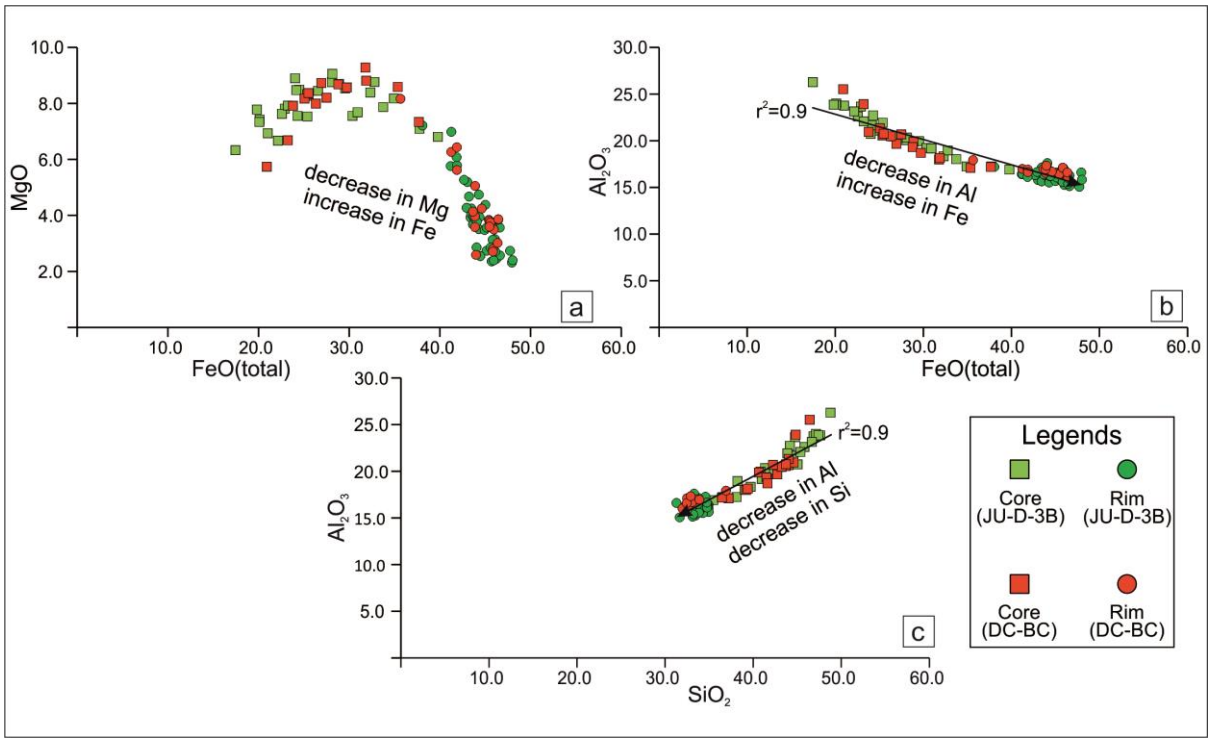

Fig. 7.8 Bi-variate plots of the major oxide composition of the berthierine clay mineral. The FeO(total) vs. MgO cross-plot suggesting a decrease in MgO content with an increase in FeO(total) content (a); the FeO(total) vs. Al_2O_3 cross-plot showing a decrease in Al_2O_3 concentration with an increase in FeO(total) (b); the SiO_2 vs. Al_2O_3 ross-plot suggests decrease in Al_2O_3 with respect to decrease in SiO_2 content (c).

Table 7.2a EPMA spot analysis of major oxides (wt%) of green clay (berthierine) from the dark grey limestone (BDL=Below detection level).

Sample name	DataSet/Point	Na_2O	MgO	Al_2O_3	SiO_2	P_2O_5	K_2O	CaO	Cr_2O_3	MnO	Fe_2O_3(total)	Total	Comment
JU-D-3B	4 / 1	0.1	7.5	18.7	39.2	0.0	0.1	1.2	0.1	0.1	24.1	91.0	Core
	6 / 1	0.1	5.8	19.7	38.9	0.0	0.0	1.1	0.0	0.0	19.4	85.0	
	8 / 1	0.1	6.6	21.3	41.8	0.0	0.1	1.0	0.0	0.0	19.8	90.6	
	11 / 1	0.1	6.5	21.1	42.1	0.0	0.0	0.8	0.0	0.0	19.7	90.3	
	13 / 1	0.0	6.8	20.7	39.1	0.0	0.0	0.7	0.0	0.0	22.3	89.7	
	17 / 1	0.0	7.3	16.8	35.0	0.1	0.0	0.9	0.0	0.0	26.1	86.2	
	19 / 1	0.1	8.0	18.0	36.6	0.1	0.0	0.8	0.0	0.0	27.6	91.2	
	23 / 1	0.1	6.3	19.1	37.1	0.0	0.0	0.9	0.0	0.0	22.7	86.2	
	25 / 1	0.1	7.5	16.3	35.4	0.0	0.0	1.1	0.0	0.0	32.0	92.3	
	28 / 1.	0.1	7.1	15.0	33.2	0.0	0.0	1.2	0.0	0.0	33.8	90.5	
	30 / 1	0.1	6.3	15.4	32.6	0.0	0.1	1.0	0.0	0.1	37.4	92.9	
	32 / 1	0.1	7.0	16.1	34.9	0.0	0.1	1.0	0.0	0.0	33.5	92.8	
	35 / 1	0.1	7.4	17.2	35.2	0.0	0.1	0.8	0.0	0.0	28.3	89.1	
	37 / 1	0.1	5.5	22.8	42.3	0.0	0.0	0.8	0.0	0.0	16.8	88.3	
	39 / 1	0.1	7.6	16.4	33.1	0.0	0.0	1.0	0.0	0.0	31.5	89.7	
	1 / 1	0.2	7.1	21.8	43.3	0.0	0.2	0.7	0.0	0.0	20.1	93.4	
	18 / 1	0.2	7.1	16.5	35.8	0.0	0.1	0.7	0.0	0.0	25.9	86.3	
	48 / 1	0.2	6.1	15.1	31.7	0.0	0.1	0.6	0.0	0.0	39.5	93.4	
	53 / 1	0.2	7.6	19.5	40.0	0.0	0.2	0.6	0.0	0.0	24.1	92.3	
	55 / 1	0.2	6.6	19.5	39.5	0.0	0.2	0.7	0.0	0.0	21.6	88.4	
	57 / 1	0.2	6.9	19.1	39.3	0.0	0.2	0.8	0.0	0.0	22.4	88.8	
	59 / 1	0.2	6.2	18.1	36.2	0.0	0.2	0.7	0.0	0.0	23.3	84.8	
	61 / 1	0.3	7.6	18.5	39.0	0.0	0.2	0.8	0.0	0.0	26.6	92.9	
	80 / 1	0.2	6.7	17.0	36.7	0.0	0.1	0.7	0.0	0.0	29.8	91.2	
	87 / 1	0.2	6.7	16.8	35.9	0.0	0.1	0.8	0.0	0.0	30.1	90.6	
	85 / 1	0.2	5.2	18.1	36.5	0.0	0.2	0.7	0.0	0.0	19.3	80.2	
	87 / 1	0.2	6.7	16.8	35.9	0.0	0.1	0.8	0.0	0.0	30.1	90.6	

	5 / 1	0.1	2.5	15.2	30.9	0.0	0.1	1.3	0.0	0.0	45.8	95.8	
	7 / 1	0.1	3.6	14.5	31.7	0.0	0.0	1.4	0.0	0.0	43.7	95.0	
	9 / 1	0.0	2.1	14.4	28.8	0.0	0.1	1.3	0.0	0.0	44.7	91.4	
	12 / 1	0.1	2.8	14.3	30.1	0.0	0.0	1.0	0.0	0.1	46.0	94.5	
	14 / 1	0.0	3.6	14.4	31.1	0.0	0.0	1.4	0.0	0.0	43.9	94.5	
	18 / 1	0.1	2.3	12.5	26.2	0.0	0.0	2.2	0.0	0.0	43.8	87.1	
	20 / 1	0.1	4.0	14.1	29.7	0.0	0.1	1.2	0.0	0.0	41.5	90.7	
	24 / 1	0.1	4.5	13.7	29.7	0.0	0.0	1.2	0.0	0.1	41.3	90.5	
	26 / 1	0.0	3.6	14.7	30.8	0.0	0.0	1.1	0.0	0.0	43.9	94.2	
	29 / 1	0.1	3.6	13.8	30.8	0.0	0.0	1.5	0.0	0.0	42.5	92.3	
	31 / 1	0.1	3.3	14.8	30.9	0.0	0.0	1.1	0.0	0.0	43.3	93.6	
	33 / 1	0.1	2.3	14.4	29.4	0.0	0.0	1.0	0.0	0.0	45.8	93.1	
	36 / 1	0.1	5.0	14.2	30.2	0.0	0.1	1.2	0.1	0.0	39.6	90.4	
	38 / 1	0.1	4.0	13.2	28.2	0.0	0.0	1.2	0.0	0.0	41.2	87.9	
	40 / 1	0.1	3.1	13.7	30.2	0.0	0.1	1.8	0.1	0.0	43.4	92.5	
	2 / 1	0.2	3.1	13.1	28.7	0.0	0.1	1.1	0.0	0.0	43.8	90.1	**Rim**
	49 / 1	0.2	3.1	14.4	30.7	0.0	0.1	1.0	0.0	0.0	45.0	94.7	
	54 / 1	0.2	3.6	15.0	31.9	0.0	0.1	0.8	0.0	0.0	44.6	96.2	
	56 / 1	0.1	3.9	13.8	29.6	0.0	0.2	0.9	0.0	0.0	44.0	92.3	
	58 / 1	0.2	2.6	15.9	31.7	0.0	0.1	0.8	0.0	0.0	44.9	96.3	
	60 / 1	0.2	3.6	14.6	31.0	0.0	0.1	0.8	0.0	0.0	44.5	94.7	
	62 / 1	0.2	3.7	15.1	32.0	0.0	0.2	0.8	0.0	0.0	44.7	96.6	
	81 / 1	0.2	2.8	14.3	29.9	0.0	0.1	1.0	0.0	0.0	45.5	93.9	
	86 / 1	0.1	3.0	12.9	28.2	0.0	0.2	1.0	0.0	0.0	44.0	89.4	
	88 / 1	0.2	3.8	15.4	30.3	0.0	0.1	0.9	0.0	0.0	43.3	94.0	
	3 / 1	0.1	2.1	14.8	27.8	0.0	0.1	1.3	0.1	0.1	47.4	93.6	
	10 / 1	0.1	2.1	14.2	29.2	0.0	0.1	2.0	0.0	0.0	44.7	92.4	
	15 / 1	0.1	2.4	14.5	29.4	0.0	0.0	1.1	0.0	0.1	45.3	92.9	
	16 / 1	0.1	5.2	14.7	31.0	0.0	0.0	0.9	0.1	0.0	41.6	93.5	
	27 / 1	0.0	3.3	14.0	29.8	0.0	0.0	1.1	0.0	0.0	45.1	93.4	
	34 / 1	0.1	6.1	14.4	29.8	0.1	0.0	0.8	0.0	0.0	40.0	91.4	

	43 / 1	0.1	2.1	15.2	29.7	0.0	0.0	1.0	0.0	0.0	45.6	93.9	
	8 / 1	0.1	6.4	15.2	32.3	0.0	0.1	0.6	0.0	0.0	37.4	92.2	
	33 / 1	0.2	3.2	14.3	30.3	0.0	0.1	0.7	0.0	0.1	44.7	93.5	
	37 / 1	0.2	2.2	14.1	28.4	0.0	0.1	3.3	0.0	0.0	42.9	91.2	
	43 / 1	0.2	3.1	13.7	29.8	0.0	0.1	0.7	0.0	0.0	44.8	92.5	
	44 / 1	0.2	4.8	14.8	31.2	0.0	0.1	0.8	0.0	0.0	42.9	94.9	
	45 / 1	0.2	5.3	14.1	30.5	0.0	0.1	0.7	0.0	0.0	40.7	91.7	
	46 / 1	0.1	3.3	13.4	28.8	0.0	0.1	0.7	0.0	0.0	44.8	91.3	
	47 / 1	0.2	3.9	15.4	32.1	0.0	0.1	0.9	0.0	0.0	44.1	96.8	
	50 / 1	0.2	2.6	14.8	30.3	0.0	0.2	0.8	0.0	0.0	45.4	94.2	
	89 / 1	0.2	3.4	15.8	29.8	0.0	0.2	0.7	0.0	0.0	43.8	93.8	
	90 / 1	0.2	2.0	13.4	27.5	0.0	0.1	0.8	0.0	0.0	45.2	89.2	

Table 7.2b EPMA spot analysis of major oxides (wt%) of green clay (berthierine) from dark grey limestone (BDL=Below detection level).

Sample name	DataSet/Point	Na_2O	MgO	Al_2O_3	SiO_2	P_2O_5	K_2O	CaO	Cr_2O_3	MnO	Fe_2O_3(total)	Total	Comment
DC-BC	4 / 1	0.4	8.2	15.9	34.6	0.0	0.2	0.9	0.0	0.1	31.2	91.5	Core
	6 / 1	0.5	7.7	17.3	37.5	0.0	0.1	1.1	0.0	0.0	26.3	90.4	
	8 / 1	0.3	7.2	14.4	31.2	0.0	0.1	1.0	0.0	0.0	33.0	87.2	
	12 / 1	0.3	7.4	18.4	39.1	0.0	0.1	1.0	0.0	0.0	25.2	91.5	
	14 / 1	0.6	7.4	18.1	38.5	0.0	0.2	1.0	0.0	0.0	24.9	90.7	
	16 / 1	0.4	5.0	22.3	40.5	0.0	0.2	0.6	0.0	0.0	20.3	89.4	
	25 / 1	0.5	7.0	18.1	38.1	0.1	0.2	1.0	0.0	0.0	25.8	90.7	
	30 / 1	0.5	7.7	15.9	34.6	0.0	0.1	0.9	0.0	0.1	31.1	90.9	
	35 / 1	0.7	7.0	18.6	39.6	0.0	0.2	0.8	0.7	0.0	23.5	91.2	
	59 / 1	0.6	7.7	17.6	36.0	0.0	0.1	0.9	0.0	0.0	28.4	91.4	
	71 / 1	0.4	7.7	17.2	37.0	0.0	0.1	1.1	0.0	0.0	28.5	92.0	
	85 / 1	0.2	7.1	17.9	36.5	0.0	0.1	0.8	0.0	0.0	26.4	89.1	
	90 / 1	0.2	7.2	18.8	38.7	0.0	0.1	0.8	0.0	0.0	24.5	90.3	
	106 /1	0.3	5.8	20.9	39.2	0.0	0.1	0.8	0.0	0.0	22.6	89.7	
	112 / 1	0.4	7.6	18.8	39.7	0.0	0.1	0.9	0.0	0.0	25.7	93.3	
	114 / 1	0.3	7.4	16.2	36.0	0.0	0.1	0.8	0.0	0.0	28.6	89.4	
	116 / 1	0.2	6.3	14.7	31.1	0.0	0.1	0.8	0.0	0.0	35.7	88.8	
	5 / 1	0.3	4.5	14.6	29.1	0.0	0.1	0.8	0.0	0.0	42.9	92.4	Rim
	7 / 1	0.3	3.0	14.1	27.9	0.0	0.1	1.2	0.0	0.0	44.1	90.8	
	9 / 1	0.3	3.4	14.5	28.7	0.0	0.1	1.1	0.0	0.0	44.4	92.5	
	13 / 1	0.2	3.3	14.3	28.4	0.0	0.1	1.2	0.0	0.0	43.9	91.4	
	15 / 1	0.5	3.6	15.2	29.8	0.0	0.1	1.2	0.0	0.0	43.7	94.2	
	17 / 1	0.4	5.6	15.1	30.1	0.0	0.1	1.1	0.0	0.0	40.8	93.1	
	26 / 1	0.4	3.2	14.2	28.1	0.0	0.1	0.9	0.0	0.1	43.6	90.6	
	31 / 1	0.4	3.0	13.8	27.5	0.0	0.1	0.9	0.0	0.0	42.4	88.3	
	36 / 1	0.4	4.7	14.3	28.5	0.0	0.1	1.0	0.0	0.0	39.2	88.3	
	60 / 1	0.4	5.6	14.4	28.8	0.0	0.0	1.0	0.0	0.0	40.1	90.3	
	72 / 1	0.3	3.7	15.1	29.9	0.1	0.1	1.0	0.0	0.0	43.2	93.4	

	86 / 1	0.2	7.3	16.1	33.0	0.0	0.0	0.9	0.0	0.0	35.5	93.1	
	91 / 1	0.2	3.6	14.2	28.0	0.0	0.1	0.9	0.0	0.0	42.0	89.1	
	107 / 1	0.3	3.2	13.4	26.8	0.0	0.1	0.9	0.1	0.1	43.2	88.0	
	113 / 1	0.3	2.5	15.1	28.6	0.0	0.1	1.1	0.0	0.0	44.8	92.5	
	115 / 1	0.3	3.0	14.0	28.0	0.0	0.0	1.0	0.0	0.1	40.3	86.7	
	117 / 1	0.3	2.3	14.8	28.1	0.0	0.1	1.1	0.0	0.1	44.0	90.8	
	10 / 1	0.3	2.6	14.2	27.8	0.0	0.1	0.9	0.0	0.1	44.1	90.0	
	40 / 1	0.5	2.2	14.9	28.3	0.4	0.2	1.6	0.1	0.0	41.9	90.1	

Table 7.3a Structural formula of green clay (berthierine).

Sample name		Tetrahedra		Octahedra				Interlayer			
	Comment	Si	Al	Al	Fe^{3+}	Fe^{2+}	Mg	Ca	Na	K	Total Octa.
JU-D-3B	Core	1.88	0.12	0.94	0.16	0.79	0.54	0.01	0.01	0.01	2.44
		1.95	0.05	1.11	0.13	0.66	0.43	0.01	0.01	0.00	2.34
		1.95	0.05	1.12	0.13	0.63	0.46	0.01	0.01	0.00	2.34
		1.97	0.03	1.13	0.13	0.63	0.45	0.01	0.01	0.00	2.34
		1.88	0.12	1.05	0.15	0.73	0.49	0.00	0.00	0.00	2.42
		1.82	0.18	0.84	0.19	0.93	0.57	0.01	0.00	0.00	2.52
		1.80	0.20	0.84	0.19	0.93	0.59	0.01	0.01	0.00	2.54
		1.87	0.13	1.01	0.16	0.78	0.48	0.01	0.01	0.00	2.43
		1.76	0.24	0.72	0.22	1.09	0.56	0.01	0.01	0.00	2.59
		1.72	0.28	0.64	0.24	1.20	0.55	0.01	0.01	0.00	2.63
		1.67	0.33	0.61	0.26	1.31	0.48	0.01	0.01	0.01	2.67
		1.75	0.25	0.70	0.23	1.15	0.53	0.01	0.01	0.00	2.60
		1.79	0.21	0.81	0.20	0.98	0.56	0.00	0.01	0.00	2.55
		1.99	0.01	1.25	0.11	0.54	0.38	0.01	0.01	0.00	2.28
		1.71	0.29	0.71	0.22	1.11	0.58	0.01	0.01	0.00	2.62
		1.96	0.04	1.12	0.12	0.62	0.48	0.00	0.01	0.01	2.35
		1.85	0.15	0.86	0.18	0.91	0.55	0.00	0.02	0.01	2.50
		1.64	0.36	0.56	0.28	1.40	0.47	0.00	0.02	0.01	2.71
		1.89	0.11	0.97	0.16	0.78	0.54	0.00	0.02	0.01	2.44
		1.93	0.07	1.05	0.14	0.72	0.48	0.00	0.02	0.01	2.39
		1.91	0.09	1.01	0.15	0.75	0.50	0.00	0.02	0.01	2.40
		1.87	0.13	0.97	0.16	0.82	0.48	0.00	0.02	0.01	2.44
		1.86	0.14	0.90	0.17	0.87	0.54	0.00	0.02	0.01	2.48
		1.82	0.18	0.82	0.20	1.01	0.49	0.00	0.02	0.01	2.53
		1.80	0.20	0.80	0.21	1.03	0.50	0.00	0.01	0.01	2.54
		1.95	0.05	1.09	0.14	0.70	0.42	0.00	0.02	0.02	2.35
		1.80	0.20	0.80	0.21	1.03	0.50	0.00	0.01	0.01	2.54

	Rim	1.61	0.39	0.54	0.33	1.63	0.19	0.01	0.01	0.00	2.69
		1.64	0.36	0.53	0.31	1.55	0.28	0.01	0.01	0.00	2.67
		1.58	0.42	0.51	0.34	1.68	0.18	0.01	0.00	0.00	2.70
		1.60	0.40	0.49	0.33	1.67	0.22	0.01	0.01	0.00	2.72
		1.63	0.37	0.52	0.31	1.57	0.28	0.01	0.00	0.00	2.69
		1.54	0.46	0.40	0.35	1.76	0.20	0.01	0.01	0.00	2.71
		1.61	0.39	0.52	0.31	1.55	0.33	0.01	0.01	0.01	2.70
		1.62	0.38	0.50	0.31	1.54	0.36	0.01	0.01	0.00	2.71
		1.62	0.38	0.53	0.31	1.58	0.29	0.01	0.00	0.00	2.70
		1.65	0.35	0.52	0.31	1.56	0.29	0.01	0.01	0.00	2.67
		1.63	0.37	0.55	0.31	1.56	0.26	0.01	0.01	0.00	2.68
		1.59	0.41	0.50	0.34	1.69	0.18	0.01	0.01	0.00	2.72
		1.63	0.37	0.54	0.29	1.46	0.40	0.01	0.02	0.00	2.69
		1.60	0.40	0.48	0.32	1.60	0.34	0.01	0.01	0.00	2.73
		1.63	0.37	0.50	0.32	1.60	0.25	0.01	0.01	0.00	2.67
		1.60	0.40	0.46	0.33	1.67	0.26	0.01	0.02	0.01	2.72
		1.62	0.38	0.51	0.32	1.62	0.25	0.01	0.02	0.01	2.70
		1.64	0.36	0.54	0.31	1.57	0.27	0.00	0.02	0.01	2.70
		1.60	0.40	0.48	0.33	1.63	0.31	0.00	0.01	0.01	2.74
		1.63	0.37	0.59	0.32	1.58	0.20	0.00	0.02	0.01	2.68
		1.62	0.38	0.52	0.32	1.59	0.28	0.00	0.02	0.01	2.71
		1.63	0.37	0.54	0.31	1.56	0.28	0.00	0.02	0.01	2.70
		1.60	0.40	0.50	0.33	1.66	0.22	0.01	0.02	0.01	2.71
		1.59	0.41	0.45	0.34	1.70	0.26	0.01	0.01	0.01	2.74
		1.59	0.41	0.55	0.31	1.56	0.30	0.00	0.02	0.01	2.71
		1.51	0.49	0.46	0.35	1.77	0.17	0.01	0.01	0.00	2.75
		1.59	0.41	0.50	0.33	1.66	0.17	0.01	0.01	0.00	2.66
		1.59	0.41	0.51	0.33	1.67	0.19	0.01	0.01	0.00	2.71
		1.62	0.38	0.53	0.30	1.49	0.40	0.01	0.01	0.00	2.72
		1.60	0.40	0.48	0.33	1.65	0.26	0.01	0.00	0.00	2.73
		1.60	0.40	0.50	0.29	1.47	0.49	0.00	0.01	0.00	2.75

		1.58	0.42	0.54	0.33	1.66	0.17	0.01	0.02	0.00	2.71
		1.67	0.33	0.60	0.27	1.33	0.49	0.00	0.01	0.01	2.69
		1.61	0.39	0.51	0.33	1.63	0.25	0.00	0.02	0.01	2.72
		1.57	0.43	0.48	0.32	1.62	0.18	0.02	0.02	0.01	2.61
		1.61	0.39	0.49	0.33	1.66	0.25	0.00	0.02	0.01	2.73
		1.62	0.38	0.52	0.30	1.52	0.37	0.00	0.02	0.01	2.72
		1.63	0.37	0.52	0.30	1.49	0.42	0.00	0.02	0.01	2.72
		1.59	0.41	0.46	0.34	1.69	0.27	0.00	0.01	0.01	2.76
		1.63	0.37	0.55	0.31	1.53	0.30	0.01	0.02	0.01	2.69
		1.60	0.40	0.53	0.33	1.65	0.20	0.00	0.02	0.01	2.71
		1.57	0.43	0.55	0.32	1.58	0.27	0.00	0.02	0.01	2.72
		1.56	0.44	0.46	0.35	1.76	0.17	0.00	0.02	0.01	2.75

Table 7.3b Structural formula of green clay (berthierine).

Sample name		Tetrahedra		Octahedra				Interlayer			
	Comment	Si	Al	Al	Fe^{3+}	Fe^{2+}	Mg	Ca	Na	K	Total Octa.
DC-BC	Core	1.75	0.25	0.69	0.22	1.08	0.62	0.01	0.04	0.01	2.60
		1.85	0.15	0.85	0.18	0.89	0.56	0.01	0.05	0.01	2.48
		1.69	0.31	0.61	0.24	1.22	0.58	0.01	0.04	0.01	2.65
		1.88	0.12	0.92	0.17	0.83	0.53	0.01	0.03	0.01	2.45
		1.87	0.13	0.91	0.17	0.83	0.53	0.01	0.06	0.01	2.44
		1.93	0.07	1.18	0.13	0.66	0.36	0.00	0.04	0.01	2.32
		1.86	0.14	0.90	0.17	0.86	0.51	0.01	0.05	0.01	2.45
		1.75	0.25	0.71	0.22	1.08	0.58	0.01	0.05	0.01	2.59
		1.91	0.09	0.97	0.15	0.77	0.51	0.00	0.07	0.01	2.40
		1.78	0.22	0.81	0.19	0.96	0.57	0.01	0.06	0.01	2.53
		1.81	0.19	0.81	0.19	0.96	0.57	0.01	0.03	0.01	2.52
		1.83	0.17	0.88	0.18	0.90	0.53	0.00	0.02	0.01	2.50
		1.88	0.12	0.95	0.16	0.81	0.52	0.01	0.02	0.01	2.45
		1.89	0.11	1.07	0.15	0.74	0.42	0.01	0.03	0.01	2.39
		1.87	0.13	0.92	0.17	0.83	0.53	0.01	0.03	0.01	2.45
		1.82	0.18	0.79	0.20	0.99	0.56	0.00	0.03	0.01	2.54
		1.67	0.33	0.60	0.26	1.31	0.50	0.00	0.02	0.01	2.67
	Rim	1.57	0.43	0.49	0.32	1.58	0.36	0.00	0.03	0.01	2.75
		1.55	0.45	0.47	0.33	1.67	0.25	0.01	0.03	0.01	2.73
		1.55	0.45	0.48	0.33	1.65	0.27	0.01	0.03	0.00	2.73
		1.56	0.44	0.48	0.33	1.65	0.27	0.01	0.02	0.01	2.73
		1.57	0.43	0.52	0.32	1.58	0.28	0.01	0.05	0.01	2.70

		1.58	0.42	0.52	0.29	1.47	0.44	0.01	0.04	0.00	2.72
		1.56	0.44	0.48	0.33	1.66	0.27	0.00	0.04	0.01	2.74
		1.56	0.44	0.49	0.33	1.65	0.26	0.00	0.04	0.01	2.73
		1.59	0.41	0.52	0.30	1.50	0.39	0.01	0.05	0.01	2.71
		1.57	0.43	0.49	0.30	1.50	0.45	0.01	0.04	0.00	2.74
		1.59	0.41	0.53	0.31	1.57	0.29	0.01	0.03	0.01	2.71
		1.67	0.33	0.63	0.25	1.23	0.55	0.01	0.02	0.00	2.66
		1.57	0.43	0.50	0.32	1.61	0.30	0.00	0.02	0.00	2.74
		1.54	0.46	0.45	0.34	1.70	0.28	0.00	0.03	0.01	2.76
		1.55	0.45	0.52	0.33	1.67	0.20	0.01	0.03	0.01	2.71
		1.60	0.40	0.55	0.32	1.58	0.25	0.01	0.03	0.00	2.69
		1.55	0.45	0.52	0.33	1.67	0.19	0.01	0.03	0.01	2.71
		1.55	0.45	0.49	0.34	1.69	0.22	0.00	0.03	0.00	2.73
		1.57	0.43	0.55	0.32	1.60	0.19	0.01	0.05	0.01	2.65

7.7 Rare Earth Elemental Concentration of the Dark Grey Limestone:

The concentration of REE is very low, varying from 79.3 to 146.0 ppm. The dark grey limestone is enriched with light rare earth elements (LREE) compared to heavy rare earth elements (HREE) (Fig. 7.9a), with LREE/HREE values ranging from 14.6–24.3. The chondrite-normalized spider diagram also depicts the LREE enrichment with respect to HREE with a prominent Eu-anomaly (Fig. 7.9a).

The chondrite-normalized REE spider diagram is characteristic of volcaniclastic sediment (Plank and Langmuir, 1998; Sturesson et al., 2000; Mishra and Sen, 2018). The Rb (ppm) vs. K_2O (wt%) plot also indicates a volcaniclastic source of the green-clay bearing limestone at the basal part of the Kallankurichchi Formation (Fig. 7.9b) (Andreozzi et al., 1997).

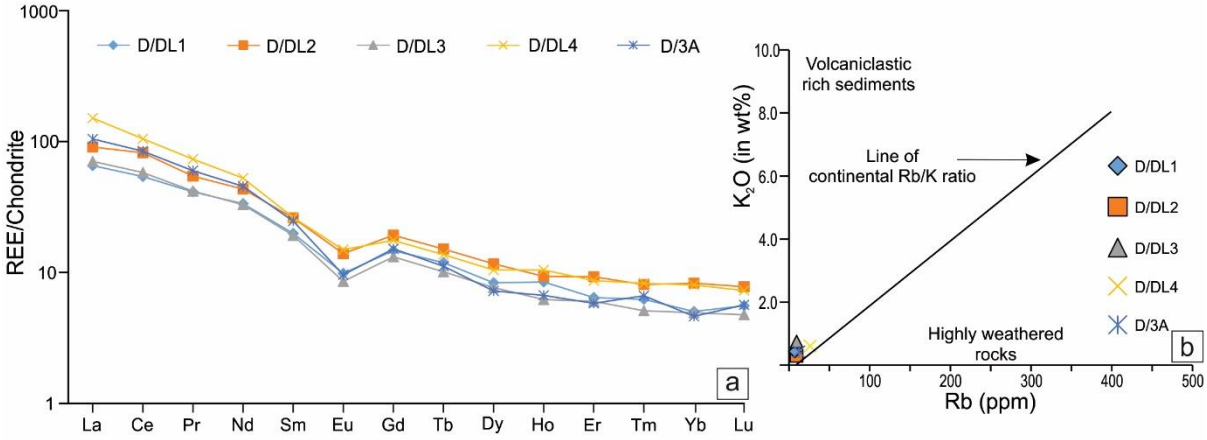

Fig. 7.9 Chondrite normalized REE pattern of the dark grey limestone of the Kallankurichchi Formation showing slight LREE enrichment over HREE (a); Rb (ppm) vs. K_2O plot of the dark grey limestone suggesting a low Rb and low K_2O concentration characteristic of volcaniclastic rich sediments (line of continental Rb/K ratio and the zones are marked after Mishra and Sen, (2018) (b).

7.8 Discussion:

7.8.1 Tectonics and depositional environment:

The berthierine clay mineral within the basal dark grey to grey limestone of the overall ~60 m thick, Kallankurichchi Formation originates in a reducing condition. The dark colour of the impure limestone supports the reducing depositional condition. In the rest of the succession, the Kallankurichchi Formation appears light yellow. The entire limestone is fossiliferous, barring this part where fossils are rare, thereby supporting the inhospitable reducing environment. The scree conglomerates and debris flow conglomerates at the basal part of this formation point to a revival of tectonic unrest in the Cauvery rift basin. The presence of numerous slide planes associated with the scree conglomerates supports the view. The scree conglomerates at the base of the slope is followed upward by debris flow deposits (Figs. 7.2a–b). The penetrated and fractured clasts signify that a steep slope was created during the initial stage of the limestone deposition (Fig. 7.2a). The presence of large carbonate clasts within these scree conglomerates suggests that the subsidence continued even after the initiation of carbonate deposition. Possibly due to this basin rejuvenation, the basin might have subsided enough and developed the reducing condition close to the seafloor.

7.8.2 Origin of berthierine:

The presence of angular to sub-rounded quartz and feldspar framework grains within the dark grey limestone suggests very little transportation (Figs. 7.3a-d) and questions whether the berthierine could be of detrital origin. However, the growth of fine berthierine crystals vertically on the grain boundary (Figs. 7.4a, c) is a characteristic of the authigenic origin (Iijima and Matsumoto, 1982; Hornibrook and Longstaffe, 1996; Fu et al., 2015; Ma et al., 2022). The occurrences of berthierine along feldspar cleavages and as pore-lining cement further reinstates this interpretation. Berthierine formation was frequent within the dark grey limestone, as precursor minerals were replaced thoroughly. However, petrographic and scanning electron microscopy show perfect preservation of the euhedral to subhedral grain

morphology of the precursor metastable volcaniclastic minerals in places that are altered to berthierine (Figs. 7.4 a, c). The poorly sorted, angular to sub-angular grains, suggesting the rapid deposition of sediments with little or no transportation, along with the relics of devitrified sideromelane glass, argue for a volcaniclastic source of the sediments (Figs. 7.4h, i).

Authigenic berthierine formation requires an abundant supply of iron in the depositional environment as well as a reducing condition to facilitate iron reduction and mobilization (Harder, 1978; Berner, 1981; Iijima and Matsumoto, 1982; Curtis et al., 1985; Young, 1989; Hornibrook and Longstaffe, 1996; Toth and Fritz, 1997; Huggett et al., 2010; Mu et al., 2015; Tang et al., 2017a; Ma et al., 2022). The origin of berthierine can be explained by different chemical pathways, which include i) crystallization from SiO_2-$Al(OH)_3$-$Fe(OH)_3$ precursor gel (Ma et al., 2022), ii) diagenetic alteration of kaolinite and iron-(oxy)hydroxide under reducing condition or from glauconite (Harder, 1978; Bhattacharyya, 1983; Taylor, 1990; Toth and Fritz, 1997; Huggett et al., 2010; Tang et al., 2017a; Ma et al., 2022), iii) replacement of calcareous oolites and iv) direct precipitation from a Fe-Mg-rich siliceous hydrothermal fluid (Wang et al., 2023b). The mineralogical and micro-textural evidence refutes the presence of kaolinite or glauconite substrate on which the berthierine mineral has formed. The compositional difference in partially altered grains in which the rims are enriched in FeO(total) with a compact, less porous network of small berthierine flakes and the cores are rich in MgO, Al_2O_3, and SiO_2, showing poor arrangement of large berthierine flakes (Figs. 7.4a-d) suggests a chemical reaction pathway of berthierine formation initiated along the grain boundary and progressed towards the core of the grains (Figs. 7.4a-d). The chemical evolution pathway of the berthierine suggests a strong influence of porewater in its formation. Thus, the dissolution and precipitation model is the most plausible explanation for the origin of the berthierine from the basal limestone of the Kallankurichchi Formation (cf. Wang et al., 2023b). Most feldspar grains exhibit berthierine formation along its cleavage, suggesting dissolution and precipitation as the most viable pathway. The compositional similarity among different types of berthierine formation completely altered grains, rims of the partially altered grains, and along the feldspar

cleavages also suggests a dissolution and authigenic precipitation for the berthierine formation (Figs. 7.4e-g).

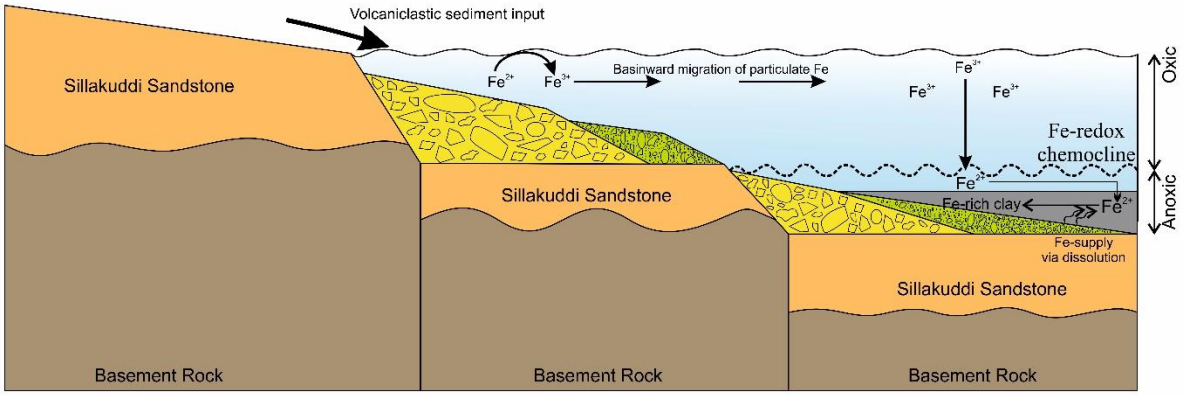

Fig. 7.10 A generalized model for the deposition of the basal part of the Kallankurichchi Formation. Note that the deposition of volcaniclastic detritus below the Fe-redoxcline creates anoxic conditions, which is ideal for berthierine formation. (The yellow and green units in the model represent the clast-supported and the matrix-supported scree conglomerate, respectively).

7.8.3 Source of iron for the berthierine:

Recent studies on ocean elemental modeling suggest a significant amount of Fe-sequestration associated with the abundant authigenic green marine clay formation on the ocean floor (Baldermann et al., 2022; Ma et al., 2022). Although terrestrial riverine input of particulate Fe, hydrothermal fluid injection, or low-grade metamorphism can supply a potentially significant amount of Fe into the depositional environment, the sedimentological, petrological, and mineral geochemical characteristics strongly suggest the volcaniclastic sediment as the precursor of the berthierine in Kallankurichchi Formation. Volcaniclastic rocks, especially mafic igneous rocks, are characterized by a metastable mineral assemblage rich in Fe and Mg and easily alter into clay (García-Romero et al., 2005; Gifkins et al., 2005;

Mitra et al., 2017; Gong et al., 2018; Hong et al., 2019). Dissolution of volcanic glass is strongly dependent on the solution composition, temperature, and fluid/rock ratio (Alt et al., 2010; Mitra et al., 2017); the feldspar dissolution depends on several factors, which include crystal structure, Al/Si order, temperature, pH, surface area, organic acids, chemical affinity and the precipitation of secondary minerals (Yuan et al., 2019). Under average oceanic salinity, the dissolution of ferromagnesian minerals can contribute significantly to enriching the porewater with iron and other necessary elements. In addition, early dissolution of feldspar grains can release a significant amount of Al^{3+} and alkali metals (such as Ca^{2+}, K^{+}, and Na^{+}) in a slightly acidic environment (pH <~5), which in an open system with a high fluid/rock ratio could result in a reduction in the K^{+} activity of the porewater (Stillings and Brantley, 1995; Sutton and Maynard, 1996; Fritz and Toth, 1997; Yuan et al., 2015, 2017, 2019; Sun et al., 2016; Mitra et al., 2017). However, the K-poor nature of the authigenic clay could also indicate meteoric water interaction (Jeans et al., 2000). As the cleavage planes of the feldspar grains act as conduits of porewater, the subsequent dissolution creates high K^{+} activity within the micro-environment, promoting K-rich clay formation (such as glauconite) (Dasgupta et al., 1990; Jiménez-Millán and Castro, 2008; Banerjee et al., 2015; Mandal et al., 2020). Although the depositional environment for the dark grey limestone of the Kallankurichchi Formation is relatively deeper (compared to other part of the limestone), below the redoxcline, continued rifting and upliftment during its formation may result in the circulation of subsurface meteoric water via small-scale faults and fractures within confined aquifers with emerged recharge area (Jiménez-Millán and Castro, 2008). The introduction of meteoric/freshwater influx for K-poor clay authigenesis is postulated since meteoric/freshwaters are undersaturated in alkali concentration and, thus, more susceptible to leaching of alkali metals during authigenic clay mineral formation (Odin and Matter, 1981; El Albani et al., 2005; Sun et al., 2016; Roy Choudhury et al., 2022b, 2022a). The subsidence during the post-rift adjustment helps to create oxygen-depleted depositional conditions favorable for berthierine formation, which can be corroborated by the dominance of Fe^{2+} in the clay structure and the presence of pyrite. The conglomerate with slide planes at the basal part of the dark grey limestone supports this contention. The uplifted blocks formed during the rifting of the Cauvery basin can serve as an emerged recharge area, supplying a

significant portion of meteoric groundwater into the depositional environment where the berthierine has formed (Fig. 7.10). Berthierine is unstable and often transforms into chamosite with a similar chemical composition but a different structure (the latter being chlorite with 14 Å basal d-spacing). This transformation is temperature dependent, and previous workers have reported that at least 70°C temperature is required for the berthierine to transform into chamosite structurally (Toth and Fritz, 1997; Tang et al., 2017a; Tounekti et al., 2021). From the available oxygen isotope signature ($\delta^{18}O$) of the bulk rock samples of the Kallankurichchi Formation (Madhavaraju et al., 2015), the maximum possible diagenetic temperature is to be calculated as ~56.2°C using the equation presented in Anderson and Arthur (1983) (see Alberti et al., 2013 for corrected equation). The abundant calcite cementation might have terminated pore-fluid percolation, thus preserving the 'proto-berthierine' in many grains.

7.9 Conclusion:

The present study has aimed to identify and characterize the green clay minerals, which occur at the basal part of the Kallankurichchi Formation of the Cauvery Basin, India. The sedimentological studies of the host sediment combined with the geochemical and mineralogical investigations of the green clay mineral phases, suggest the deposition of authigenic berthierine formation within a shallow marine depositional environment. The following conclusions can be drawn from the present study:

a) Authigenic berthierine forms within the basal part of the early Maastrichtian Kallankurichchi Formation of the Cauvery Basin. The berthierine clay primarily occurs as pseudomorphs of volcaniclastic grains besides forming along the cleavages of feldspars. The abundance of angular quartz and feldspar framework grains and the fresh and partially palagonitized sideromelane glass suggests a volcaniclastic source of the sediments. The exotic mode of occurrence of berthierine as grain pseudomorph is reported for the first time from the rock record.

b) The geochemical signature of the 7 Å berthierine clay exhibits a Mg-, Si-, Al-rich core composition with a Fe-rich rim, suggesting possible maturation from a ‘proto’-berthierine composition to ‘matured’ berthierine composition. The iron in the clay is dominantly ferrous.

c) The origin of the berthierine at the basal part of the Kallankurichchi Formation can be corroborated by volcaniclastic sediment supply into a pericratonic rift basin. The basin subsidence along the slide planes carried the sediments below Fe redoxcline, promoting a favourable oxygen-depleted environment for berthierine authigenesis. The dark-coloured, comparatively fossil-free limestone overlying the scree conglomerates also supports the idea of tectonic subsidence.

d) The source of iron for the berthierine grains must be the dissolution of volcaniclastic particles. The grain morphology and SEM micro-textural study coupled with the chondrite normalized REE pattern of the limestone suggests volcaniclastic grains as the primary source of the framework grains.

CHAPTER- 8

CHARACTERIZATION OF SHELLBANK

8.1 Introduction:

Shellbanks are always important findings for interpreting the sedimentological and biological evolution of a basin. Massive almost intact fossil shell accumulations require particular conditions to be formed and may provide valuable insights into the sedimentary environments favoring such concentrations. Shallow-water shell beds are rare on reefless settings. Four shellbanks have been recognized within the Kallankurichchi Limestone Formation, Ariyalur Group, Cauvery Basin, India during the present endeavor. These shellbanks are dominantly consists of robust *Gryphea* (Bivalvia) fossils and are identified based on their living orientation and mode of preservation. The matrix present within the shellbanks is dark in colour and lime-mud in composition. It provides an opportunity to understand the conditions that led to the formation and preservation of a massive shell bed at shallow water settings. In contrast to the shellbanks the fossils present in other parts of the entire formation are mostly fragmented in nature. Considering the repetitive nature of occurrence and its associated facies during the present study, it has been interpreted that the shellbanks likely to be deposited in a shallow marine regime. This paper adopts characterization of shellbanks and its differences from the associated facies by means of physical as well as chemical.

Cretaceous Cauvery Basin of India always special to paleontologists because of its rich fossiliferous deposits. It received increasing attention for yielding paleobiogeologic data and its usefulness in stratigraphy and sedimentology. However, preservation of hard shells is very conspicuous features in the bio-stratigraphic history of the Cauvery basin. However, concentrations of calcitic hard shells that bear the imprints of living habits within a stratigraphic succession always important to paleontologists and sedimentologists because of its immense significance in interpreting the then paleoenvironmental conditions and their stratigraphic significance (Fürsich et al., 1995; Radley and Barker, 2000). They can also provide valuable information about the sedimentation rate, condition of bottom substrate, nutrient levels, temperature, and salinity (Lazo et al., 2005). The fossil shells considering its in-situ preservation or post-mortem transported, used for facies analysis, correlation of marker-bed, and also determine the paleohydraulic regimes (Seilacher, 1985; Kidwell et al., 1986; Peng et al., 2024) of a particular succession. These shell beds likely formed through a

combination of sedimentary and biological processes within a specific paleoenvironmental conditions. Four such in-situ sedentary rudist bivalve shell horizons have been identified within the fossiliferous Kallankurichchi Limestone Formation of Ariyalur Group, Cauvery basin. This study mainly focuses on the characterization of the rudist bivalve colonies and its associated facies which ultimately help to develop conceptual model for the evolution of the Kallankurichchi Limestone Formation. Besides, the associated facies of these rudist bivalve colonies have also been considered for developing the depositional model. The salinity variation and paleoproductivity of the in-situ bivalve colonies have been inferred during the deposition of the limestone formation.

8.2 Occurrence of sedentary bivalve colonies:

The ~ 60 m thick fossiliferous Kallankurichchi Limestone Formation is conspicuously enriched with well-preserved rudist bivalve *Gryphea* identified as *Pycnodonte* sp. (Ayyasami, 2006) in four successive horizons within the entire succession. It overlies generally on the fair-weather ripple laminated facies and overlies by the storm facies. The average bed thickness of the *Gryphea* colony 65 cm though lateral thickness variation is conspicuous (Fig. 8.1a). The beds have sharp top where shell concentration is high, but gradational at bottom contact. Shell concentrations of the colonies also vary laterally. The bed geometry is more or less tabular though highly irregular in nature (Fig. 8.1b). The beds are generally massive in nature and devoid of any primary sedimentary structures (Fig. 8.1c). The shells are in densely packed. Grey colored lime-mud admixed with shell hash fill the space between the shells and within the shell cavities (Fig. 8.1d). All the shells are generally concave-up in attitude, but little exceptions are also there. The average diameter of the shell is 14 cm.

Interpretation:

Well preserved, large numbers of thick and relatively heavy shells of *Pycnodonte* sp. and that too in living concave-up condition suggests that the concentrations of fossil shells are the result of in-situ growth or colonization. These in-situ growths of sedentary bivalve colony, where bivalves are preserved as their original life mode, are identified as ‘shellbanks’

(Srimani, 2024a). Distinct lateral variation in shell density without any apparent taphonomic control probably reflects deliberate choice of living organisms about spots to flourish. Indistinct lower surfaces of the beds in contrast to their upper surfaces are in agreement with this contention of in-situ growth. Exclusive occurrence of this rudist *Pycnodonte* colonization on top of fair-weather beds is possibly because of enhanced production rate of these sedentary organisms at favorable calm and quite condition. Because of active bioturbation, strata are usually massive and lack of physical sedimentary structures. Some random orientation of shells is always explicable with bioturbation.

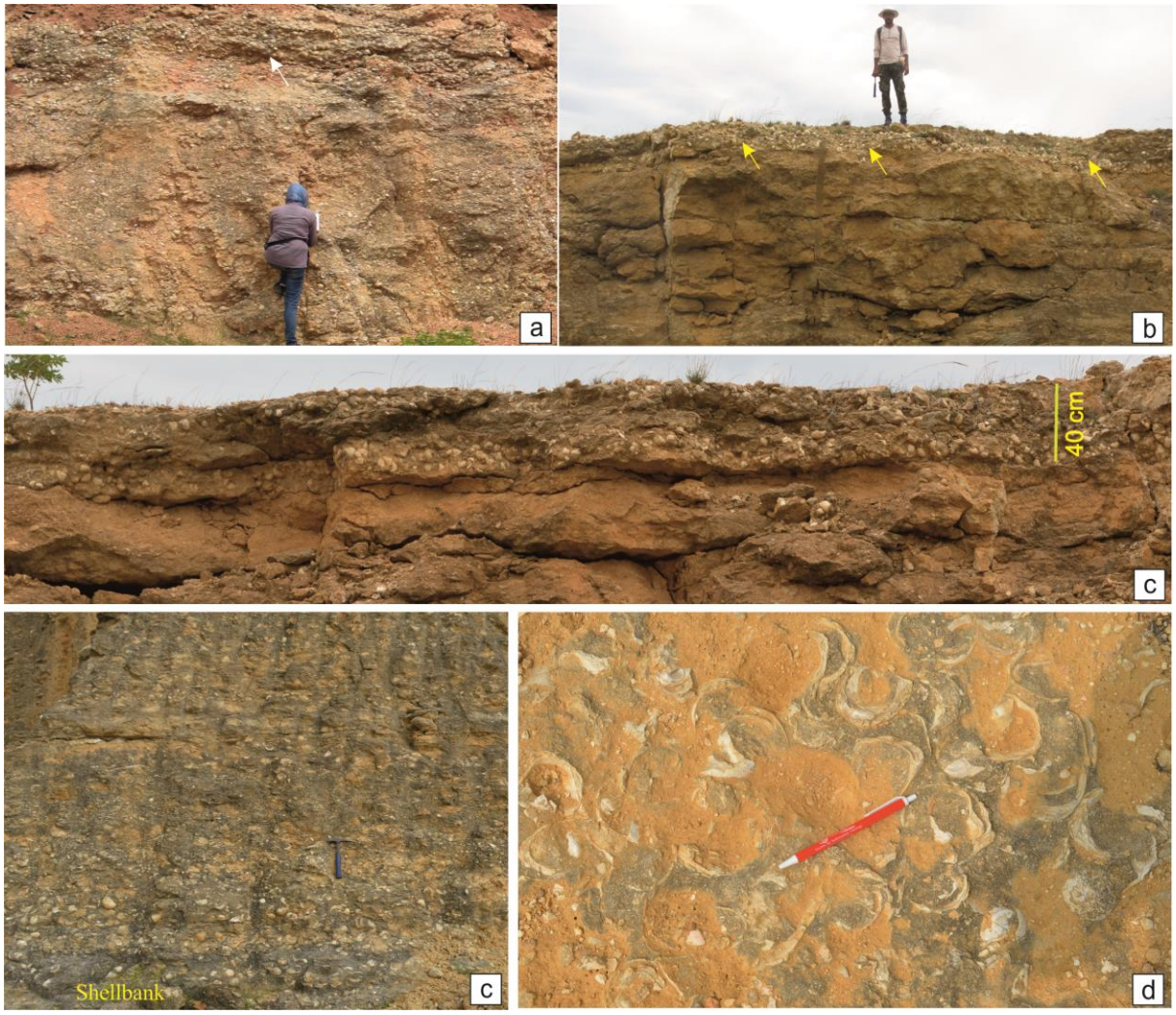

Fig. 8.1 Shellbanks: lateral variation of bed thickness of rudist bivalve *Pycnodonte* colony (marked by white arrow) (a); tabular bed geometry (yellow arrowed) (b); massive bed without any primary sedimentary structures (c); all the shells are preserved in their live-mode (concave-up position), note grey colored lime-mud matrix between the shells (d).

8.3 Distribution of fossils within shellbanks:

Previous research has established biozonation based on fossil oysters, with certain zones identified as acme zones characterized by the dominance of specific species in megafossil occurrences, the *Pycnodonte (Phygraea) vesicularis* Zone. The shellbank present within the Kallankurichchi Limestone Formation consists of Gryphaeidae including *Agerostrea ungulata* (Schlotheim), *Exogyra*, *Planospirites ostracina* (Lamarck) and

Rastellum (Arcostrea) pectinatum (Lamarck). Abundance of these three bivalves e.g., *Rastellum* sp., *Pycnodonte* sp., *Exogyra* sp. in the Kallankurichchi Formation, where the shellbank extends about 5km in length. The deposits are readily mined for their concentration of bivalves that give a cement grade for the carbonates. The characteristic large oysters of the Kallankurichchi Formation may represent low sedimentation rate during their proliferation. This forms a prominent horizon and is easily marked on the map. Most of the *Pycnodonte* sp. of the Kallankurichchi Formation are large (~15cm in length), thick and well-preserved. Length of Bivalves *Rastellum/Lopha* sp. is varying from excessively large shell (~22 cm in diameter) to small (~8 cm in diameter) (Fig. 8.2). *Exogyra* sp. from the Kallankurichchi Formation are approximately 5 cm in length. Even in the thick shellbank articulated valves are almost absent, though the fossils are well preserved.

Fig. 8.2 Distribution of other fossils within shellbanks. Note, *Lopha* sp (arrowed, yellow).

8.4 Geochemical analysis of shellbank sediments:

The X-Ray diffraction (XRD) analysis of the whole-rock sample of the shellbank facies reveals a series of several sharp, symmetric peaks (Fig. 8.3). The sharp and symmetric peaks with d-spacing of 3.84 Å, 3.02 Å, 2.49 Å, 2.27 Å and 2.09 Å situated at 23.12° 2θ, 29.47° 2θ, 36.05° 2θ, 39.49° 2θ and 43.24° 2θ respectively, are characteristics of calcite. The mineralogical analysis of the shellbank facies also refutes any diagenetic alteration.

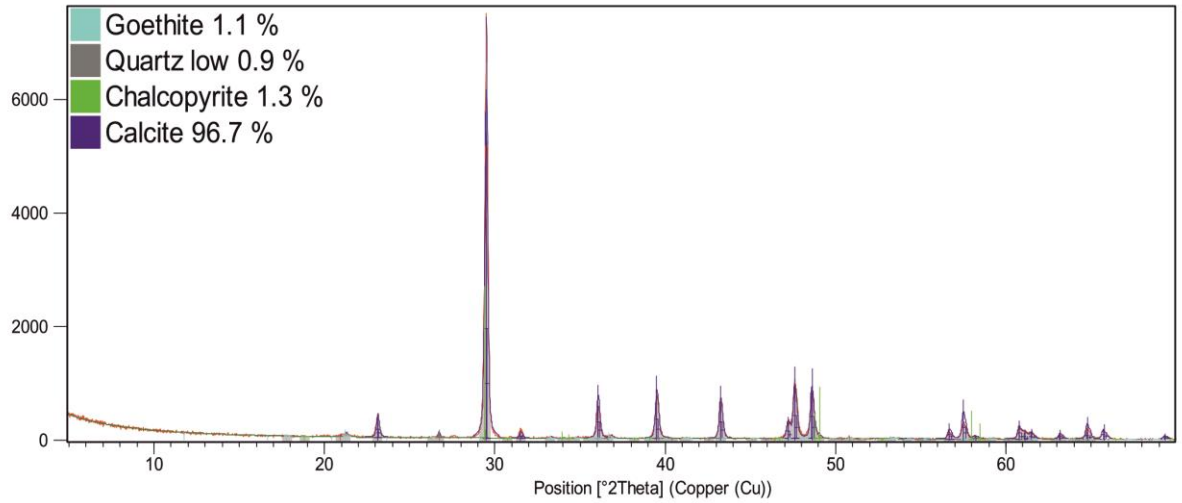

Fig. 8.3 X-Ray diffractogram of the whole rock powder (<63 μm grain size) of the shellbank sediments.

Generally, carbonate rock contains plethora of trace elements like Mg, Sr, Fe, Mn, Ba, Cu, Cd, Zn, etc (Tucker & Wright, 1990). The major, minor and trace elemental analysis of the shellbank sediments of Kallankurichchi Limestone Formation shows some distinctive geochemical character. The four shellbanks are apparently enriched in Zn, Ni, Co and P. Besides, presence of Ba, Rb, Sr, Pb, Cd, Cu, Cr, Mn in the shellbank sediments has also been observed. Paleoproductivity proxies e.g., P/Ti, Ba/Ti, are high. Enrichment factors (EF) of Zn, Co and Ba are also distinctly higher. Sr EF is also high in shellbank sediments. It is relevant to mention that Sr content in seawater increased significantly during the Late Cretaceous period (Antonelli, et al., 2017). B/Ga values vary within the shellbanks, slightly in the higher range. The average B/Ga value is 36.8. Ni/Co values falls well below 5.0 and V/Cr ratio varies between 1.2 to 1. The rare earth element (REE) i.e., LREE/HREE distribution demonstrates a flattened pattern (Fig. 8.4).

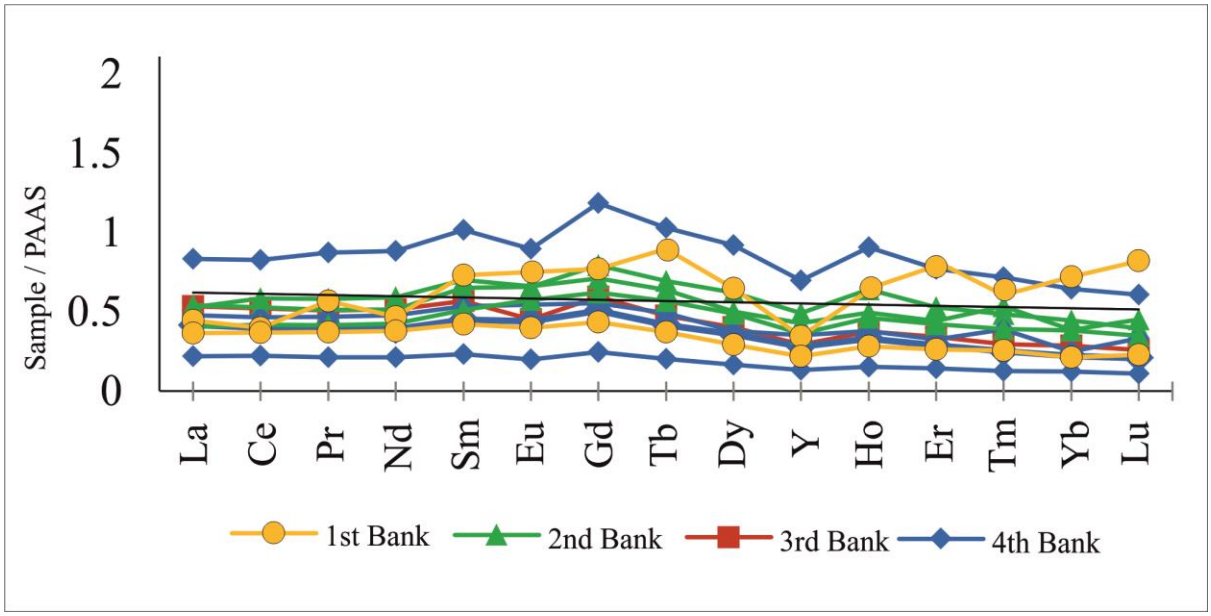

Fig. 8.4 PAAS normalized REE pattern showing distribution of LREE and HREE.

Enrichment of the above-mentioned elements and its enrichment factors and also P/Ti, Ba/Ti ratios indicate high paleoproductivity of the shellbanks as it is expected for the growth of a shellbank. High enrichment factor of Zn, Co and Ba indicate organic carbon enhanced during the deposition of the shellbank. B/Ga uses as paleosalinity proxy during shellbank formation which is higher in range. The average values of B/Ga indicate its restricted marine origin (Wang et al., 2020). The variation of paleosalinity within the range may be due to the mixing of sea water during storm or high tide within the restricted zone. Paleoredox sensitive elemental ratios Ni/Co, V/Cr suggests oxic paleoenvironment (Jones and Manning, 1994), likely to be very shallow water condition. This further corroborates stagnation at the depositional site. Flat REE pattern indicates shallow sea water character (Deng et al., 2017)

8.5 Discussion:

The Kallankurichchi Limestone Formation of Ariyalur Group is a well-studied for its fossil abundance. However, the inferred shellbanks have never been discussed with relation to its depositional dynamics and stratigraphic architecture. Moreover, there are no documentation of Late Cretaceous rudist bivalve colonies from India so far. These shellbanks have been correlated with maximum flooding surface (Ayyasami, 2006; Nagendra et al.,

2011; 2018) which is a bit difficult proposition, because during the present study four numbers of shellbanks have been identified within the formation. It provides an opportunity to understand the conditions that led to the formation and preservation of a massive shell bed at shallow water settings. In contrast to the shellbanks the fossils present in other parts of the entire formation are mostly fragmented in nature. Previously, all the fossiliferous horizons had been identified as storm deposits (Fürsich et al., 1995). However, the well-preserved, intact life mode position of fossil *Pycnodonte* is difficult to satisfy its storm origin. Earlier these banks have been correlated with maximum flooding surfaces (MFS) during the high stand of sea-level (Nagendra et al., 2002). On the other hand, the storm facies associated with these shellbanks consists of profuse broken shells and the containing fossils are haphazardly oriented (Fig. 8.5a). The laterally persistent shellbank with tabular geometry matches well with storm interpretation but the concave-up live position of the intact *Pycnodonte* shell (83%) is difficult to explain in a storm bed (Fig. 8.5b). The present study shows that these shellbanks dominated by *Pycnodonte* fossils deposited in a relatively calm and quite restricted condition which matches well with the habitat of *Pycnodonte* bivalve.

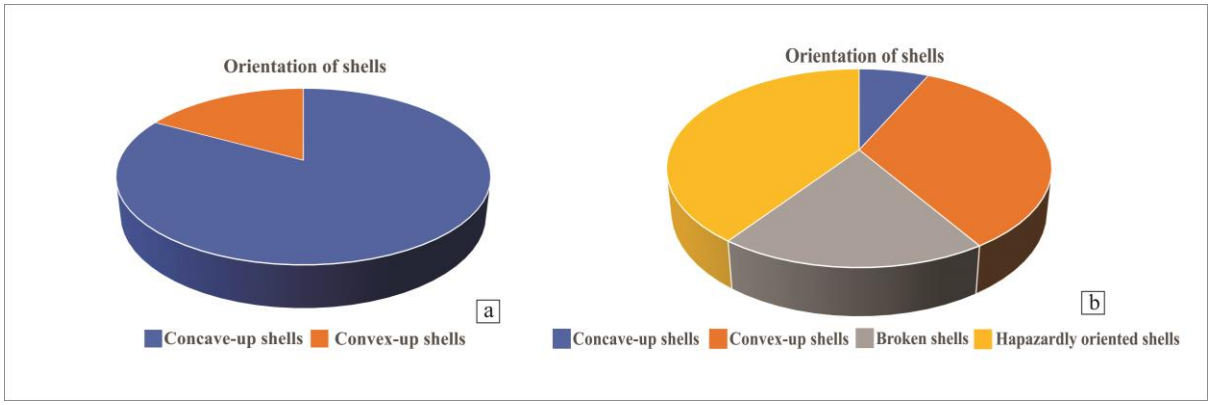

Fig. 8.5 Orientation of shells (whether concave-up i.e., live position or convex-up i.e., current stable position (a); distribution of shells in graded storm facies (b).

Overall, the Kallankurichchi Limestone deposited in a shallow marine agitated condition. The previously discussed (Chapter- 2) largescale cross-stratified calcarenite beds with convex-up geometry possibly formed the bars. The favorable condition for the shellbank horizons, dominated by *Pycnodonte* fossils possibly developed on the leeward side of the bar which is likely to be relatively quiet water condition, depicted by a hypothetical model (Fig.

8.6). The inferred paleogeography satisfies the proliferation of this organism. The geochemical condition (discussed in Chapter- 4) also supports their growth.

8.6 Implications:

a) **Stratigraphic utility:** Phanerozoic Limestones are typically abundantly fossiliferous, with exceptionally intact and well-preserved fossil remains, but this formation holds special attention as fossils are in living position, identified it as shellbanks. As the cretaceous climate is comparatively warmer, probably the increased temperature facilitated growth of the shellbanks. About 5 km extending shellbank deposits are readily mined for their concentration of bivalves that give a cement grade for the carbonates. It can be used as marker horizon for stratigraphic correlation. These shellbanks cannot be correlated with maximum flooding surface because they are occurring in multiple levels and occurring mostly with shallow water rippled and chevron facies.

b) **Paleoenvironmental interpretation:** Further, we can also interpret the paleoenvironment by considering several factors like preservation and orientation of shells as well as geochemistry of shellbank sediments. The *Pycnodonte* shells are preserved here in Kallankurichchi Limestone indicates calm and quite environmental condition within an overall agitated condition. Their in-situ live-mode position supports this contention. Possibly the calm and quite condition developed behind the bars. The broken and convex-up shells with haphazard orientation indicate high energy environments, likely to be storm. The storm beds associated with the shell banks are event beds which are the product of both erosion and reworking (Ando, 2019) of shellbanks. The shellbanks are deposited in oxic environments with high paleosalinity (as it is formed in restricted environments) and paleoproductivity.

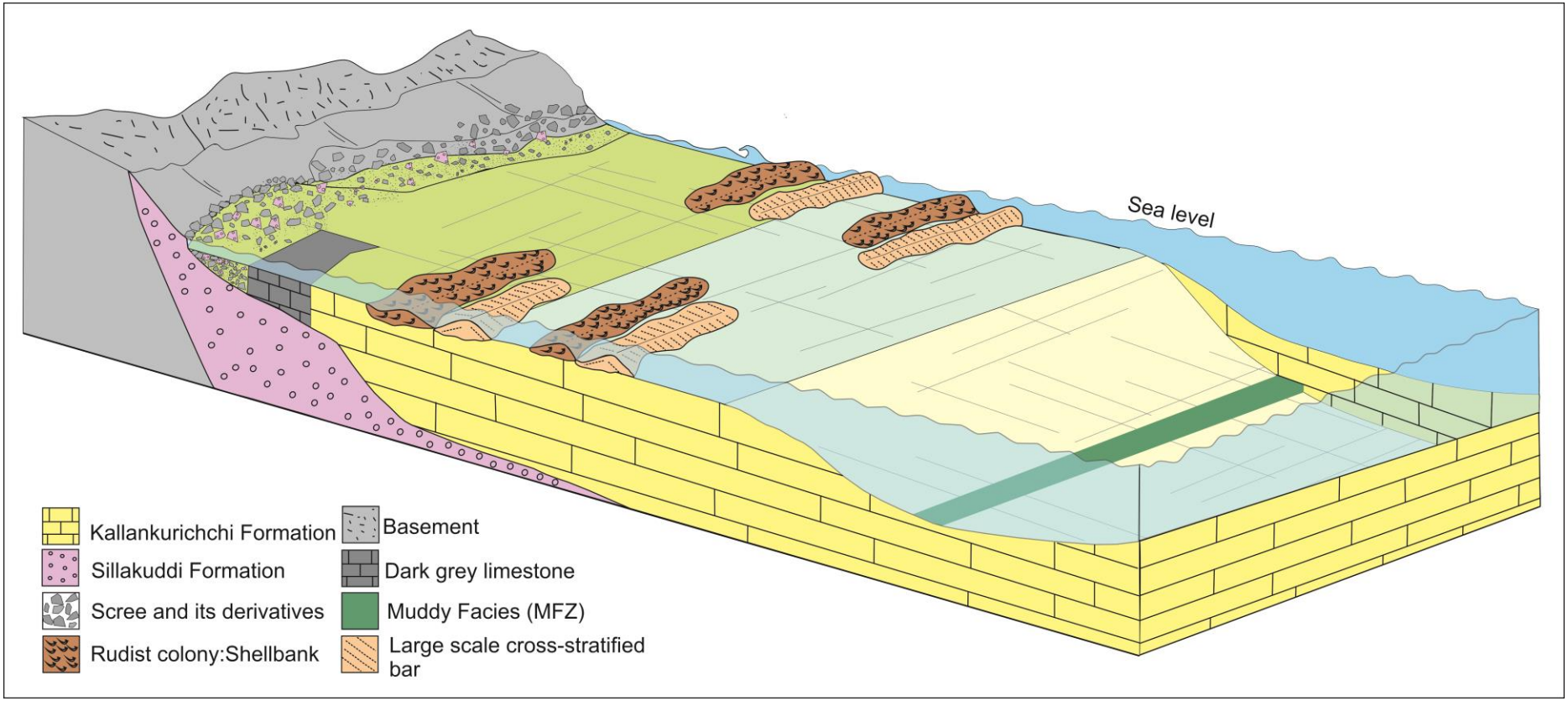

Fig. 8.6 Development of Shellbank behind the large-scale cross-stratified bar, which acted as barrier.

CHAPTER- 9

BIVALVE *Pycnodonte* sp.: A PROXY FOR PALEOTEMPERATURE AND PALEOSALINITY

9.1 Introduction:

The fossil bivalve *Pycnodonte* (Ayyasami, 2006) present within the shellbanks of Early Maastrichtian Kallankurichchi Limestone Formation of the Cauvery basin, India, has been considered in this chapter. Maastrichtian age is an important time interval in earth history because in its early stage there was blooming of organism followed by disappearance of many biotas in the late stage possibly for the volcanic episodes (Madhavaraju et al., 2015). However, the report of early Maastrichtian temperature is less, compared to its later part. The record of early Maastrichtian even poorly constrained in the then lower latitude sedimentary basin. The main objective is to reconstruct the paleoenvironment/paleogeomorphology of the studied area and to infer the paleoclimate, paleotemperature and related aspects that prevailed during the early Maastrichtian time. Overall, the Cretaceous Cauvery Basin of India always took a special interest to paleontologists because of its rich fossil assemblages. It received more attention for yielding paleobiologic data to establish the biostratigraphy of the basin (Ayyasami and Banerji, 1984; Hart et al., 1999; Ayyasami, 2006). The Kallankurichchi Limestone Formation is highly fossiliferous amongst all the formations present within the Cretaceous Cauvery Basin (Nagendra et al., 2018). However, related sedimentological interpretation is lacking in most cases though in situ and post-mortem transported fossil assemblages i.e., thanatocoenosis assemblages are well preserved within this formation. The fossils preserved in their original living mode yields valuable information regarding paleoenvironment and paleoclimatic reconstructions since they carry the signatures of original habitats and ocean chemistry. The fossil assemblages present in the formation with post-mortem transportation history are also provided the idea regarding the paleohydraulic regime of the basin (Fürsich, 1982; Futterer, 1982; Hagdorn and Mundlos, 1982; Kidwell and Jablonski, 1983; Aigner, 1985; Kidwell, 1985; Seilacher, 1985). *Gryphea* shells inhabiting in the outer shelf setting, serve as excellent indicators of environmental fluctuations of the Kallankurichchi Formation during the early Maastrichtian period. It is chosen because of its ubiquitous occurrence from geologic to seasonal timescales (Bougeois et al., 2015).

The in-situ preserved fossil shell horizons are identified at four levels in the Kallankurichchi Limestone, dominantly consist of Gryphaeidae bivalves *Pycnodonte* sp. (Ayyasami, 2006). The shells were collected only from shellbanks cemented with micritic

matrix to ensure that they surrogate for their endemic paleoenvironment. The average shell thickness of a single valve ca. 4 cm and length of the shell ~9cm. During the present study unaltered *Pycnodonte* sp. has been considered for geochemical studies. The *Pycnodonte* sp. consists of alternate laminae of variable thickness (Fig. 9.1). Individual growth lamina records the climatic fluctuations in the form of variable growth rates and chemical changes. The studied specimen precipitated their shells annually, driven by the sinking of organic detritus from the surface. As these bivalves are sessile organisms, it is expected to records perfect environmental changes in their calcite shells (Putten et al., 2000; Elliot et al., 2003; Immenhauser et al., 2005; Zakharov et al., 2006; Hippler et al., 2009). These thick, large and calcitic bivalve shells are also potential to document the early Maastrichtian paleoclimate with the help of various geochemical proxies. The paleosalinity, paleoproductivity and paleotemperature of the early Maastrichtian time have also been inferred and compared. The $\delta^{18}O$ values from the alternate lamina thickness variation of *Pycnodonte* sp. has been used to reconstruct the seawater temperature and to assess the effects of oscillatory magnitude of temperature through their ontogenic variation, if any (Surge et al. 2003; Ivany et al. 2004; Kaandorp et al. 2005). For that reason, the shells were collected only from four specific horizons where shells are preserved in in-situ position, to ensure that they give proxy for their endemic paleoenvironment. This chapter adopts carbon and oxygen isotope geochemistry of successive growth laminae of low-Mg calcitic *Gryphea* species *Pycnodonte* sp.

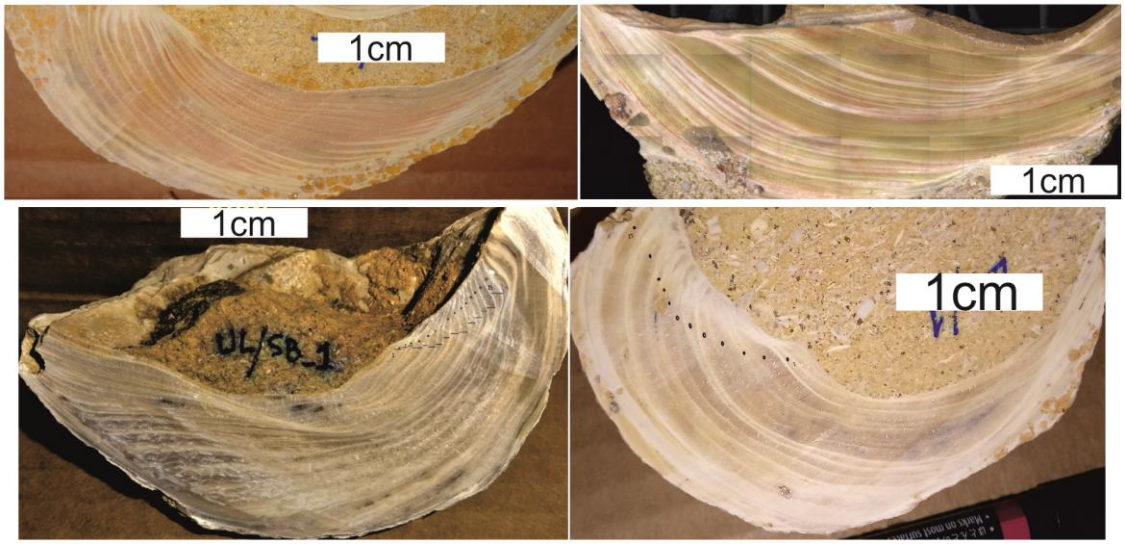

Fig. 9.1 Fossil *Pycnodonte* sp. consists of alternate laminae of variable thickness (the four samples collected from four different horizons).

9.2 Depositional condition of *Pycnodonte* sp.:

The fossil bivalve *Pycnodonte* sp. has been previously reported from the Kallankurichchi Formation (Ayyasami, 2006 and references therein). This species is described as reclining in nature, inhabiting the muddy bottoms of shallow marine shelf where sedimentation rate is low (Brezina et al., 2014). A small attachment area at the juvenile stage suggests that they led a cemented mode of life at that stage. During the adult stage, the bivalve detaches from the substrate and lie freely on the muddy substrate (Hayami and Kase, 1992; Brezina et al., 2014; De Winter et al., 2018). This bivalve possesses a thick left valve (lower one) and a much thinner lid like (upper one) right valve because of their epifaunal life mode. Individual valves of this genus vary considerably in dimension, convexity and shell wall thickness depending upon the age of the organism and the environment they grow (Brezina et al., 2014; De Winter et al., 2018) (Fig. 9.2). These relatively thick valves with well-developed calcitic shell layers and their longer life spans make them the most suitable species for paleoenvironmental interpretation (Brezina et al., 2014). The broad geographic distribution and the abundance of *Pycnodonte* shells in widely-varying paleolatitudes and geological settings, especially during the Cretaceous, make them a promising archive for high resolution climate reconstructions. The incremental growth of the shell records seasonal-scale variations and the shell material provide precise and better time resolution (De Winter et al., 2018). As these bivalve shells are always thick, they can preserve a longer depositional history. This particular species does not show significant vital effect variation, rather have limited kinetic effects and disequilibrium fractionation of stable isotopes. These bivalves take up nutrients and other elements directly from the seawater, so it can be used as a proxy for the paleo-oceanic conditions ((De Winter et al., 2018).

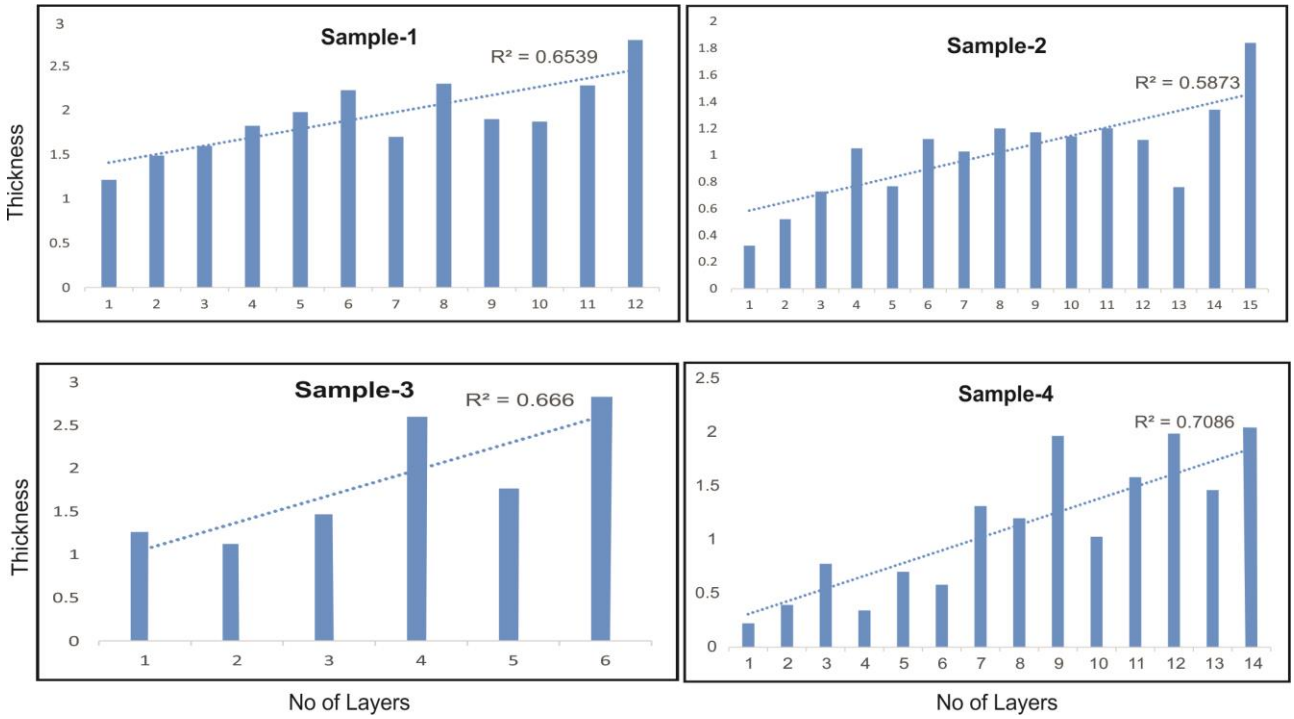

Fig. 9.2 Overall increase in lamina thickness with maturity of shell.

9.3 Selection of shell for analysis:

9.3.1 Shell microstructure:

Petrographic observation of the bivalve shells reveals a layered structures defined by prominent honey-comb layering with very well-preserved breaks in growth lines (Fig. 9.3a, b). The breaks, characterized by lack of honeycomb structure and closely-spaced growth laminae mark the cessation of the growth of organism which are followed again by successive honey-comb layers. The thickness of growth lines also changes within same species (Fig. 9.3a, b). The thickness of successive lamellae indicates duration of the growth season and shows that the overall growth rate decreases with age. The thickness of collected *Pycnodonte* sample from First shellbank ranges between 1.36-3.6 mm; thickness from the second shellbank varies between 0.51-1.83 mm; similarly, the lamellae thickness from third and fourth varies 1.12-2.8 mm and 0.22-2.20 mm respectively (Fig. 9.2). As the growth rate decreases to mature shell, so the lamellae thickness increases ontogenetically.

Petrographic observation of the shellbank facies reflects preservation of the pristine calcitic test and refutes any diagenetic alteration as no textural alteration have been observed (Fujioka et al., 2019). As quality of shell preservation varies dramatically, the petrographic observation, aided with in-situ geochemical analysis, were crucial for selecting the best-preserved unaltered shell for oxygen isotope analysis and determination of paleo-temperature. Thickness variation in all the four shells has also taken in account.

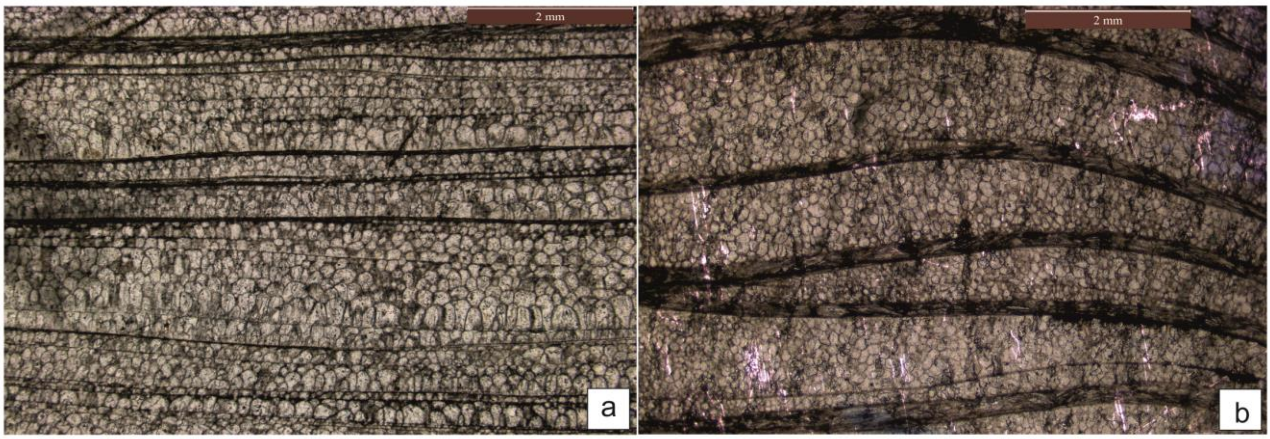

Fig. 9.3 Honey-comb layering with very well-preserved growth lines: thin (a) and thick growth lines (b).

9.3.2 Growth line analysis:

Growth lines manifest as dark-colored disruptions and faint bands in biogenic carbonates formed through accretion, indicating periods of slowed or cessation of growth. In bivalves, these lines appear as concentric patterns across various taxa, indicating their development during environmental or physical stress such as tidal exposure, availability of nutrients and or extreme temperatures (De Winter et al., 2020). With prolonged growth cessation, growth lines typically darken in appearance (Fig. 9.3a, b). Growth lines serve as valuable indicators for understanding the growth strategies employed by organisms. The distance between adjacent growth lines, known as growth increments, was measured in the direction of growth indicates maturity of shell (Posenato et al., 2022; Ichimura et al., 2024).

The growth pattern of the shell is segmented into time intervals of roughly equal duration (Dunca and Mutvei, 2001), resulting in the formation of growth increments and growth lines. Growth increments signify phases of rapid growth, while growth lines indicate periods of slower growth. Both are essential for conducting sclerochronological analyses.

9.3.3 Shell chemistry using µ-XRF:

The polished surface of shells was utilized to create high-resolution elemental abundance maps, employing a micro-X-ray fluorescence (µXRF) scanner. XRF point-by-point line scanning are conducted on the shell layer in the growth direction of the rudist shell, across a polished section of the hinge of the shell, oriented perpendicular to the growth layers for trace elemental profiling (De Winter et al., 2017). As quality of shell preservation varies dramatically, we have chosen the best-preserved unaltered shell for geochemical analysis to get original result of paleotemperature. Shell is mainly composed of Ca. 98.82697% and Mg is very limited 0.519683%. Nutrient element Fe and S is also present in 0.28% and 0.12%. Mn value is very negligible 0.04% which supports that the shells are unaltered (Table 9.1; Fig. 9.4). Concentration of Sr is relatively high or same with sea water (Fig. 9.5).

So, proper preservation of shell growth line with shell microstructure indicates original shell preservation. Textural relationship combined with the trace element model can be utilized to infer the shell selection.

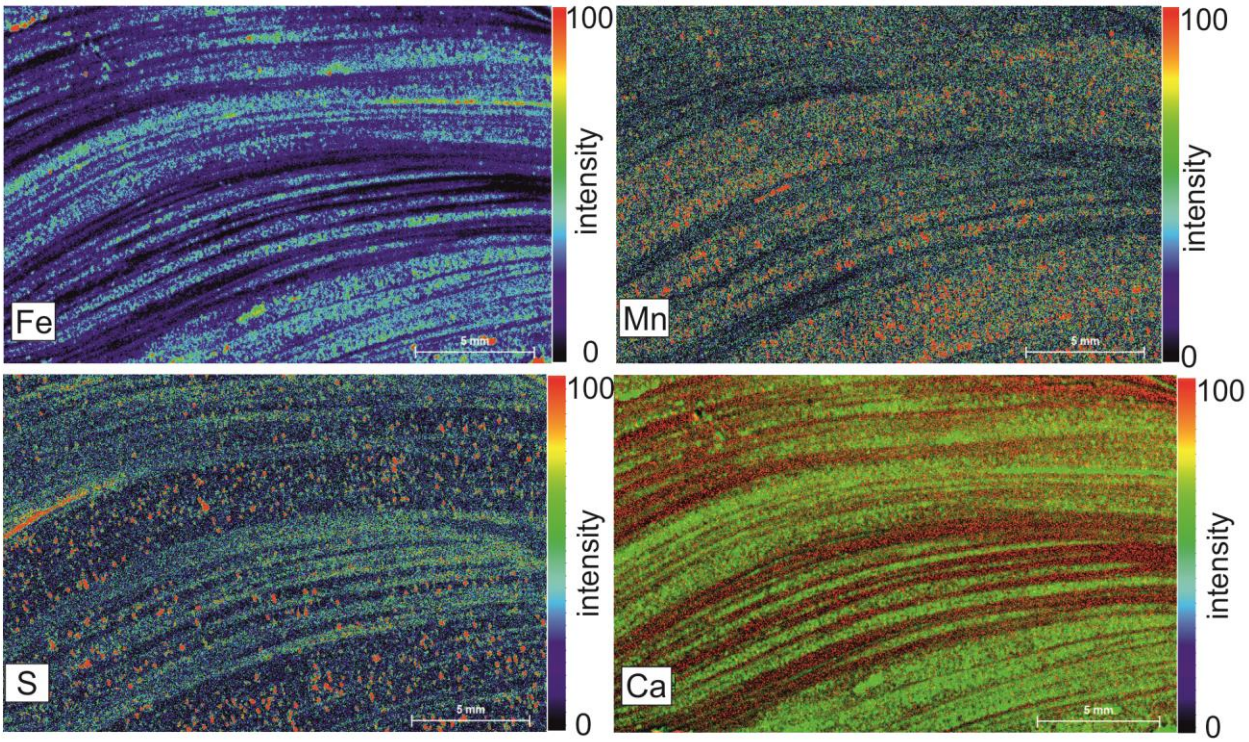

Fig. 9.4 Overview of colour scanning and µ-XRF mapping.

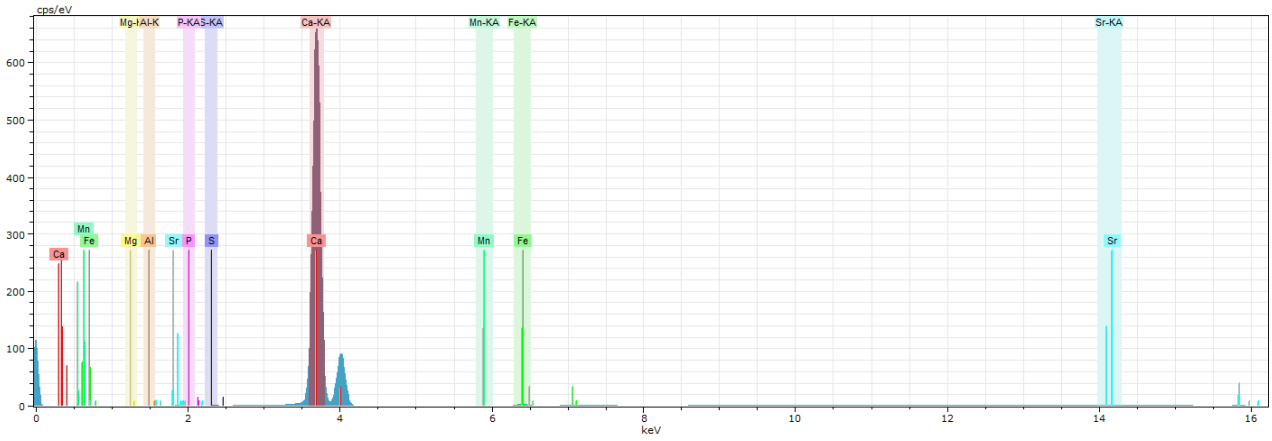

Fig. 9.5 Elemental spectrum of shells determined by µ-XRF scanning.

Table 9.1 Representation of µ-XRF analysis of *Pycnodonte* sp.

UL/SB1					
Points	**Ca**	**Fe**	**S**	**Mn**	**Sr**
1	99.18	0.40	0.19	0.08	0.16
2	98.94	0.49	0.18	0.19	0.19
3	99.50	0.18	0.03	0.14	0.05
4	99.53	0.18	0.11	0.14	0.04
5	99.62	0.15	0.10	0.02	0.11
6	98.92	0.76	0.09	0.11	0.12
7	99.40	0.21	0.09	0.12	0.18
8	98.98	0.58	0.10	0.08	0.26
9	99.29	0.23	0.19	0.13	0.17
10	99.32	0.37	0.14	0.08	0.09
11	99.29	0.36	0.00	0.18	0.16
12	99.32	0.36	0.11	0.11	0.11
13	99.22	0.40	0.09	0.23	0.06
14	99.65	0.04	0.00	0.14	0.17
15	99.06	0.32	0.31	0.20	0.10
16	98.86	0.92	0.08	0.08	0.06
norm. wt.%	98.9	0.4	0.1	0.1	0.1

9.4 Sclerochronological profiles:

The dense and resilient foliated calcite present in the umbonal area, effectively preserves the primary environmental signature by resisting post-mortem alteration. So, our chemical analyses were directed towards this area, in accordance with methodologies established by prior studies (Surge and Lohmann, 2008; Goodwin et al., 2013; Bougeois et al., 2014). The diagenetic screening strongly suggests that the geochemical data preserved in the studied shells are likely to withstand the post mortem alterations during burial.

9.4.1 Elemental composition:

The individual growth layers in the shell cross section yield records of Calcium (Ca), Magnesium (Mg) and Iron (Fe), with minor amount of other trace metals including Manganese (Mn), Sulfur (S), Zinc (Zn) and Strontium (Sr). The normalized Ca concentration

ranges from 52709.71- 64452.8 ppm (average 57965 ppm). Mg content varies from 1100.91 to 1484.29 ppm. The concentration of Fe remains <2000 ppm and Mn remains <800 ppm (ranges of Mn vary between 499.50- 754.25 ppm). Strontium (Sr) also serves as diagenetic marker because of its markedly distinct partition coefficients between marine and meteoric waters (Kinsman, 1969). The Sr concentration gradually increases 135.12 ppm to 725.83 ppm ontogenetically i.e., from older to younger layers. Both iron (Fe) and manganese (Mn) serve as indicators of diagenetic alteration. They preferentially enriched during recrystallization shell (Brand and Veizer, 1980; Al-Aasm and Veizer, 1986a). Mn also serves as a redox-sensitive elements (Freitas et al., 2006). The skeletons of primary producers exhibit enrichment in Barium (Ba) (Marali et al., 2017; De Winter et al., 2018) and micronutrients like Zn, Cd, Cu, Ni, Co, V which are known to be absorbed into bivalve shells. Changes of their concentration reflects changes in paleoproductivity (Guo et al., 2013; De Winter et al., 2018) (Table 9.2).

Frequently employed geochemical proxies of these carbonate archives include conventional light stable isotope values such as $\delta^{13}C$ (McConnaughey & Gillikin, 2008), $\delta^{18}O$ (Jones & Quitmyer, 1996) and or trace elemental abundances, notably Ca, Mg, Sr, Mn, N, Li, S or Fe or some elements to calcium ratios (Mg/Ca, Sr/Ca, Ba/Ca, Mn/Ca and rare earth element) (Whittaker & Kyser, 1993; Klein et al., 1996a; Freitas et al., 2006; Thebault et al., 2009; Bau et al., 2010; Azmy et al., 2011; Yan et al., 2013; Immenhauser et al., 2016) (Table 9.3). The Mg/Ca ratio varies between 34.13 mMol/mol to 48.1 mMol/Mol while the Sr/Ca 12.62- 59.12 though Ba/Ca ratios are almost negligible (Table 9.3).

Table 9.2 Representation of trace elemental composition of *Pycnodonte* sp.

Sample Name		Na	Mg	Al	Ca	Fe	Li	Be	B	Sc
SB/5	Youngest layer	683.71	1441.71	360.24	64452.80	443.98	0.45	0.01	33.52	0.09
SB/4		375.21	1484.29	292.26	59128.06	1270.68	0.25	0.00	41.46	0.11
SB/3		271.63	1414.68	275.01	57333.36	1429.29	0.08	0.00	39.15	0.08
SB/2		295.24	1100.91	180.13	52709.71	1363.15	0.08	0.01	36.89	0.07
SB/1	Oldest layer	146.79	1151.21	738.24	56204.89	2233.21	0.13	0.01	60.63	0.16
Sample Name		**V**	**Cr**	**Mn**	**Co**	**Ni**	**Cu**	**Zn**	**Ga**	**Se**
SB/5	Youngest layer	4.13	172.67	532.85	5.62	550.23	28.75	133.95	0.24	1.55
SB/4		4.27	132.88	597.80	3.91	204.01	33.86	97.18	0.13	1.29
SB/3		2.43	1.24	499.50	1.20	275.91	20.64	19.10	0.06	0.71
SB/2		3.77	44.50	513.11	2.14	162.22	7.76	37.90	0.10	0.31
SB/1	Oldest layer	8.24	28.41	754.26	2.41	42.71	8.09	45.02	0.19	0.65
Sample Name		**Rb**	**Sr**	**Ba**	**La**	**Ce**	**Pr**	**Nd**	**Sm**	**Eu**
SB/5	Youngest layer	0.82	725.83	11.09	0.31	0.60	0.07	0.85	0.05	0.01
SB/4		0.62	335.69	12.18	0.39	0.69	0.08	0.23	0.06	0.02
SB/3		0.34	266.29	4.96	1.54	2.94	0.32	1.19	0.19	0.03
SB/2		0.34	174.01	4.35	0.39	0.61	0.07	0.28	0.04	0.02
SB/1	Oldest layer	1.14	135.13	21.37	1.10	2.47	0.21	0.25	0.15	0.05
Sample Name		**Gd**	**Tb**	**Dy**	**Y**	**Ho**	**Er**	**Tm**	**Yb**	**Lu**
SB/5	Youngest layer	0.05	0.01	0.04	0.23	0.01	0.02	0.00	0.01	0.00
SB/4		0.06	0.01	0.04	0.30	0.01	0.03	0.01	0.02	0.01
SB/3		0.17	0.02	0.08	0.43	0.01	0.04	0.01	0.03	0.01
SB/2		0.05	0.01	0.04	0.31	0.02	0.03	0.01	0.02	0.01
SB/1	Oldest layer	0.16	0.03	0.12	0.73	0.03	0.06	0.01	0.05	0.01
Sample Name		**Pb**	**Th**	**U**	**Zr**	**Nb**	**Mo**	**Hf**		
SB/5	Youngest layer	5.62	0.11	0.17	2.03	0.03	0.38	0.03		
SB/4		8.45	0.05	1.11	1.97	0.05	0.00	0.03		
SB/3		2.69	0.39	0.73	1.90	0.04	0.00	0.03		
SB/2		1.49	0.02	0.43	2.16	0.04	0.08	0.03		
SB/1	Oldest layer	2.59	0.09	1.14	2.47	0.10	0.04	0.05		

Table 9.3 Trace elemental ratio of *Pycnodonte* sp.

Sample Name		**Mg/Ca** (mMol/Mol)	**Sr/Ca** ppm	**Mn/Ca** ppm	**B / Ga** ppm	**Sr / Ba** ppm
SB/5	Youngest layer	37.28	59.12	6.01	138.21	65.42
SB/4		41.84	29.80	7.35	316.34	27.57
SB/3		41.12	24.38	6.34	631.12	53.64
SB/2		34.81	17.33	7.08	370.21	40.04
SB/1	Oldest layer	34.14	12.62	9.76	320.79	6.32

9.4.2 Carbon and Oxygen isotopic composition:

Oxygen and carbon isotopic ratios were measured on single species across 60 m interval. The geochemical analyses focused specifically on shells with intact fibrous-prismatic ultrastructures. Sclerochronological profiles for stable isotope analyses were obtained from longitudinal thick sections of the left valves, excluding areas of recrystallization, fine cracks, or borings from sponges and other bioeroders. The samples (approximately 100 μg) were obtained from the shell layers following their growth direction.

Shells are exhibiting cyclic variations in $\delta^{18}O$ and/or $\delta^{13}C$ (Fig. 9.6). The $\delta^{13}C$ and $\delta^{18}O$ values in four samples collected from different stratigraphic level from bottom to top along its different ontogenetic stages fluctuate between −5.51 and −0.73‰ and between –1.52 and 2.14‰, respectively (Table 9.4). Zakharov et al. (2011) reported $\delta^{18}O$ and $\delta^{13}C$ values (respectively −5.6 to −2.0‰ and −2.2 to 2.6‰) from bivalve species *Lopha* sp. from this formation.

The cycles of $\delta^{18}O$ are understood to primarily indicate seasonal changes in paleotemperature. Meanwhile, variations in $\delta^{13}C$ may signify shifts in the $\delta^{13}C$ of marine dissolved inorganic carbon due to seasonal fluctuations in marine productivity, changes in the metabolic activity of mollusks throughout the seasons, or a combination thereof (Steuber, 1999).

Table 9.4 Overview of stable isotope results in this study

LL			
δ18O (‰ VPDB)	**δ13C(‰ VPDB)**	**Temperature**	**Salinity**
-3.46	-1.71	26.97	122.69
-5.51	-0.91	37.32	123.37
-3.49	-1.07	27.11	123.60
-3.72	-0.90	28.22	123.27
-3.19	-1.19	25.69	122.47
-3.78	-1.44	28.51	123.18
-3.25	-1.22	25.97	124.04
-3.10	-0.84	25.27	121.69
-4.94	-1.54	34.33	124.31
-3.13	-0.70	25.41	125.84
-2.65	-0.07	23.18	120.41
-4.58	-2.25	32.49	124.61

UL-SB1			
δ18O (‰ VPDB)	**δ13C(‰ VPDB)**	**Temperature**	**Salinity**
-2.99	-0.16	24.76	125.47
-3.40	-0.98	26.68	123.60
-4.36	-1.93	31.39	121.18
-3.14	-0.51	25.46	124.70
-3.46	-0.96	26.99	123.62
-3.11	-0.53	25.33	124.67
-2.67	-0.56	23.29	124.81
-2.75	-0.22	23.66	125.48
-2.59	-0.23	22.90	125.53
-2.98	-0.15	24.69	125.50
-2.85	-0.41	24.09	125.05
-1.51	0.41	18.15	127.39
-0.89	0.97	15.55	128.85
-0.73	1.31	14.89	129.63
-1.00	1.22	15.99	129.29

UL-SB2			
δ18O (‰ VPDB)	**δ13C(‰ VPDB)**	**Temperature**	**Salinity**
-2.83	1.37	24.01	128.70
-3.29	1.11	26.18	127.94
-2.01	2.14	20.30	130.68
-2.59	1.56	22.92	129.20
-3.30	1.39	26.23	128.50
-2.28	1.82	21.49	129.89
-2.52	1.59	22.60	129.29
-3.14	1.30	25.47	128.39

TC-UL			
δ18O (‰ VPDB)	**δ13C(‰ VPDB)**	**Temperature**	**Salinity**
-1.63	0.69	18.67	127.89
-2.05	0.06	20.50	126.40
-2.40	-0.07	22.06	125.97
-2.34	-0.59	21.79	124.93
-1.68	0.12	18.85	126.72
-3.43	-1.08	26.83	123.37
-2.36	-0.26	21.85	125.59
-3.02	-0.86	24.89	124.03
-3.01	-0.45	24.84	124.89
-4.20	-1.19	30.59	122.77
-3.83	-0.64	28.75	124.08
-3.82	-0.50	28.69	124.37
-5.04	-1.52	34.84	121.68
-2.88	0.46	24.23	126.81

	Samples collected from
LL	first (lowermost) shellbank
UL-SB1	second shellbank
UL-SB2	third shellbank
TC-UL	fourth (topmost) shellbank

9.5 Reconstruction of paleoenvironmental conditions:

Shellbanks are always important to interpret the sedimentological and biological evolution of a basin. Massive almost intact fossil shell accumulations require particular conditions to be formed and may provide valuable insights into the sedimentary environments favouring such concentrations. The present study aims to quantify this trend and juxtapose it with a more precisely calibrated sedimentological framework.

9.5.1 Paleotemperature estimation:

Bivalve shells offer a precise chronology due to the periodic accretion of calcium carbonate along all expanding shell edges (Schöne and Surge, 2012). Shell oxygen isotope ratios ($\delta^{18}O_{shell}$) offer an excellent method for estimating paleotemperature because almost all bivalve species form their shells in close proximity to to oxygen isotopic equilibrium with the environment (Epstein and Mayeda, 1953; Wefer and Berger 1991, Schöne and Surge, 2014). Molluscs inhabiting the environments with typical marine salinity primarily respond to the latter factor, specifically to seasonal fluctuations in seawater temperature, assuming a consistent seawater $\delta^{18}O$. For each 1°C rise in temperature, equilibrium oxygen isotope precipitation of calcium carbonates decreases by approximately 0.24‰ (Craig, 1965). As the *Pycnodonte sp.* does not exert vital effects and are usually considered good paleoclimatic indicators (Criss, 1999; Rodland et al., 2003). Calcite secreting organisms incorporate oxygen into their shells directly from seawater, thus preserving the isotopic ratio of the water (Criss, 1999). Plotting $\delta^{13}C$ isotopic values against $\delta^{18}O$ in a binary plot, the clustering of oyster shell values is observed around the average of Cretaceous warm water skeleton (Fig. 9.7). Shell production occurred nearly year-round according to these growth patterns, indicating that the full seasonal amplitudes of $\delta^{18}O$ and $\delta^{13}C$ are preserved in the shells (Buchardt and Fritz, 1978).

Paleotemperatures (T) were calculated by the equation given by Anderson and Arthur (1983):

$$T\ (°C) = 16.0 - 4.14*(\delta^{18}O_{sam} - \delta^{18}O_{sw}) + 0.13(\delta^{18}O_{sam} - \delta^{18}O_{sw})^2$$

With $\delta^{18}O_{sam}$ as the isotope composition of the analyzed sample (V-PDB) and $\delta^{18}O_{sw}$ as the isotope ratio of the seawater from which the calcite originally precipitated. Assuming an ice-free Cretaceous world, $\delta^{18}O_{sw}$ of ~1‰ V-SMOW has been used (Shackleton and Kennett, 1975).

During the early Maastrichtian period, paleotemperatures inferred from the $\delta^{18}O$ values of rudist bivalves indicate fluctuations spanning a range of 24.8±3 °C. Paleotemperature calculated from the first shellbank is around 28.04 °C. As anticipated the temperature calculated from the shells is, on average, the lowest at third shellbank, around

22.9 °C on sea-bottom. At the topmost level, $\delta^{13}C$ values again turns dominantly negative. Concurrently the shellbank paleotemperature increased considerably to about 24.8 °C because of shallowing. The derived temperatures can then be compared to the sea level fluctuations.

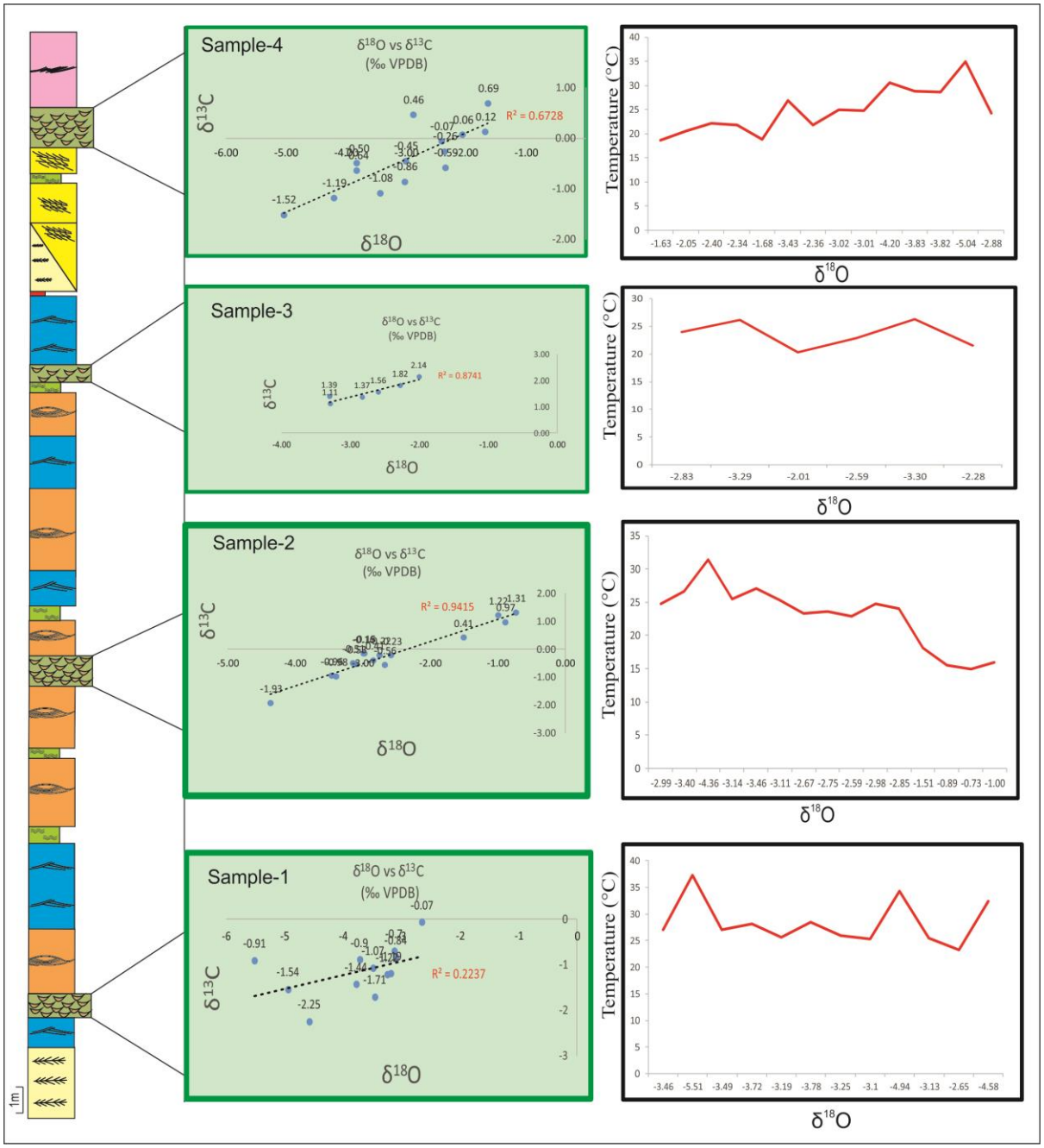

Fig. 9.6 Correlation of $\delta^{13}C$ and $\delta^{18}O$ & cyclical variation of paleotemperature (Srimani et al., 2022).

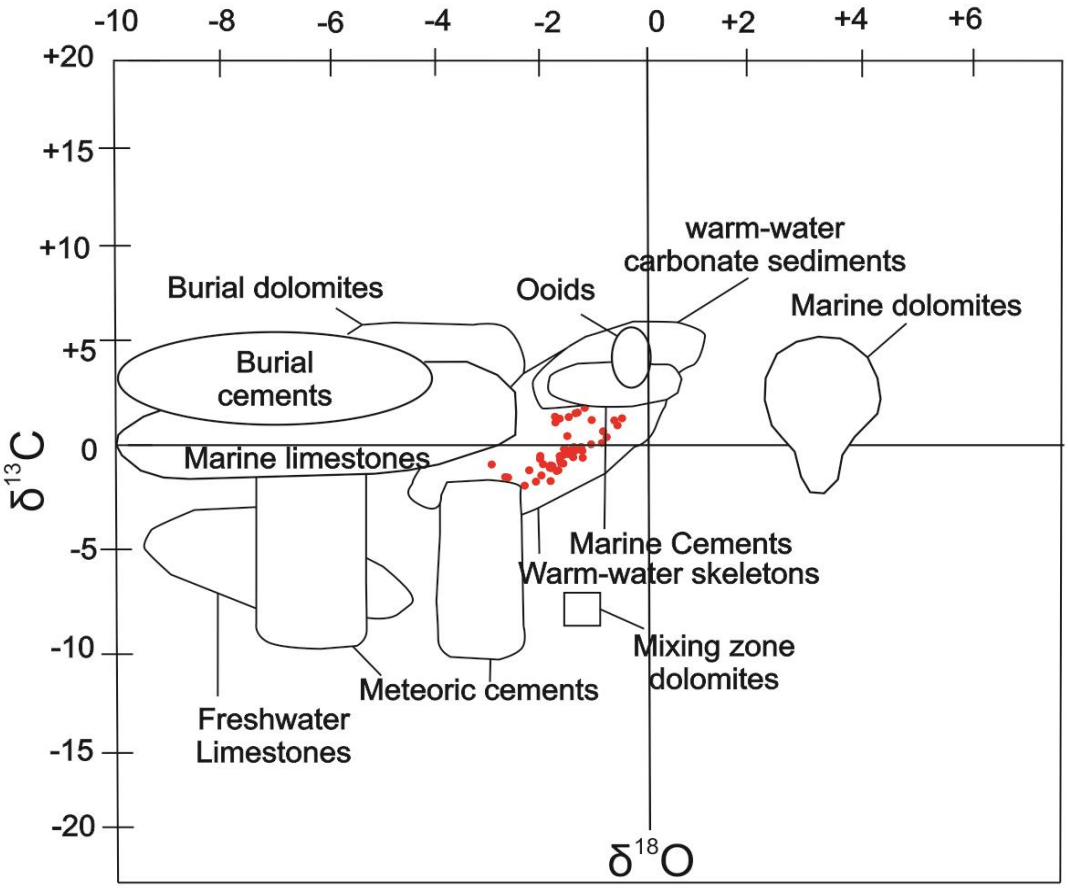

Fig. 9.7 Binary plotting of $\delta^{13}C$ against $\delta^{18}O$. Note, the clustering (red colored) of values around warm water skeleton zone (following Nelson and Smith, 1996).

9.5.2 Paleosalinity:

There has been no investigation of the potential of *Pycnodonte* sp. shells as paleosalinity records based on their geochemical signature so far. Salinity varies between 121.0 to 130.67 following $Z= a(\delta^{13}C+50) + b(\delta^{18}O+50)$ (Keith and Weber, 1964), which indicated shallow marine environment. Here, a and b are 2.048 and 0.498 respectively. Limestones with a Z-value above 120 signifies their depositional environment as marine (Table 9.4). Paleosalinity of sea water derived from the the shells generally considerably

high, B/Ga ~355.33 and Sr/Ba ~38.59 respectively (Table 9.3), interpreted as high salinity marine environment (Wei and Algeo, 2020). Thus, individual fossil shells open multi-century windows into past environment and provide details on paleosalinity.

9.6 Conclusion:

Large scale extensive shell bed in the Late Cretaceous (Maastrichtian) Kallankurichchi Formation of Ariyalur Group yielded an extraordinary assemblage of well-preserved mollusks. Phanerozoic Limestone are often abundantly fossiliferous, containing exceptionally well-preserved, uncompacted fossil remains, but this formation holds special attention as fossils are in living position, identified it as shellbanks. Rate of sedimentation was sufficiently low to allow colonisation of *Pycnodonte*. The shell record is always depending on the physiological optimum, like, warm temperatures, high nutrient supply, low number of predators (Schöne et al., 2006). During the Cretaceous period, a calcitic sea provided ample calcite to organisms for their shell growth. The paleotemperature calculated from the $\delta^{18}O$ values was around ~24.8 °C (average). Within the middle shellbanks, the shells are enriched in the heavier carbon isotope suggesting deepening of the depositional environment and increase in distance from the carbonate basin margin. Concurrently the degree of dilution by detrital quartz dropped. As anticipated the temperature calculated from the shells is, on average, the lowest at the mid-level, around 22.9°C (Md) on sea-bottom. At the topmost level, at the base of the HST, $\delta^{13}C$ values again turns dominantly negative. Concurrently the shellbank paleotemperature increased considerably to about 24.8°C (Md) because of shallowing. Depth-control on seafloor paleotemperature is thus apparent. Moreover, the estimated isotopic temperature aligns with the late Cretaceous paleogeographic position and inferred paleoclimatic conditions of India, as indicated by fossil assemblages. Paleosalinity of sea water derived from the micritic matrix between the shells in the banks is generally considerably high, B/Ga and Sr/Ba ranging from 20.60-49.00 and 0.7-1.9 respectively (Wei and Algeo, 2020).

The warm overall temperature and the near-tropical positioning of the continent facilitated the formation of thick-shelled rudist bivalve colony. The elevated temperature may enhance different carbonate production rate, which resulted the variation in lamina thickness

(Jones 1980; Jones et al. 1989). Subsequent to their deposition, the molluscs were protected from any possible escape, physical or biological reworking and bacterial decay. Though the organisms were sessile, their shells being highly convoluted were prone to post-mortem rolling downslope. For that reason, the shells were collected only from shellbanks cemented with micritic matrix to ensure that they give proxy for their endemic paleoenvironment. The integration of trace element records with stable carbon and oxygen isotope measurements demonstrates the intricate interaction between environmental and physiological factors influencing the incorporation of trace elements and stable isotopes into bivalve shells in this region. Calculations based on Cretaceous paleoclimatic data, it is inferred that the globally averaged surface temperature during this period was 6 to 14°C warmer than at present (Barron and Washington, 1982). Further, an upper ocean temperature survey of Cretaceous time span, extending from low to middle latitude carry significant implications for comprehending the evolution of the Cretaceous greenhouse climate, as detailed in the subsequent Table 9.5.

Isotopic records derived from the isotopic composition of Maastrichtian bivalve shells within the Ariyalur Group of the Cauvery Basin suggest that this region at middle latitudes persisted within a tropical climatic zone during the early Maastrichtian period (Fig. 9.8). The findings appear to be linked to the onset of global warming during the early Late Cretaceous period.

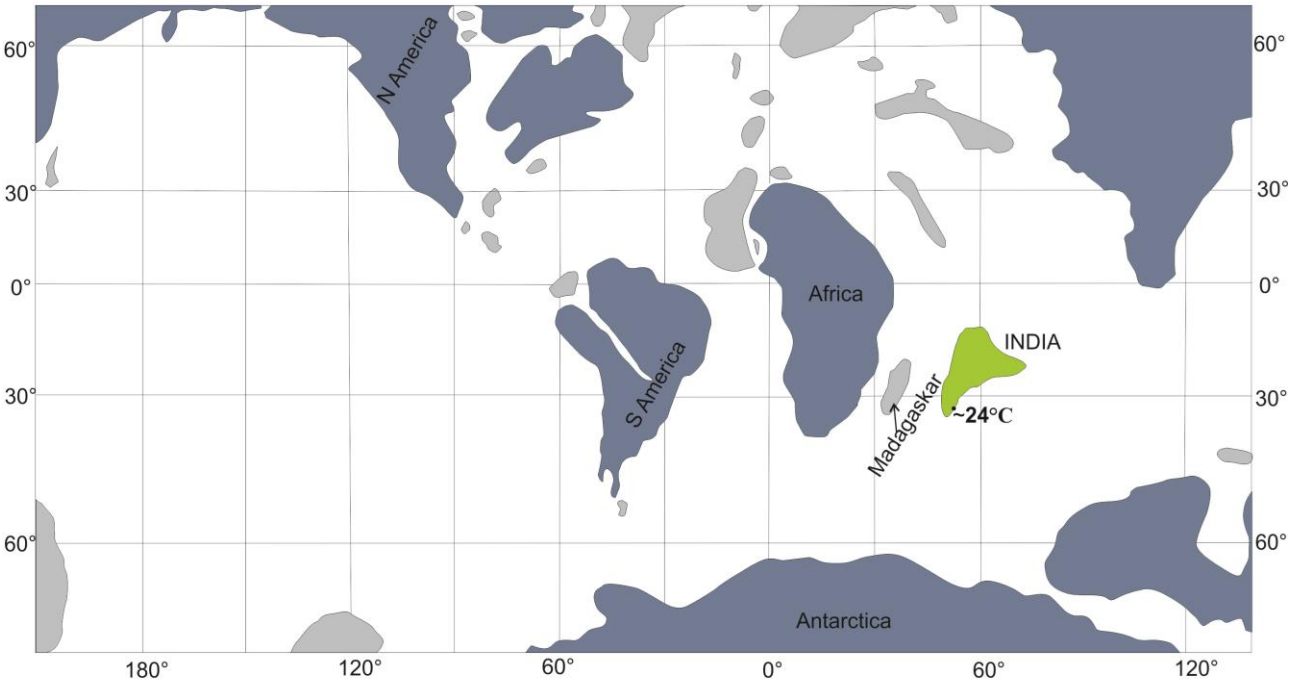

Fig. 9.8 Map showing India's position during Late Cretaceous time and the palaeotemperatures corroborates with tropical climate (modified after Zakharov et al., 2011).

Repository of Paleotemperature (Late Cretaceous Period)					
Author	**Time**	**Location**	**Temp (°C)**	**Environment**	**Organism**
Zakharov et al.,2011	Early Maastrichtian	Cauvery Basin, South India	21.2-22	Sea Bottom	*Lopha* Bivalve
Huber et al., 2002	Late Albian-Maastrichtian	30° N, North Atlantic	20-12-09	Deep Sea, Sea bottom	Foraminifera
Jelby et al., 2014	Early Maastrichtian	Denmark	13.6-14.3	Sea bottom	Brachiopods & calcereous nanofossils
Ayyasami, 2006	Late Cretaceous	Cauvery Basin, South India	36.73	Sea Bottom	*Rastellum* bivalve
Saltzman & Barron, 1982	Late Cretaceous	NA	5. to 16	Sea Bottom	*Inoceramus*
Shazly et al., 2011	Late Cenomanian	Egypt	24.5-31.5	Sea bottom	Rudist
Pirrie & Marshall, 1990	Late Cretaceous	Antarctica	13.6	Sea bottom	Belemnites
Harlou et al., 2016	Maastrichtian	Northern Denmark	10	Sea floor	Brachiopod
Tourtelot & Rye, 1969	Late Cretaceous	Western Interior Region of North America	30	Sea bottom	*Inoceramus*
Winter et al., 2018	Late Cretaceous	Argentina	11	Sea bottom	*Pycnodonte*
		NA	27.3 ± 2.5		
Cramer et al., 2011	Late Cretaceous	NA	13	Deep ocean	Benthic Foraminifera
Peterson et al., 2016	Campanian-Late Maastrichtian	Western Interior Seaway (Central United State)	5 to 21	NA	Molluscs (Bivalves & Gastropods)
Obrien et al., 2017	NA	NA	21	Sea Surface	Planktonic Foraminifera
Bowen, 1961	Late Cretaceous	Europe, India (Uttatur), Japan	13.-25.1	Sea Surface	Belemnoidea (Nektonic)
Niebhur & Joachimski, 2002	Mid Campanian	North Germany	12.5±2	Sea Surface	Belemnites
Sorensen et al., 2015	Early Cenomanian	Sweden	12.5	Sea Surface	Belemnites
Steuber, 1999	Late Cretaceous	Greece, Turkey, Somalia and the Arabian Peninsula	30-32.5	Sea Surface	Rudist (Hippuritacea)
Urey et al., 1951	Late Cretaceous	England, Denmark, South Eastern, United States	15-16	Sea Surface	Belemnites
Walliser et al., 2018	Late Cretaceous	Western Interior Seaway	17±4.1	Sea Surface	*Inoceramus*

Author	Time	Location	Temp (°C)	Environment	Organism
Zakharov et al., 2007	Campanian	Western Circum-Pacific	24.2	Sea Surface	Mollusca & Foraminifera
	NA	Eastern Circum-Pacific	26.4	NA	NA
	NA	Koryak Upland	22.4-25.5	NA	NA
	NA	South Alaska	19.4	NA	NA
Friedrich et al., 2012	Mid to Late Cretaceous	Western equatorial Atlantic, Demerara Rise	35	Sea Surface	Planktic Foraminifera
			20	Sea bottom	Benthic Foraminifera
Jenkyns et al., 2004	Late Cretaceous	Arctic	15	Sea Surface	Marine plankton, Crenarchaeota
Pearson et al., 2001	Late Cretaceous to Eocene	South Atlantic Ocean	28–32	Sea Surface	Foraminifera
Linnert et al., 2014	Maastrichtian	N Atlantic Shelf	28	Sea Surface	Planktic Foraminifera
Sellwood et al., 1994	Cenomanian	Atlantic & Pacific Ocean	18.4-25.9	Sea Surface	Planktic Foraminifera
OConnor et al., 2019	Cenomanian to Campanian	Southern High Latitudes	27-37	Sea Surface	Planktic Foraminifera
Parrish & Spicer, 1988	Campanian-Maastrichtian	California Forest	2 to 8	Land/Terrestrial	*Tsuga mertensiana* (Plant)
Wolfe & Upchurch, 1987	Campanian	North America	8.00	Land/Terrestrial	Leaf Assemblages & *Dicotyledonous* woods
Golovneva, 2000	Late Cretaceous	N-Eastern Asia, Edmonton	1.8-17 (cold to warm)	Land/Terrestrial	Flora
Spicer & Parrish, 1990	Coniacian	Northern Alaska	13	Land/Terrestrial	Plant
	Maastrichtian		5		
Madhavaraju et al., 2015	Late Cretaceous	Cauvery Basin, South India	56.2	Shallow marine limestone	Bulk rock
Puceat et al., 2007	Late Cretaceous	NA	NA	Upper Ocean	Fish Tooth
Zhang et al., 2019	Late Cretaceous	Review paper	3-28(avg. 15)	Terrestrial	
			8-33(avg. 23)	Marine	
Our result	Maastrichtian	Cauvery Basin, India	24.8	Sea bottom	*Pycnodonte* (Gryphoid Bivalve)

Table 9.5 Global record of temperature during Late Cretaceous time.

PART-III

COMPENDIUM

CHAPTER- 10

SUMMARY AND CONCLUSION

An integration of the depositional scenario of the late Cretaceous Kallankurichchi Limestone Formation, discussed in piecemeal in the preceding chapters, is attempted in this chapter. The intricacies that emerged during the study prompted focused attention to interpret the evolution of the formation. A collage of snapshots taken through space and time would probably allow a vision of the then time regarding to the paleoclimate and paleoenvironment during deposition of the formation. The present thesis has made some significant contribution for the advancement in Late Cretaceous geology of the Cauvery Basin which bear global significance as well.

The Kallankurichchi Limestone Formation stands out as a veritable treasure trove for paleontologists, boasting an abundance of fossils that have fascinated researchers for years. Hundreds of papers already been published from this formation focusing overwhelmingly on its biological aspects. The taxonomy related study and biostratigraphy has so far been done meticulously. An immense gap in knowledge still persists regarding the detailed sedimentological aspects of the Kallankurichchi Limestone. Despite efforts to identify the paleogeography of deposition, the resolution remains poor, often relying solely on fossil content. This has led to confusion and disparities in initiation and evolution of the Kallankurichchi basin. The lithostratigraphic and sequence stratigraphic analyses has not been done properly so far. The dynamics of sedimentation, particularly event deposition, and the modes of paleogeographic shifts have remained elusive, contributing to the aforementioned disparities. Tectonic and paleogeomorphic elements that could reveal crucial aspects of basin configuration have gone unrecognized. The implications of diversely oriented paleocurrent current systems have been overlooked so far. Furthermore, the environmental controls on sediment geochemistry have yet to be fully elucidated.

In this dissertation, I endeavor to shed light on these overlooked aspects and many others within the realm of sedimentology, stratigraphy and geochemistry. Through high-resolution facies analyses, my aim is to enhance our understanding of the Kallankurichchi Limestone Formation and contribute to fill the gaps in our knowledge of sedimentation dynamics and paleogeographic evolution of the Kallankurichchi Limestone Formation.

Notably, the identification of scree cones at the base of the formation unveils a rejuvenated history of basin tectonics, contributing significantly to a robust framework for

reconstructing the basin's evolutionary trajectory. The underlying marine Sillakuddi Sandstone Formation is overlained by the Kallankurichchi Limestone imply shift from a siliciclastic depocenter to a carbonate depositional system. The scree and related mass flow deposits present in successive layers at the basal part, spreading over both spatial and temporal scales speaks regarding the paleogeographic shifts, and provide invaluable insights into the basin's evolutionary history. The presence of carbonate clasts/ fossil fragments along with large blocks of sandstone from the Sillakuddi Formation imply that the renewed rifting/subsidence of the basin continued even after the deposition of carbonate sediments. Presence of clasts of mixed composition (both siliciclastic and carbonate) within the screes are rarely reported from the rock record and discussed in detailed in preceding Chapter 6 (Srimani, 2024) The presence of numerous slide planes within these clastic sediments supports the tectonic rejuvenation. The recurrent tectonic pulses helped to develop mass flows in the down current direction. The preservation of a thin transgressive lag deposits between the Sillakuddi Sandstone and Kallankurichchi Limestone Formation, though rarely preserved also support transgression of the sea during the subsidence. Certainly, the scale of subsidence was not same all along the basal contact as dark grey limestone appeared, at places, only at the basal part of the limestone containing abundant green clay minerals formed by the alteration of metastable framework grains. The X-Ray Diffraction analysis of the green clay help to identify a rare mineral berthierine (by the strong ~7 Å basal spacing) which has never been reported from this formation. The unusual appearance of berthierine as grain pseudomorphs, rarely reported from the rock record, revealed the dissolution of metastable volcaniclastic grains in a slightly acidic, oxygen-depleted depositional environment as the primary mechanism of authigenesis. Possibly due to the basin subsidence during the post tectonic readjustment, the basin might have subsided enough in some parts helped to develop the reducing condition close to the seafloor favored berthierine formation.

A comprehensive paleoenvironmental and paleogeographic analyses of the fossiliferous carbonate succession of Kallankurichchi Formation deepen our understanding of the genesis of the constituent facies. They are broadly divisible into two facies associations, viz., (1) Wave-dominated and (2) Tide-dominated. A distinct ‘thin muddy facies’ (15 cm) is demarcated the boundary between these two associations. Besides, the two facies associations four numbers of shell beds have been identified within the Maastrichtian Kallankurichchi

Formation, yielded an extraordinary assemblages of well-preserved molluscs. These exceptionally well-preserved, intact fossil assemblages dominated by rudist bivalve *Pycnodonte*, preserved in original life mode, identified as shellbanks. The overall major oxide and trace element data, a powerful tool for interpreting paleodepositional environments including paleoredox and paleosalinity support the observations inferred earlier across different facies associations. Paleoredox data suggests anoxic conditions in the lowermost part, while rest of the succession indicates oxic conditions. These also supports the reason behind the proliferation of organisms.

Rate of sedimentation was sufficiently low to allow colonisation of *Pycnodonte*. $\delta^{13}C$ and $\delta^{18}O$ values from the alternate lamina of these *Pycnodonte* shells, in general, display a fair degree of uniformity that corresponds to open marine condition. The palaeotemperature at sediment-water interface calculated from $\delta^{18}O$ is around 24.8°C, supports the Late Cretaceous greenhouse climate.

The shellbeds are associated with some storm deposits. The diverse sedimentation dynamics uncovered a clear distinction between authigenic and allogenic sediments, laying an essential foundation for biostratigraphic studies and the analysis of faunal paleobathymetry. Further genetic subdivisioning of sediments offers an unprecedented visualization of the sedimentation process. Examination of paleogeographic shifts over space and time aids in understanding the evolutionary history of the basin in considerable detail. Additionally, paleoenvironmental and paleogeographic analyses deepen our comprehension of the origins of the facies comprising the formations.

With a thin tidal deposit at its base, the wave dominated basinward facies association (transgressive system tract/TST) is overlain by the muddy facies, likely to be the maximum flooding surface (MFS). This surface is followed by shallowing upward succession (highstand systems tract/HST) dominated again by tidal features.

Envisioning ancient geography, climate, redox potential through a maze of raging controversies and instilling adequate confidence in their reconstruction a comprehensive physico-chemical analysis of sediments and sequences is the cherished goal of this deliberation.

REFERENCES

Acharyya, S.K. and Lahiri, T.C., 1991. Cretaceous palaeogeography of the Indian subcontinent; a review. *Cretaceous Research*, *12*(1), pp.3-26.

Adams, A. and MacKenzie, I., 1998. Carbonate sediments and rocks under the microscope: a colour atlas. CRC Press.

Adatte, T., Keller, G., Stüben, D., Harting, M., Kramar, U., Stinnesbeck, W., Abramovich, S. and Benjamini, C., 2005. Late Maastrichtian and K/T paleoenvironment of the eastern Tethys (Israel): mineralogy, trace and platinum group elements, biostratigraphy and faunal turnovers. *Bulletin de la Société Géologique de France*, *176*(1), pp.37-55.

Aigner, T., 1985. Biofabrics as dynamic indicators in nummulite accumulations. *Journal of Sedimentary Research*, *55*(1), pp.131-134.

Al-Aasm, I.S. and Veizer, J., 1986. Diagenetic stabilization of aragonite and low-Mg calcite; I, Trace elements in rudists. *Journal of Sedimentary Research*, *56*(1), pp.138-152.

Alberti, M., Fürsich, F.T. and Pandey, D.K., 2013. Seasonality in low latitudes during the Oxfordian (Late Jurassic) reconstructed via high-resolution stable isotope analysis of the oyster *Actinostreon marshi* (J. Sowerby, 1814) from the Kachchh Basin, western India. *International Journal of Earth Sciences*, *102*, pp.1321-1336.

Alberti, M., Pandey, D.K., Sharma, J.K., Swami, N.K. and Uchman, A., 2017. Slumping in the upper Jurassic Baisakhi formation of the Jaisalmer Basin, western India: Sign of synsedimentary tectonics?. *Journal of Palaeogeography*, *6*(4), pp.321-332.

Algeo, T.J., Kuwahara, K., Sano, H., Bates, S., Lyons, T., Elswick, E., Hinnov, L., Ellwood, B., Moser, J. and Maynard, J.B., 2011. Spatial variation in sediment fluxes, redox conditions, and productivity in the Permian–Triassic Panthalassic Ocean. *Palaeogeography, Palaeoclimatology, Palaeoecology*, *308*(1-2), pp.65-83.

Alt, J.C., Laverne, C., Coggon, R.M., Teagle, D.A., Banerjee, N.R., Morgan, S., Smith-Duque, C.E., Harris, M. and Galli, L., 2010. Subsurface structure of a submarine hydrothermal system in ocean crust formed at the East Pacific Rise, ODP/IODP Site 1256. *Geochemistry, Geophysics, Geosystems*, *11*(10).

Anderson, T.F. and Arthur, M.A., 1983. Stable isotopes of oxygen and carbon and their application to sedimentologic and paleoenvironmental problems.

Ando, H., 2019. Taphonomy and Sedimentological Significance of Oyster Shell Beds within Cretaceous Transgressive Sediments in Japan. *Open Journal of Geology*, *9*(10), pp.547.

Andreozzi, M., Dinelli, E. and Tateo, F., 1997. Geochemical and mineralogical criteria for the identification of ash layers in the stratigraphic framework of a foredeep; the Early Miocene Mt. Cervarola Sandstones, northern Italy. *Chemical Geology*, *137*(1-2), pp.23-39.

Antonelli, M.A., Pester, N.J., Brown, S.T. and DePaolo, D.J., 2017. Effect of paleoseawater composition on hydrothermal exchange in midocean ridges. *Proceedings of the National Academy of Sciences*, *114*(47), pp.12413-12418.

Arguden, A.T. and Rodolfo, K.S., 1986. Sedimentary facies and tectonic implications of lower Mesozoic alluvial-fan conglomerates of the Newark basin, northeastern United States. *Sedimentary Geology*, *51*(1-2), pp.97-118.

Ayyasami, K., 1990. Cretaceous heteromorph ammonoid biostratigraphy of southern India. *Newsletters on Stratigraphy*, *2*, pp.111-118.

Ayyasami, K., 2006. Role of oysters in biostratigraphy: A case study from the Cretaceous of the Ariyalur area, southern India. *Geosciences Journal*, *10*(3), pp.237-247.

Ayyasami, K. and Banerji, R.K., 1984. Cenomanian-Turonian transition in the Cretaceous of southern India. Bulletin of the Geological Society of Denmark, 33(1), pp.21-30.

Ayyasami, K. and Jagannatharao, B.R., 1978. On the possible faunal break at the contact of Trichinopoly and Ariyalur Groups in the Cretaceous succession of Tiruchirappalli District, Tamil Nadu. In *Proceedings of the VII Indian Colloquium on Micropaleontology and Stratigraphy; Madras, India*, pp.3-4.

Ayyasami, K., Radhakrishnan, K. and Lingaraj, O., 1992. Stratigraphy of the Cretaceous rocks around Kilapalavur, Tiruchchirappalli District, Tamil Nadu. *Journal of the Palaeontological Society of India*, *37*, pp.109-112.

Aziz, S.A., 1988. Some echinoid remains from Dalmiapuram Formation and Kallakudi reefoidal Limestone (Lower Cretaceous), Trichnopoly Subbasin, South India, pp.11-30.

Azmy, K., Brand, U., Sylvester, P., Gleeson, S.A., Logan, A. and Bitner, M.A., 2011. Biogenic and abiogenic low-Mg calcite (bLMC and aLMC): Evaluation of seawater-REE composition, water masses and carbonate diagenesis. *Chemical Geology*, *280*(1-2), pp.180-190.

Bailey, S.W., 1988. Odinite, a new dioctahedral-trioctahedral Fe3+-rich 1: 1 clay mineral. *Clay minerals*, *23*(3), pp.237-247.

Baldermann, A., Banerjee, S., Czuppon, G., Dietzel, M., Farkaš, J., Löhr, S., Moser, U., Scheiblhofer, E., Wright, N.M. and Zack, T., 2022. Impact of green clay authigenesis on element sequestration in marine settings. *Nature Communications*, *13*(1), pp.1527.

Baldermann, A., Grathoff, G.H. and Nickel, C., 2012. Micromilieu-controlled glauconitization in fecal pellets at Oker (Central Germany). *Clay Minerals*, *47*(4), pp.513-538.

Bandyopadhyay, S., Chatterjee, S. and Scotese, C., 2010. The wandering Indian plate and its changing biogeography during the Late Cretaceous-Early Tertiary period. *New aspects of Mesozoic biodiversity*, pp.105-126.

Banerjee, S., Bansal, U. and Thorat, A.V., 2016. A review on palaeogeographic implications and temporal variation in glaucony composition. *Journal of Palaeogeography*, *5*(1), pp.43-71.

Banerjee, S., Bansal, U., Pande, K. and Meena, S.S., 2016. Compositional variability of glauconites within the Upper Cretaceous Karai Shale Formation, Cauvery Basin, India: implications for evaluation of stratigraphic condensation. *Sedimentary Geology*, *331*, pp.12-29.

Banerjee, S., Mondal, S., Chakraborty, P.P. and Meena, S.S., 2015. Distinctive compositional characteristics and evolutionary trend of Precambrian glaucony: Example from Bhalukona Formation, Chhattisgarh basin, India. *Precambrian Research*, *271*, pp.33-48.

Banerjee, S., Roy Choudhury, T., Saraswati, P.K. and Khanolkar, S., 2020. The formation of authigenic deposits during Paleogene warm climatic intervals: a review. *Journal of Palaeogeography*, *9*, pp.1-27.

Banerji, R.K., 1968. Late Cretaceous foraminiferal biostratigraphy of Pondicherry area, south India. *Mem. Geol. Soc. India*, *2*, pp.30-49.

Banerji, R.K., 1972. Stratigraphy and Micropalaeontology of the Cauvery Basin. part-I, Exposed area. *Jour. Pal. Soc. India*, *17*, pp.1-24.

Banerji, R.K., 1973. Foraminiferal Biostratigraphy and Geological Evolution of the Thanjavur Sub-Basin, South India. *Geological Society of India*, *14*(3), pp.257-274.

Banerji, R.K., 1983. Evolution of the Cauvery basin during Cretaceous. In *Symposium on Cretaceous of India: palaeoecology, palaeogeography and time boundaries*, pp.22-39.

Banerji, R.K. and Mohan, R., 1970. Foraminiferal Biostratigraphy of Meso-Cenozoic Sequence of the' Cauvery Basin, South India. *Geological Society of India*, *11*(4), pp.348-357.

Banerji, R.K. and Sastri, V.V., 1979. Quantification of Foraminiferal Biofacies and Reconstruction of Palaeobiogeography of the Cauvery Basin. *Geological Society of India*, *20*(12), pp.571-586.

Bansal, U., Banerjee, S. and Borgohain, D., 2021. Records of Marine Transgressions and Paleo-Depositional Conditions Imprinted Within Cretaceous Glauconites of India. *Mesozoic Stratigraphy of India: A Multi-Proxy Approach*, pp.443-467.

Bansal, U., Pande, K., Banerjee, S., Nagendra, R. and Jagadeesan, K.C., 2019. The timing of oceanic anoxic events in the Cretaceous succession of Cauvery Basin: Constraints from 40Ar/39Ar ages of glauconite in the Karai S hale Formation. *Geological Journal*, *54*(1), pp.308-315.

Bao, S.X., Zhou, H.Y., Peng, X.T., Ji, F.W. and Yao, H.Q., 2008. Geochemistry of REE and yttrium in hydrothermal fluids from the Endeavour segment, Juan de Fuca Ridge. *Geochemical Journal*, *42*(4), pp.359-370.

Barron, E.J. and Washington, W.M., 1982. Cretaceous climate: a comparison of atmospheric simulations with the geologic record. *Palaeogeography, Palaeoclimatology, Palaeoecology*, *40*(1-3), pp.103-133.

Bathurst, R.G., 1972. *Carbonate sediments and their diagenesis*. Elsevier.

Bau, M., 1991. Rare-earth element mobility during hydrothermal and metamorphic fluid-rock interaction and the significance of the oxidation state of europium. *Chemical geology*, *93*(3-4), pp.219-230.

Bau, M., Balan, S., Schmidt, K. and Koschinsky, A., 2010. Rare earth elements in mussel shells of the Mytilidae family as tracers for hidden and fossil high-temperature hydrothermal systems. *Earth and Planetary Science Letters*, *299*(3-4), pp.310-316.

Beaufort, D., Rigault, C., Billon, S., Billault, V., Inoue, A., Inoué, S. and Patrier, P., 2015. Chlorite and chloritization processes through mixed-layer mineral series in low-temperature geological systems–a review. *Clay minerals*, *50*(4), pp.497-523.

Berner, R.A., 1981. A new geochemical classification of sedimentary environments. *Journal of Sedimentary Research*, *51*(2), pp.359-365.

Bhatia, M.R., 1985. Rare earth element geochemistry of Australian Paleozoic graywackes and mudrocks: provenance and tectonic control. *Sedimentary geology*, *45*(1-2), pp.97-113.

Bhattacharyya, D.P., 1983. Origin of berthierine in ironstones. *Clays and clay minerals*, *31*, pp.173-182.

Blanford, H.F., 1862. *On the Cretaceous and other rocks of the South Arcot, and Trichinopoly districts, Madras*. Government of India.

Bolhar, R., Kamber, B.S., Moorbath, S., Whitehouse, M.J. and Collerson, K.D., 2005. Chemical characterization of earth's most ancient clastic metasediments from the Isua Greenstone Belt, southern West Greenland. *Geochimica et Cosmochimica Acta*, *69*(6), pp.1555-1573.

Bolhar, R., Whitehouse, M.J., Weaver, S.D. and Cole, J.W., 2006. Geochemical variability of zircons from the cretaceous separation point batholith (New Zealand)—Clues to sources and igneous processes. *Geochimica et Cosmochimica Acta Supplement*, *70*(18), pp. A57-A57.

Bose, P.K. and Chanda, S.K., 1986. Storm deposits and hummocky cross-stratification: A geological viewpoint.

Bose, P.K. and Sarkar, S., 1991. Basinal autoclastic mass flow regime in the Precambrian Chanda limestone formation, Adilabad, India. *Sedimentary geology*, *73*(3-4), pp.299-315.

Bose, P.K., Chaudhuri, A.K. and Seth, A., 1988. Facies, flow and bedform patterns across a storm-dominated inner continental shelf: Proterozoic Kaimur Formation, Rajasthan, India. *Sedimentary Geology*, *59*(3-4), pp.275-293.

Bose, P.K., Mazumder, R. and Sarkar, S., 1997. Tidal sandwaves and related storm deposits in the transgressive Protoproterozoic Chaibasa Formation, India. *Precambrian Research*, *84*(1-2), pp.63-81.

Bose, P.K., Sarkar, S., Mukhopadhyay, S., Saha, B. and Eriksson, P., 2008. Precambrian basin-margin fan deposits: Mesoproterozoic Bagalkot Group, India. *Precambrian Research*, *162*(1-2), pp.264-283.

Bougeois, L., de Rafélis, M., Reichart, G.J., de Nooijer, L. and Dupont-Nivet, G., 2015, April. Using Mg/Ca on oyster shells as paleoclimatic proxy, example from the Paleogene of Central Asia. In *EGU General Assembly Conference Abstracts* (p. 493).

Bowen, R., 1961. Oxygen isotope paleotemperature measurements on Cretaceous Belemnoidea from Europe, India and Japan. *Journal of Paleontology*, pp.1077-1084.

Brand, U. and Veizer, J., 1980. Chemical diagenesis of a multicomponent carbonate system; 1, Trace elements. *Journal of Sedimentary Research*, *50*(4), pp.1219-1236.

Brezina, S.S., Romero, M.V., Casadío, S. and Bremec, C., 2014. Boring polychaetes associated with Pycnodonte (Phygraea) vesicularis (Lamarck) from the Upper Cretaceous of Patagonia. A case of commensalism?. *Ameghiniana*, *51*(2), pp.129-140.

Brindley, G.W., 1982. Chemical compositions of berthierines—A review. *Clays and clay Minerals*, *30*(2), pp.153-155.

Bromley, R.G., 1968. Burrows and borings in hardgrounds. Verlag nicht ermittelbar.

Brown, J.S., 1943. Suggested use of the word microfacies. *Economic Geology*, *38*(4), p.325.

Bruckschen, P., Bruhn, F., Meijer, J., Stephan, A. and Veizer, J., 1995. Diagenetic alteration of calcitic fossil shells: Proton microprobe (PIXE) as a trace element tool. *Nuclear Instruments and Methods in Physics Research Section B: Beam Interactions with Materials and Atoms*, *104*(1-4), pp.427-431.

Buchardt, B. and Fritz, P., 1978. Strontium uptake in shell aragonite from the freshwater gastropod Limnaea stagnalis. *Science*, *199*(4326), pp.291-292.

Burke, K. and Dewey, J.F., 1973. An outline of Precambrian plate development. *Implications of continental drift to the earth sciences*, *2*, pp.1035-1045.

Calvert, S.E., Pedersen, T.F. and Thunell, R.C., 1993. Geochemistry of the surface sediments of the Sulu and South China Seas. *Marine Geology*, *114*(3-4), pp.207-231.

Canaval, L.R. and Rode, B.M., 2015. The hydration properties of Eu (II) and Eu (III): An ab initio quantum mechanical molecular dynamics study. *Chemical Physics Letters*, *618*, pp.78-82.

Catuneanu, O., 2022. Principles of sequence stratigraphy. Newnes.

Catuneanu, O., Galloway, W.E., Kendall, C.G.S.C., Miall, A.D., Posamentier, H.W., Strasser, A. and Tucker, M.E., 2011. Sequence stratigraphy: methodology and nomenclature. *Newsletters on stratigraphy*, *44*, pp.173-245.

Cerling, T.E., 1991. Carbon dioxide in the atmosphere: evidence from Cenozoic and Mesozoic paleosols. *American Journal of Science;(United States)*, *291*(4).

Chakraborty, N., 2016. Barremian-Coniacian Sediments and Sequence Building in the Pondicherry Sub-Basin of Cauvery Basin, India. Unpublished Ph.D. Thesis, Jadavpur University, Kolkata, pp.210

Chakraborty, N. and Sarkar, S., 2018. Syn-sedimentary tectonics and facies analysis in a rift setting: Cretaceous Dalmiapuram Formation, Cauvery Basin, SE India. *Journal of Palaeogeography*, *7*(2), pp.146-167.

Chakraborty, N., Mandal, A., Nagendra, R., Srimani, S., Banerjee, S. and Sarkar, S., 2021. Cretaceous Deposits of India: A Review. *Mesozoic Stratigraphy of India: a multi-proxy approach*, pp.39-85.

Chakraborty, N., Sarkar, S., Mandal, A., Mejiama, W., Tawfik, H.A., Nagendra, R., Bose, P.K. and Eriksson, P.G., 2017. Physico-chemical characteristics of the Barremian-Aptian siliciclastic rocks in the Pondicherry embryonic rift sub-basin, India. In *Sediment Provenance* (pp. 85-121). Elsevier.

Chakraborty, N., Srimani, S., Mondal, I., Mandal, S., Nagendra, R., Sarkar, S., (in press). Sequence development in relation to sedimentation history of the Cretaceous-Miocene Cauvery Basin: a new outlook. In: *Geology of Cauvery Basin in South India, Taylor and Francis Group, E*dited by Jain S. and Chakraborty N.

Chakraborty, P.P., 2011. Slides, soft-sediment deformations, and mass flows from Proterozoic Lakheri Limestone Formation, Vindhyan Supergroup, central India, and their implications towards basin tectonics. *Facies*, *57*(2), pp.331-349.

Chan, S.A., Kaminski, M.A., Al-Ramadan, K. and Babalola, L.O., 2017. Foraminiferal biofacies and depositional environments of the Burdigalian mixed carbonate and siliciclastic Dam Formation, Al-Lidam area, Eastern Province of Saudi Arabia. *Palaeogeography, Palaeoclimatology, Palaeoecology*, *469*, pp.122-137.

Chand, S., Radhakrishna, M. and Subrahmanyam, C., 2001. India–East Antarctica conjugate margins: rift-shear tectonic setting inferred from gravity and bathymetry data. *Earth and Planetary Science Letters*, *185*(1-2), pp.225-236.

Chraiki, I., Chi Fru, E., Somogyi, A., Bouougri, E.H., Bankole, O., Ghnahalla, M. and El Albani, A., 2023. Blooming of a microbial community in an Ediacaran extreme volcanic lake system. *Scientific Reports*, *13*(1), p.9080.

Chari, M.N., Sahu, J.N., Banerjee, B., Zutshi, P.L. and Chandra, K., 1995. Evolution of the Cauvery basin, India from subsidence modelling. *Marine and Petroleum Geology*, *12*(6), pp.667-675.

Chatterjee, S., and Bajpai, S., 2016. India's northward drift from Gondwana to Asia during the Late Cretaceous-Eocene. *Proc Indian Natn Sci Acad*, *82(3)*, pp.479-487.

Chatterjee, S., Scotese, C.R. and Bajpai, S., 2017. The restless Indian plate and its epic voyage from Gondwana to Asia: its tectonic, paleoclimatic, and paleobiogeographic evolution.

Chaudhuri, S. and Cullers, R.L., 1979. The distribution of rare-earth elements in deeply buried Gulf Coast sediments. *Chemical Geology*, *24*(3-4), pp.327-338.

Chen, C., Mu, C.L., Zhou, K.K., Liang, W., Ge, X.Y., Wang, X.P., Wang, Q.Y. and Zheng, B.S., 2016. The geochemical characteristics and factors controlling the organic matter accumulation of the Late Ordovician-Early Silurian black shale in the Upper Yangtze Basin, South China. *Marine and Petroleum Geology*, *76*, pp.159-175.

Chiplonkar, G.W., 1985. Attempts at litho and biostratigraphic subdivision of the Upper Cretaceous rocks of South India, a review.

Chiplonkar, G.W., and Phansalkar, V.G., 1976. Comments on the biostratigraphy of the Upper Cretaceous rocks of South India. Proceedings of the IV Indian colloquium on Micropalaeontology and stratigraphy, Banaras 26-32.

Chiplonkar, G.W. and Tapaswi, P.M., 1974. Bivalvia from the Upper Cretaceous of Trichinopoly District, South India–Part 1: Inoceramidae. *Recent researches in geology*, *3*, pp.87-123.

Chiplonkar, G.W. and Tapaswi, P.M., 1979. Biostratigraphy, age and affinities of the bivalve fauna of the Cretaceous of Tiruchirapalli District, South India.

Clayton, R.N., Friedman, I., Graf, D.L., Mayeda, T.K., Meents, W.F. and Shimp, N.F., 1966. The origin of saline formation waters: 1. Isotopic composition. *Journal of Geophysical Research*, *71*(16), pp.3869-3882.

Collinson, J.D., Mountney N., Thompson, D.B., 1982. Sedimentary Structures-Third edition.

Collinson, J.W., Hammer, W.R., Askin, R.A. and Elliot, D.H., 2006. Permian-Triassic boundary in the central transantarctic Mountains, Antarctica. *Geological Society of America Bulletin*, *118*(5-6), pp.747-763.

Corbin, J.C., Person, A., Iatzoura, A., Ferre, B. and Renard, M., 2000. Manganese in Pelagic carbonates: indication of major Tectonic events during the geodynamic evolution of a passive

continental margin (the Jurassic European Margin of the Tethys–Ligurian Sea). *Palaeogeography, Palaeoclimatology, Palaeoecology*, *156*(1-2), pp.123-138.

Craddock, P.R., Bach, W., Seewald, J.S., Rouxel, O.J., Reeves, E. and Tivey, M.K., 2010. Rare earth element abundances in hydrothermal fluids from the Manus Basin, Papua New Guinea: Indicators of sub-seafloor hydrothermal processes in back-arc basins. *Geochimica et Cosmochimica Acta*, *74*(19), pp.5494-5513.

Craig, H., 1965. The measurement of oxygen isotope paleotemperatures. *Stable isotopes in oceanographic studies and paleotemperatures: Consiglio Nazionale delle Richerche*, pp.161-182.

Cramer, B.S., Miller, K.G., Barrett, P.J. and Wright, J.D., 2011. Late Cretaceous–Neogene trends in deep ocean temperature and continental ice volume: Reconciling records of benthic foraminiferal geochemistry (δ18O and Mg/Ca) with sea level history. *Journal of Geophysical Research: Oceans*, *116*(C12).Criss, R.E., 1999. *Principles of stable isotope distribution*. Oxford University Press.

Curtis, C.D., Hughes, C.R., Whiteman, J.A. and Whittle, C.K., 1985. Compositional variation within some sedimentary chlorites and some comments on their origin. *Mineralogical Magazine*, *49*(352), pp.375-386.

Dasgupta, S., Chaudhuri, A.K. and Fukuoka, M., 1990. Compositional characteristics of glauconitic alterations of K-feldspar from India and their implications. *Journal of Sedimentary Research*, *60*(2), pp.277-281.

De Baar, H.J., Bacon, M.P., Brewer, P.G. and Bruland, K.W., 1985. Rare earth elements in the Pacific and Atlantic Oceans. *Geochimica et Cosmochimica Acta*, *49*(9), pp.1943-1959.

De Raaf, J.F.M., Boersma, J.R. and Van Gelder, S., 1977. Wave-generated structures and sequences from a shallow marine succession, Lower Carboniferous, County Cork, Ireland. *Sedimentology*, *24*(4), pp.451-483.

De Winter, N.J., Goderis, S., Dehairs, F., Jagt, J.W., Fraaije, R.H., Van Malderen, S.J., Vanhaecke, F. and Claeys, P., 2017. Tropical seasonality in the late Campanian (late Cretaceous): Comparison between multiproxy records from three bivalve taxa from Oman. *Palaeogeography, palaeoclimatology, palaeoecology*, *485*, pp.740-760.

De Winter, N.J., Goderis, S., Van Malderen, S.J., Sinnesael, M., Vansteenberge, S., Snoeck, C., Belza, J., Vanhaecke, F. and Claeys, P., 2020. Subdaily-scale chemical variability in a Torreites sanchezi rudist shell: Implications for rudist paleobiology and the Cretaceous day-night cycle. *Paleoceanography and Paleoclimatology*, *35*(2), p.e2019PA003723.

De Winter, N.J., Vellekoop, J., Vorsselmans, R., Golreihan, A., Soete, J., Petersen, S.V., Meyer, K.W., Casadio, S., Speijer, R.P. and Claeys, P., 2018. An assessment of latest Cretaceous Pycnodonte vesicularis (Lamarck, 1806) shells as records for palaeoseasonality: a multi-proxy investigation. *Climate of the Past*, *14*(6), pp.725-749.

Debruyne, D., Hulsbosch, N., Van Wilderode, J., Balcaen, L., Vanhaecke, F. and Muchez, P., 2015. Regional geodynamic context for the Mesoproterozoic Kibara Belt (KIB) and the Karagwe-Ankole Belt: Evidence from geochemistry and isotopes in the KIB. *Precambrian Research*, *264*, pp.82-97.

Demina, L.L., Galkin, S.V. and Shumilin, E.N., 2009. Bioaccumulation of some trace elements in the biota of hydrothermal fields of the Guaymas Basin (Gulf of California). *Boletín de la Sociedad Geológica Mexicana*, *61*(1), pp.31-45.

Dias, A.S. and Barriga, F.J., 2006. Mineralogy and geochemistry of hydrothermal sediments from the serpentinite-hosted Saldanha hydrothermal field (36 34′ N; 33 26′ W) at MAR. *Marine Geology*, *225*(1-4), pp.157-175.

Dickson, J.A.D., 1965. A modified staining technique for carbonates in thin section. *Nature*, *205*(4971), pp.587-587.

Ding, X., Ye, S., Yuan, H. and Krauss, K.W., 2018. Spatial distribution and ecological risk assessment of heavy metals in coastal surface sediments in the Hebei Province offshore area, Bohai Sea, China. *Marine pollution bulletin*, *131*, pp.655-661.

Do Campo, M., del Papa, C., Nieto, F., Hongn, F. and Petrinovic, I., 2010. Integrated analysis for constraining palaeoclimatic and volcanic influences on clay–mineral assemblages in orogenic basins (Palaeogene Andean foreland, Northwestern Argentina). *Sedimentary Geology*, *228*(3-4), pp.98-112.

Dolnicki, P. and Grabiec, M., 2022. The thickness of talus deposits in the periglacial area of SW Spitsbergen (Fugleberget Mountainside) in the light of slope development theories. *Land*, *11*(2), p.209.

Dong, D.T., Qiu, L.W., Ma, P.J., Yu, G.D., Wang, Y.Z., Zhou, S.B., Yang, B.L., Huang, H.Q., Yang, Y.Q. and Li, X., 2022. Initiation and evolution of coarse-grained deposits in the Late Quaternary Lake Chenghai source-to-sink system: From subaqueous colluvial apron (subaqueous fans) to Gilbert-type delta. *Journal of Palaeogeography*, *11*(2), pp.194-221.

Dunca, E. and Mutvei, H., 2001. Comparison of microgrowth pattern in Margaritifera margaritifera shells from south and north Sweden. *American Malacological Bulletin*, *16*(1-2), pp.239-250.

Dunham, R.J., 1962. Classification of carbonate rocks according to depositional textures.

Dymond, J., Suess, E. and Lyle, M., 1992. Barium in deep-sea sediment: A geochemical proxy for paleoproductivity. *Paleoceanography*, *7*(2), pp.163-181.

El Albani, A., Meunier, A. and Fürsich, F., 2005. Unusual occurrence of glauconite in a shallow lagoonal environment (Lower Cretaceous, northern Aquitaine Basin, SW France). *Terra Nova*, *17*(6), pp.537-544.

El-Shazly, S., Košťák, M., Abdel-Gawad, G., Kloukčová, B., Saber, S.G., Salama, Y.F., Mazuch, M. and Žák, K., 2011. Carbon and oxygen stable isotopes of selected Cenomanian

and Turonian rudists from Egypt and Czech Republic, and a note on changes in rudist diversity. *Bulletin of Geosciences*, *86*(2), pp.209-226.

Elliot, M., Demenocal, P.B., Linsley, B.K. and Howe, S.S., 2003. Environmental controls on the stable isotopic composition of Mercenaria mercenaria: potential application to paleoenvironmental studies. *Geochemistry, Geophysics, Geosystems*, *4*(7).

Epstein, S. and Mayeda, T., 1953. Variation of O18 content of waters from natural sources. *Geochimica et cosmochimica acta*, *4*(5), pp.213-224.

Eriksson, K.A. and Simpson, E.L., 2000. Quantifying the oldest tidal record: the 3.2 Ga Moodies Group, Barberton greenstone belt, South Africa. *Geology*, *28*(9), pp.831-834.

Eriksson, K.A., Simpson, E.L. and Mueller, W., 2006. An unusual fluvial to tidal transition in the mesoarchean Moodies Group, South Africa: A response to high tidal range and active tectonics. *Sedimentary Geology*, *190*(1-4), pp.13-24.

Flügel, E. and Flügel, E., 1982. Introduction to facies analysis. *Microfacies Analysis of Limestones*, pp.1-26.

Folk, R.L., 1959. Practical petrographic classification of limestones. *AAPG bulletin*, *43*(1), pp.1-38.

Folk, R.L., 1962. Spectral subdivision of limestone types.

Föllmi, K.B., 2012. Early Cretaceous life, climate and anoxia. *Cretaceous Research*, *35*, pp.230-257.

Freitas, P.S., Clarke, L.J., Kennedy, H., Richardson, C.A. and Abrantes, F., 2006. Environmental and biological controls on elemental (Mg/Ca, Sr/Ca and Mn/Ca) ratios in shells of the king scallop Pecten maximus. *Geochimica et Cosmochimica Acta*, *70*(20), pp.5119-5133.

Friedrich, O., Norris, R.D. and Erbacher, J., 2012. Evolution of middle to Late Cretaceous oceans—a 55 my record of Earth's temperature and carbon cycle. *Geology*, *40*(2), pp.107-110.

Frimmel, H.E., 2009. Trace element distribution in Neoproterozoic carbonates as palaeoenvironmental indicator. *Chemical Geology*, *258*(3-4), pp.338-353.

Fritz, S.J., Toth, T.A., 1997. An Fe-berthierine from a cretaceous laterite: Part II. Estimation OF Eh, pH and pC02 conditions of formation. Clay Clay Miner. 45, 580–586.

Fu, Y., van Berk, W., Schulz, H.M. and Mu, N., 2015. Berthierine formation in reservoir rocks from the Siri oilfield (Danish North Sea) as result of fluid–rock interactions: Part II. Deciphering organic–inorganic processes by hydrogeochemical modeling. *Marine and Petroleum Geology*, *65*, pp.317-326.

Fujioka, H., Takayanagi, H., Yamamoto, K. and Iryu, Y., 2019. The effects of meteoric diagenesis on the geochemical composition and microstructure of Pliocene fossil Terebratalia coreanica and Laqueus rubellus brachiopod shells from northeastern Japan. *Progress in Earth and Planetary Science*, *6*, pp.1-23.

Fürsich, F.T., 1982. Rhythmic bedding and shell bed formation in the Upper Jurassic of East Greenland. In *Cyclic and event stratification* (pp. 208-222). Berlin, Heidelberg: Springer Berlin Heidelberg.

Fürsich, F.T. and Pandey, D.K., 1999. Genesis and environmental significance of Upper Cretaceous shell concentrations from the Cauvery Basin, southern India. *Palaeogeography, Palaeoclimatology, Palaeoecology*, *145*(1-3), pp.119-139.

Fürsich, F.T., Freytag, S., Röhl, J. and Schmid, A., 1995. Palaeoecology of benthic associations in salinity-controlled marginal marine environments: examples from the Lower Bathonian (Jurassic) of the Causses (southern France). *Palaeogeography, Palaeoclimatology, Palaeoecology*, *113*(2-4), pp.135-172.

Fürsich, F.T., Singh, I.B., Joachimski, M., Krumm, S., Schlirf, M. and Schlirf, S., 2005. Palaeoclimate reconstructions of the Middle Jurassic of Kachchh (western India): an integrated approach based on palaeoecological, oxygen isotopic, and clay mineralogical data. *Palaeogeography, Palaeoclimatology, Palaeoecology*, *217*(3-4), pp.289-309.

Futterer, E., 1982. Experiments on the distinction of wave and current influenced shell accumulations. In *Cyclic and event stratification* (pp. 175-179). Berlin, Heidelberg: Springer Berlin Heidelberg.

Gallup, D.L., 1998. Geochemistry of geothermal fluids and well scales, and potential for mineral recovery. *Ore geology reviews*, *12*(4), pp.225-236.

Garcia-Frank, A., Ureta, S. and Mas, R., 2012. Iron-coated particles from condensed Aalenian–Bajocian deposits: evolutionary model (Iberian Basin, Spain). *Journal of Sedimentary Research*, *82*(12), pp.953-968.

García-Romero, E., Vegas, J., Baldonedo, J.L. and Marfil, R., 2005. Clay minerals as alteration products in basaltic volcaniclastic deposits of La Palma (Canary Islands, Spain). *Sedimentary Geology*, *174*(3-4), pp.237-253.

Gifkins, C.C., Herrmann, W. and Large, R.R., 2005. *Altered volcanic rocks: A guide to description and interpretation*. University of Tasmania.

Gili, E., Skelton, P.W., Vicens, E. and Obrador, A., 1995. Corals to rudists—an environmentally induced assemblage succession. *Palaeogeography, Palaeoclimatology, Palaeoecology*, *119*(1-2), pp.127-136.

Golovneva, L.B., 2000. The Maastrichtian (Late Cretaceous) climate in the northern hemisphere. *Geological Society, London, Special Publications*, *181*(1), pp.43-54.

Gong, N., Hong, H., Huff, W.D., Fang, Q., Bae, C.J., Wang, C., Yin, K. and Chen, S., 2018. Influences of sedimentary environments and volcanic sources on diagenetic alteration of volcanic tuffs in South China. *Scientific Reports*, *8*(1), pp.7616.

Goodwin, D.H., Gillikin, D.P. and Roopnarine, P.D., 2013. Preliminary evaluation of potential stable isotope and trace element productivity proxies in the oyster Crassostrea gigas. *Palaeogeography, Palaeoclimatology, Palaeoecology*, *373*, pp.88-97.

Govindan, A., 1972. Upper Cretaceous planktonic foraminifera from the Pondicherry area, South India. *Micropaleontology*, pp.160-193.

Govindan, A., 1977. Late Cretaceous and Lower Tertiary foraminiferal genus *Bolivinoides* from the Cauvery Basin, South India and its paleobiogeographical significance. *Geol. Soc. India*, *18 (8)*, pp.459-476.

Govindan, A., 1978. Selected Upper Cretaceous benthonic foraminifera from the Cauvery Basin, south India and paleobathymetric interpretation, *In:* VII Indian colloq. Micropal and stratigraphy,Pune, pp.58.

Govindan, A. 1980. Cretaceous foraminifera from the eastern part of Indian Peninsula and their paleoclimatological significance. Bull. ONGC 17, 1-9.

Govindan, A., Ravindran, C.N. and Rangaraju, M.K., 1996. Cretaceous stratigraphy and planktonic foraminiferal zonation of the Cauvery basin, South India. *Memoirs-Geological Society of India*, pp.155-188.

Greenwood, B. and Sherman, D.J., 1986. Hummocky cross-stratification in the surf zone: flow parameters and bedding genesis. *Sedimentology*, *33*(1), pp.33-45.

Guha, A.K. and Nathan, D.S., 1996. *Bryozoan fauna of the Ariyalur Group (Late Cretaceous), Tamil Nadu and Pondicherry, India* (Vol. 49). Geological Survey of India.

Guo, H., Du, Y., Kah, L.C., Huang, J., Hu, C., Huang, H. and Yu, W., 2013. Isotopic composition of organic and inorganic carbon from the Mesoproterozoic Jixian Group, North China: Implications for biological and oceanic evolution. *Precambrian Research*, *224*, pp.169-183.

Hagdorn, H. and Mundlos, R., 1982. Allochthonous coquinas in the Upper Muschelkalk-Caused by storm events. *Cyclic and event stratification*, pp.199-199.

Hallam, A., 1981. A revised sea-level curve for the early Jurassic. *Journal of the Geological Society*, *138*(6), pp.735-743.

Hancock, J.M. and Kauffman, E.G., 1979. The great transgressions of the Late Cretaceous. *Journal of the Geological Society*, *136*(2), pp.175-186.

Harder, H., 1978. Synthesis of iron layer silicate minerals under natural conditions. *Clays and Clay Minerals*, *26*(1), pp.65-72.

Harlou, R., Ullmann, C.V., Korte, C., Lauridsen, B.W., Schovsbo, N.H., Surlyk, F., Thibault, N. and Stemmerik, L., 2016. Geochemistry of Campanian–Maastrichtian brachiopods from the Rørdal-1 core (Denmark): Differential responses to environmental change and diagenesis. *Chemical Geology*, *442*, pp.35-46.

Harms, J.C., Southard, J.B., Spearing, D.R. and Walker, R.G., 1975. *Depositional environments as interpreted from primary sedimentary structures and stratification sequences*. SEPM Society for Sedimentary Geology.

Hart, M., Joshi, A. and Watkinson, M., 1999. Palaeoecology and Stratigraphical setting of the Kallankuruchchi Limestone Formation (U. Cretaceous), SE India. In *European Palaeontol Ass Workshop, Abstract Vol, Lisboa* (pp. 47-51).

Hay, W.W., 2008. Evolving ideas about the Cretaceous climate and ocean circulation. *Cretaceous Research*, *29*(5-6), pp.725-753.

Hayami, I. and Kase, T., 1992, April. 935. A new cryptic species of Pycnodonte from Ryukyu Islands: a living fossil oyster. In *Transactions and proceedings of the Paleontological Society of Japan. New series* (Vol. 1992, No. 165, pp. 1070-1089). Palaeontological Society of Japan.

Hippler, D., Buhl, D., Witbaard, R., Richter, D.K. and Immenhauser, A., 2009. Towards a better understanding of magnesium-isotope ratios from marine skeletal carbonates. *Geochimica et Cosmochimica Acta*, *73*(20), pp.6134-6146.

Hong, H., Zhao, L., Fang, Q., Algeo, T.J., Wang, C., Yu, J., Gong, N., Yin, K. and Ji, K., 2019. Volcanic sources and diagenetic alteration of Permian–Triassic boundary K-bentonites in Guizhou Province, South China. *Palaeogeography, Palaeoclimatology, Palaeoecology*, *519*, pp.141-153.

Hornibrook, E.R. and Longstaffe, F.J., 1996. Berthierine from the lower cretaceous Clearwater formation, Alberta, Canada. *Clays and Clay Minerals*, *44*(1), pp.1-21.

Huber, B.T., Norris, R.D. and MacLeod, K.G., 2002. Deep-sea paleotemperature record of extreme warmth during the Cretaceous. *Geology*, *30*(2), pp.123-126.

Huggett, J., Adetunji, J., Longstaffe, F. and Wray, D., 2017. Mineralogical and geochemical characterisation of warm-water, shallow-marine glaucony from the Tertiary of the London Basin. *Clay Minerals*, *52*(1), pp.25-50.

Huggett, J., Gale, A.S. and McCarty, D., 2010. Petrology and palaeoenvironmental significance of authigenic iron-rich clays, carbonates and apatite in the Claiborne Group, Middle Eocene, NE Texas. *Sedimentary Geology*, *228*(3-4), pp.119-139.

Hussain, A. and Chaudhary, M.N., 2023. Microfacies and Depositional Environmental Studies of Lockhart Formation of Chhangla Gali Area, Hazara Basin, Pakistan. *International Journal of Special Education*, *38*(1).

Ichimura, S., Takayanagi, H., Iryu, Y., Takahashi, S. and Oji, T., 2024. Shallow-water temperature seasonality in the middle Cretaceous mid-latitude northwestern Pacific. *Frontiers in Marine Science*, *11*, p.1324436.

Iljima, A. and Matsumoto, R., 1982. Berthierine and chamosite in coal measures of Japan. *Clays and Clay Minerals*, *30*, pp.264-274.

Immenhauser, A., Nägler, T.F., Steuber, T. and Hippler, D., 2005. A critical assessment of mollusk 18O/16O, Mg/Ca, and 44Ca/40Ca ratios as proxies for Cretaceous seawater temperature seasonality. *Palaeogeography, Palaeoclimatology, Palaeoecology*, *215*(3-4), pp.221-237.

Immenhauser, A., Schoene, B.R., Hoffmann, R. and Niedermayr, A., 2016. Mollusc and brachiopod skeletal hard parts: Intricate archives of their marine environment. *Sedimentology*, *63*(1), pp.1-59.

Isson, T.T. and Planavsky, N.J., 2018. Reverse weathering as a long-term stabilizer of marine pH and planetary climate. *Nature*, *560*(7719), pp.471-475.

Ivany, L.C., Wilkinson, B.H., Lohmann, K.C., Johnson, E.R., McElroy, B.J. and Cohen, G.J., 2004. Intra-annual isotopic variation in Venericardia bivalves: implications for early Eocene temperature, seasonality, and salinity on the US Gulf Coast. *Journal of Sedimentary Research*, *74*(1), pp.7-19.

Jacob, K. and Sastry, M.V.A., 1950. On the occurrence of Globotruncana in Uttatur stage of the Trichinopoly Cretaceous, South India. *Sci. and Cult*, *16*(6), pp.266-268.

Jain, K.P., 1976. An Upper Cretaceous dinoflagellate assemblage from Vriddhachalam area, Cauvery Basin, South India. *Journal of Palaeosciences*, *25*(1-3), pp.146-160.

Jaitly, A.K. and Mishra, S.K., 2007. Approaches to palaeoecology: A case study from the Late Cretaceous (Campanian-Maastrichtian) benthic bivalves of Ariyalur, Tamil Nadu. *Journal-Geological Society of India*, *69*(1), p.97.

Jaitly, A.K. and Mishra, S.K., 2009. Campanian-Maastricthian (Late Cretaceous) veneroids (Bivalvia: Heterodonta) from the Ariyalur Group, South India. *Palaeoworld*, *18*(4), pp.251-262.

Jaitly, A.K., Mishra, S.K. and Sen, S., 2014. Shell Microstructure of Late Cretaceous (Maastrichtian) Oysters from Ariyalur, Tamil Nadu. *Journal of the Geological Society of India*, *84*, pp.41-54.

James, N.P. and Choquette, P.W., 1983. Diagenesis 6. Limestones—the sea floor diagenetic environment. *Geoscience Canada*.

Jeans, C.V., Wray, D.S., Merriman, R.J. and Fisher, M.J., 2000. Volcanogenic clays in Jurassic and Cretaceous strata of England and the North Sea Basin. *Clay Minerals*, *35*(1), pp.25-55.

Jenkyns, H.C., Forster, A., Schouten, S. and Sinninghe Damsté, J.S., 2004. High temperatures in the late Cretaceous Arctic Ocean. *Nature*, *432*(7019), pp.888-892.

Jelby, M.E., Thibault, N., Surlyk, F., Ullmann, C.V., Harlou, R. and Korte, C., 2014. The lower Maastrichtian Hvidskud succession, Møns Klint, Denmark: calcareous nannofossil biostratigraphy, carbon isotope stratigraphy, and bulk and brachiopod oxygen isotopes. *Bulletin of the Geological Society of Denmark*, *62*(89), p.e104.

Jiménez-Millán, J. and Castro, J.M., 2008. K-feldspar alteration to gel material and crystallization of glauconitic peloids with berthierine in Cretaceous marine sediments—sedimentary implications (Prebetic Zone, Betic Cordillera, SE Spain). *Geological Journal*, *43*(1), pp.19-31.

Jones, B. and Manning, D.A., 1994. Comparison of geochemical indices used for the interpretation of palaeoredox conditions in ancient mudstones. *Chemical geology*, *111*(1-4), pp.111-129.

Jones, D.S., 1980. Annual cycle of shell growth increment formation in two continental shelf bivalves and its paleoecologic significance. *Paleobiology*, *6*(3), pp.331-340.

Jones, D.S. and Quitmyer, I.R., 1996. Marking time with bivalve shells: oxygen isotopes and season of annual increment formation. *Palaios*, pp.340-346.

Jones, D.S., Arthur, M.A. and Allard, D.J., 1989. Sclerochronological records of temperature and growth from shells of Mercenaria mercenaria from Narragansett Bay, Rhode Island. *Marine Biology*, *102*, pp.225-234.

Kaandorp, R.J., Wesselingh, F.P. and Vonhof, H.B., 2006. Ecological implications from geochemical records of Miocene Western Amazonian bivalves. *Journal of South American Earth Sciences*, *21*(1-2), pp.54-74.

Kale, A.S., 2011. Comments on 'Sequence surfaces and paleobathymetric trends in Albian to Maastrichtian sediments of Ariyalur area, Cauvery Basin, India'from Nagendra, Kannan, Sen, Gilbert, Bakkiaraj, Reddy, and Jaiprakash (Marine and Petroleum Geology, 2010. *Marine and Petroleum Geology*, *28*(6), pp.1252-1259.

Kaminski, M.A., Aksu, A., Box, M., Hiscott, R.N., Filipescu, S. and Al-Salameen, M., 2002. Late Glacial to Holocene benthic foraminifera in the Marmara Sea: implications for Black Sea–Mediterranean Sea connections following the last deglaciation. *Marine Geology*, *190*(1-2), pp.165-202.

Kathal, P.K., Nagendra, R., Raja, R., Reddy, A.N., Jayaprakash, B.C. and Bhavani, R., 2002. Outcrop Sequence Stratigraphy of the Maastrichtian Kallankurchchi formation, Ariyalur Group, Tamil Nadu. *Geological Society of India*, *60*(3), pp.355-357.

Keller, G., Adatte, T., Bajpai, S., Mohabey, D.M., Widdowson, M., Khosla, A., Sharma, R., Khosla, S.C., Gertsch, B., Fleitmann, D. and Sahni, A., 2009. K–T transition in Deccan Traps of central India marks major marine Seaway across India. *Earth and Planetary Science Letters*, *282*(1-4), pp.10-23.

Keller, G., Jaiprakash, B.C. and Reddy, A.N., 2016. Maastrichtian to Eocene subsurface stratigraphy of the Cauvery Basin and correlation with Madagascar. *Journal of the Geological Society of India*, *87*, pp.5-34.

Kent, D.V. and Muttoni, G., 2008. Equatorial convergence of India and early Cenozoic climate trends. *Proceedings of the National Academy of Sciences*, *105*(42), pp.16065-16070.

Keith, M.L. and Weber, J.N., 1964. Carbon and oxygen isotopic composition of selected limestones and fossils. *Geochimica et cosmochimica acta*, *28*(10-11), pp.1787-1816.

Kidwell, S.M., 1985. Palaeobiological and sedimentological implications of fossil concentrations. *Nature*, *318*(6045), pp.457-460.

Kidwell, S.M. and Jablonski, D., 1983. Taphonomic feedback ecological consequences of shell accumulation. In *Biotic interactions in recent and fossil benthic communities* (pp. 195-248). Boston, MA: Springer US.

Kidwell, S.M., Fürsich, F.T. and Aigner, T., 1986. Conceptual framework for the analysis and classification of fossil concentrations. *Palaios*, pp.228-238.

Kimberley, M.M., 1994. Debate about ironstone: has solute supply been surficial weathering, hydrothermal convection, or exhalation of deep fluids?. *Terra Nova*, *6*(2), pp.116-132.

Kinsman, D.J., 1969. Interpretation of Sr (super+ 2) concentrations in carbonate minerals and rocks. *Journal of Sedimentary Research*, *39*(2), pp.486-508.

Klein, R.T., Lohmann, K.C. and Thayer, C.W., 1996. Bivalve skeletons record sea-surface temperature and δ18O via Mg/Ca and 18O/16O ratios. *Geology*, *24*(5), pp.415-418.

Kossmat, F., 1897. The Cretaceous deposits of Pondicherry. *Records of the geological Survey of India*, *30*(2), pp.51-110.

Kozłowska, A. and Maliszewska, A., 2015. Berthierine in the Middle Jurassic sideritic rocks from southern Poland. *Geological Quarterly*, *59*(3), pp.551-564.

Krishna, J., 1987. Biological evidence for better appreciation of the Indian Gondwana. *Journal of Palaeosciences*, *36*, pp.268-284.

Ku, T.C.W. and Walter, L.M., 2003. Syndepositional formation of Fe-rich clays in tropical shelf sediments, San Blas Archipelago, Panama. *Chemical Geology*, *197*(1-4), pp.197-213.

Kumar, N. and Sanders, J.E., 1976. Characteristics of shoreface storm deposits; modern and ancient examples. *Journal of Sedimentary Research*, *46*(1), pp.145-162.

Lal, N.K., Siawal, A. and Kaul, A.K., 2009. Evolution of east coast of India—A plate tectonic reconstruction. *Journal of the Geological Society of India*, *73*, pp.249-260.

Large, R.R., Mukherjee, I., Gregory, D.D., Steadman, J.A., Maslennikov, V.V. and Meffre, S., 2017. Ocean and atmosphere geochemical proxies derived from trace elements in marine

pyrite: implications for ore genesis in sedimentary basins. *Economic Geology*, *112*(2), pp.423-450.

Latimer, J.C. and Filippelli, G.M., 2002. Eocene to Miocene terrigenous inputs and export production: geochemical evidence from ODP Leg 177, Site 1090. *Palaeogeography, Palaeoclimatology, Palaeoecology*, *182*(3-4), pp.151-164.

Lazo, D.G., Cichowolski, M., Rodríguez, D.L. and Aguirre-Urreta, M.B., 2005. Lithofacies, palaeoecology and palaeoenvironments of the Agrio Formation, lower cretaceous of the Neuquén Basin, Argentina. *Geological Society, London, Special Publications*, *252*(1), pp.295-315.

Lei, H., Jiang, Q., Huang, W. and Luo, P., 2024. Middle Permian astronomically forced upwelling in the Yangtze carbonate platform: Implications for organic matter preservation and benthic biomass. *Marine and Petroleum Geology*, *160*, pp.106575.

Li, Q., Wu, S., Xia, D., You, X., Zhang, H. and Lu, H., 2020. Major and trace element geochemistry of the lacustrine organic-rich shales from the Upper Triassic Chang 7 Member in the southwestern Ordos Basin, China: Implications for paleoenvironment and organic matter accumulation. *Marine and Petroleum Geology*, *111*, pp.852-867.

Linnert, C., Robinson, S.A., Lees, J.A., Bown, P.R., Pérez-Rodríguez, I., Petrizzo, M.R., Falzoni, F., Littler, K., Arz, J.A. and Russell, E.E., 2014. Evidence for global cooling in the Late Cretaceous. *Nature communications*, *5*(1), p.4194.

Liu, Z., Algeo, T.J., Arefifard, S., Wei, W., Brett, C., Landing, E. and Lev, S.M., 2024. Testing the salinity of Cambrian to Silurian epicratonic seas. *Journal of the Geological Society*, pp.jgs2023-217.

Lydekker, R., 1879. *Fossil Reptilia and Batrachia: With 6 Plates* (Vol. 1). Geological Survey Office.

Ma, J., Shi, X., Lechte, M., Zhou, X., Wang, Z., Huang, K., Rudmin, M. and Tang, D., 2022. Mesoproterozoic seafloor authigenic glauconite-berthierine: Indicator of enhanced reverse weathering on early Earth. *American Mineralogist*, *107*(1), pp.116-130.

Madhavaraju, J. and Lee, Y.I., 2009. Geochemistry of the Dalmiapuram Formation of the Uttatur Group (Early Cretaceous), Cauvery basin, southeastern India: Implications on provenance and paleo-redox conditions. *Revista mexicana de ciencias geológicas*, *26*(2), pp.380-394.

Madhavaraju, J. and Lee, Y.I., 2010. Influence of Deccan volcanism in the sedimentary rocks of Late Maastrichtian–Danian age of Cauvery basin Southeastern India: constraints from geochemistry. *Current Science*, pp.528-537.

Madhavaraju, J. and Ramasamy, S., 1999. Rare earth elements in limestones of Kallankurichchi formation of Ariyalur group, Tiruchirapalli Cretaceous, Tamil Nadu. *Geological Society of India*, *54*(3), pp.291-301.

Madhavaraju, J., Kolosov, I., Buhlak, D., Armstrong-Altrin, J.S., Ramasamy, S. and Mohan, S.P., 2004. Carbon and oxygen isotopic signatures in Albian-Danian limestones of Cauvery basin, southeastern India. *Gondwana Research*, *7*(2), pp.519-529.

Madhavaraju, J., Ramasamy, S., Ruffell, A. and Mohan, S.P., 2002. Clay mineralogy of the Late Cretaceous and Early Tertiary Successions of the Cauvery Basin (southeastern India): Implications for sediment source and palaeoclimates at the K/T boundary. *Cretaceous Research*, *23*(2), pp.153-163.

Madhavaraju, J., Sial, A.N., Rakhinath, R., Ramasamy, S., Lee, Y.I. and Ramachandran, A., 2015. Carbon, oxygen and strontium isotopic signatures in Maastrichtian-Danian limestones of the Cauvery Basin, South India. *Geosciences Journal*, *19*, pp.237-256.

Malarkodi, N., Özcan, E., Venkataraman, D., Somappa, S.C., Gowda, S., Nagaraja, P.K.T. and Yücel, A.O., 2017. Lepidorbitoides (foraminifera) from the lower Maastrichtian Kallankuruchchi Formation, Cauvery Basin, India: morphometry and paleobiogeography. *Cretaceous Research*, *77*, pp.143-157.

Mandal, A., 2017. Facies Analysis and Sequence-Building in Parts of the Lower Cretaceous Bhuj Formation, Kutch, India. Unpublished Ph.D. Thesis, Jadavpur University, Kolkata, pp.261.

Mandal, A., Koner, A., Sarkar, S., Tawfik, H.A., Chakraborty, N., Bhakta, S. and Bose, P.K., 2016. Physico-chemical tuning of palaeogeographic shifts: Bhuj formation, Kutch, India. *Marine and Petroleum Geology*, *78*, pp.474-492.

Mandal, S., Banerjee, S., Sarkar, S., Mondal, I. and Roy Choudhury, T., 2020. Origin and sequence stratigraphic implications of high-alumina glauconite within the Lower Quartzite, Vindhyan Supergroup. *Marine and Petroleum Geology*, *112*, p.104040.

Mandal, S., Choudhuri, A., Mondal, I., Sarkar, S., Chakraborty, P.P. and Banerjee, S., 2019. Revisiting the boundary between the Lower and Upper Vindhyan, Son valley, India. *Journal of Earth System Science*, *128*, pp.1-16.

Mandal, S., Srimani, S., Mondal, I., Choudhuri, A., Das, A., Das, K., Banerjee, S. and Sarkar, S., 2024. Seismic-Aseismic impact on marine depositional dynamics and sedimentary architecture: Study on multilayer - multiscale SSDS in Proterozoic Rohtas Limestone, India. *Sedimentary Geology* (accepted).

Marali, S., Schöne, B.R., Mertz-Kraus, R., Griffin, S.M., Wanamaker Jr, A.D., Butler, P.G., Holland, H.A. and Jochum, K.P., 2017. Reproducibility of trace element time-series (Na/Ca, Mg/Ca, Mn/Ca, Sr/Ca, and Ba/Ca) within and between specimens of the bivalve Arctica islandica–A LA-ICP-MS line scan study. *Palaeogeography, palaeoclimatology, palaeoecology*, *484*, pp.109-128.

Markl, R.G., 1974. Evidence for the breakup of eastern Gondwanaland by the early Cretaceous. *Nature*, *251*(5472).

McConnaughey, T.A. and Gillikin, D.P., 2008. Carbon isotopes in mollusk shell carbonates. *Geo-Marine Letters*, *28*, pp.287-299.

McCrory, V.L. and Walker, R.G., 1986. A storm and tidally-influenced prograding shoreline—Upper Cretaceous Milk River Formation of Southern Alberta, Canada. *Sedimentology*, *33*(1), pp.47-60.

McLennan, S.M., 2001. Relationships between the trace element composition of sedimentary rocks and upper continental crust. *Geochemistry, Geophysics, Geosystems*, *2*(4).

Mclennan, S.M., 2018. Rare earth elements in sedimentary rocks: influence of provenance and sedimentary processes. In *Geochemistry and mineralogy of rare earth elements* (pp. 169-200). De Gruyter.

Mishra, M. and Sen, S., 2018. Petrological study of the early Mesoproterozoic Glauconitic Sandstone and Olive Shale members from the Semri Group, Vindhyan Supergroup in Central India: Implications to input from intrabasinal felsic volcanic source and glauconitization. *Geological Journal*, *53*(3), pp.857-876.

Mitra, S., Mitra, K., Gupta, S., Bhattacharya, S., Chauhan, P. and Jain, N., 2017. Alteration and submergence of basalts in Kachchh, Gujarat, India: implications for the role of the Deccan Traps in the India–Seychelles break-up. *Geological Society, London, Special Publications*, *445*(1), pp.47-67.

Molenaar, N. and Zijlstra, J.J.P., 1997. Differential early diagenetic low-Mg calcite cementation and rhythmic hardground development in Campanian-Maastrichtian chalk. *Sedimentary Geology*, *109*(3-4), pp.261-281.

Moore, D.M. and Reynolds, R.C., 1997. X-Ray Diffraction and the Identification and Analysis of Clay Minerals. Oxford University Press, Oxford [England].

Morford, J.L. and Emerson, S., 1999. The geochemistry of redox sensitive trace metals in sediments. *Geochimica et Cosmochimica Acta*, *63*(11-12), pp.1735-1750.

Mu, N., Schulz, H.M., Fu, Y., Schovsbo, N.H., Wirth, R., Rhede, D. and van Berk, W., 2015. Berthierine formation in reservoir rocks from the Siri oilfield (Danish North Sea) as result of fluid–rock interactions: part I. Characterization. *Marine and Petroleum Geology*, *65*, pp.302-316.

Mulder, T. and Alexander, J., 2001. The physical character of subaqueous sedimentary density flows and their deposits. *Sedimentology*, *48*(2), pp.269-299.

Mullins, H.T., Dolan, J., Breen, N., Andersen, B., Gaylord, M., Petruccione, J.L., Wellner, R.W., Melillo, A.J. and Jurgens, A.D., 1991. Retreat of carbonate platforms: response to tectonic processes. *Geology*, *19*(11), pp.1089-1092.

Murthy, K.S., Chaudhuri, A., Ramana, L.V., Rao, M.V. and Dobriyal, J.P., 2008. Hydrocarbon Exploration of Syn Rift Sediments in Nagapattinam Sub Basin, Cauvery Basin-A Case Study. In *7th biannual exhibition and conference on geophysics, Hyderabad* (Vol. 443).

Nagendra R., 2015. Outcrop sequence stratigraphy of Cretaceous of Trichinopoly. Cretaceous field guide- Sequence stratigraphic prospective.

Nagendra, R. and Nallapa Reddy, A., 2021. Litho-Biostratigraphy and Depositional Environment of Albian-Maastrichtian Sedimentary Succession of Cauvery Basin in Ariyalur Area. *Mesozoic Stratigraphy of India: a multi-proxy approach*, pp.553-586.

Nagendra, R. and Reddy, A.N., 2017. Major geologic events of the Cauvery Basin, India and their correlation with global signatures–A review. *Journal of Palaeogeography*, *6*(1), pp.69-83.

Nagendra, R., Bhavani, R., Dinakaran, V., Reddy, A.N. and Jaiprakash, B.C., 2001. Outcrop sequence stratigraphy of Kallankurchchi Formation of Velliperinjiyam mine, and its correlation with Tancem mine, Ariyalur Group, Tamilnadu. *Indian Journal of Petroleum Geology*, *10*(2), pp.23-36.

Nagendra, R., Kannan, B.K., Sen, G., Gilbert, H., Bakkiaraj, D., Reddy, A.N. and Jaiprakash, B.C., 2011. Sequence surfaces and paleobathymetric trends in Albian to Maastrichtian sediments of Ariyalur area, Cauvery Basin, India. *Marine and Petroleum Geology*, *28*(4), pp.895-905.

Nagendra, R., Nagarajan, R., Bakkiaraj, D. and Armstrong-Altrin, J.S., 2011. Depositional and post-depositional setting of Maastrichtian limestone, Ariyalur Group, Cauvery Basin, South India: a geochemical appraisal. *Carbonates and Evaporites*, *26*, pp.127-147.

Nagendra, R., Raja, R., Reddy, A.N., Jaiprakash, B.C. and Bhavani, R., 2002. Outcrop sequence stratigraphy of the Maastrichtian Kallankurchchi Formation, Ariyalur Group, Tamil Nadu. *Geological Society of India*, *59*(3), pp.243-248.

Nagendra, R., Reddy, A.N., Jaiprakash, B.C., Gilbert, H., Zakharov, Y.D. and Venkateshwarlu, M., 2018. Integrated Cretaceous stratigraphy of the Cauvery Basin, South India. *Stratigraphy*, *15*(4).

Nelson, C. S. and Smith, A.M., 1996. Stable oxygen and carbon isotope compositional fields for skeletal and diagenetic components in New Zealand Cenozoic nontropical carbonate sediments and limestones: A synthesis and review, *New Zealand Journal of Geology and Geophysics*, 39(1), pp.93–107.

Nameroff, T.J., Balistrieri, L.S. and Murray, J.W., 2002. Suboxic trace metal geochemistry in the eastern tropical North Pacific. *Geochimica et Cosmochimica Acta*, *66*(7), pp.1139-1158.

Narayanan, V. and Scheibnerová, V., 1975. Lingulogavelinella and Orithostella (Foraminifera) from the Utatur Group of the Trichinopoly Cretaceous, south (peninsular) India. *Revista española de micropaleontología*, *7*(1), pp.25-36.

Narayanan, V., 1977. Biozonation of the Uttatur Group, Trichinopoly, Cauvery Basin. *Geological Society of India*, *18*(8), pp.415-428.

Nemec, W. and Steel, R., 1984. Alluvial and coastal conglomerates: their significant features and some comments on gravelly mass-flow deposits.

Norris, R.D., Bice, K.L., Magno, E.A. and Wilson, P.A., 2002. Jiggling the tropical thermostat in the Cretaceous hothouse. *Geology*, *30*(4), pp.299-302.

Nøttvedt, A. and Kreisa, R.D., 1987. Model for the combined-flow origin of hummocky cross-stratification. *Geology*, *15*(4), pp.357-361.

Niebuhr, B. and Joachimski, M.M., 2002. Stable isotope and trace element geochemistry of Upper Cretaceous carbonates and belemnite rostra (Middle Campanian, north Germany). *Geobios*, *35*(1), pp.51-64.

O'Brien, C.L., Robinson, S.A., Pancost, R.D., Damsté, J.S.S., Schouten, S., Lunt, D.J., Alsenz, H., Bornemann, A., Bottini, C., Brassell, S.C. and Farnsworth, A., 2017. Cretaceous sea-surface temperature evolution: Constraints from TEX86 and planktonic foraminiferal oxygen isotopes. *Earth-Science Reviews*, *172*, pp.224-247.

O'Connor, L.K., Robinson, S.A., Naafs, B.D.A., Jenkyns, H.C., Henson, S., Clarke, M. and Pancost, R.D., 2019. Late Cretaceous temperature evolution of the southern high latitudes: A TEX86 perspective. *Paleoceanography and Paleoclimatology*, *34*(4), pp.436-454.

Odin, G.S. and Matter, A., 1981. De glauconiarum origine. Sedimentology 28, 611–641.

Odin, G.S., 1988. *Green marine clays: oolitic ironstone facies, verdine facies, glaucony facies and celadonite-bearing rock facies-a comparative study*. Elsevier.

Parrish, J.T. and Spicer, R.A., 1988. Late Cretaceous terrestrial vegetation: a near-polar temperature curve. *Geology*, *16*(1), pp.22-25.

Pearson, P.N., Ditchfield, P.W., Singano, J., Harcourt-Brown, K.G., Nicholas, C.J., Olsson, R.K., Shackleton, N.J. and Hall, M.A., 2001. Warm tropical sea surface temperatures in the Late Cretaceous and Eocene epochs. *Nature*, *413*(6855), pp.481-487.

Peng, Y., Durkin, P.R., Martin, H.K., Leckie, D.A., Horner, S.C. and Hubbard, S.M., 2024. Early Cretaceous evolution of the McMurray Formation: A review toward a better understanding of the paleo-depositional system. *Earth-Science Reviews*, pp.104740.

Perry, C.T. and Beavington-Penney, S.J., 2005. Epiphytic calcium carbonate production and facies development within sub-tropical seagrass beds, Inhaca Island, Mozambique. *Sedimentary Geology*, *174*(3-4), pp.161-176.

Petersen, S.V., Tabor, C.R., Lohmann, K.C., Poulsen, C.J., Meyer, K.W., Carpenter, S.J., Erickson, J.M., Matsunaga, K.K., Smith, S.Y. and Sheldon, N.D., 2016. Temperature and salinity of the Late Cretaceous western interior seaway. *Geology*, *44*(11), pp.903-906.

Phansalkar, V.G. and Kumar Mary, K., 1983. Biostratigraphy of Utatur and Trichinopoly groups of the upper Cretaceous of Trichinopoly district, Tamilnadu. In *Memorial volume in hommage to Prof. KV Kelkar* (pp. 183-195).

Piper, D.Z., 1974. Rare earth elements in the sedimentary cycle: a summary. *Chemical geology*, *14*(4), pp.285-304.

Pirrie, D. and Marshall, J.D., 1990. High-paleolatitude late Cretaceous paleotemperatures: new data from James Ross Island, Antarctica. *Geology*, *18*(1), pp.31-34.Plank, T. and Langmuir, C.H., 1998. The chemical composition of subducting sediment and its consequences for the crust and mantle. *Chemical geology*, *145*(3-4), pp.325-394.

Porrenga, D.H., 1967. Glauconite and chamosite as depth indicators in the marine environment. *Marine Geology*, *5*(5-6), pp.495-501.

Posamentier, H.W., Jervey, M.T. and Vail, P.R., 1988. Eustatic controls on clastic deposition I—conceptual framework.

Posamentier, H.W. and Walker, R.G., 2006. *Facies models revisited*. SEPM Society for Sedimentary Geology.

Posenato, R., Crippa, G., de Winter, N.J., Frijia, G. and Kaskes, P., 2022. Microstructures and sclerochronology of exquisitely preserved Lower Jurassic lithiotid bivalves: Paleobiological and paleoclimatic significance. *Palaeogeography, Palaeoclimatology, Palaeoecology*, *602*, p.111162.

Powell, C.M., Roots, S.R. and Veevers, J.J., 1988. Pre-breakup continental extension in East Gondwanaland and the early opening of the eastern Indian Ocean. *Tectonophysics*, *155*(1-4), pp.261-283.

Prabhakar, K.N. and Zutshi, P.L., 1993. Evolution of southern part of Indian east coast basins. *Geological Society of India*, *41*(3), pp.215-230.

Prothero, D.R. and Schwab, F., 1996. An introduction to sedimentary rocks and stratigraphy. *Sedimentary Geology, New York, WH Freeman and Company*, *575*.

Pucéat, E., Lécuyer, C., Donnadieu, Y., Naveau, P., Cappetta, H., Ramstein, G., Huber, B.T. and Kriwet, J., 2007. Fish tooth δ18O revising Late Cretaceous meridional upper ocean water temperature gradients. *Geology*, *35*(2), pp.107-110.

Radley, J.D. and Barker, M.J., 2000. Palaeoenvironmental significance of storm coquinas in a Lower Cretaceous coastal lagoonal succession (Vectis Formation, Isle of Wight, southern England). *Geological Magazine*, *137*(2), pp.193-205.

Radulović, V. and Ramamoorthy, K.R.,1992. Late Cretaceous (Early Maastrichtian) brachiopods from South India. *Senckenbergiana lethaea*, *72*, pp.77-89.

Rai, J., Malarkodi, N. and Singh, A.B.H.A., 2013. Terminal Maastrichtian age calcareous nannofossils preceding K/T mass extinction from Ariyalur Formation, Vridhhachalam area, south India. *Special Publication Geological Society of India*, *1*, pp.1-15.

Ramanathan, R.M. and Rao, V.R., 1984. Quantitative Study On The Assemblages Of Cretaceous Planktonic Foraminiferal Genus Rotalipora. *Journal of the Palaeontological Society of India*, *29*, pp.6-18.

Ramkumar, M., 1996. Occurrence of hardgrounds in the Kallankurichchi Formation (Lower Maestrichtian), Ariyalur Group, Tiruchy District, South India and their significance. *Indian Journal of Petroleum Geology*, *5*(2), pp.83-97.

Ramkumar, M., 2000. Lithostratigraphy, depositional history and constraints on sequence stratigraphy of the Kallankurichchi Formation (Lower Maastrichtian) Ariyalur group, South India. *Geološki anali Balkanskoga poluostrva*, *63*(1), pp.19-42.

Ramkumar, M., 2006. A storm event during the Maastrichtian in the Cauvery basin, south India. *Geološki anali Balkanskoga poluostrva*, *67*(1), pp.35-40.

Ramkumar, M., Stüben, D. and Berner, Z., 2009. in the Cauvery Basin, South India: implications on palaeoclimate, productivity and weathering. *CURRENT SCIENCE*, *97*(2), p.262.

Ramkumar, M., Stüben, D. and Berner, Z., 2004. Lithostratigraphy, depositional history and sea level changes of the Cauvery Basin, southern India. *Geološki anali Balkanskoga poluostrva*, *65*(1), pp.1-27.

Ramkumar, M., Siddiqui, N.A., Rai, J., Desai, B.G. and Menier, D., 2021. Opportunistic colonizers in the Kallankurichchi Formation, Cauvery Basin, South India: Implications on Maastrichtian environmental stress. *Geological Journal*, *56*(4), pp.2060-2071.

Rangaraju, M.K., A., A., Prabhakar, K.N., 1993. Tectono-stratigraphy, structural styles, evolutionary model and hydrocarbon habitat, Cauvery and Palar basins, in: Biswas, S.K., Dave, A., Garg, P., Pandey, J., Maithani, A., Thomas, N.J. (Eds.), Proc. Second Seminar on Petroliferous Basins of India: Dehra Dun. *Indian Petroleum Publication*, pp. 371–388.

Rao, L.R., 1957, June. Fossil foraminifera from the cretaceous rocks of South India: Part I. Ariyalur area orbitoids. In *Proceedings/Indian Academy of Sciences* (Vol. 45, No. 6, pp. 263-281). New Delhi: Springer India.

Rao, C.O. & Naqvi, LH. (1977) Petrography, geochemistryand factor analysis of a Lower Ordovician subsurface sequence, Tasmania, Australia. 1. *sedim. Petrol.* 47, pp.1036-1055.

Rao, A.S. and Sastry, A.R., 1964. An account of the flowering plants of Indore district in Madhya Pradesh. *Nelumbo-The Bulletin of the Botanical Survey of India*, pp.267-286.

Rasheed, D.A. and Ravindran, C.N., 1978. Foraminiferal biostratigraphic studies of the Ariyalur Group of Tiruchirapalli Cretaceous rocks of Tamil Nadu State. In *Proceedings 7th Colloquium on Micropalaeontology and Stratigraphy* (pp. 321-336).

Reading H.G., 1996 Sedimentary Environments: Processes, Facies and Stratigraphy- Third Edition, Blackwell publishing.

Reading, H.G. ed., 2009. *Sedimentary environments: processes, facies and stratigraphy*. John Wiley & Sons.

Reddy, A.N., Jaiprakash, B.C., Rao, M.V., Chidambaram, L. and Bhaktavatsala, K.V., 2013, June. Sequence stratigraphy of late Cretaceous successions in the Ramnad sub-basin, Cauvery Basin, India. In *Proc. XXIII Indian Colloquium on Micropaleontology and Stratigraphy and International Symposium on Global Bioevents in Earth's History. Geol. Soc. India Spec. Publ* (No. 1, pp. 78-97).

Reijmer, J.J.G., Mulder, T. and Borgomano, J., 2015. Carbonate slopes and gravity deposits. *Sedimentary Geology*, *317*, pp.1-8.

Remírez, M.N., Algeo, T.J., Shen, J., Liu, J., Gilleaudeau, G. and Zhou, L., 2024. Low-salinity conditions in "marine" Late Triassic-Early Jurassic Neuquén Basin of Argentina: Challenges in paleosalinity interpretation. *Palaeogeography, Palaeoclimatology, Palaeoecology*, p.112216.

Rimmer, S.M., 2004. Geochemical paleoredox indicators in Devonian–Mississippian black shales, central Appalachian Basin (USA). *Chemical Geology*, *206*(3-4), pp.373-391.

Riquier, L., Tribovillard, N., Averbuch, O., Joachimski, M.M., Racki, G., Devleeschouwer, X. and Riboulleau, A., 2005. Productivity and bottom water redox conditions at the Frasnian-Famennian boundary on both sides of the Eovariscan Belt: constraints from trace-element geochemistry. In *Developments in Palaeontology and Stratigraphy* (Vol. 20, pp. 199-224). Elsevier.

Robinson, P., 1980. Determination of calcium, magnesium, manganese, strontium, sodium and iron in the carbonate fraction of limestones and dolomites. *Chemical Geology*, *28*, pp.135-146.

Rodine, J.D. and Johnson, A.M., 1976. The ability of debris, heavily freighted with coarse clastic materials, to flow on gentle slopes. *Sedimentology*, *23*(2), pp.213-234.

Rodland, D.L., Kowalewski, M., Dettman, D.L., Flessa, K.W., Atudorei, V. and Sharp, Z.D., 2003. High-resolution analysis of δ18O in the biogenic phosphate of modern and fossil lingulid brachiopods. *The Journal of geology*, *111*(4), pp.441-453.

Rodríguez-Tovar, F.J., Uchman, A., Martín-Algarra, A. and O'Dogherty, L., 2009. Nutrient spatial variation during intrabasinal upwelling at the Cenomanian–Turonian oceanic anoxic event in the westernmost Tethys: An ichnological and facies approach. *Sedimentary Geology*, *215*(1-4), pp.83-93.

Rohrlich, V., Price, N.B. and Calvert, S.E., 1969. Chamosite in the recent sediments of Loch Etive, Scotland. *Journal of Sedimentary Research*, *39*(2).

Ross, D.J. and Bustin, R.M., 2009. Investigating the use of sedimentary geochemical proxies for paleoenvironment interpretation of thermally mature organic-rich strata: Examples from

the Devonian–Mississippian shales, Western Canadian Sedimentary Basin. *Chemical Geology*, *260*(1-2), pp.1-19.

Roy Choudhury, T., Banerjee, S., Khanolkar, S. and Meena, S.S., 2021. Paleoenvironmental conditions during the paleocene–eocene transition imprinted within the glauconitic giral member of the barmer basin, India. *Minerals*, *12*(1), p.56.

Roy Choudhury, T., Banerjee, S., Khanolkar, S., Saraswati, P.K. and Meena, S.S., 2021. Glauconite authigenesis during the onset of the Paleocene-Eocene Thermal Maximum: A case study from the Khuiala Formation in Jaisalmer Basin, India. *Palaeogeography, Palaeoclimatology, Palaeoecology*, *571*, p.110388.

Roy Choudhury, T., Khanolkar, S. and Banerjee, S., 2022. Glauconite authigenesis during the warm climatic events of Paleogene: Case studies from shallow marine sections of Western India. *Global and Planetary Change*, *214*, p.103857.

Roy Choudhury, T., Srimani, S., Mondal, I., Chakrabarty, A., Banerjee, S. and Sarkar, S., 2024. Berthierine authigenesis as grain pseudomorph? A new insight from the early Maastrichtian Kallankurichchi Formation, India. *Applied Clay Science*, *249*, p.107255.

Rudmin, M., Roberts, A.P., Horng, C.S., Mazurov, A., Savinova, O., Ruban, A., Kashapov, R. and Veklich, M., 2018. Ferrimagnetic iron sulfide formation and methane venting across the Paleocene-Eocene Thermal Maximum in shallow marine sediments, ancient West Siberian Sea. *Geochemistry, Geophysics, Geosystems*, *19*(1), pp.21-42.

Saltzman, E.S. and Barron, E.J., 1982. Deep circulation in the Late Cretaceous: oxygen isotope paleotemperatures from Inoceramus remains in DSDP cores. *Palaeogeography, Palaeoclimatology, Palaeoecology*, *40*(1-3), pp.167-181.

Samanta, P., Mukhopadhyay, S., Sen, A., Ghosh, N. and Bumby, A., 2022. Precambrian fans on opposite margins of an intracratonic rift basin; palaeogeography, palaeoclimate and provenance: Neoproterozoic Badami Group, Karnataka, India. *Sedimentary Geology*, *428*, p.106050.

Sanmartín, I., 2011. A paleogeographic history of the Southern Hemisphere.

Sarkar, S. and Koner, A., 2020. Ancient rip current records and their implications: an example from the Cretaceous Ukra Member, Kutch, India. *Journal of Palaeogeography*, *9*, pp.1-17.

Sarkar, S., Chakraborty, N., Mandal, A., Banerjee, S., Bose, P.K. and 2014. Siliciclastic–carbonate mixing modes in the river-mouth bar palaeogeography of the Upper Cretaceous Garudamangalam Sandstone (Ariyalur, India). *Journal of Palaeogeography*, *3*(3), pp.233-256.

Sarkar, S., Mazumder, R. and Bose, P.K., 1999. Changing bedform dynamics: some observations from Proto-Proterozoic Chaibasa Formation, India. *Journal of the Indian Association of Sedimentologists*, *18*, pp.31-40.

Sarkar, S., Banerjee, S., Eriksson, P.G. and Catuneanu, O., 2005. Microbial mat control on siliciclastic Precambrian sequence stratigraphic architecture: examples from India. *Sedimentary Geology*, *176*(1-2), pp.195-209.

Sarkar, S., Banerjee, S. and Chakraborty, S., 1995. Synsedimentary seismic signature in Mesoproterozoic Koldaha Shale, Kheinjua Formation, central India. *Indian Journal of Earth Science*, *22*, pp.158-164.

Sarkar, S., Bose, P.K. and Bandhyopadhayay, S., 1991. Intertidal occurrence of mesoscale scours in the Bay of Bengal, India, and their implications. *Sedimentary geology*, *75*(1-2), pp.29-37.

Sarkar, S., Bose, P.K. and Eriksson, P.G., 2011. Neoproterozoic tsunamiite: Upper Bhander Sandstone, Central India. *Sedimentary Geology*, *238*(1-2), pp.181-190.

Sarkar, S., Chakraborty, P.P., Bhattacharya, S.K. and Banerjee, S., 1998. C 12-Enrichment along intraformational unconformities within Proterozoic Bhander limestone, Son Valley, India and its implication. *Carbonates and evaporites*, *13*, pp.108-114.

Sarkar, S., Eriksson, P.G. and Chakraborty, S., 2004. Epeiric sea formation on Neoproterozoic supercontinent break-up: A distinctive signature in coastal storm bed amalgamation. *Gondwana Research*, *7*(2), pp.313-322.

Sastri, V.V. and Raiverman, V., 1968. On the basin study programme of the Cretaceous-Tertiary sediments of the Cauvery basin. *Cretaceous-Tertiary Formations of South India, Mem. Geol. Soc. India*, *2*, pp.143-152.

Sastri, V.V., Sinha, R.N., Singh, G. and Murti, K.V.S., 1973. Stratigraphy and tectonics of sedimentary basins on east coast of peninsular India. *AAPG Bulletin*, *57*(4), pp.655-678.

Sastri, V.V., 1980. Stratigraphy and sediments of some coastal basins of India-an overview. Bulletin Oil and Natural Gas Commission 17(1), 269-276.

Sastri, V.V., Venkatachala, B.S. and Narayanan, V., 1981. The evolution of the east coast of India. *Palaeogeography, Palaeoclimatology, Palaeoecology*, *36*(1-2), pp.23-54.

Sastry, M.V.A., Rao, B.R.J. and Mamgain, V. D., 1965. Campanion horizon in Ariyalur stage of Trichinopoly Cretaceous, Bull. Geol. Soc. of India 2 (4), 88-90.

Sastry, M.V.A., Rao, B.R.J. and Mamgain, V.D., 1968. Biostratigraphic zonation of the Upper Cretaceous Formation of Trichinopoly district, South India. Memoir of the Geological Society of India 2, 10-17.

Sastry, M.V.A. and Mamgain, V.D., 1971. The marine Mesozoic formations of India. *Rec. Geol. Surv. India*, *101*(2), p.62177.

Sastry, M.V.A. and Misra, R.S., 1977. Cretaceous microfauna of India. *Biovigyanam*, *3*, pp.171-192.

Schlager, W. and Philip, J., 1990. Cretaceous carbonate platforms. *Cretaceous resources, events and rhythms: background and plans for research*, pp.173-195.

Schoene, B. and Surge, D.M., 2012. Treatise online no. 46: part N, revised, volume 1, chapter 14: bivalve sclerochronology and geochemistry. *Treatise online*.

Scholle, P.A., 1973. Carbonate Rock Constituents. Textures. Cements and Porosities. *American Association of Petroleum Geologists Memoir*, *27*.

Scholle, P.A. and Ulmer-Scholle, D.S., 2003. *A color guide to the petrography of carbonate rocks: grains, textures, porosity, diagenesis, AAPG Memoir 77* (Vol. 77). AAPG.

Schöne, B.R., Rodland, D.L., Fiebig, J., Oschmann, W., Goodwin, D., Flessa, K.W. and Dettman, D., 2006. Reliability of multitaxon, multiproxy reconstructions of environmental conditions from accretionary biogenic skeletons. *The Journal of Geology*, *114*(3), pp.267-285.

Schöne, B.R. and Surge, D., 2014. Bivalve shells: ultra high-resolution paleoclimate archives. *Past Global Changes Magazine*, *22*(1), pp.20-21.

Scoffin, T.P., 1987. Carbonate sediments and rocks: Glasgow. *Blackie, 274p*.

Scotese, C.R., 2015. Some thoughts on global climate change: the transition from icehouse to hothouse. *Paleomap project*, *21*(2).

Šegvić, B., Zanoni, G. and Moscariello, A., 2020. On the origins of eogenetic chlorite in verdine facies sedimentary rocks from the Gabon Basin in West Africa. *Marine and Petroleum Geology*, *112*, p.104064.

Seilacher, A., 1985. Bivalve morphology and function. *Series in Geology, Notes for Short Course*, *13*, pp.88-101.

Sellwood, B.W., Price, G.D. and Valdest, P.J., 1994. Cooler estimates of Cretaceous temperatures. *Nature*, *370*(6489), pp.453-455.

Shackleton, N. J., and Kennett, J. P., 1975, Paleotemperature history of the Cenozoic and the initiation of Antarctic glaciation: Oxygen and carbon isotope analyses in DSDP sites 277, 279, and 281, in Initial reports of the Deep Sea Drilling Project, Volume 29: Washington, D. C., U.S. Government Printing Office, p. 743–755.

Shanmugam, G. and Wang, Y., 2015. The landslide problem. *Journal of Palaeogeography*, *4*(2), pp.109-166.

Sheldon, N.D. and Retallack, G.J., 2003. Low oxygen levels in earliest Triassic soils: Comment and Reply: REPLY. *Geology*, *31*(1), pp.20-21.

Sorby, H.C., 1879. The structure and origin of limestones. *The Popular science review*, *3*(9), pp.134-137.

Sørensen, A.M., Ullmann, C.V., Thibault, N. and Korte, C., 2015. Geochemical signatures of the early Campanian belemnite Belemnellocamax mammillatus from the Kristianstad Basin in Scania, Sweden. *Palaeogeography, palaeoclimatology, palaeoecology*, *433*, pp.191-200.

Spicer, R.A. and Parrish, J.T., 1990. Late Cretaceous–early Tertiary palaeoclimates of northern high latitudes: a quantitative view. *Journal of the Geological Society*, *147*(2), pp.329-341.

Srimani, S., 2024. Scree conglomerate and its derivatives in the Upper Cretaceous Kallankurichchi Limestone, Ariyalur Group, Cauvery Basin, South India. *Journal of Palaeogeography*.

Srimani, S., 2024a. Characterization of shellbanks of the Kallankurichchi Limestone Formation, Ariyalur Group: A physico-chemical approach. In: *Geology of Cauvery Basin in South India, Taylor and Francis Group, E*dited by Jain S. and Chakraborty N. (submitted revised version).

Srimani, S., Das, A. and Sarkar, S. 2020. Siliciclastic scree and its derivatives in the Late Cretaceous Kallankurichchi Limestone, India. *Humboldt Kolleg Conference*, Abstract Volume, pp.71.

Srimani, S., Koner, A. and Choudhuri, A. 2022. Isotope and Trace Element Signatures of Paleoenvironment of *Gryphea* Shell Banks in the Kallankurichchi Limestone, Ariyalur Group, Cauvery Basin, India. *21st International Sedimentological Congress, Beijing, China*, Abstract Volume, pp.1945.

Srimani, S., Koner, A., Choudhuri, A., Sarkar, S. 2022a. Distinctive petrography and geochemistry of facies in Kallankuruchi limestone Formation, Cauvery Basin, India. *38th Convention of Indian Association of Sedimentologist, Delhi University*, Abstract Volume, pp.24.

Srimani, S., Mandal, S. and Sarkar, S., 2021. Facies and Microfacies Analysis of Kallankurichchi Formation, Ariyalur Group with an Inkling of Sequence Stratigraphy. *Mesozoic Stratigraphy of India: A Multi-Proxy Approach*, pp.529-552.

Srivastava, D.K., 2003. A new species of Cassiduloid echinoid Gongrochanus Kier, 1962 from the late Cretaceous (Maastrichtian) rocks of the Ariyalur area, Tamilnadu, India. *J Palaeontol Soc India*, *48*, pp.59-64.

Srivastava, R.P. and Tewari, B.S., 1967. Biostratigraphy of the Ariyalur stage, Cretaceous of Trichinopoly. *Journal of the Palaeontological Society of India*, *12*, pp.48-54.

Steuber, T., 1999. Isotopic and chemical intra-shell variations in low-Mg calcite of rudist bivalves (Mollusca-Hippuritacea): disequilibrium fractionations and late Cretaceous seasonality. *International Journal of Earth Sciences*, *88*, pp.551-570.

Stillings, L.L. and Brantley, S.L., 1995. Feldspar dissolution at 25 C and pH 3: Reaction stoichiometry and the effect of cations. *Geochimica et Cosmochimica Acta*, *59*(8), pp.1483-1496.

Stoliczka, F., 1867. Cretaceous Fauna of Southern India. Volume 2. The Gastropoda. Palaeontologica Indica, being Figures and Descriptions of the Organic Remains Procured during the Progress of the Geological Survey of India. *Memoirs of the Geological Survey of India, Calcutta*.

Stoliczka, F., 1871. Cretaceous fauna of southern India. 3, The Pelecypoda, with a review of all known genera of this class, fossil and Recent. *Geol. Surv. India, Palaeont. Indica*, *537*.

Stoliczka, F., 1873. Cretaceous fauna of southern India. *Memoirs of the Geological Survey of India*, *4*, pp.66-69.

Sturesson, U., Heikoop, J.M. and Risk, M.J., 2000. Modern and Palaeozoic iron ooids—a similar volcanic origin. *Sedimentary Geology*, *136*(1-2), pp.137-146.

Sun, X., Higgins, J. and Turchyn, A.V., 2016. Diffusive cation fluxes in deep-sea sediments and insight into the global geochemical cycles of calcium, magnesium, sodium and potassium. *Marine Geology*, *373*, pp.64-77.

Sundaram, R. and Rao, P.S., 1979. Lithostratigraphic classification of Uttattur and Trichinopoly groups of Upper Cretaceous rocks of Tiruchirapalli district, Tamil Nadu.

Sundaram, R. and Rao, P.S., 1986. Lithostratigraphy of Cretaceous and Palaeocene rocks of Tiruchirapalli District, Tamil Nadu, South India. *Records of the Geological Survey of India*, *115*(5), pp.9-23.

Sundaram, R., Henderson, R.A., Ayyasami, K. and Stilwell, J.D., 2001. A lithostratigraphic revision and palaeoenvironmental assessment of the Cretaceous System exposed in the onshore Cauvery Basin, southern India. *Cretaceous Research*, *22*(6), pp.743-762.

Surge, D. and Lohmann, K.C., 2008. Evaluating Mg/Ca ratios as a temperature proxy in the estuarine oyster, Crassostrea virginica. *Journal of Geophysical Research: Biogeosciences*, *113*(G2).

Surge, D.M., Lohmann, K.C. and Goodfriend, G.A., 2003. Reconstructing estuarine conditions: oyster shells as recorders of environmental change, Southwest Florida. *Estuarine, Coastal and Shelf Science*, *57*(5-6), pp.737-756.

Sutton, S.J., Maynard, J.B. and Sutton, S., 1996. Basement unconformity control on alteration, St. Francois Mountains, SE Missouri. *The Journal of Geology*, *104*(1), pp.55-70.

Sverjensky, D.A., 1984. Europium redox equilibria in aqueous solution. *Earth and Planetary Science Letters*, *67*(1), pp.70-78.

Swift, D.J., Figueiredo, A.G., Freeland, G.L. and Oertel, G.F., 1983. Hummocky cross-stratification and megaripples; a geological double standard?. *Journal of Sedimentary Research*, *53*(4), pp.1295-1317.

Tang, D., Shi, X., Jiang, G., Zhou, X. and Shi, Q., 2017. Ferruginous seawater facilitates the transformation of glauconite to chamosite: An example from the Mesoproterozoic Xiamaling Formation of North China. *American Mineralogist*, *102*(11), pp.2317-2332.

Tang, D., Shi, X., Ma, J., Jiang, G., Zhou, X. and Shi, Q., 2017. Formation of shallow-water glaucony in weakly oxygenated Precambrian ocean: An example from the Mesoproterozoic Tieling Formation in North China. *Precambrian Research*, *294*, pp.214-229.

Taylor, K.G., 1990. Berthierine from the non-marine Wealden (Early Cretaceous) sediments of south-east England. *Clay Minerals*, *25*(3), pp.391-399.

Taylor, K.G. and Curtis, C.D., 1995. Stability and facies association of early diagenetic mineral assemblages; an example from a Jurassic ironstone-mudstone succession, UK. *Journal of Sedimentary Research*, *65*(2a), pp.358-368.

Taylor, S.R. and McLennan, S.M., 1985. The continental crust: its composition and evolution.

Tewari, A., Hart, M.B. and Watkinson, M.P., 1996. A revised lithostratigraphic classification of the Cretaceous rocks of the Trichinopoly district, Cauvery basin, Southeast India. In *Contributions to the XV Indian colloquium on micropalaeontology and stratigraphy* (pp. 789-800). Dehra Dun: Palaeontological Society of India.

Tewari, A., Hart, M.B. and Watkinson, M.P., 1996. Foraminiferal recovery after the mid-Cretaceous oceanic anoxic events (OAEs) in the Cauvery Basin, southeast India. *Geological Society, London, Special Publications*, *102*(1), pp.237-244.

Tewari, B.S., Srivastava and R. P.,1965. On the occurrence of Globotruncana in Ariyalur stage of Trichinopoly Cretaceous, Current Science 34 (5), 150-151.

Thébault, J., Schöne, B.R., Hallmann, N., Barth, M. and Nunn, E.V., 2009. Investigation of Li/Ca variations in aragonitic shells of the ocean quahog Arctica islandica, northeast Iceland. *Geochemistry, Geophysics, Geosystems*, *10*(12).

Tinterri, R.O., 2011. Combined flow sedimentary structures and the genetic link between sigmoidal-and hummocky-cross stratification. *GeoActa*, *10*(4), pp.1-43.

Tostevin, R., Shields, G.A., Tarbuck, G.M., He, T., Clarkson, M.O. and Wood, R.A., 2016. Effective use of cerium anomalies as a redox proxy in carbonate-dominated marine settings. *Chemical Geology*, *438*, pp.146-162.

Toth, T.A. and Fritz, S.J., 1997. An Fe-berthierine from a cretaceous laterite: Part I. Characterization. *Clays and Clay Minerals*, *45*(4), pp.564-579.

Tounekti, A., Boukhalfa, K., Choudhury, T.R., Soussi, M. and Banerjee, S., 2021. Global and local factors behind the authigenesis of Fe-silicates (Glauconite/Chamosite) in Miocene strata of Northern Tunisia. *Journal of African Earth Sciences*, *184*, p.104342.

Tourtelot, H.A. and Rye, R.O., 1969. Distribution of oxygen and carbon isotopes in fossils of Late Cretaceous age, Western Interior region of North America. *Geological Society of America Bulletin*, *80*(10), pp.1903-1922.

Tribovillard, N., Algeo, T.J., Lyons, T. and Riboulleau, A., 2006. Trace metals as paleoredox and paleoproductivity proxies: an update. Chemical geology, 232(1-2), pp.12-32.

Tucker, M.E., 1985. Shallow-marine carbonate facies and facies models. *Geological Society, London, Special Publications*, *18*(1), pp.147-169.

Tucker, M.E. and Wright, V.P., 2009. *Carbonate sedimentology*. John Wiley & Sons.

Tyrrell, T., 1999. The relative influences of nitrogen and phosphorus on oceanic primary production. *Nature*, *400*(6744), pp.525-531.

Urey, H.C., Lowenstam, H.A., Epstein, S. and McKinney, C.R., 1951. Measurement of paleotemperatures and temperatures of the Upper Cretaceous of England, Denmark, and the southeastern United States. *Geological Society of America Bulletin*, *62*(4), pp.399-416.

Van Houten, F.B. and Bhattacharyya, D.P., 1982. Phanerozoic oolitic ironstones--Geologic record and facies model. *Annual Review of Earth and Planetary Sciences*, *10*(1), pp.441-457.

Van Houten, F.B. and Purucker, M.E., 1984. Glauconitic peloids and chamositic ooids-favorable factors, constraints, and problems. *Earth-Science Reviews*, *20*(3), pp.211-243.

Van Houten, F.B. and Purucker, M.E., 1985. On the origin of glauconitic and chamositic granules. *Geo-Marine Letters*, *5*, pp.47-49.

Vander Putten, E., Dehairs, F., Keppens, E. and Baeyens, W., 2000. High resolution distribution of trace elements in the calcite shell layer of modern Mytilus edulis: environmental and biological controls. *Geochimica et Cosmochimica Acta*, *64*(6), pp.997-1011.

Veizer, J. and Demovic, R., 1974. Strontium as a tool in facies analysis. Journal of Sedimentary Research, 44(1), pp.93-115.

Velde, B., 2003. *Green clay minerals* (Vol. 7, p. 407).

Venkatachalapathy, R. and Ragothaman, V., 1995. A foraminiferal zonal scheme for the mid-Cretaceous sediments of the Cauvery Basin, India. *Cretaceous Research*, *16*(4), pp.415-433.

Vincent et al., 2006 Vincent, B., Rambeau, C., Emmanuel, L. and Loreau, J.P., 2006. Sedimentology and trace element geochemistry of shallow-marine carbonates: an approach to paleoenvironmental analysis along the Pagny-sur-Meuse Section (Upper Jurassic, France). *Facies*, *52*, pp.69-84.

Walliser, E.O., Mertz-Kraus, R. and Schöne, B.R., 2018. The giant inoceramid Platyceramus platinus as a high-resolution paleoclimate archive for the Late Cretaceous of the Western Interior Seaway. *Cretaceous Research*, *86*, pp.73-90.

Walker, R.G., 1984. Turbidites and associated coarse clastic deposits. *Facies models. 2nd ed., 176*.

Walker, R.G., 1990. Facies modeling and sequence stratigraphy: perspective. *Journal of Sedimentary Research*, *60*(5).

Walker, R.G., 1992. Facies model: response to sea level change. *Geol. Asso. Canada*, *409*.

Wang, N., French, D., Dai, S., Graham, I.T., Zhao, L., Song, X., Zheng, J., Gao, Y., Wang, Y., 2023a. Origin of chamosite and berthierine: Implications for volcanic-ash-derived Nb-Zr-REY-Ga mineralization in the Lopingian sequences from eastern Yunnan, SW China. J. Asian Earth Sci. 253, 105703.

Wang, L., Zhang, Y., Xing, E., Peng, Y. and Yu, D., 2020. Distribution of Trace Elements, Sr-C Isotopes, and Sedimentary Characteristics as Paleoenvironmental Indicator of the Late Permian Linxi Formation in the Linxi Area, Eastern Inner Mongolia. *Journal of Chemistry*, *2020*, pp.1-17.

Wang, N., French, D., Dai, S., Graham, I.T., Zhao, L., Song, X., Zheng, J., Gao, Y. and Wang, Y., 2023. Origin of chamosite and berthierine: Implications for volcanic-ash-derived Nb-Zr-REY-Ga mineralization in the Lopingian sequences from eastern Yunnan, SW China. *Journal of Asian Earth Sciences*, *253*, p.105703.

Watkinson, M.P., Hart, M.B. and Joshi, A., 2007. Cretaceous tectonostratigraphy and the development of the Cauvery Basin, southeast India. *Petroleum Geoscience*, *13*(2), pp.181-191.

Wefer, G. and Berger, W.H., 1991. Isotope paleontology: growth and composition of extant calcareous species. *Marine geology*, *100*(1-4), pp.207-248.

Wei, W. and Algeo, T.J., 2020. Elemental proxies for paleosalinity analysis of ancient shales and mudrocks. *Geochimica et Cosmochimica Acta*, *287*, pp.341-366.

Whittaker, S.G. and Kyser, T.K., 1993. Variations in the neodymium and strontium isotopic composition and REE content of molluscan shells from the Cretaceous Western Interior seaway. *Geochimica et Cosmochimica Acta*, *57*(16), pp.4003-4014.

Wignall, P.B. and Twitchett, R.J., 1996. Oceanic anoxia and the end Permian mass extinction. *Science*, *272*(5265), pp.1155-1158.

Williams, G.E., 1979. Sedimentology, stable-isotope geochemistry and palaeoenvironment of dolostones capping late Precambrian glacial sequences in Australia. *Journal of the Geological Society of Australia*, *26*(7-8), pp.377-386.

Wilson, J.L., 2012. *Carbonate facies in geologic history*. Springer Science & Business Media.

Wolfe, J.A. and Upchurch Jr, G.R., 1987. North American nonmarine climates and vegetation during the Late Cretaceous. *Palaeogeography, Palaeoclimatology, Palaeoecology*, *61*, pp.33-77.

Wright, V.P., 1990. Equatorial aridity and climatic oscillations during the early Carboniferous, southern Britain. *Journal of the Geological Society*, *147*(2), pp.359-363.

Wright, V.P. and Tucker, M., 1990. Carbonate sediments and limestones: constituents. Carbonate Sedimentology. Blackwell, Oxford, pp.1-27.

Li, X., Gang, W., Yao, J., Gao, G., Wang, C., Li, J., Liu, Y., Guo, Y. and Yang, S., 2020. Major and trace elements as indicators for organic matter enrichment of marine carbonate rocks: A case study of Ordovician subsalt marine formations in the central-eastern Ordos Basin, North China. *Marine and Petroleum Geology*, *111*, pp.461-475.

Yadagiri, P. and Ayyasami, K., 1979. A new stegosaurian dinosaur from Upper Cretaceous sediments of south India. *Geological Society of India*, *20*(11), pp.521-530.

Yan, H., Shao, D., Wang, Y. and Sun, L., 2013. Sr/Ca profile of long-lived Tridacna gigas bivalves from South China Sea: A new high-resolution SST proxy. *Geochimica et Cosmochimica Acta*, *112*, pp.52-65.

Yang, W., 2007. Transgressive wave ravinement on an epicontinental shelf as recorded by an Upper Pennsylvanian soil-nodule conglomerate-sandstone unit, Kansas and Oklahoma, USA. *Sedimentary Geology*, *197*(3-4), pp.189-205.

Young, T.P., 1989. Phanerozoic ironstones: an introduction and review. *Geological Society, London, Special Publications*, *46*(1), pp.ix-xxv.

Yuan, G., Cao, Y., Gluyas, J. and Jia, Z., 2017. Reactive transport modeling of coupled feldspar dissolution and secondary mineral precipitation and its implication for diagenetic interaction in sandstones. *Geochimica et Cosmochimica Acta*, *207*, pp.232-255.

Yuan, G., Cao, Y., Gluyas, J., Li, X., Xi, K., Wang, Y., Jia, Z., Sun, P. and Oxtoby, N.H., 2015. Feldspar dissolution, authigenic clays, and quartz cements in open and closed sandstone geochemical systems during diagenesis: Typical examples from two sags in Bohai Bay Basin, East China. *AAPG Bulletin*, *99*(11), pp.2121-2154.

Yuan, G., Cao, Y., Schulz, H.M., Hao, F., Gluyas, J., Liu, K., Yang, T., Wang, Y., Xi, K. and Li, F., 2019. A review of feldspar alteration and its geological significance in sedimentary basins: From shallow aquifers to deep hydrocarbon reservoirs. *Earth-science reviews*, *191*, pp.114-140.

Zakharov, Y.D., Popov, A.M., Shigeta, Y., Smyshlyaeva, O.P., Sokolova, E.A., Nagendra, R., Velivetskaya, T.A. and Afanasyeva, T.B., 2006. New Maastrichtian oxygen and carbon

isotope record: Additional evidence for warm low latitudes. *Geosciences Journal*, *10*, pp.347-367.

Zakharov, Y.D., Shigeta, Y., Nagendra, R., Safronov, P.P., Smyshlyaeva, O.P., Popov, A.M., Velivetskaya, T.A. and Afanasyeva, T.B., 2011. Cretaceous climate oscillations in the southern palaeolatitudes: New stable isotope evidence from India and Madagascar. *Cretaceous Research*, *32*(5), pp.623-645.

Zakharov, Y.D., Shigeta, Y., Tanabe, K., Iba, Y., Smyshlyaeva, O.P., Sokolova, E.A., Popov, A.M., Velivetskaya, T.A. and Afanasyeva, T.B., 2007. Campanian climatic change: isotopic evidence from Far East, North America, North Atlantic and Western Europe. *Acta Geologica Sinica-English Edition*, *81*(6), pp.1049-1069.

Zhang, K. and Shields, G.A., 2022. Sedimentary Ce anomalies: Secular change and implications for paleoenvironmental evolution. *Earth-Science Reviews*, *229*, pp.104015.

Zhang, L., Hay, W.W., Wang, C. and Gu, X., 2019. The evolution of latitudinal temperature gradients from the latest Cretaceous through the Present. *Earth-Science Reviews*, *189*, pp.147-158.

Zhao, J., Jin, Z., Jin, Z., Geng, Y., Wen, X. and Yan, C., 2016. Applying sedimentary geochemical proxies for paleoenvironment interpretation of organic-rich shale deposition in the Sichuan Basin, China. *International Journal of Coal Geology*, *163*, pp.52-71.

Zhao, Y., Wei, W., Santosh, M., Hu, J., Wei, H., Yang, J., Liu, S., Zhang, G., Yang, D. and Li, S., 2022. A review of retrieving pristine rare earth element signatures from carbonates. *Palaeogeography, Palaeoclimatology, Palaeoecology*, *586*, p.110765.